



Epithelial folding and migration

Aurélien Villedieu

► To cite this version:

Aurélien Villedieu. Epithelial folding and migration. Cellular Biology. Sorbonne Université, 2019. English. NNT : 2019SORUS400 . tel-03139853

HAL Id: tel-03139853

<https://theses.hal.science/tel-03139853>

Submitted on 12 Feb 2021

HAL is a multi-disciplinary open access archive for the deposit and dissemination of scientific research documents, whether they are published or not. The documents may come from teaching and research institutions in France or abroad, or from public or private research centers.

L'archive ouverte pluridisciplinaire **HAL**, est destinée au dépôt et à la diffusion de documents scientifiques de niveau recherche, publiés ou non, émanant des établissements d'enseignement et de recherche français ou étrangers, des laboratoires publics ou privés.



Inserm
La science pour la santé
From science to health



PSL

UPMC
SORBONNE UNIVERSITÉS



Université Pierre et Marie Curie

École doctorale Complexité du vivant

Institut Curie

U934/UMR3215 Génétique et biologie du développement

Équipe de Polarité, Division et Morphogenèse

Epithelial folding and migration

Aurélien VILLEDIEU

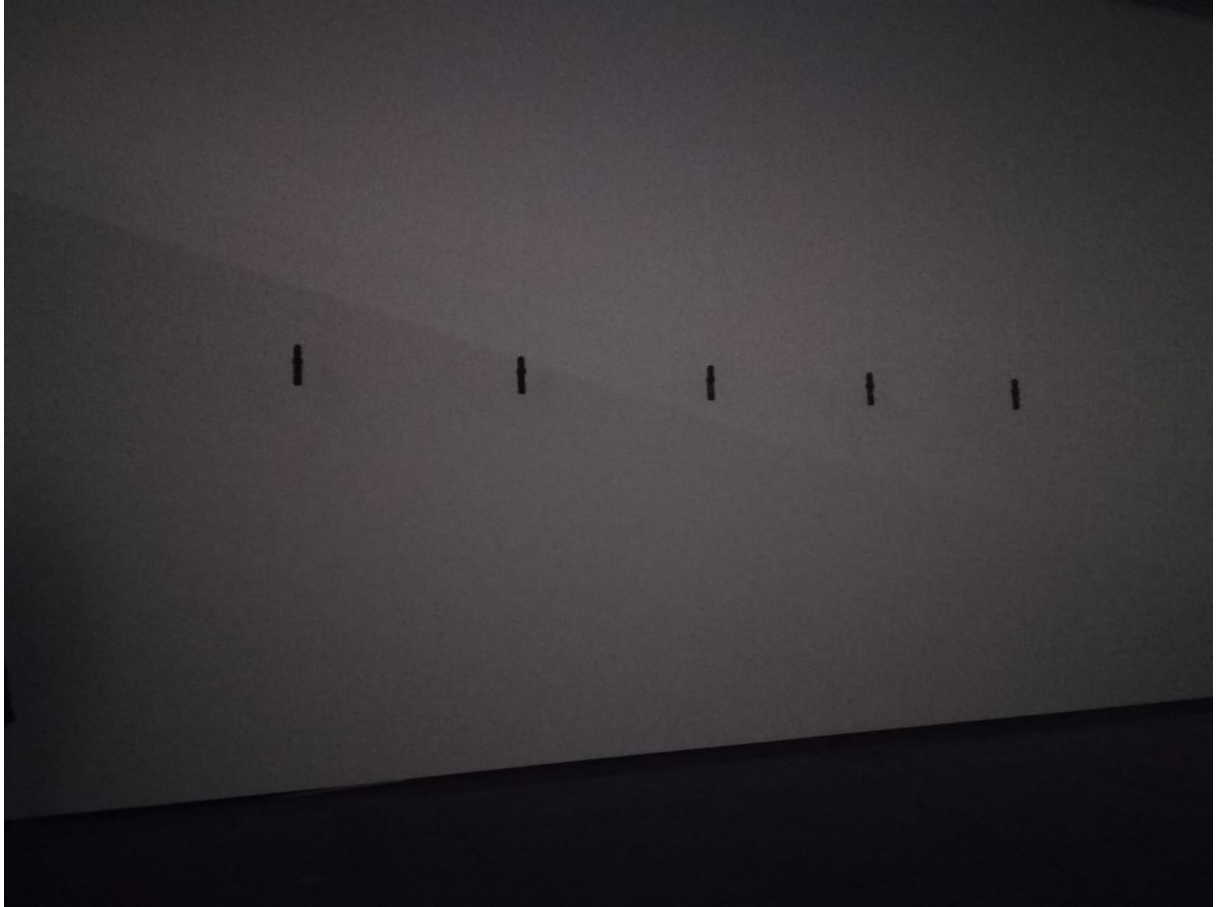
Thèse de doctorat de Biologie Cellulaire et Moléculaire

Dirigée par Yohanns BELLAÏCHE

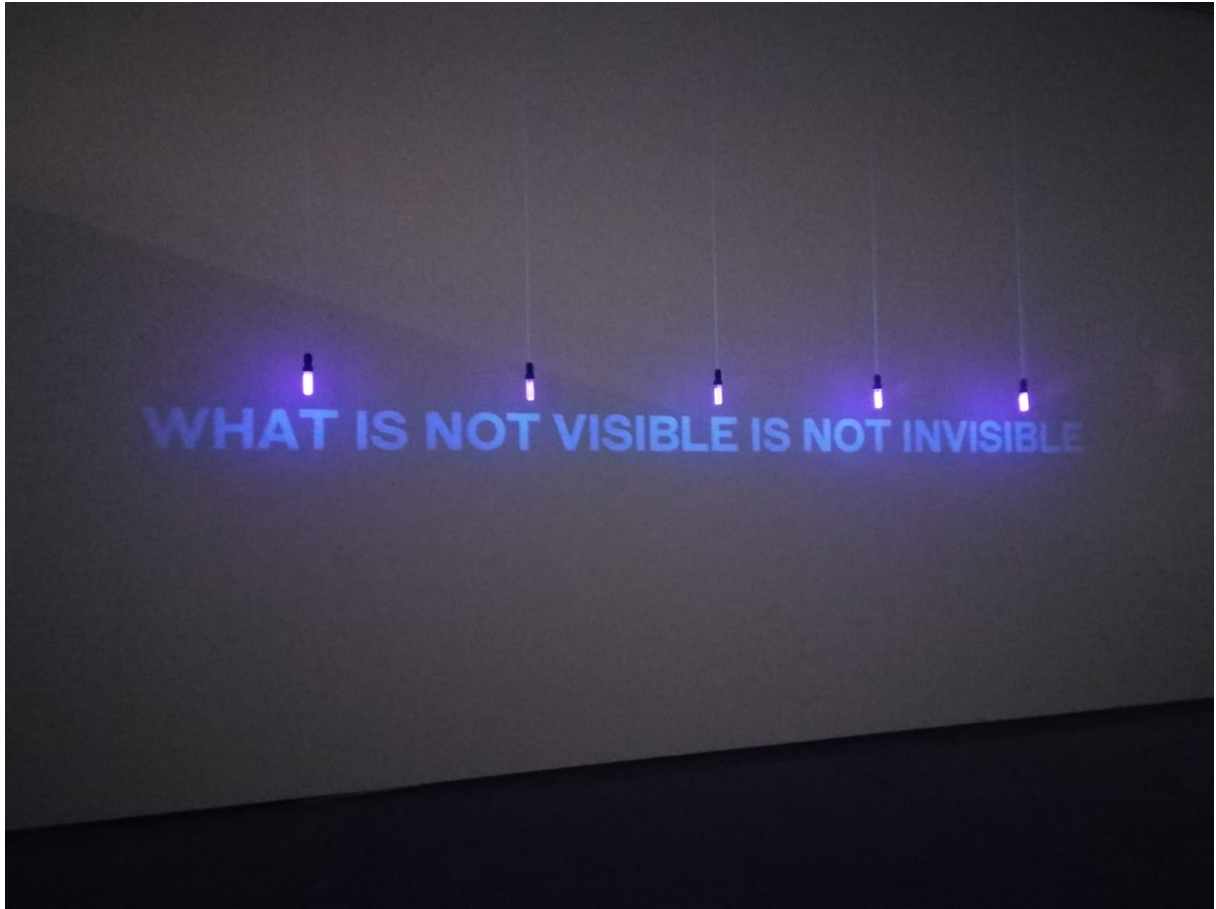
Soutenance le 9 octobre 2019, devant un jury composé de :

Yohanns BELLAÏCHE
Floris BOSVELD
Michel LABOUESSE
Roberto MAYOR
Jérôme SOLON
Magali SUZANNE
Xavier TRÉPAT

Directeur de thèse
Co-encadrant de thèse
Examineur et président du jury
Examineur
Rapporteur
Examinatrice
Rapporteur



Julien DISCRIT, *What is not Visible is not Invisible*, 2008, installation, invisible ink, UV light, presence detector, view of the installation at Mac-Val, 2018.



Julien DISCRIT, *What is not Visible is not Invisible*, 2008, installation, invisible ink, UV light, presence detector, view of the installation at Mac-Val, 2018.

ABSTRACT

Epithelial invagination and migration

In many developmental contexts, epithelial folding is accompanied by neighboring tissue flows towards the invagination site. To assess the idea of a long-range coupling between invagination and tissue flow, we have studied two macroscopic morphogenetic events happening during *Drosophila* metamorphosis: the invagination of the head-to-thorax boundary and the anterior dorsal thorax flow. Using large-scale laser ablations or locally disrupting MyosinII contractility in the invaginating region, we have found that head-thorax interface invagination is an active process which is providing a pulling force locally driving thorax flow. However, we have discovered that thorax flow is also partly autonomous, and thereby can actively provide a pushing force towards the invagination site. Using forward genetic methods, we have uncovered that thorax flow rely on collective migration on the apical extracellular matrix (ECM), depending on the secretion of the ZP protein Dumpy and on planar polarity cues. We have furthermore shown *in vivo* that regions of active thorax migration are specifically associated with low apical ECM deformation. Taken together, my PhD work uncovers a new mechanism coordinating tissue folding and tissue flow, and emphasizes the importance of tissue-matrix interaction in epithelial mechanics and morphogenesis.

RÉSUMÉ

Formation d'un pli et migration dans un épithélium

Dans de nombreux contextes développementaux, la formation d'un pli dans un épithélium est accompagnée d'un déplacement des tissus adjacents en direction de la zone d'invagination. Afin de tester l'idée d'un couplage à long rayon d'action entre un processus d'invagination et un flux tissulaire, nous avons étudié deux mouvements morphogénétiques qui surviennent durant la métamorphose de la drosophile : l'invagination de la frontière séparant la tête du thorax et un déplacement coordonné des cellules du thorax antérieur. En utilisant des techniques d'ablation laser ou de perturbations localisées de la contractilité de la Myosine II dans la région qui se plie, nous avons découvert que l'invagination de l'interface entre la tête et le thorax est un processus actif qui fournit une force de traction qui met localement en mouvement le thorax. Cependant, nous avons également découvert que le flux directionnel de thorax est en partie autonome, et qu'il peut être à l'origine d'une force de poussée active vers la zone d'invagination. En utilisant des méthodes de génétique, nous avons observé que le flux de thorax dépend d'une migration collective des cellules du thorax sur la matrice extracellulaire apicale. Cette migration s'appuie sur la sécrétion de la protéine Dumpy et sur des informations de polarité planaire. Qui plus est, nous avons montré *in vivo* que les régions thoraciques migrant activement sont spécifiquement associées à de faibles déformations de la matrice extracellulaire apicale. En conclusion, mes travaux de thèse mettent en exergue l'existence d'un nouveau mécanisme de couplage entre invagination et flux de tissu et illustrent l'importance de l'interaction entre le tissu et les matrices extracellulaires dans la mécanique et la morphogénèse épithéliales.

Acknowledgements

“Working in science is a serious thing, but we mainly do it for pleasure” was one of the first things Yohanns Bellaïche and Floris Bosveld told me when I first came to the lab searching for an internship. During the internship and the four years of PhD that followed this first meeting, Yohanns and Floris kept on communicating to me both their passionate enthusiasm for science and their scientific rigor, and I am truly thankful to them for that. Both of them were deeply involved in the supervision of my PhD work, and to use Yohanns and Floris’ favorite expressions, I think we shared a lot of scientific “excitement” and many “crazy ideas” – we also faced many challenges and disappointment, which I learnt are key aspects of the life of a researcher. I would like to thank Yohanns in particular for having given to me the opportunity to work on an exploratory subject, providing me both sufficient freedom and supervision to feel fulfilled in my research project. I am also grateful for his constant efforts of mentoring, communicating his passion for science, his creativity and his scientific integrity, involving me in paper review and grant writing processes, and giving me the opportunity to attend national and international meetings. I would also like to thank Floris for having contaminated me with his infectious passion for experimental work.

Bellaïche’s team and Curie Institute constitute a dream environment for an experimentalist interested in multidisciplinary approaches, providing almost unlimited material resources and a whole range of scientific expertise. I am very grateful for having had the opportunity to do my PhD in such an environment. I would like to thank Floris and Maria Balakireva for teaching me the basics of *Drosophila* genetics, Stéphane Rigaud for his patience in teaching the basics of Matlab coding, Boris Guirao for his lessons about PIV and tissue deformation, Isabelle Gaugué for her crash course on molecular biology, and Lorette Noiret for her help in statistics. I also thank the whole Bellaïche’s team, past and current members, for having given to me the opportunity to share their inspiring works and their expertise during labmeetings and lab retreats, for the inputs they have given on my works and the experimental help they have provided, and for the lively and friendly environment they have built every day in the lab. A special thanks to Isabelle Gaugué, Stéphane Pelletier and Amina Joudat, who have built many fly lines that I have used in my project, to Stéphane Rigaud, who has developed a

method of image projection that is at the basis of many quantifications I have carried out, to Maria Balakireva, whose work on mapping transcription factors expression in dorsal thorax has been a basis for designing experiments, and to Lale Alpar, who is and will be helping me finishing experiments after my PhD defense. Thanks as well to the whole 4th floor of the BDD (*Biologie du Développement* department), especially the fly teams (Allison Bardin's, Pierre Leopold's and Jean-René Huynh's teams) for the debates, the musics and the endless chats shared in the flyroom, and thanks to the fly facility platform for providing a necessary support on fly work.

I am particularly grateful to BDD imaging platform (in particular Olivier Leroy, Olivier Renaud and Aurélien Dauphin) for their very efficient help for setting up live-imaging and laser ablation experiments. Thanks as well for teaching me how to write macros in Fiji: I think this has considerably helped me adopting quantitative approaches during my PhD work. I would also like to highlight the quality of scientific interaction in BDD department: I am notably grateful for having had the opportunity to share my work with colleagues every year during the weekly unit seminars and during the unit retreats. Thanks as well to Jean-Léon Maître for organizing monthly meetings about tissue mechanics in Curie Institute, to the organizers of Drosphil'île-de-France meetings and to the organizers of MorphoClub in Pasteur Institute, who gave me the opportunity to share my PhD work.

I would as well like to thank all the external collaborators who have contributed to my PhD work. Catalina Manieu, who works in Patricio Olguin's team in Chili, has participated to the establishment of muscle laser ablation protocol and was the first to observe flow defects in *dsh*¹ mutant background. François Graner, Mélina Durande, Satoshi Yamashita and Hélène Delanoë-Ayari are currently working on models to help integrating the data I have obtained during my PhD. I also thank Edouard Hannezo and David Lubensky for the inspiring discussions about modelling that we have shared.

A big thanks to people who have contributed to the correction and the improvement of my PhD manuscript, especially Floris and Yohanns for the scientific and English corrections, and Bruno and Mario for their precious help in edition. I thank in advance the two reviewers, Jérôme Solon and Xavier Trépat, for their comment on the manuscript.

To finish with, I would also like to thank people who supported me during my PhD, and greatly participated in making these 4 years memorable. Thanks to all the *Merak bonhommes*, and especially the *Valentine-dis-nous-tout* team, for bringing me all over the world, from Voisine to Gaspésie, and for making everyday life special. I warmly thank Thomas, Zabeth,

Valentine, Anne, Céline, Coco and Laurent, Léa and Victor, Sarah, and all the persons that came (sometimes from far) to attend my oral presentation. Thanks to Maheva and Roberta for our music session on BDD rooftop. Thanks to all my friends, especially Maxime, Salomé and Pauline, and my family for their support. I particularly thank my mother for having communicated to me her passion for basic research and biology, and for always being a wise counselor during our daily phone calls. I thank my father, my sister and my brother for their constant support and love. A special thanks to Alban, who has segmented apical protrusions during a whole morning. Thanks to Julian, Mateo and Chiara for growing up more and more every day. Finally, I thank Bruno, the main contributor of my happiness during the four years of my PhD.

Table of Contents

ABSTRACT / RÉSUMÉ.....	7
<i>Acknowledgements</i>	9
Introduction	17
Organization of the introduction.....	21
A/ Generalities about epithelial tissues	21
1) Definition and relevance of epithelial structure.....	21
2) Generalities about epithelial apico-basal polarity and adhesion.....	22
a) Apico-basal cell polarity.....	22
b) Molecular mechanisms of apico-basal polarity.....	24
3) Generalities about epithelial planar cell polarity.....	24
a) Core PCP pathway (and vertebrate non-canonical Wnt pathway).....	25
b) Fat/Dachsous pathway and its link with core PCP pathway.....	26
c) Additional apical planar polarity cues.....	27
d) Basal planar polarity.....	28
4) Generalities about epithelial acto-myosin pools.....	28
a) Junctional cortical pool: from rings to supra-cellular acto-myosin cables.....	28
b) Junctional medial pool.....	29
c) Apical pool.....	29
d) Basal and lateral pool.....	29
5) Graphical summary of part A/: Polarity and contractility, the morphogenetic potential of epithelial cells (Figure 1).....	30
B/ Out-of-plane epithelial morphogenesis	32
1) Models based on forces directed along the apico-basal axis (z).....	33
a) Apoptotic apico-basal forces.....	33
b) Epithelial-mesenchymal transition and apico-basal forces.....	34
c) Apico-basal shrinkage by active lateral domain shrinkage.....	35
d) Apico-basal shift of adherens junctions.....	35
e) Limits of bending models based on intrinsic apico-basal force dynamics.....	36
f) Interaction with external substratum and migratory bending force.....	37
2) Models based on conversion of dynamics perpendicular to the folding axis (y) into forces directed along the apico-basal axis (z).....	38
a) Cell wedging: a conserved cell shape change associated with folding.....	39
b) Apical constriction as a mechanism for cell wedging.....	40
c) Apical constriction: constraint of neighboring tissues and tissue geometry.....	41
d) Synergy between apical constriction and apico-basal forces.....	42
e) Basal relaxation as an alternative mechanism for cell wedging.....	42
f) Can radial/perpendicular influx of cells participate to folding?.....	43
3) Models based on conversion of dynamics parallel to the folding axis (x) into forces directed along the apico-basal axis (z).....	44
a) Circumferential tension and pit formation.....	44
b) Acto-myosin cables and groove formation.....	46
4) Graphical summary of part B/: Typology of epithelial folding dynamics (Figure 11).....	48

C/ In-plane epithelial morphogenesis.....	49
C1/ Active in-plane epithelial morphogenesis.....	49
1) Active tissue surface reduction.....	50
a) Surface reduction by cell surface shrinkage and tissue thickening.....	50
b) Surface reduction without tissue volume conservation.....	51
c) Reconcile apical shrinkage models: Planar or out-of-plane outputs?.....	52
2) Active tissue surface expansion.....	53
a) Surface expansion by apical and basal surfaces increase and tissue thinning.....	53
b) Surface expansion by cell growth after division and cell integration.....	54
3) Active convergent extension.....	54
4) Active translocation.....	56
a) Edge effects and collective migration.....	57
b) Emerging properties of migration based on edge-effects.....	58
c) Edge-independent collective migration.....	60
C2/ Coupling with neighboring events and morphogenesis.....	62
1) Passive tissue surface reduction.....	62
2) Passive tissue surface expansion and stretching.....	63
a) Impact of the underlying layers.....	63
b) Intra-epithelium coupling.....	64
3) Passive convergent extension.....	67
4) Graphical summary of part C2/: Typology of tissue surface changes as a result of coupling with adjacent tissues (Figure 20).....	68
5) Passive translocation and swirling.....	70
C3/ Graphical summary of part C/: Typology of the mechanisms leading to in-plane epithelial morphogenesis (Figure 22).....	73

Part1: Analysis of neck invagination dynamics

Contraction of a curved acto-myosin cable and a supra-cellular basal acto-myosin network is associated with epithelial folding.....	75
--	-----------

Context.....	77
Summary.....	77

Results.....	78
Presumptive neck region gradually bends during metamorphosis.....	78
Bending region constricts along the direction parallel to the fold axis.....	80
Neck invagination is associated with a contractile acto-myosin cable.....	82
Neck acto-myosin cable is curved and could act as a “tissue-scale cytokinetic ring”....	84
A basal contractile supra-cellular network is present in neck folding region.....	86
Modulation of MyosinII contractility regulates neck invagination speed.....	88

Discussion.....	93
Association between interface contractility and tissue invagination.....	93
Boundary acto-myosin cable and invagination: Towards a model of a “tissue-scale cytokinetic ring”?.....	94
Proposition of an experiment to test the validity of “tissue-scale cytokinetic ring” mechanism.....	96
Basal tension increase and neck invagination.....	96
Assessing the role of additional mechanisms during neck invagination.....	98
What is triggering neck invagination onset?.....	99
 Part2: Analysis of anterior thorax flows	
Collective cell migration on the apical extracellular matrix participates to thorax morphogenesis.....	101
Context.....	103
Summary.....	104
 Results.....	104
Characterization of <i>Drosophila</i> dorsal thorax flow.....	104
Thorax flow is only anteriorly coupled with head-to-thorax interface invagination....	107
Thorax A-P flow is mostly autonomous.....	114
Interaction with the apical ECM is necessary for thorax flow.....	119
Dorsal thorax cells interact with the apical ECM using adhesive polarized apical protrusions.....	122
Core PCP pathway is locally required for migration and apical protrusions polarity...126	
<i>Stripe</i> regulates thorax flow and protrusion polarity in synergy with core PCP pathway. .135	
Dumpy deposition pattern correlates with migration velocity pattern, and is partly regulated by <i>stripe</i>	143
<i>Dpy</i> expression is necessary for most of the thorax flow to occur.....	146
Thorax migration is dispensable for early neck invagination.....	150
Posterior thorax (Position _{AP} =50-150%) flow is dependent on anterior thorax (Position _{AP} =0-50%) flow pulling from 22hAPF to 35hAPF.....	153
 Discussion.....	158
A cell-based crawling on the apical ECM.....	158
A cell-based mechanism of collective migration.....	158
A migration on the apical ECM.....	158
Perspectives: Study the regulation of apical protrusive activity.....	159
Role of <i>Dpy</i> in thorax migration.....	161
Perspectives: Study stronger mutant backgrounds.....	161
Tissue deformation by collective cell migration.....	162
Tissue-scale mechanical coupling.....	163
Planar cell polarity and patterning information.....	164

Part3: Analysis of matrix motion *in vivo*

Low deformation of the apical extracellular matrix is associated with persistent

migration *in vivo*.....167

Context.....169

Summary.....170

Results.....170

Study of the mechanics of ECM-tissue interface by laser ablation.....170

Stretching after ablation is patterned across the tissue.....170

All thorax cells are mechanically coupled to the apical ECM.....172

Estimation of the proportion of protrusions that are attached to the apical ECM....176

The gradient of ECM motion after ablation is shifted anteriorly in *sr^l* mutant.....178

Relationships between migration speed, Dpy deposition rate, protrusion polarity and behaviors of protrusions and ECM after ablation, in control and *sr^l*.....179

Study of ECM-tissue interface mechanics in physiological conditions.....181

Dpy::YFP fibers show local movements of various amplitudes across the thorax...181

Tissue shows a gradient of motion persistence.....182

ECM motion is associated with underlying tissue similar motion.....184

Discussion.....187

How to interpret the gradient of ECM motion?.....187

Perspectives: Study ECM motion in more contexts.....188

Perspectives: More deeply characterize ECM motion.....188

Towards the idea of a gradient of ECM stiffness and *in vivo* collective durotaxis?.....189

Material and methods.....191

A/ *Drosophila melanogaster* genetics.....192

1) *Drosophila* stocks list.....192

2) Overexpression and downregulation of protein activity.....194

3) Genetic mosaicism.....194

B/ Fixed tissue imaging.....194

C/ Live-imaging.....195

1) Pupa collection and mounting.....195

2) Imaging.....195

3) Detection of the adherens junction plane and projection.....196

4) Spatio-temporal registration of the time-lapse movies.....196

a) Spatial registration.....196

b) Temporal registration.....197

5) Quantification of tissue flows.....197

a) PIV analysis and preprocessing.....197

b) Lagrangian description.....198

c) Normalization.....199

d) Mean velocity kymographs and standard deviation kymographs.....199

e) Comparison of mean velocity kymographs between conditions.....199

f) Calculation of global orientation of thorax flow.....200

6) Quantification of tissue deformations.....	200
7) Quantification of neck invagination dynamics.....	200
a) Quantification of tissue depth.....	200
b) Quantification of local tissue slope and neck indentation.....	201
c) Correction of velocities and tissue deformation for tissue curvature.....	202
8) Quantification of cell aspect ratio and anisotropy orientation.....	204
9) 3D visualization of live-imaging data.....	204
10) Inference of Lagrangian coordinates for pictures taken at late time points.....	204
11) Quantification of apical protrusion polarity.....	205
12) Laser ablations.....	207
a) Large-scale repeated ablations.....	207
b) Single-junction ablation and junction tension/friction estimation.....	208
c) Multicellular basal and apical ablations and apical and basal tension/friction estimation.....	208
d) Ablation and protrusion stretching.....	208
e) Ablation and Dpy::YFP recoil analysis.....	209
f) Muscle ablation in control and <i>Act>Dpy^{RNAi}</i>	210
13) Dpy::YFP levels quantification.....	211
a) Repetitive bleaching.....	211
b) Estimation of deposition rates.....	211
c) Calculation of Dpy::YFP enrichment in clones overexpressing <i>sr</i>	211
14) Quantification of <i>sr</i> ::GFP levels.....	212
15) Cell body tilt analysis.....	212
16) Quantification of the distance between tissue and cuticle chitin-rich layer.....	213
17) Quantification of basal fibers alignment.....	213
18) Quantification of MyosinII enrichment on the head and the thorax side.....	214
19) Quantification of microchaetes orientation.....	214
20) Adult scutellum aspect ratio calculation.....	215
21) <i>Ex vivo</i> experiments.....	215
22) Analysis of tissue and ECM motion.....	216
a) Imaging and PIV analysis of Dpy::YFP fibers and cell contours motion within 2min intervals.....	216
b) Calculation of mobility, global movement, fluctuation around global movement and persistence.....	216
c) Comparison between tissue and Dpy displacements fields.....	217
D/ Statistics.....	218
Conclusion.....	219
Table of figures.....	223
Bibliography.....	227

Introduction

Introduction

Developmental biology is the study of the processes enabling multicellular organisms to grow and self-organize. The acquisition of specific 3D shapes is fundamental for the functionality of organs, and can be directly linked with the viability and the fitness of organisms. Understanding how tissues grow and deform to give rise to precise organs and organisms shapes is thus of particular interest, and is the focus of a branch of developmental biology called morphogenesis.

The mechanisms involved in morphogenesis happen at many scales, from the molecular scale to the tissue scale. Molecular machines, assembly of sub-cellular structures, cellular processes, multi-cellular and tissue-scale dynamics all contribute to give rise to reproducible tissue architectures and organ shapes during development. Studying these processes is not only important to better understand the development of multicellular organisms, but also gives insight into possible causes of developmental pathologies and malformations. What is more, processes involved in morphogenesis are also involved in homeostasis, regeneration, wound healing and cancer. As a result, the study of basic principles of morphogenesis has a medical interest.

During the first steps of embryogenesis, tissues organize as sheets of cells, called epithelia. Epithelia are also present in later life cycle phases, and constitute major building blocks of multicellular organisms. The study of epithelial morphogenesis is thus fundamental to both understand early embryonic morphogenesis and organogenesis. One fundamental process of epithelial morphogenesis is the formation of folds within an epithelium. Epithelial folding is involved in numerous embryonic developmental steps, like gastrulation and neurulation, and allow the formation of grooves, pits and outgrowth throughout development. In addition to epithelial fold formation, epithelial morphogenesis is associated with complex epithelial tissue flows. These flows can result from a process called cell migration. Cell migration enables cells to actively displace by applying traction forces on their surroundings. Cell migration is both involved in epithelial cell translocation and epithelial tissue deformation. Moreover, cell migration is involved in cancer progression and metastasis. Understanding epithelial migration thus allows to gain insight both into morphogenesis and cancer.

During my thesis, I have studied the fundamental mechanisms underlying both epithelial folding and epithelial migration, using *Drosophila melanogaster* as a model system. During its life cycle, *Drosophila* undergoes metamorphosis, during which the larva transforms into an adult. During metamorphosis, *Drosophila* dorsal thorax epidermis undergoes major deformations, and has been used as a model system to study epithelial morphogenesis. In continuity with this work, I have used this system and focused on two dorsal epidermis regions: the head-to-thorax interface, and the anterior thorax.

In the first part of my thesis report, based on live-imaging experiments, I will show that the head-thorax interface progressively folds during pupal development, giving rise to the formation of the neck of the adult *Drosophila*. Combining live-imaging and *Drosophila* genetics tools, I will notably show that two supra-cellular acto-myosin structures, an apical cable and a basal network made of parallel bundles, are associated with neck folding dynamics. Taken together, the results presented in this first part shed light on a possible new mechanism underlying epithelial folding.

In the second part of my thesis report, I will focus on the study of the flow of anterior thorax that accompanies neck folding. Combining live-imaging, laser ablation and *Drosophila* genetics tools, I will quantitatively assess the coupling between neck invagination and thorax flow. I will show that neck invagination provides a pulling force leading to local thorax flow. Moreover, I will show that thorax flow is also partly autonomous. I will dissect the genetic, cellular and mechanical basis of this autonomous thorax flow, and provide evidence that thorax cells actively migrate on the apical extracellular matrix (ECM). Taken together, the results presented in this second part shed light on the contribution of epithelial migration to dorsal thorax morphogenesis, and on its interplay with epithelial folding.

Understanding the mechanics of cell interaction with the substratum it migrates on is of key interest to understand cell migration. In the third part of my thesis, I will further study the interaction between dorsal thorax cells and the apical ECM, and use dorsal thorax as a model system to analyze the motion of the apical ECM constituents *in vivo*. I will show that the constituent of the inner part of the apical ECM are locally set in motion by migrating thorax cells. I will highlight the association between low apical ECM deformation and high tissue migration persistence. Taken together, the results presented in this third part paves the way for future *in vivo* study of apical ECM mechanical properties, and suggest that a pattern in ECM stiffness might regulate epithelial migration and epithelial deformation.

Based on the results of my thesis work, I propose that head-thorax interface folding and anterior thorax migration constitute a new model system to study epithelial folding, epithelial migration and their interplay.

Organization of the introduction

During my PhD, I have focused my work on the study of morphogenesis of epithelia. Epithelia are tissues organized as sheet of cells that constitute major building blocks of multicellular organisms. The polarized architecture, the connectivity and the contractility of epithelia are structural properties that are key to allow the emergence of epithelial deformation and morphogenesis. Understanding the molecular regulation of epithelial structure is thus of interest to understand how epithelia shape during development. In the present introduction, I will thus first review the fundamental properties of epithelial structure that confer a morphogenetic potential to epithelial cells (section A, summarized in Figure 1), and present the main molecular pathways underlying them (a special attention will be paid to planar cell polarity pathways in *Drosophila*, as they are involved in the mechanism of collective migration I will present in the part 2 of “Results” section). I will then review the different known mechanisms leading to epithelial morphogenesis (section B and C). This review will be subdivided into two parts: the description of out-of-plane morphogenesis (leading to deformations that alter the plane of the epithelium, like epithelial folding, section B, summarized in Figure 11), and the description of in-plane-morphogenesis (leading to surface changes within the plane of the epithelium, section C, summarized in Figure 22).

While reviewing current knowledge about epithelial morphogenesis, I will insist on open or debated aspects in the field, and highlight the contribution of my PhD work to these issues (presented in small blue frames throughout the introduction).

A/ Generalities about epithelial tissues

1) Definition and relevance of epithelial structure

Epithelia are defined as tissues which are organized as sheets of interconnected cells and are key constituents of Metazoa at all life stages. The embryo is composed of epithelial sheets that deform and differentiate to give rise to all cell types and organs of the organisms. In later life stages, the epithelial structures of the epidermis, the gut or the respiratory tract provide a barrier between the internal and external milieu. Epithelia also line internal organs and are key constituents of secretory organs.

Epithelia show two fundamental features. First, epithelia are polarized structures. The epithelial cells display an apico-basal polarity, which enables the differentiation of the inner and outer surfaces of the epithelium, and is at the basis of directional flows across the tissue.

In addition, epithelia also display polarization across the plane of the tissue, known as planar cell polarity. This polarity along organs symmetry axes is essential for cell and epithelial morphogenesis. Second, epithelia display a high level of cohesiveness. This cohesiveness emerges from the organization of specialized cell-cell junction networks that allow epithelial cells to be tightly linked and mechanically coupled with their neighbors.

I will here briefly summarize the molecular basis of polarity, adhesion and contractility that are relevant in the framework of epithelial morphogenesis.

2) Generalities about epithelial apico-basal polarity and adhesion

a) Apico-basal cell polarity

Epithelial cells display a clear cortical regionalization along their apico-basal axis. Four main domains can be distinguished: an apical domain, a junctional domain, a lateral domain and a basal domain (Figure 1A-E). I will here briefly review the properties and functions of each of these domains.

The apical domain is the domain which constitutes the apical surface of the epithelium (Figures 1A, 1E). As a consequence, it is in contact with a specific extracellular milieu. This extracellular milieu can be the external milieu, for instance in the gut or epidermis, or an internal milieu such as the blood in the blood vessels. The apical domain can also be covered by an apical extracellular matrix (ECM), like in the insect epidermis¹, trachea² and gut³, or in the human sensory epithelium of the cochlea⁴. The apical domain can bind to the apical ECM^{5,6,7} (this process will be illustrated in C1/2)a), C1/4)c, C2/2)b) and C2/5)). The apical domain often displays apical protrusions that can give rise to highly specialized structures. For instance, in the gut epithelium, the apical domain of enterocytes show actin rich membrane extensions called microvilli, which are involved in nutrient absorption⁸ or microbial resistance⁹, and the regulation of their length is linked with cell volume regulation¹⁰. In the human organ of Corti in the inner ear, hair cells harbor highly organized apical bundles, stereocilia, which are required for the perception of sound¹¹. In *Drosophila*, both larval and adult epidermal cells harbor precisely shaped apical extensions, which give rise to the trichomes on the cuticle¹². Frequently, apical protrusions are motile. For instance, ependymal cells of the neuro-epithelium are covered by motile cilia, whose beating movements are involved in cerebro-spinal fluid flowing¹³, while the cilia harboring cells covering the inner surfaces of the airways are involved in the transport of mucus¹⁴. Thus, the apical domain can show various morphologies, allowing for various epithelial functions.

The junctional domain is pivotal for intercellular adhesion within epithelia¹⁵ (Figure 1B). This domain exhibits high levels of proteins involved in cell-cell adhesion and constitutes a belt of adhesion surrounding each epithelial cell and mediates most of the adhesion of the epithelial cell to its neighbors. It is composed of two adjacent subdomains, the tight junction¹⁶ and the adherens junction¹⁷. On the one hand, tight junctions are composed of transmembrane proteins (claudins, occludins and tricellulin) that interact between juxtaposed cells to create a paracellular diffusion barrier¹⁶. Tight junction proteins recruit Zonula Occludens (ZO) proteins and Rho-GTPases, which regulate acto-myosin cytoskeleton dynamics¹⁶. On the other hand, adherens junctions are mainly composed of the transmembrane protein E-cadherin (epithelial cadherin)¹⁷. The extracellular domain of E-Cadherin can bind to the extracellular domain of E-Cadherin in a neighboring cell, thereby establishing a homophilic bond between two adjacent cells¹⁸. Furthermore, E-Cadherin proteins can also interact with E-Cadherin proteins within the same cell, leading to the formation of E-Cadherin clusters that are thought to strengthen intercellular adhesion stability¹⁹. The intracellular domain of E-Cadherin binds to α and β -Catenins²⁰, which in turn interact with F-actin and actin regulators like Vinculin²¹ and Afadin²². Thus, the adherens junction connects the plasma membrane with the cortical acto-myosin cytoskeleton and therefore account for most of the mechanical coupling between epithelial cells.

The lateral domain of epithelial cells also plays a role in cell-cell adhesion, displaying scattered cell-cell adhesion contacts mediated by Cadherin/Catenin complexes. In some contexts, contractile acto-myosin networks present on the lateral domain of an epithelial cell drive cell apico-basal shortening^{23,24,25} (Figure 1C, these processes will be detailed in B/2/c, C1/1/a and C1/2/a sections).

The basal domain of epithelial cells constitutes the basal surface of the tissue (Figure 1D). Epithelial tissues are often covered by a basal ECM²⁶, and bind to it by forming focal adhesions containing integrin complexes²⁷. The basal domain can show highly organized cytoskeleton structures. For instance, in the *Drosophila* follicular epithelium, the basal domain harbors parallel actin rich stress fibers and polarized basal protrusions, which have been shown to be necessary for collective rotational migration of the epithelium²⁸ (this process will be detailed in C1/4/c section). The basal domain is thus a specialized domain linking the ECM and basal acto-myosin cytoskeleton.

b) Molecular mechanisms of apico-basal polarity

Three main molecular complexes define and maintain apico-basal subdivision of epithelial cells into the apical, junctional and basolateral domains²³. The transmembrane protein Crumbs recruits a set of cytoplasmic proteins (Moesin, β -Spectrin, Stardust, PatJ, Par-6 and aPKC) to the apical domain. The protein Bazooka binds adherens junction constituents, Armadillo and Echinoid, and acts as a landmark for junctional domain assembly by recruiting the Cadherin/Catenin complex. Finally, the baso-lateral domain is marked by the localization of a complex composed of Discs large, Lethal giant larvae, Scribble and Par-1 proteins. These three polarity complexes dynamically interact to confine their localization to specific locations along the apico-basal axis (Figure 1A). On the one hand, the interaction between Crumbs apical complex and Bazooka is necessary to limit the apical expansion of the adherens junctions^{29,30}. On the other hand, Par-1 dependent phosphorylation of Bazooka and aPKC dependent phosphorylation of Lethal giant larvae inhibits apical and junctional complex assembly in the baso-lateral domain^{31,32}. Thus, a constant dynamic interaction between these polarity complexes is required to maintain and regulate apico-basal polarity in epithelial cells. Regulation of these interactions can result in changes in apico-basal domains relative heights (this process will be detailed in A/1/d section).

3) Generalities about epithelial planar cell polarity

In addition to apico-basal polarity, epithelial cells can show a front-back polarity, known as planar cell polarity (PCP, Figure 1F). PCP is prominent when looking at specialized apical structures. For instance, stereocilia hair bundles of mouse inner ear hair cells show a stereotypical V-shape that point in a similar direction across the tissue³³. In *Drosophila* pupal or larval epidermises, each cell has one or several polarized hair-like structures at the back of its apical domain, forming cuticle decoration called trichomes³⁴. The pupal epidermis also harbors multicellular sensory organs, named microchaetes. The cell divisions giving rise to microchaetes and the final multicellular arrangement of microchaetes are both planar polarized³⁵. Moreover, the ommatidia, the building blocks of the *Drosophila* compound eye, are organized in a planar polarized fashion³⁶. Classical genetic studies of trichomes, microchaetes and ommatidia have been instrumental to identify the genes involved in PCP establishment in epithelia. I will here review the main PCP pathways discovered in *Drosophila* (Figure 1F), and briefly mention their vertebrate homologs.

a) Core PCP pathway (and vertebrate non-canonical Wnt pathway)

Screenings for mutations giving rise to defects in planar polarization of *Drosophila* apical epidermal structures have enabled the discovery of core PCP pathway genes³⁴. The core PCP pathway is composed of the transmembrane protein Frizzled (Fz), the atypical cadherin Starry night (Stan, also called Flamingo), the transmembrane protein Van Gogh (Vang, also called Strabismus) and the cytoplasmic proteins Disheveled (Dsh), Diego (Dgo) and Prickle (Pk). The interaction between these proteins allows the asymmetrical assembly of polarity complexes in the cortex of the junctional domain. Indeed, in *Drosophila* wing, while Fz, Dsh and Dgo are only found at the distal pole of the cell, Vang and Pk are localized at the proximal pole of the cells. Stan, on the other hand, localizes both at the proximal and the distal poles of the cells. By which mechanism this front-back asymmetry is set and maintained is still a focus of ongoing research³⁷. Cell intrinsic mechanisms may contribute to asymmetric PCP protein localization. Indeed, in mammalian cell cultures, it has been shown that Dsh prevents Pk accumulation by targeting it for degradation through the recruitment of the ubiquitin ligase SMURF³⁸. Similarly, the ubiquitin ligase Culin regulates Pk localization in *Drosophila*³⁹. However, asymmetric PCP protein localization is mainly thought to be the consequence rather than the cause of PCP³⁶. Accordingly, intercellular interactions are pivotal to account for asymmetric PCP protein localization, as revealed by extensive clonal loss and gain of function studies of PCP genes in the *Drosophila* abdomen, wing and eye. Clonal *fz* and *vang* loss of function, as well as clonal overexpression of all core PCP proteins, alters planar cell polarity beyond the clone, in surrounding wild type tissue. This effect is called domineering non-autonomy. While it has been proposed that a mutual inhibition between Fz/Dsh and Vang/Pk could lead to domineering non-autonomy, clear molecular mechanisms are still lacking³⁷.

Fz, which is involved in the well-known Wnt/ β -Catenin signaling pathway, is also involved in PCP establishment in vertebrate systems. The involvement of Wnt ligands in vertebrate PCP establishment led to the idea that Wnt ligands not only underlie classical Wnt/ β -Catenin pathway signaling, but are also part of a “non-canonical Wnt PCP pathway”. Wingless, the main Wnt ligand in *Drosophila*, is also involved in *Drosophila* planar cell polarity by providing long-range directional information to core PCP pathways actors⁴⁰.

b) Fat/Dachsous pathway and its link with core PCP pathway

The atypical cadherins Fat (Ft) and Dachsous (Ds)⁴¹ and the Golgi kinase Four-jointed (Fj), which regulates Ft/Ds heterophilic interaction⁴², constitute a planar polarity module which is complementary to core PCP pathway⁴³. Indeed, mutations in Ft/Ds pathway genes lead to trichomes planar polarity defects⁴⁴. Moreover, planar polarized localization of Dachs myosin is regulated by the Ft/Ds pathway, and mutation of *Dachs* also leads to planar polarity defects⁴⁵. As Fj and Ds display tissue-scale gradients of expression, it has been proposed that their expression act as global planar polarity cues, that in turn would be locally refined by the core PCP module^{44,46}. This model, even if it elegantly accounts for robustness in PCP, remains controversial. Notably, it has been shown that the Ds tissue-scale gradient is unlikely to be informative, as homogeneous Ds expression rescues *ds* mutation⁴⁷. In the wing, the planar polarization of core PCP and Ft/Ds pathway proteins have been precisely described in time and in space. Proteins of the core PCP and Ft/Ds pathways appear to switch from a divergent polarity phase to a convergent polarity phase, suggesting that the cross-talk between these two pathways is dynamic and non-systematic⁴⁸. Interestingly, in a Ft/Ds-dependent manner, the ratio between Spiny legs (Sple) and Pk (two isoforms encoded by the *prickle* locus) do not encode the orientation, but rather the global direction of PCP (front-to-back or back-to-front direction)⁴⁹. This explains why wing and eye cells are planar polarized in an opposed manner along the Ds gradient (eg. Ds and Fz asymmetric localization is opposite in the two systems)⁴⁹. Notably, in the wing, where the Pk isoform is more abundant, Sple overexpression triggers a global polarity reversal. The physical binding between Sple/Pk and Ds/Dachs could play a role in the coupling of the Ft/Ds and core PCP pathways⁴⁹. Accordingly, when Sple is overexpressed in the wing, both core PCP and Ft/Ds polarity align in the same way⁴⁸.

While the nature and the relevance of the interaction between the Ft/Ds and core PCP pathways are still debated, some studies indicate that the Ft/Ds PCP pathway act independently of the core PCP pathway to regulate planar polarized cell behaviors^{45,50}. In *Drosophila* posterior dorsal thorax it has been shown that the Fj/Ds gradient polarizes Dachs to control polarized cell rearrangements⁴⁵. Moreover, more recently, it has been shown that in *Drosophila* abdomen, the Fj/Ds gradients control polarized cell shape changes, leading to the rotation and alignment of abdominal cells, and hence of the trichomes they bear⁵⁰. Interestingly, in the abdomen, cells contain multiple trichomes. The alignment of the multiple trichomes within each cell is solely dependent on core PCP pathway and independent of Ft/Ds pathway. Ft/Ds pathway solely regulates global rotation of abdominal cells and of the array of trichomes they contain⁵⁰. It thus appears that Ft/Ds pathway could act in a parallel manner to core PCP pathway to regulate planar polarity fields.

In vertebrates, Fat4/Dchs1 pathway is required for kidney morphogenesis^{51,52} and mouse neuronal migration⁵³. Whether Ft/Ds module is required for planar cell polarity in other vertebrate developmental contexts remains to be studied⁴³.

c) Additional apical planar polarity cues

The Ft/Ds and/or core PCP pathways are necessary for PCP establishment in *Drosophila* epidermis. However, they are not sufficient to fully account for planar polarization of trichomes. First, mechanics can alter planar polarity fields. Indeed, global morphogenetic tension and tissue deformation can participate to planar polarity fields rotation by pure tissue remodeling independently of PCP pathways⁵⁴. Moreover, mechanical tension exerted by the muscles on epidermal tendon cells has also been reported to trigger rotation of epithelial cells in mutant conditions, leading to a final disorganized pattern of trichomes planar polarity⁵⁵. Likewise, additional biochemical pathways are hypothesized to complement Ft/Ds and core PCP pathways. In fact, in the wing, even when disrupting both Ft/Ds and PCP pathways, trichomes still show a preferential orientation towards wing veins⁴⁸. The nature of the polarizing signal emitted by the veins and its relevance in physiological conditions remains unknown. Another example of additional biochemical PCP cue can be found in the abdomen, as revealed by *fz* or *stan* mutant flies. While pleurae (lateral epidermis) show random trichome orientation, trichomes remain robustly polarized in large pieces of the tergites (dorsal epidermis) and the pleurites (ventral epidermis)⁵⁶. In these mutants, what signal provides the robustness to disruptions of core PCP pathway remains unexplored. We hypothesize that patterned expression factors may control additional PCP pathways that locally complement core PCP pathway.

In the second part of my thesis, I will show that the expression of the transcription factor Stripe, which is associated with muscle insertion sites on the epidermis, is patterned in *Drosophila* dorsal thorax and acts in parallel with core PCP to orient planar polarity when core PCP pathway is disrupted.

Finally, planar polarization of MyosinII during *Drosophila* gastrulation does not depend on classical PCP pathways, but is the result of maternal genes: gap genes, pair-rule genes⁵⁷ and Toll genes⁵⁸, which are expressed along the antero-posterior axis in overlapping stripes (a more detailed description of this process can be found in C1/3 section). How this patterning is converted into planar polarization of MyosinII is yet to be discovered.

d) Basal planar polarity

Studies of the *Drosophila* follicular epidermis have revealed the existence of a PCP pathway acting at the basal epithelial surface. Like core apical PCP proteins, which display asymmetric localization on the junctional domain of the cells, the cadherin Fat2 and the protein Lar show an asymmetric localization on the basal surface of the cells. Their asymmetric localization regulates the formation of polarized protrusions at the front of each cell thereby driving collective tissue crawling and rotation around the germ cells to shape the future embryo^{59,60} (a more detailed description of this process can be found in C1/4/c section).

4) Generalities about epithelial acto-myosin pools

Acto-myosin networks are the main sources of contractility in epithelial cells. The different dynamic pools of acto-myosin present in epithelial cells contribute, both cell-autonomously and non-cell-autonomously, to cell deformation, displacement, extrusion or division. These dynamics are the basis of many epithelial morphogenetic events. I will here review the different pools of acto-myosin that have been identified in epithelial cells. Their relevance during morphogenetic processes will be discussed in the following sections of the introduction (sections B and C).

a) Junctional cortical pool: from rings to supra-cellular acto-myosin cables

The main pool of acto-myosin cytoskeleton can be found at the level of the adherens junction. The junctional acto-myosin network is organized as a cortical ring (Figure 1B) that interacts with adhesion complexes through α -Catenin and β -Catenin⁶¹. This cortical cytoskeleton is a contractile structure, thereby conferring the apical cell area with a contractile potential. As adjacent cells also display junctional cortical rings of acto-myosin, a junction between two cells is associated with two adjacent cortical acto-myosin enrichments, and hence a resulting line tension. Junctional cortical contractility is thus relevant to understand single junction dynamics. At the point where three cells meet, specific cortical proteins localize (Glistactin⁶², Anakonda⁶³ and Sidekick⁶⁴) to give rise to the formation of a specialized junctional domain called tricellular junction, or vertex. At the scale of the tissue, the ensemble of adherens junctions, the cortical cytoskeleton they are associated with, and vertices forms a contractile network which mechanically equilibrates to give rise to architectures closely resembling networks of foams (Figure 1B). The 2D vertex model, based on equations of equilibrium of forces at vertices, is a simplification of Plateau models used for modelling 2D networks of foams⁶⁵ and is a powerful model to study adherens junction network architecture⁶⁶.

The junctional cortical acto-myosin pool is not necessarily homogeneous around the cell, and its heterogeneity can lead to anisotropic subcellular forces driving junction dynamics. For instance, PCP cues polarize the distribution of the junctional cortical acto-myosin network, which drives junction shrinkage during germband extension in *Drosophila*⁶⁷ (Figure 1G, a

more detailed description of this process can be found in C1/3 section). Interestingly, polarization of junctional cortical acto-myosin also arise at the boundary between two developmental compartments⁶⁸ (Figure 1J). At the tissue scale, these boundary enrichments give rise to the assembly of supra-cellular acto-myosin cables, formed by aligned junctions enriched in acto-myosin, and separate the two facing tissue compartments. The assembly of boundary acto-myosin is thought to be driven by an asymmetry in gene expression between the facing compartments of two different identities. Interestingly, supra-cellular boundary cables have been shown to prevent cell mixing between two adjacent compartments by creating a tension boundary, thereby orienting both rearrangements⁶⁹ and cell divisions^{70,71} along the boundary.

b) Junctional medial pool

While most of the junctional cytoskeleton concentrates cortically, a specific medial acto-myosin pool has been identified during specific morphogenetic processes (Figure 1B, in orange). The two main examples of the assembly of such structures are found in *Drosophila* mesoderm during invagination⁷² and in *Drosophila* amnioserosa during dorsal closure⁷³. In these two cell populations, a radial distribution of cytoskeletal proteins underlies the assembly of a contractile medial meshwork, which interacts with the cell cortex to regulate apical cell constriction (a more detailed description of this process can be found in B/2/b section).

c) Apical pool

While in the field of epithelial morphogenesis, studies of acto-myosin dynamics have been mainly focused on the junctional cytoskeleton pools, less is known about the structure and dynamics of acto-myosin networks at the cell apex. Apical actin dynamics have been observed, and linked with the formation of structures with various degrees of organization, ranging from dynamic structures like filopodia and lamellipodia to highly organized structures like the V-shaped bundles in vertebrate cochlear cells. Interestingly, in *Drosophila* larval abdominal cells, planar polarization of the apical domain can give rise to the formation of apical protrusions necessary for cell crawling⁷⁴ (Figure 1I, a more detailed description of this process can be found in C1/4/c section).

d) Basal and lateral pool

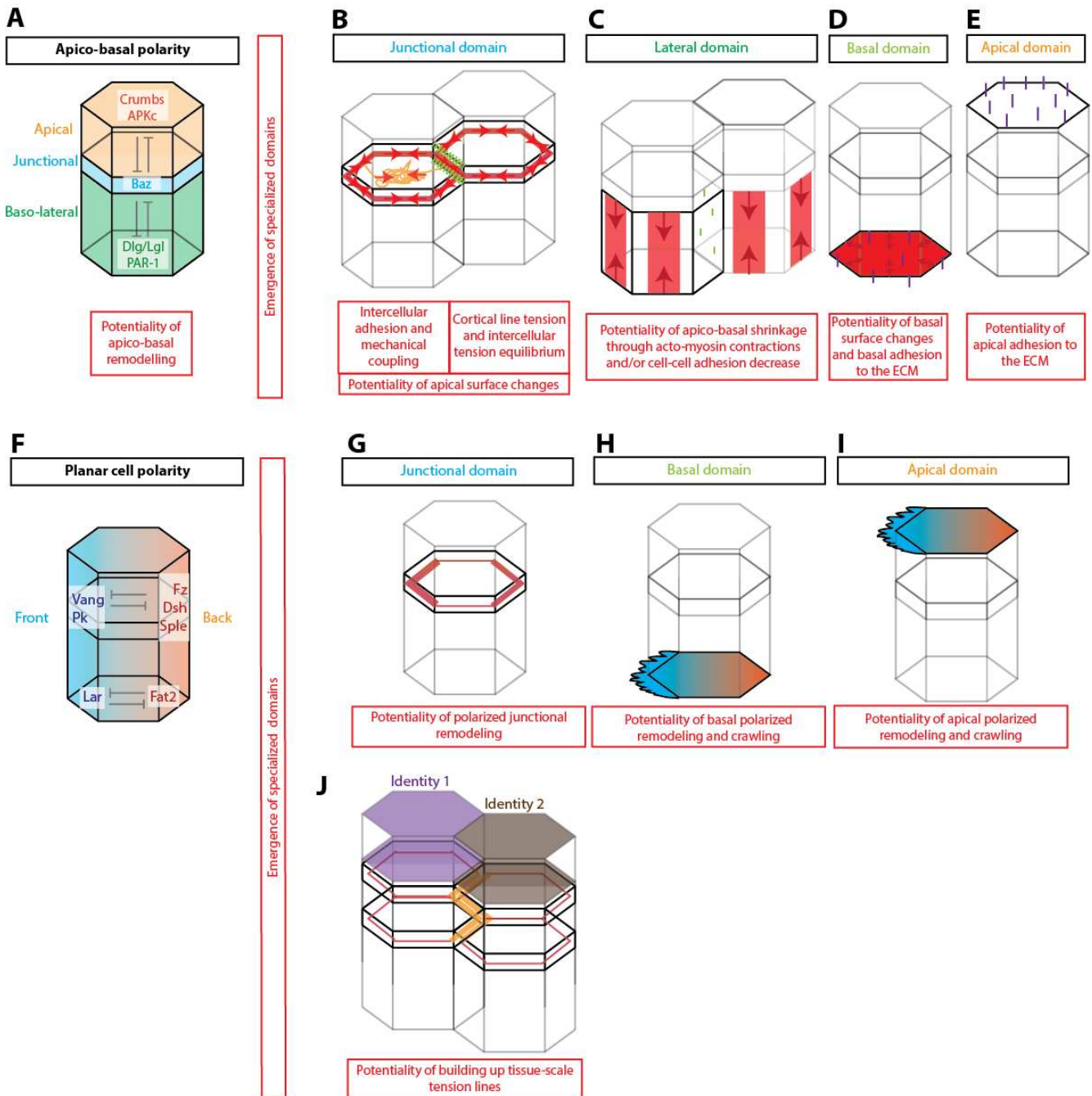
Acto-myosin cytoskeletal structures can also be found in the basal and lateral domains of epithelial cells. These structures regulate basal-lateral mechanical forces, as revealed by laser ablation in *Drosophila* wing disc, to facilitate tissue folding⁷⁵ (Figure 1D, more details about basal tension and folding can be found in section B/2/e)). Additionally, planar polarization of the basal surface and emission of planar polarized protrusions can give rise to cell crawling⁵⁹ (Figure 1H, a more detailed description of this process can be found in section C1/4/c section).

5) Graphical summary of part A/: Polarity and contractility, the morphogenetic potential of epithelial cells (Figure 1)










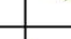



Fig.1: Apico-basal and planar polarities allow the emergence of specialized domains in epithelial cells. The assembly of contractile acto-myosin networks and cell-cell adhesion complexes in these domains confer distinct morphogenetic potentials to epithelial cells and tissues.

Epithelial cells harbor 4 main domains, an apical, a junctional, a lateral and a basal domain. The apico-basal regionalization of an epithelial cell is dependent on a network of cross inhibitions between apico-basal protein determinants, which can give rise to changes in the respective heights of the apical, lateral and baso-lateral domains (**A**). The junctional domain is pivotal for the adhesion and the mechanical coupling between adjacent epithelial cells. The junctional adhesion complexes interact with cortical and medial acto-myosin pools, allowing the emergence of junctional contractile potential (**B**). The lateral domain can be associated with contractile acto-myosin networks, enabling it to actively contract or relax (**C**). The basal surface can be associated with contractile acto-myosin networks, enabling it to contract or relax, and mediates adhesion to the basal ECM (**D**). The apical surface can be associated with adhesion to the apical ECM (**E**). Epithelial cells are planar polarized, as a result of planar cell polarity pathways (**F**). Planar polarization of cortical acto-myosin can give rise to polarized junctional shrinkage (**G**). The planar polarization of the basal domain can give rise to the emission of basal protrusions, required for example in cell crawling (**H**). The planar polarization of the apical domain can give rise to the emission of apical protrusions, enabling for example cell crawling (**I**). The interface between two epithelial domains of different genetic identities can be marked by a junctional cortical enrichment of acto-myosin, building tissue-scale supra-cellular acto-myosin cables (**J**).

This figure summarizes information of section A/, more details for each panel can be found in the text, and more details about associated morphogenetic processes will be shown in sections B and C.



Legend

	epithelial cell outline		apico-basal polarity fields		planar polarity fields		cell-cell adhesion		cross inhibition		contractility		
	junctional cortical acto-myosin pool		lateral acto-myosin pool		basal acto-myosin pool		cell-ECM adhesion		apical medial acto-myosin pool		acto-myosin cable		protrusions

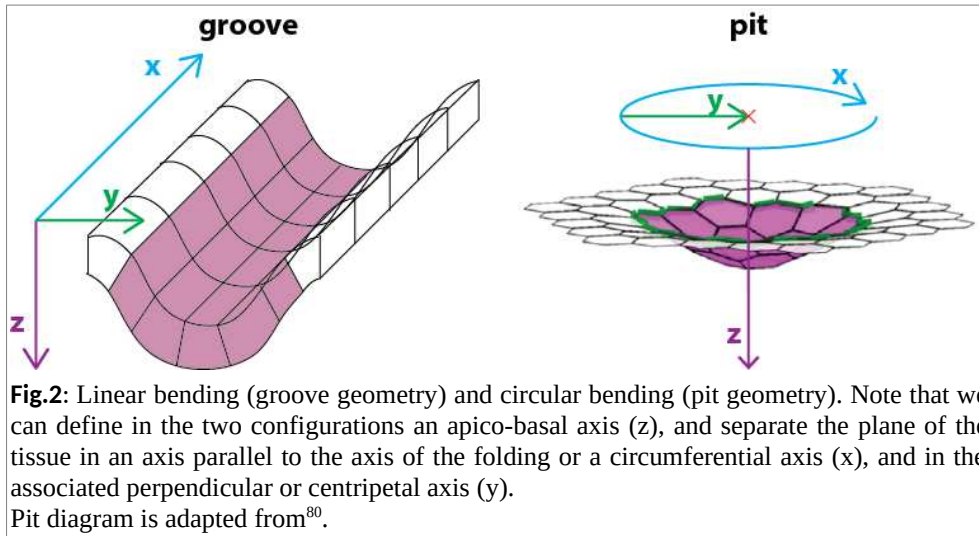
B/ Out-of-plane epithelial morphogenesis

Epithelial morphogenesis is the study of epithelial tissue deformation during development. The surface of an epithelium defines a flat or a curved plane. Epithelial deformation can be subdivided into two classes: deformations that alter the plane of the epithelium (out-of-plane morphogenesis), leading to the creation of folds, pits or outgrowth, and deformations that happen within the plane of the epithelium, without deforming epithelial plane (in-plane deformation), that lead to surface area changes. I will here review mechanism leading to out-of-plane deformations. In-plane deformations will be reviewed in section C/.

During development, epithelial sheets can reorganize to adopt complex and reproducible out-of-plane structures. Out-of-plane epithelial morphogenesis underlies the formation of complex organs shapes required for their specialized functions. Epithelial bending is a key process enabling the complexification of embryo 3D organization. It is a fundamental morphogenetic event occurring during several developmental phases such as gastrulation, neural tube formation or organogenesis.

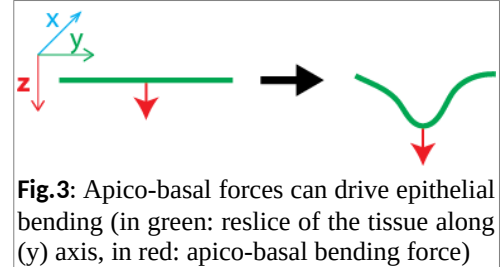
Notably, in insects, bending of the epidermis epithelium is crucial to globally shape the organisms. Indeed, the epidermis of insects secretes a series of apical extracellular matrices at each stage of the insect life cycle. These rigid matrices, called cuticles, constitute the exoskeleton of the insect. This exoskeleton constrains the shape of the tagmata (body segments) and of all the appendages. Thus, the morphogenesis of the epidermis prior to and during cuticle formation is crucial for global insect morphology¹.

Out-of-plane morphogenesis can give rise to invagination or outgrowth formation. We will here focus on the formation of invagination within epithelial tissues. The formation of an invagination within an epithelial sheet implies the existence of forces or dynamics that are directed along the apico-basal axis (z) within the fold, and that locally direct bending and deepening of the fold inside the organ or the organism. Recent studies have identified mechanisms directly driving such apico-basal bending forces^{76,77,75,78}. However, invagination bending forces are more commonly proposed to result from forces generated within the plane of the tissue⁷⁹. Here, I will review models accounting for epithelial folding, distinguishing them based on the orientation (apico-basal, or planar) of the active mechanisms that drive bending. Moreover, the main examples that will be reviewed are the formation of grooves, in which we can define an axis parallel to groove orientation (x), and the associated perpendicular axis (y, Figure 2). As a consequence, I will further distinguish planar mechanisms, based on the axis (x or y) they preferentially act along. Examples of circular invagination, leading to the formation of pits, will sometimes be invoked. In this case, I will distinguish circumferential dynamics (x) from centripetal dynamics (y, Figure 2).



1) Models based on forces directed along the apico-basal axis (z)

Apico-basal forces that are locally applied to an epithelial tissue constitute the most straightforward and intuitive explanation to account for epithelial invagination (Figure 3). Inward pulling forces are indeed expected to trigger both local inward bending and deepening of the fold, assuming low apico-basal deformability of the cells. However, relevance of such apico-basal bending forces has only been recently identified. I will here review the different cellular and molecular mechanisms that can lead to the exertion of apico-basal forces or to apico-basal remodeling, and eventually epithelium bending.



a) Apoptotic apico-basal forces

Apoptosis has been identified as a trigger for invagination during *Drosophila* leg morphogenesis. Inhibition of programmed cell death can indeed impair or even suppress the formation of joints in the legs, which are marked invaginations separating the leg segments⁸¹. Furthermore, induction of apoptosis is sufficient to trigger the formation of steady grooves in ectopic locations⁷⁶. Interestingly, apoptotic cells have been shown to display an apico-basal acto-myosin structure while they delaminate from the tissue⁷⁶. The contractility of this apico-basal structure⁸² has been shown to create an apico-basal force leading to the local and transient bending of the apical surface of the epithelium. Recently, the mechanism of this apoptotic force has been shown to involve the nucleus as a mechanical relay between the apico-basal myosin structure and the basal surface to generate apico-basal forces⁸². The apico-

basal forces generated by apoptotic cells are thought to be amplified by a mechano-transduction relay of neighboring cells. Indeed, cells neighboring an apoptotic cell are responding to the apoptotic pulling force by apically constricting, thereby increasing and stabilizing local surface folding. As a result, patterned apoptosis within the tissue can trigger local apico-basal forces and initiate invagination specifically at the location of the future joints of the leg⁷⁶.

Apoptosis is associated with bending in various other contexts. Notably, apoptosis has been shown to be necessary to form the invagination separating the maxillary and mandibular lobes in *Drosophila* larva⁸³. The formation of this groove depends on the pro-apoptotic gene *Reaper*, which is locally activated by the Hox gene *Deformed*⁸³. Apoptosis has also been observed during neural tube closure in vertebrates, where disruption of apoptosis has been linked with a delay in neural tube closure in mouse⁸⁴ and defects in neural tube closure in chicken⁸⁵. Nevertheless, while apoptosis is clearly linked with mechanisms of tissue bending by exerting apico-basal forces in the context of *Drosophila* leg morphogenesis, it remains unclear whether this mechanism could be generalized to these other cases.

b) Epithelial-mesenchymal transition and apico-basal forces

Epithelial-mesenchymal transition (EMT) is a process leading to the transformation of an epithelial structure into a less connective and organized mesenchyme. EMT is especially well-studied for its relevance in cancerology⁸⁶. It has been recently shown that EMT in *Drosophila* mesoderm cells is associated with the formation of apico-basal contractile myosin structures that considerably contribute to the folding of the mesoderm, especially in later phases⁷⁷. Non-apoptotic delamination thus appears as a driving force for apico-basal force exertion leading to tissue bending. Understanding to what extent EMT could drive epithelial folding in other contexts is still a promising unexplored research area⁷⁷.

The discovery of cell-based apico-basal mechanisms during *Drosophila* mesoderm invagination directly echoes the fact that, based on the study of mesoderm invagination in *C. riparius*, the ancestral mechanism of mesoderm invagination in insects is based on sparse individual cell delamination events, without keeping an “epithelial-like” structure that would synchronize individual events⁸⁷. We thus hypothesize that apico-basal forces described in *Drosophila* might be the remnant of an ancestral mechanism which is still driving individual cell delamination in *C. riparius*. Accordingly, ectopic expression of two genes involved in *Drosophila* mesoderm invagination (*Folded gastrulation* and *T48*) is sufficient to transform *C. riparius* mesoderm invagination into a “*Drosophila*-like” organized mesoderm invagination, suggesting the proximity between the morphogenetic programs of these two species.

c) Apico-basal shrinkage by active lateral domain shrinkage

Lateral domain shrinkage is another mechanism enabling apico-basal forces exertion and bending. Epithelial bending can indeed be obtained *in silico*, in a 3D vertex model, by implementing lateral shrinkage in a stripe of cells⁷⁵. The relevance of such a mechanism has recently been shown during the formation of a specific fold in *Drosophila* wing disc⁷⁵. The cells of this invagination region were shown to be associated with transient and repeated accumulations of MyosinII on their lateral sides. Interestingly, laser ablation at lateral cell edges enriched in MyosinII triggers an apico-basal recoil. Thus, lateral acto-myosin structures can exert an apico-basal force. Furthermore, pulses of lateral MyosinII enrichments correlate with local apical bending. Active shrinkage of the lateral domain is thus proposed to be a driving force for epithelial invagination. Apico-basal shrinkage has also been observed during ascidian endoderm invagination²⁵. In this system, invagination takes place in two phases. Endoderm cells first apically constrict, leading to a flattening of the tissue, but no invagination. In a second phase, endoderm cells apico-basally constrict, leading to the invagination of the endoderm. Notably, this second phase is associated with an increase in mono-phosphorylated myosin on the lateral domains of the cells, suggesting that basolateral myosin contractility promotes apico-basal cell shrinkage.

d) Apico-basal shift of adherens junctions

The apico-basal position of the adherens junctions, and hence the relative height of the apico-basal domains of epithelial cells, are the result of a dynamic interaction between three apico-basal polarity complexes (see A/2/b section and Figure 1A). Interestingly, a change in the balance of these polarity complexes can lead to a shift in the apico-basal position of the adherens junction in the cell. Notably, during dorsal fold formation in *Drosophila* gastrula, a decrease in Par-1 has been shown to be causative for the basal shift of the adherens junction⁷⁸. A patterned decrease in Par-1 levels in the tissue is sufficient to induce a local apico-basal shrinkage of the baso-lateral domain and an expansion of the apical domain in a subset of cells. This basal shift of adherens junction level results in a curvature of the adherens junction plane, without leading to a global deformation of the cell. This mechanism thus triggers bending at the level of the junctional domain, without directly bending the apical domain. Interestingly, the apical complex protein aPKC is required to prevent the junctional domain to extend during its basal shift, and hence to build a thin curved adherens junction plane⁷⁸. In a second phase following this basal shift of adherens junction level, the apical domain descent

as well and shrinks. The microtubule minus end protein Patronin redistributes basally as a result of reduced Par-1 levels and this basal Patronin redistribution has been proposed to mechanistically account for apical domain descent, by acting on an apical network of microtubules⁸⁸.

e) Limits of bending models based on intrinsic apico-basal force dynamics

Epithelial cells can exert local apico-basal forces and drive bending using various strategies: apoptosis, cell division, lateral contractility or lowering of the adherens junction plane. However, the amount of bending that these mechanisms can offer is limited by tissue thickness. All the models presented so far are modelling invaginations in columnar epithelia (or in a tissue that has beforehand thickened, like in the case of ascidian endoderm²⁵). In this configuration, active apico-basal remodeling can lead to sufficiently high apical curvature variation to promote apical bending. However, these models are unlikely to account for tissue invaginations in which the diameter of the observed bending curvature is higher than the thickness of the tissue (Figure 4).

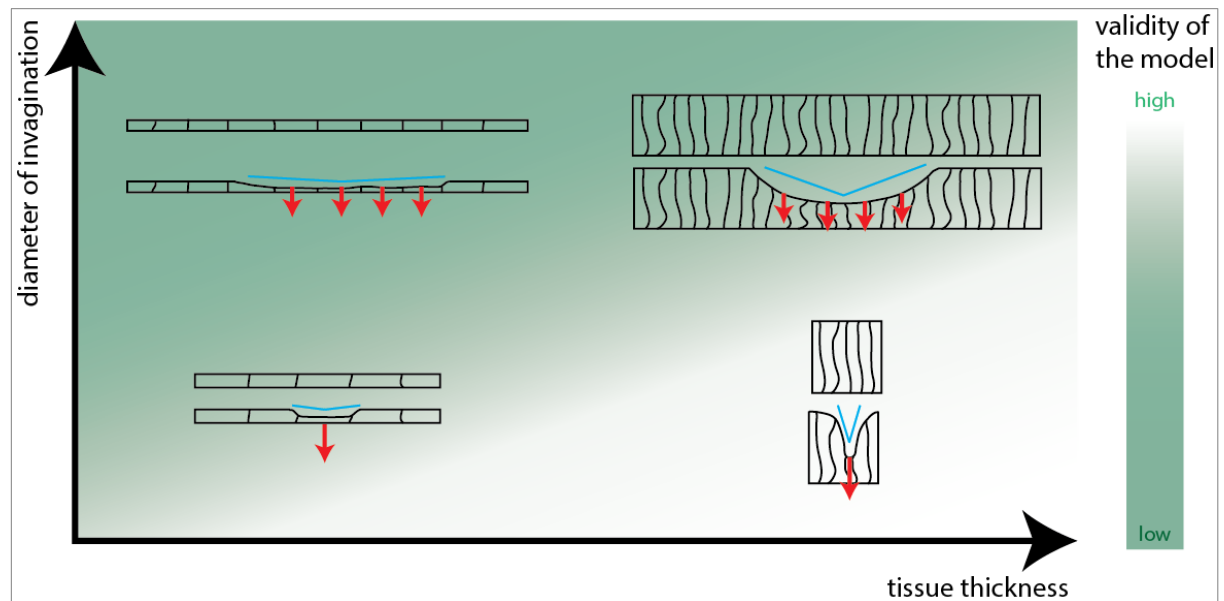


Fig.4: Phase diagram representing the effect of apico-basal shrinkage on apical curvature. Note that local invagination in thick tissues can be efficiently modelled by apico-basal shrinkage, while the model loses explanatory power for low $\frac{\text{tissue thickness}}{\text{diameter of invagination}}$ ratios. In red: apico-basal force, in blue: tissue indentation.

This trade-off between tissue thickness and the folding potential by apico-basal shrinkage could be relevant to understand why apico-basal forces are not systematically associated with folding. For instance, apoptosis is associated with tissue contraction without leading to tissue bending in the amnioserosa during dorsal closure⁸⁹ and in larval abdominal cells during metamorphosis⁹⁰. Interestingly, both the amnioserosa and abdominal larval epidermis are thin tissues. In accordance with this hypothesis, it has been proposed that apoptosis predominantly exerts apico-basal forces and promotes tissue bending in columnar epithelia, while in flat epithelia apoptosis contributes to the generation of planar forces⁹⁰.

It should be noted that models based on apoptosis/delamination differ from other apico-basal shrinkage models. In fact, many successive delamination events can progressively increase folding depth, whereas in other models, apico-basal shortening only happens once (Figure 5). Hence, delamination may be able to drive deeper folding, even in less thick epithelia, assuming that many delamination events successively happen at the leading edge of the folding region.

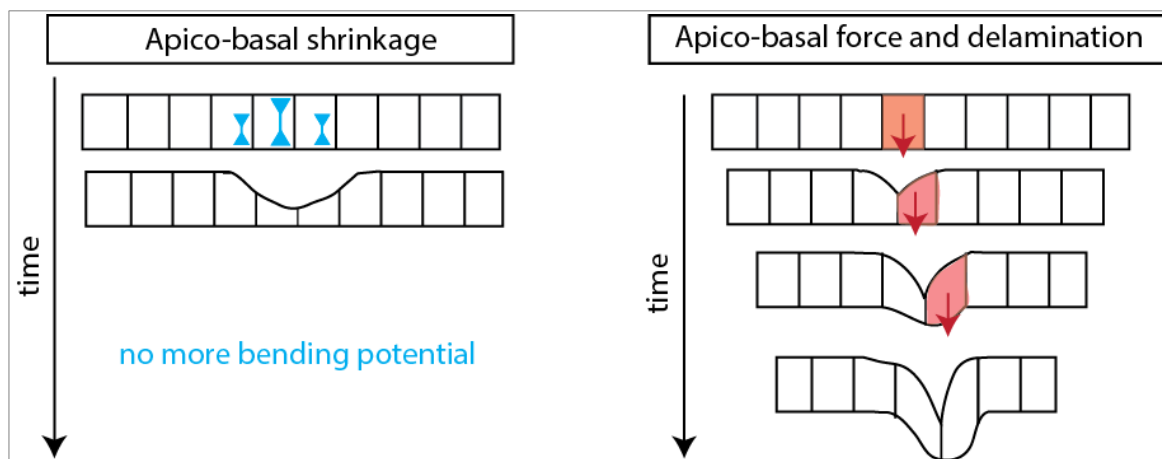


Fig.5: Additivity in time of apico-basal forces bending mechanisms. Note the possibility of additivity in time of mechanisms based on delamination, as progressive cell elimination at the leading edge can result in deeper folding of the tissue. Blue arrows represent apico-basal shrinkage; Red arrows represent apoptotic forces.

f) Interaction with external substratum and migratory bending force

Intrinsic epithelial apico-basal force exertion relies on apico-basal shrinkage, and is as a result limited by tissue thickness. However, exertion of apico-basal forces as a result of the interaction with underlying tissues could in theory lead to deep tissue bending independently of tissue thickness.

During mouse blood vessel sprouting, a tip cell is selected as a result of a competition mechanism triggered by a source of Vascular endothelial growth factor⁹¹. The selected cell

differentiates, and extends basal protrusions oriented along its apico-basal axis. Traction force exertion on the underlying substratum is thought not only to drive vessel sprouting initiation, but also to allow sprout deepening and new branch elongation⁹¹. Thus, basal apico-basal migratory forces can initiate deep pit formation. The described mechanism, however, applies to the sprouting of single cells. Whether sprouting initiation of multiple cells could be initiated by apico-basal migratory forces remains unknown.

2) Models based on conversion of dynamics perpendicular to the folding axis (y) into forces directed along the apico-basal axis (z)

While direct exertion of apico-basal forces has been recently shown to drive epithelial folding, planar dynamics have been known to drive tissue invagination for a long time. Building a simple physical model made of non-deformable brass bars and rubber bands, Lewis demonstrated in 1947 that a difference in tension between apical and basal surfaces can lead to tissue bending (Figure 6, note that a pivotal assumption of this model is the non-deformability of the lateral domains of the cells)⁹².

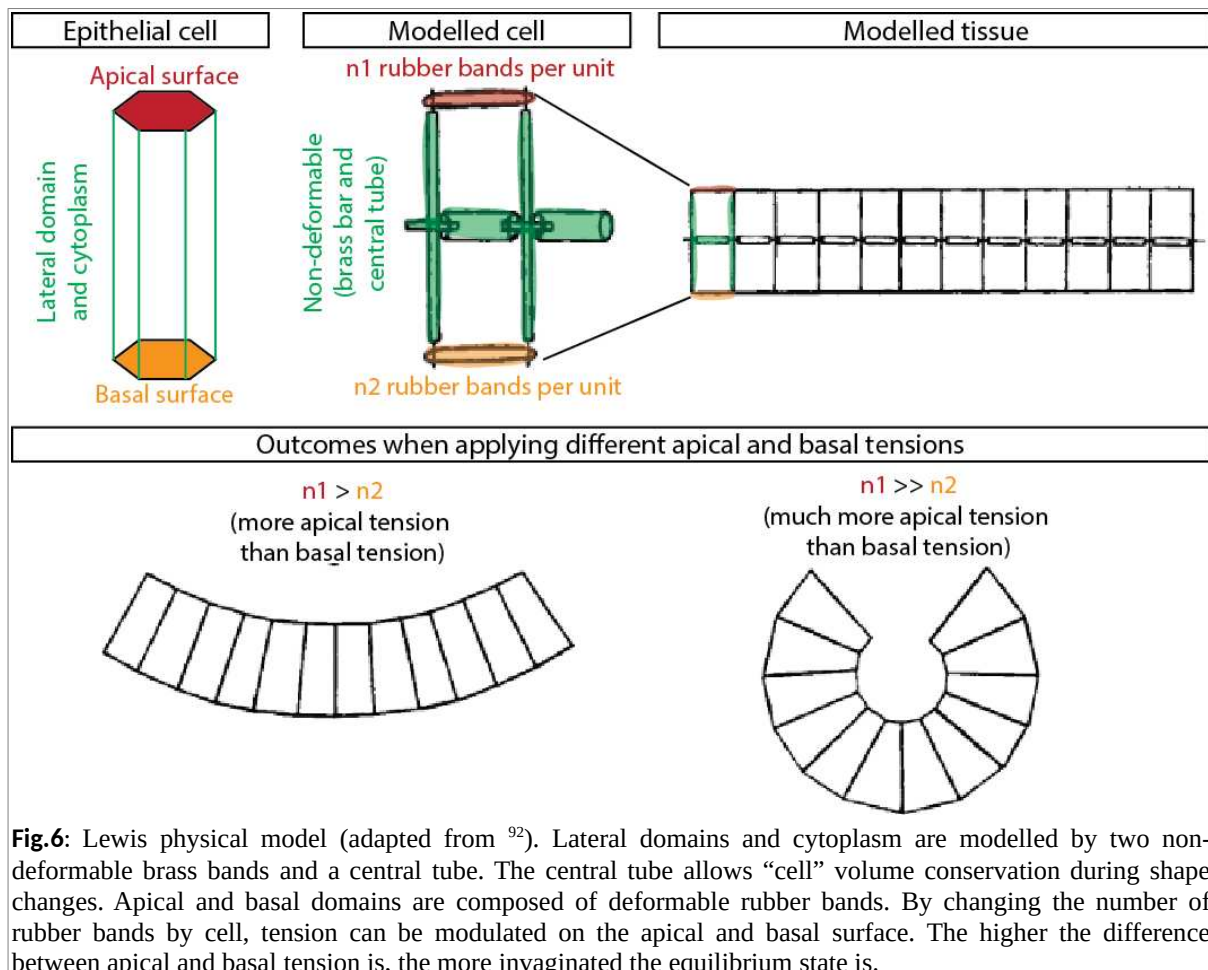


Fig.6: Lewis physical model (adapted from ⁹²). Lateral domains and cytoplasm are modelled by two non-deformable brass bands and a central tube. The central tube allows “cell” volume conservation during shape changes. Apical and basal domains are composed of deformable rubber bands. By changing the number of rubber bands by cell, tension can be modulated on the apical and basal surface. The higher the difference between apical and basal tension is, the more invaginated the equilibrium state is.

This simple physical model can be transposed to tissue deformation (Figure 7). As a result of tissue volume conservation, modulating the ratio between apical and basal surface of an epithelium should lead to resultant forces oriented along the apico-basal axis. One possible outcome of these resultant apico-basal forces could be an apico-basal elongation, without apical bending. But assuming low apico-basal deformability, the resultant apico-basal forces can result in bending (as exemplified in Lewis experiment). If we focus on groove formation, as folding occurs in a preferential orientation, the only basal/apical surface changes that are meaningful to account for folding are directed along the axis which is perpendicular to the groove (y).

Thus, changes of basal/apical surface length along (y) axis can result in apico-basal forces and drive groove formation. I will here review the main models based on this principle.

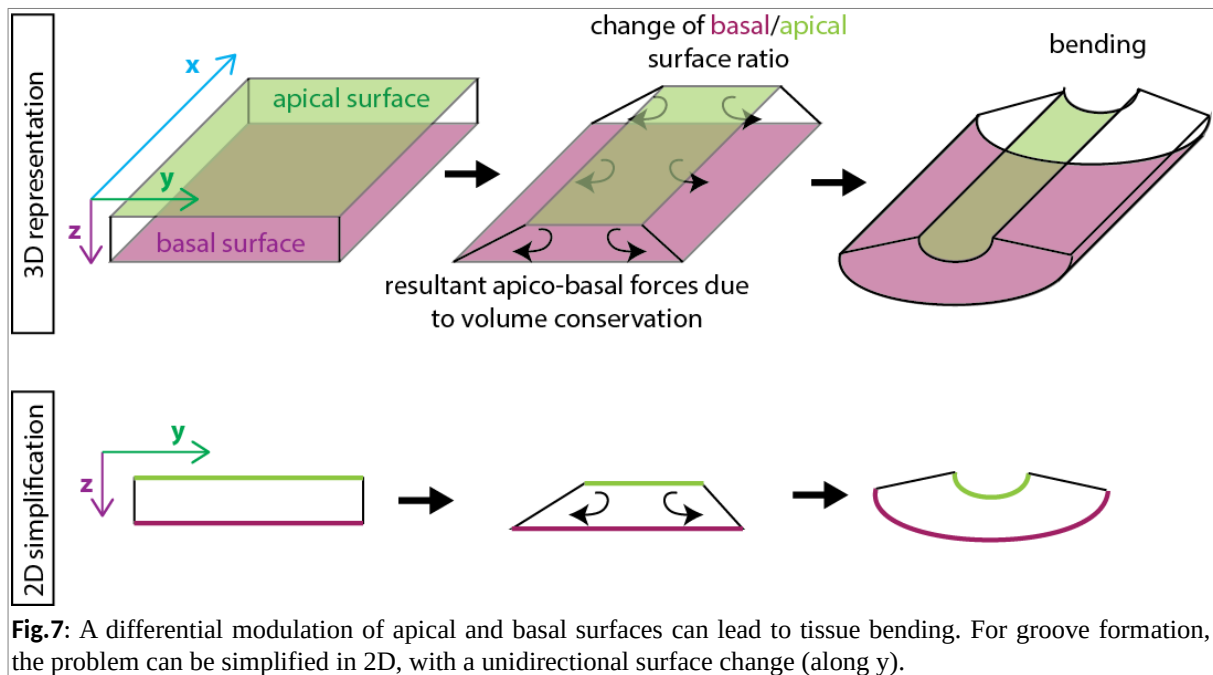


Fig.7: A differential modulation of apical and basal surfaces can lead to tissue bending. For groove formation, the problem can be simplified in 2D, with a unidirectional surface change (along y).

a) Cell wedging: a conserved cell shape change associated with folding

The most prevalent model of invagination by planar dynamics is based on a process called cell wedging. Cell wedging consists in a change of shape of cells which are located at the center of an invaginating domain, which leads to the acquisition of a so-called “bottle” shape, with reduced apical surface and increased basal surface. Cell wedging was originally observed in the blastopore lip of *Xenopus* gastrula, and was already hypothesized to play a role in tissue bending a hundred years ago⁹³. In the blastopore lip, cells indeed adopt apical sides that are highly constricted specifically perpendicularly to the fold (y), while both their basal and

lateral domains are elongated⁹⁴. Wedging appears to be a widespread phenomenon associated with epithelial bending, as it has been observed for instance in the medial fold of neural tube in vertebrate⁹⁵, in *Caenorhabditis elegans*⁹⁶, *Drosophila*⁷² and sea urchin⁹⁷ gastrulations, in regions of high curvature during mouse optic cup bending⁹⁸, in the bending regions leading to *Volvox* inside-out transitions⁹⁹ or in the *Drosophila* eye morphogenetic furrow¹⁰⁰.

b) Apical constriction as a mechanism for cell wedging

A vast literature indicates that a conserved and frequent mechanism of cell wedging is based on cell apical constriction⁷⁹. The active shrinkage of the cell apex can indeed be sufficient to lead to the acquisition of a “bottle” shape and to favor bending⁹⁴. Apical constriction has been extensively characterized in the context of *Drosophila* mesoderm invagination during gastrulation⁷⁹. In this context, the genetic network leading to mesoderm fate specification is well known (Snail and Twist transcription factors), and disruption of mesoderm fate specification leads to an inhibition of mesoderm invagination¹⁰¹. The downstream targets of these transcription factors have been identified as well. First, the loss of the secreted protein Folded Gastrulation¹⁰², or of the transmembrane protein T48 and the Gα protein Concertina¹⁰³ leads to loss of coordination during ingression. Secondly, acto-myosin dynamics regulation has been shown to be crucial to regulate mesoderm invagination. Loss of Abelson¹⁰⁴ or RhoGEF2¹⁰³, and expression of a dominant-negative form of Rho1¹⁰⁵ has been linked to F-actin and MyosinII mislocalization, leading to invagination defects. Furthermore, the phenomenology of mesoderm apical cell shrinkage has been precisely detailed. The pulsatility of a medial meshwork consisting of actin, MyosinII and Rok correlates with apical surface area variations¹⁰⁶. This medial acto-myosin pool connects to the cortical pool and the adherens junction. The formin Diaphanous has been shown to be essential to connect medial pool dynamics with the junction, converting medial pool contractility into stable junction shrinkage in a ratcheted manner⁷². Moreover, these medial/junctional acto-myosin pools form, at the scale of the mesoderm tissue, a supracellular acto-myosin network with precise connectivity and architecture. The high connectivity of this network has recently been shown to be crucial to ensure robust mesoderm cells collective invagination¹⁰⁷. Finally, the conversion of apical shrinkage into apico-basal forces has been precisely characterized using high resolution microscopy and hydrodynamics modelling. Apical shrinkage indeed triggers swirling of the cytoplasm, leading to both apico-basal extension of the cells and an apical lateral flow towards the constricting region¹⁰⁸. Strikingly, this swirling dynamics arise even in an acellular

embryo (an embryo in which lateral membranes are absent), suggesting that lateral membranes relay cytoplasm hydrodynamic behavior from a cell to another without affecting it¹⁰⁸.

Interestingly, apical constriction driven by apical acto-myosin contractility is observed in various other contexts. For example, *Xenopus* blastopore lip invagination has been recently shown to be associated with an apical localization of activated MyosinII¹⁰⁹, and apical constriction of blastopore lip cells has been shown to be regulated by the RhoGEF Plekg5¹¹⁰. Additionally, apical membrane remodeling by endocytosis has been discovered as a regulator of apical constriction rate, both in *Xenopus* blastopore lip cells and neural tube cells¹¹¹.

c) Apical constriction: constraint of neighboring tissues and tissue geometry

In order to drive tissue bending, apical constriction has to happen in a specific cell population. As a result, apically constricting cells are surrounded by non-constricting cells. To a certain extent, He and colleagues demonstrated that multicellular cytoplasm swirling caused by apical shrinkage in *Drosophila* mesoderm invagination can drive local neighboring cells to flow towards the site of invagination¹⁰⁸. But more than passively reacting to apical constriction, neighboring cells can also exert a constraint that influences the apical constriction pattern. Indeed, upon ablation of neighboring tissue, bottle cells of *Xenopus* blastopore lip tend to quickly rotate to increase blastopore lip indentation. Similar results were observed during endoderm invagination in ascidians, where disconnection of the endoderm from neighboring tissues triggered a faster invagination. Thus, it seems that a connection with neighboring tissues provides a resistive force to tissue bending.

Furthermore, pioneer experiments performed by Hardin and Keller revealed that mechanical constraints imposed by neighboring tissue influence the direction of apical constriction⁹⁴. In fact, under physiological conditions, blastopore lip cells apically constrict specifically along the animal-vegetal axis (perpendicularly to the fold, along (y) axis). When put in culture without neighboring tissues, or upon ablation of cells in the neighboring tissues in order to diminish cell density and hence neighboring tissue mechanical constraints, the anisotropy of apical contraction of blastopore lip cells is lost. Hardin and Keller thus conclude that the resistance of neighboring tissue may inhibit blastopore lip contraction along the circumferential axis (along (x) axis), and canalize apical constriction along the animal-vegetal pole (along (y) axis). This study echoes a recent study of *Drosophila* mesoderm invagination¹¹². The cells of the invaginating *Drosophila* mesoderm exhibit a clear anisotropic apical constriction, preferentially constricting along the dorso-ventral axis (perpendicularly to

the fold, along (y) axis)¹¹². Interestingly, the shape of the domain that constricts is as well anisotropic, being elongated along the antero-posterior axis (along (x) axis) and thin along the dorso-ventral axis (along (y) axis). In *spn27A* and *fat2* RNAi conditions, the shape of the constricting domain is less anisotropic¹¹². Global tension anisotropy decreases in these mutant conditions, leading to a loss of anisotropy in apical constriction¹¹². Thus, the anisotropy of the geometry of the constricting domain feeds back on apical constriction orientation, resulting in anisotropic apical constriction and anisotropic bending (e.g. the formation of a groove).

d) Synergy between apical constriction and apico-basal forces

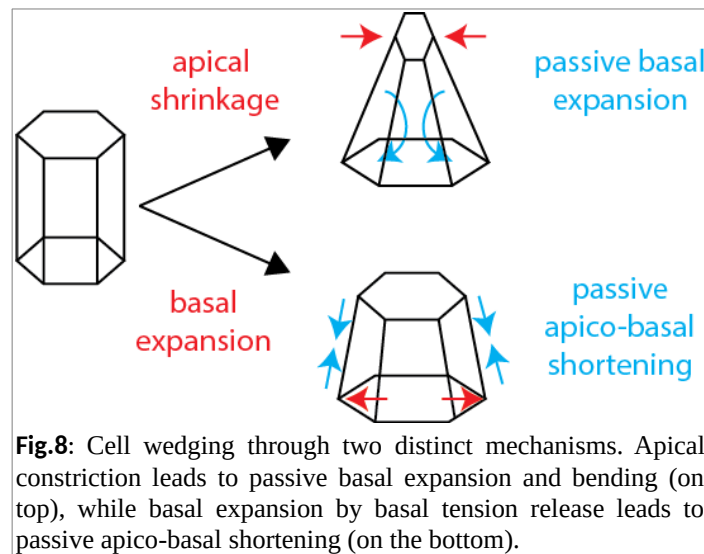
While apical constriction is one of the most prevalent models accounting for bending, whether it is sufficient to fully account for bending dynamics is unclear. Notably, even in the well described mesoderm invagination in *Drosophila*, a late phase of invagination is marked by apico-basal shrinkage without any further apical constriction¹¹³. Whether this late apico-basal shrinkage is an active process complementing apical constriction, or is a passive behavior, is unknown. Moreover, apico-basal forces triggered by EMT have been shown to synergize with apical constriction to trigger *Drosophila* mesoderm invagination⁷⁷.

Two well-described models successfully combine apico-basal forces with apical constriction as well. First, during leg joint morphogenesis, while apico-basal apoptotic forces are necessary to trigger invagination, they cannot fully account for the invagination⁷⁶. They are indeed proposed to be relayed by apical constriction of neighboring cells. This combination of bending forces successfully accounts for joint formation *in silico*⁷⁶. Secondly, during endoderm invagination in ascidians, apical constriction constitutes a first phase of invagination leading to the flattening of the endoderm and its apico-basal extension. This first phase is then followed by a phase of apico-basal shrinkage, during which most of the bending is achieved²⁵.

e) Basal relaxation as an alternative mechanism for cell wedging

In most wedging models, basal surface expansion is assumed to be a passive reaction of active apical shrinkage. However, recently it was demonstrated that basal extension can be the driving force of cell wedging (Figure 8). During *Drosophila* imaginal development, specific folds arise in the wing disc epithelium. One of this folds has been shown to arise without prominent cell apical shrinkage, but is rather associated with a basal surface extension⁷⁵. Interestingly, using laser ablation, it was not only shown that the basal surface of the

epithelium shows higher tension/friction ratios than the apical surface, but also that the basal surface of the folding region displayed less tension as compared to the basal surfaces of neighboring cells. This relaxation in basal tension relaxation depends on a local degradation of the ECM, and is sufficient to drive tissue bending⁷⁵. Thus, cell wedging can be achieved not only by apical constriction, but also by basal surface expansion and by releasing basal surface tension.



f) Can radial/perpendicular influx of cells participate to folding?

A change in apical or basal cell surface area is not the only mechanism that could trigger differential tissue surface variations required for tissue bending. For example, divisions, cell rearrangements (cell neighbor exchange) or tissue flowing towards the invagination site could participate to the tissue surface changes that are at the origin of bending. Could this flux of cells towards the invagination site participate to the invagination process? In theory, a sheet of cells undergoing increasing confinement first thickens and finally buckles when reaching a critical confinement¹¹⁴.

When put in 3D *ex vivo* culture, retinal primordium cells self-organize and recapitulate optic cup formation⁹⁸. Notably, optic cup formation relies on a final step of apical bending. Pharmacological inhibition of cell division specifically prevents this final bending from happening and therefore it was proposed that cell divisions provide a radial pushing force that participates in optic cup bending⁹⁸. Thus, radially oriented divisions appear to favor bending dynamics. Besides, during the formation of tracheal pits in *Drosophila*, cell divisions and

rearrangements show a biased radial orientation¹¹⁵. These two radially-oriented dynamics both tend to push cells towards the pit and are proposed to participate to tissue bending. Nevertheless, even if radial mitosis and rearrangements can induce a radial pushing force and increase cell density towards the invaginating region, how this force and the associated increase in cell density is converted into a bending force and not just into local tissue thickening, remains unexplored.

What is more, invaginations are often associated with neighboring tissue spreading. Whether neighboring tissue spreading could as well actively contribute to tissue folding by providing a perpendicular pushing force favoring buckling is still an unresolved issue.

In the second part of my thesis, I will study active collective migration of dorsal thorax epithelial cells and its coupling with neck invagination during *Drosophila* metamorphosis. I will provide experimental evidence showing that perpendicular influx of cells though migration does not substantially contribute to the initial bending of the neck, and that this influx is dissipated by local tissue surface variation next to the invaginating region. This data argues against the idea that perpendicular cell influx towards the zone of invagination systematically contributes to tissue buckling.

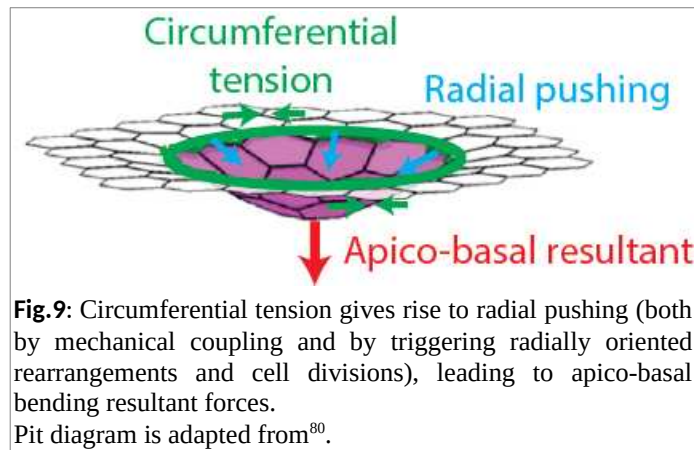
3) Models based on conversion of dynamics parallel to the folding axis (x) into forces directed along the apico-basal axis (z)

Apical constriction models can be based on a reduction of surface along the axis perpendicular to the axis of invagination (y) in the case of groove formation, or along the centripetal axis (y) in the case of pit formation. However, in a complementary fashion or independently to apical constriction, tension along the circumferential axis (x) can also be the driving force of pit formation, and recent studies suggest that tension along the axis parallel to the invagination (x) may drive groove formation.

a) Circumferential tension and pit formation

Invagination of the tracheal placode of *Drosophila* is a key model system of pit formation. Interestingly, additionally to apical constriction of a subset of cells at the center of the placode field, the placode field is surrounded by a supra-cellular acto-myosin cable¹¹⁵. This circumferential contractile cable has been proposed to drive circumferential intercalation of cells and radially oriented cell division. Both of these events tend to push cells to the center of the pit, and are proposed to participate to bending and deepening of tracheal pit. Furthermore, as modelling suggests⁸⁰, circumferential tension could trigger buckling purely by mechanical

mechanisms, without the contribution of any cellular dynamics. Thus, in this example, a circumferential tension imposed by an acto-myosin cable is converted into a radial pushing force (Figure 9). How this radial force is converted into an apico-basal force driving bending remains unclear, but it is possible that crowding triggered by radial pushing force combined with low apico-basal deformability result in a bending force. Formation of the circumferential acto-myosin cable formation at the tracheal pit depends on EGFR signaling¹¹⁵. Interestingly, in *Egfr* mutants, transient and multiple localized pits still arise in the placode field as a result of local apical constriction, suggesting that circumferential tension is necessary to synchronize placode cell ingression allowing the emergence of collective invagination of the whole placode field¹¹⁵. This observation also suggests that cell-based apico-basal forces may additionally participate to placode field invagination.



Interestingly, a similar mechanism of circumferential acto-myosin constriction is found during embryonic development of the *Drosophila* salivary glands¹¹⁶. Indeed, salivary gland placodes are surrounded by an acto-myosin cable prior to and during their internalization, and laser ablation experiments revealed that this cable is under more tension than neighboring junctions. However, unlike the cable surrounding tracheal placodes, the cable surrounding the salivary gland placode is mainly composed by cortical enrichment from cells at the salivary gland side, and not from neighboring cells. Moreover, the formation of the salivary gland acto-myosin cable does not depend on EGFR signaling, but on the asymmetric distribution of Crumbs and aPKC¹¹⁶.

Circumferential acto-myosin cables have also been observed during cyst formation upon clonal overexpression of key transcription factors regulating cell identity¹¹⁷. Using the FRT-Flp system to generate clones of aberrantly differentiated cells in the wing disc, Bielmeier and

colleagues found that aberrantly differentiated clones are surrounded by a contractile acto-myosin cable. Interestingly, depending on the size of the clone, different outcomes have been observed. While acto-myosin contractility can lead to the extrusion of individual cells, small groups of cells formed invaginated pits called cysts. For clones with less than 60 cells, the depth of the observed pit increased with cell number. However, groups of more than 100 cells did not form pits and remained within the plane of the tissue, only forming straight and locally invaginated boundaries with wild type cells. In conclusion, acto-myosin circumferential tension can lead to pit formation only in groups of cells of intermediate size. These observations were recapitulated in a 3D model of pit formation based on circumferential tension¹¹⁷.

However, tracheal placode morphogenesis may provide an example of a mechanism that allows extending the size of pit formation by circumferential tension. Indeed, it has been recently found that EFGR signaling around the invaginating placode is dynamic. While EGFR is only active in the central region during the onset of invagination, it spreads more and more radially in time, leading to the assembly of successive concentric boundary acto-myosin cables of increasing radius. This sequential radial expansion promotes tracheal pit formation, and provides an example on how a big field of cells can participate to pit formation despite the physical limitations found by Bielmeier and colleagues¹¹⁷.

b) Acto-myosin cables and groove formation

During pit formation, the tension of a circular acto-myosin cable located in the plane of the tissue triggers the buckling of the tissue that it surrounds. However, it is unclear whether linear acto-myosin cables could lead to the formation of grooves. According to the study of Bielmeier and colleagues¹¹⁷, planar linear acto-myosin cables can lead to the formation of straight boundaries, without triggering bending. However, this study only considers flat linear acto-myosin cables and it is likely that the curvature of linear acto-myosin cables leads to the conversion of cable constriction into an apico-basal force, that could result into tissue bending (Figure 10).

Interestingly, linear acto-myosin cables have been associated with the formation of transient and shallow folds at the boundary between parasegments in *Drosophila* gastrula¹²⁰. In their study, Urbano and colleagues have found that genetic or pharmacological perturbations of the inter-parasegmental acto-myosin cables suppressed folding. Moreover, they have shown that induction of the formation of acto-myosin cables at ectopic locations is

associated with the formation of grooves that are deeper than normal parasegmental grooves. They thus propose that boundaries showing an acto-myosin cable bear an intrinsic ability to trigger folding, which is normally inhibited to either give rise to flat or slightly folded interfaces. This hypothesis would explain why parasegmental grooves only appear transiently and other interfaces showing a boundary acto-myosin cable, like the intercompartmental antero-posterior boundary of the wing disc, are flat. Accordingly, the folding potential of the intercompartmental antero-posterior boundary of the wing disc can be induced in a mutant for *optomotor-blind*¹²¹.

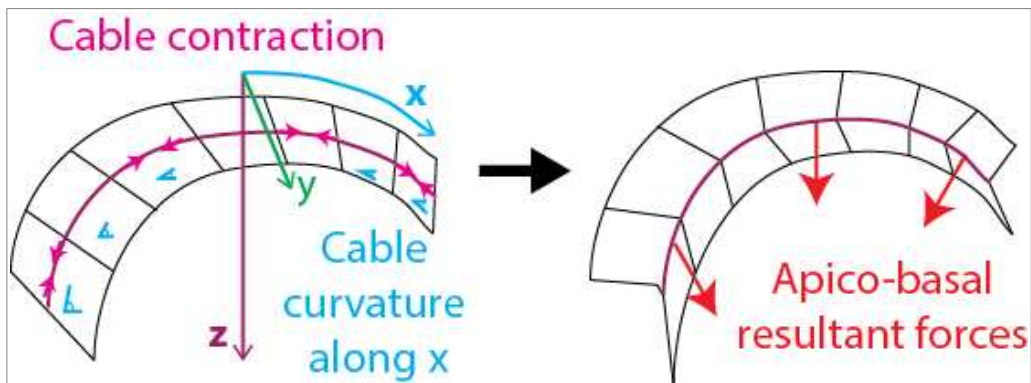


Fig.10: Contraction of a curved cable could lead to apico-basal resultant forces and bending. Note that this model is inspired by a model developed by Czerniak and colleagues¹¹⁸, in which topological curvature (but not along (x), along (y)) is invoked to model the conversion of a linear acto-myosin cable contraction into spreading in (y) (this model is further presented and discussed in Figure 19). Very similar models can also be found to account for groove formation at the cellular scale during cytokinesis¹¹⁹ (more details can be found in Figure_{part1} 4 of the “Results” section).

When imaging the first step of parasegment formation, Urbano and colleagues did not identify signs of apical constriction. This result suggest that groove formation is in this context achieved by an atypical bending mechanism. As lateral junctions of the segment interface appeared to be straighter than neighboring junctions, they proposed that an increase in lateral tension might explain how tensile interfaces can promote bending. However, this mechanism might not be sufficient to account for the deeper ectopic folding. We propose that a possible alternative mechanism might be that the curvature of the parasegmental acto-myosin cables allows the conversion of cable constriction into an apico-basal force and thus bending (Figure 10), but this alternative mechanism remains untested.

In the first part of my thesis, I will use the characterization of neck formation during *Drosophila* metamorphosis to propose a complementary model for groove formation involving the contraction of a curved linear acto-myosin cable.

4) Graphical summary of part B/: Typology of epithelial folding dynamics (Figure 11)

Apico-basal dynamics	Planar dynamics	
	Perpendicular to the folding axis	Parallel to the folding axis
<i>Drosophila</i> joint leg morphogenesis	Apical constriction in response to apoptotic force	
Endoderm invagination in ascidian	Initial apical constriction	
<i>Drosophila</i> mesoderm invagination	Apical constriction	
	<i>Drosophila</i> tracheal pit formation	
	Apical constriction Oriented cell divisions and rearrangements toward the pit	Circumferential tension of a cable surrounding the pit
<i>Drosophila</i> dorsal fold formation during gastrulation	<i>Xenopus</i> gastrulation Vertebrate neural tube folding <i>C. elegans</i> gastrulation Sea urchin gastrulation <i>Volvox</i> inside-out transition	
	Apical constriction	
<i>Drosophila</i> wing disc dorsal folding	<i>Drosophila</i> wing disk dorsal folding	<i>Drosophila</i> salivary glands pit formation
	Basal tension release	Circumferential tension of a cable surrounding the pit
Mouse vessel sprouting	Mouse optic cup formation	
	Apical constriction Radial mitotic pressure and final folding	
<i>Drosophila</i> cyst formation		in wing disc
		Circumferential tension of a cable surrounding the cyst
Inter-parasegmental grooves		in <i>Drosophila</i> embryo
		Contraction of a linear acto-myosin cable?

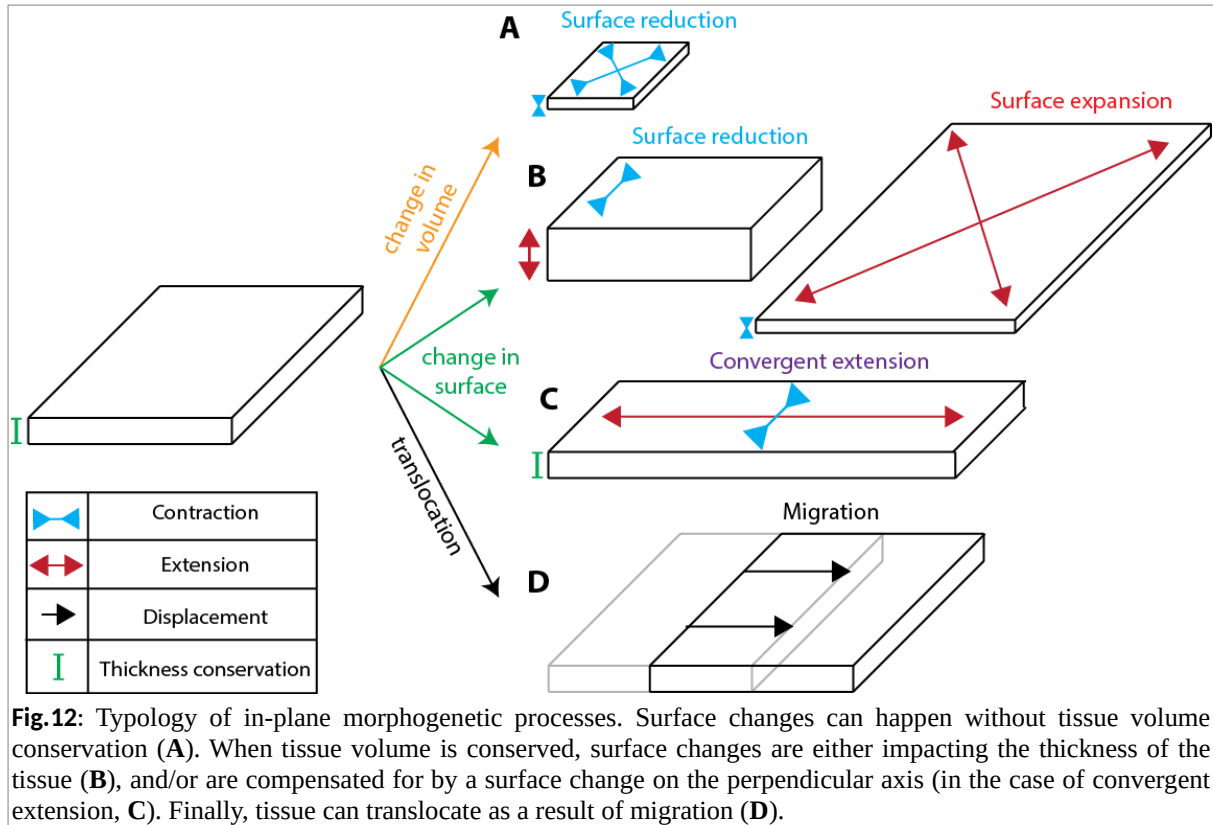
Fig.11: Typology of epithelial dynamics. Examples of epithelial folding used in section B/ are here summarized. Associated folding driving forces are indicated in grey, and classified according to the axis they act on.

C/ In-plane epithelial morphogenesis

While epithelia can display out-of-plane morphogenesis and evolve complex 3D manifolds, many epithelial morphogenetic processes happen in the plane of the tissue. Notably, tissue spreading, tissue contraction, convergent extension and collective displacement are key morphogenetic modules which are omnipresent during development and contribute considerably to the shaping of organs and organisms. I will here review the main mechanisms leading to in-plane epithelial morphogenesis, by first focusing on intrinsic active mechanisms. I will distinguish them according to the type of morphogenetic process they underlie (tissue contraction, tissue expansion, convergent extension and collective displacement, Figure 12). I will finally review passive in-plane deformations resulting from coupling with neighboring active mechanisms, and more generally discuss the idea of long-range mechanical coupling.

C1/ Active in-plane epithelial morphogenesis

Epithelial tissues can actively modulate their surface. A change in tissue surface can be either isotropic (equal in all the direction), or anisotropic (in a preferential direction). Change in length in a preferential direction, if happening with tissue volume conservation, can be accompanied by an opposite change in length in the perpendicular direction. This process is called convergent extension (Figure 12C). If not, tissue volume conservation triggers a change in tissue thickness (cuboidal-to-columnar or columnar-to-cuboidal transitions, Figure 12B). However, conservation of tissue volume is not always observed (either because cell number can decrease as a result of cell delamination events, or because cell volume can decrease in some specific contexts¹²²), and surface changes can arise without tissue thickness variation and in absence of convergent extension (Figure 12A). Here I will separate the cases in which tissue contractions and expansions occur in the presence or absence of convergent extension. Finally, an epithelial domain can translocate without deforming, leading to organ and organism morphogenesis. I will in this section only focus on the intrinsic mechanisms leading to tissue translocation (Figure 12D). Tissue deformation as a result of heterogeneity in migration potentials will be discussed in C2/. Note that in this section, I will restrict the discussion to mono-layered epithelia. Active mechanisms of deep layers of multilayered epithelia and underlying mesenchymal populations will also be reviewed in C2/ section.



1) Active tissue surface reduction

a) Surface reduction by cell surface shrinkage and tissue thickening

Epithelia can display various thicknesses. Traditionally, epithelia are subdivided into three classes according to their thickness: squamous (thin), cuboidal (intermediate) and columnar (thick). Surface reduction of the apical surface, when accompanied by similar surface reduction of the basal surface, can give rise as a result of tissue and cell volume conservation¹²³ to a thickening of the tissue. This transition thus gives rise to a conversion of a cuboidal geometry into a columnar geometry (named cuboidal-to-columnar transition).

Various active mechanisms driving cuboidal-to-columnar transition have been identified. Notably, down-regulation of lateral contractility has been proposed to drive cuboidal-to-columnar transition during *Drosophila* wing disc development¹²⁴. Dpp signaling has been shown to exclude Rho1 and MyosinII from the lateral domains, leading to an apico-basal lengthening of the cells and an increased planar cell density. Accordingly, both the loss of Dpp or disruption of Rho1 and MyosinII reduce tissue thickness and cell density.

Reduction of epithelial planar surface can also be the result of active apical surface shrinkage, secondary leading to tissue thickening and cuboidal-to-columnar transition. For

instance, prior to ascidian endoderm invagination, endoderm cells undergo an apical shrinkage and an apico-basal thickening²⁵. Apical shrinkage has been shown to be associated with an apical recruitment of activated MyosinII, while lateral domain expansion has been proposed to be a passive reaction in response to apical constriction. Similar to ascidian endoderm morphogenesis, the mammalian neural plate shows a clear thickening prior to bending. This cuboidal-to-columnar transition has been shown to depend on PTEN, which regulates both membrane lipids phosphorylation and apico-basal trafficking¹²⁵. Indeed, loss of PTEN both decreases neural plate thickening and decreases planar cell density resulting in an abnormal increase in epithelial surface area. PTEN could have a dual role in tissue thickening and surface reduction, by both promoting apical surface reduction and stabilizing an apico-basal array of microtubules, which is hypothesized to stabilize a columnar geometry¹²⁵.

Thus, planar surface and tissue thickness appear to be regulated by both apical and lateral contractility. The stabilization of tissue thickness as a result of apical and lateral tensions can be recapitulated *in silico*¹¹⁴. In concordance with the experimental data, high apical contractility is predicted to favor a columnar geometry, while high lateral contractility is predicted to favor cuboidal or squamous geometries.

b) Surface reduction without tissue volume conservation

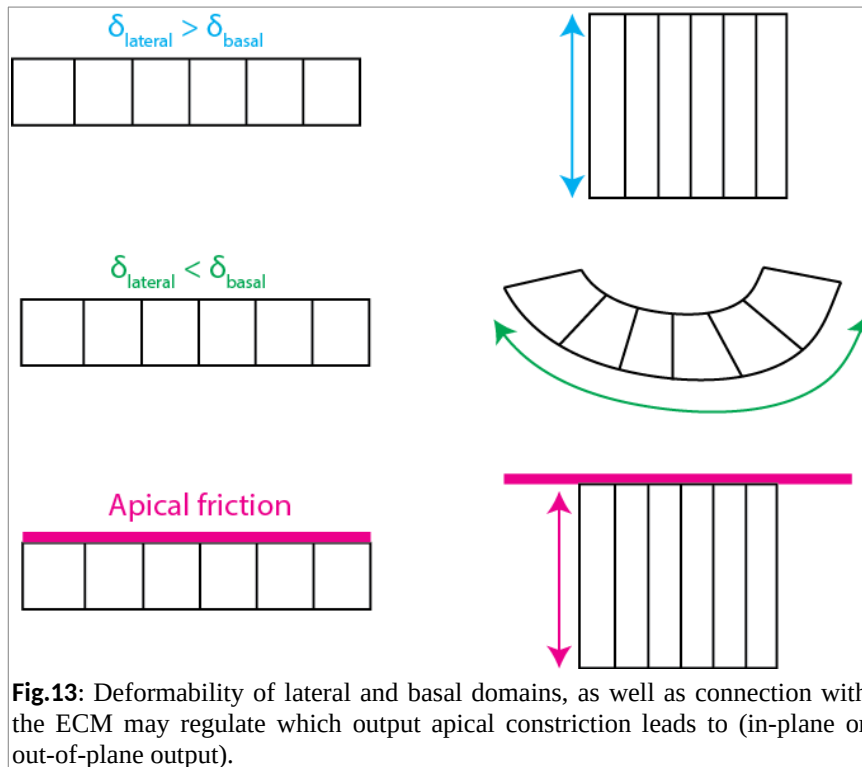
Epithelial cell surface can decrease in absence of changes in tissue thickness. Yet, such surface decrease must involve a decrease in tissue volume. Tissue volume decrease can be due to (i) cell number decrease by delamination or to (ii) cell volume decrease.

First, cell loss is a key mechanism leading to epithelial tissue surface reduction. During *Drosophila* dorsal closure, apoptosis in the amnioserosa participates to its surface reduction¹²⁶. Similarly, during *Drosophila* abdomen metamorphosis, the larval abdominal cells undergo a patterned apoptosis, leading to a global shrinkage and elimination of larval tissues, thus favoring adult tissue spreading⁸⁹.

Second, even if cell volume is often considered as fixed and tightly regulated during interphase^{123,127}, cell volume can decrease and lead to tissue shrinkage. Such a scenario has been observed during *Drosophila* dorsal closure¹²². During dorsal closure, an extra-embryonic tissue, the amnioserosa, gradually loses volume, leading to its planar shrinkage. Amnioserosa cell shrinkage has also been shown to rely on an pulsatile apical acto-myosin network that decreases the cell apical surface⁷³. This latter mechanism is similar to that of apical constriction of the *Drosophila* mesoderm during internalization¹²⁸ (see B/2/b section).

c) Reconcile apical shrinkage models: Planar or out-of-plane outputs?

Apical surface shrinkage, either through cell apical constriction or by cell delamination, can lead to both planar surface reduction or induce folding. How can we reconcile these two outputs? First, it appears that even in the model systems described here to illustrate planar apical shrinkage, bending eventually occurs after planar shrinkage (even during amnioserosa shrinkage, subtle bending can be observed at the end of tissue shrinkage phase¹²²). Thus, a continuum between planar shrinkage and bending seems to occur. Besides, we propose that the ratio between lateral and basal surface deformability ($\delta_{\text{lateral}}/\delta_{\text{basal}}$) may be key to model the output of apical constriction (Figure 13). We hypothesize that high $\delta_{\text{lateral}}/\delta_{\text{basal}}$ favors planar surface shrinkage and cuboidal-to-columnar transition, while low $\delta_{\text{lateral}}/\delta_{\text{basal}}$ favors wedging and tissue bending. Moreover, bending of the apical surface is a key feature of apical constriction bending mechanisms. We thus hypothesize that apical adhesion to an ECM inhibits wedging and forces tissues to remain planar in the presence of differential apico-basal forces. Such hypothesis may explain morphogenesis of the *Drosophila* abdomen, where larval abdominal cells adhere to the apical ECM while they progressively delaminate, yet without inducing larval tissue bending¹²⁹.



Another prominent difference between pulses of apical constriction in *Drosophila* mesoderm and amnioserosa pulsatile contraction during dorsal closure is the period of the pulsations. While mesoderm pulsatile cells contractions have a period of 1-2min and lead to invagination within 15min, amnioserosa cells contractions have a period of about 4min, and amnioserosa contraction lasts for several hours¹³⁰. Whether this difference is relevant to understand the difference in outputs of apical constriction is not known. We propose that the friction as a result of adhesion with the ECM might explain this difference, with high friction leading to longer contraction periods and planar deformations.

2) Active tissue surface expansion

a) Surface expansion by apical and basal surfaces increase and tissue thinning

While surface shrinkage can arise as a result of cell shape shrinkage and tissue thickening, the opposite scenario exists as well. Apical surface expansion can result from cell apical surface expansion, associated with a thinning of the tissue. This transition is referred to as columnar-to-cuboidal transition (Figure 14A).

Columnar-to-cuboidal transition is well described in the follicular epithelium of the *Drosophila* ovary. It has been shown that the kinase Tao is involved in preventing the accumulation of the cell-cell adhesion protein Fasciclin2 in lateral domains¹³¹. It thus appears that the down-regulation of lateral intercellular adhesion can be a driving force for lateral domain shrinkage, and passively triggers the expansion of the apical domain, presumably as a result of cell volume conservation.

Another well-described example of columnar-to-cuboidal transition can be found during *Drosophila* wing and limb pre-pupal development²⁴. During pre-pupariation, the freshly everted wing and leg discs dramatically expand their surface and decrease their thickness. It has been shown that the degradation of both apical and basal ECM are necessary for the columnar-to-cuboidal transition to occur²⁴. Moreover, after matrix degradation, lateral localization of MyosinII is associated with lateral domains shrinkage, and pharmacological inhibition of MyosinII contractility inhibits the columnar-to-cuboidal transition. Thus, like in the follicular epithelium, lateral domain shrinkage is the driving force of the columnar-to-cuboidal transition, but it in these systems shrinkage is triggered by an increase in contractility rather than by a decrease in cell-cell adhesion. Furthermore, it seems that a connection with the ECM favors a steady columnar geometry, while release of attachment allows tissue thinning and expansion.

In the second part of my thesis, I will show that tissue stretching along a preferential direction can be achieved by a novel mechanism, based on collective migration: as a result of a gradient of active migration force along the migrating region, the migrating domain can indeed stretch.

b) Surface expansion by cell growth after division and cell integration

From the initial phases of embryogenesis to organogenesis, as well as during homeostasis or tumor formation, tissue growth is associated with cell division. Thus, it is not surprising that cell division, followed by cell growth, can play a role in epithelial surface expansion (Figure 14B). For example, mouse blood vessels elongation involves cell division⁹¹, and during their expansion, the histoblast niches in the *Drosophila* abdomen display a high division rate while the pupa is undergoing metamorphosis¹³².

Increase in cell number in the epithelial sheet, however, does not necessarily involve cell division. Indeed, cells can actively insert into an epithelium, in a process called radial intercalation (Figure 14B). Radial intercalation is well described in *Xenopus* mucociliary epithelium¹³³. This process is involved in homeostasis, allowing cell renewal.

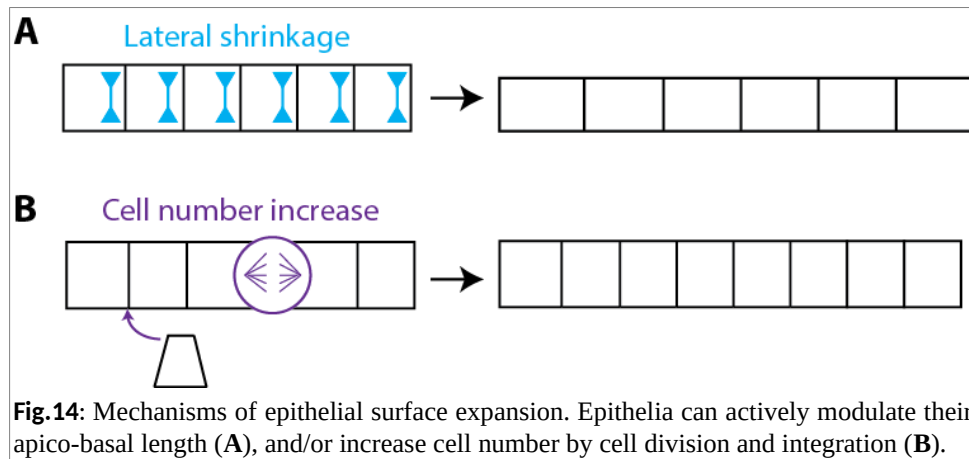


Fig.14: Mechanisms of epithelial surface expansion. Epithelia can actively modulate their apico-basal length (A), and/or increase cell number by cell division and integration (B).

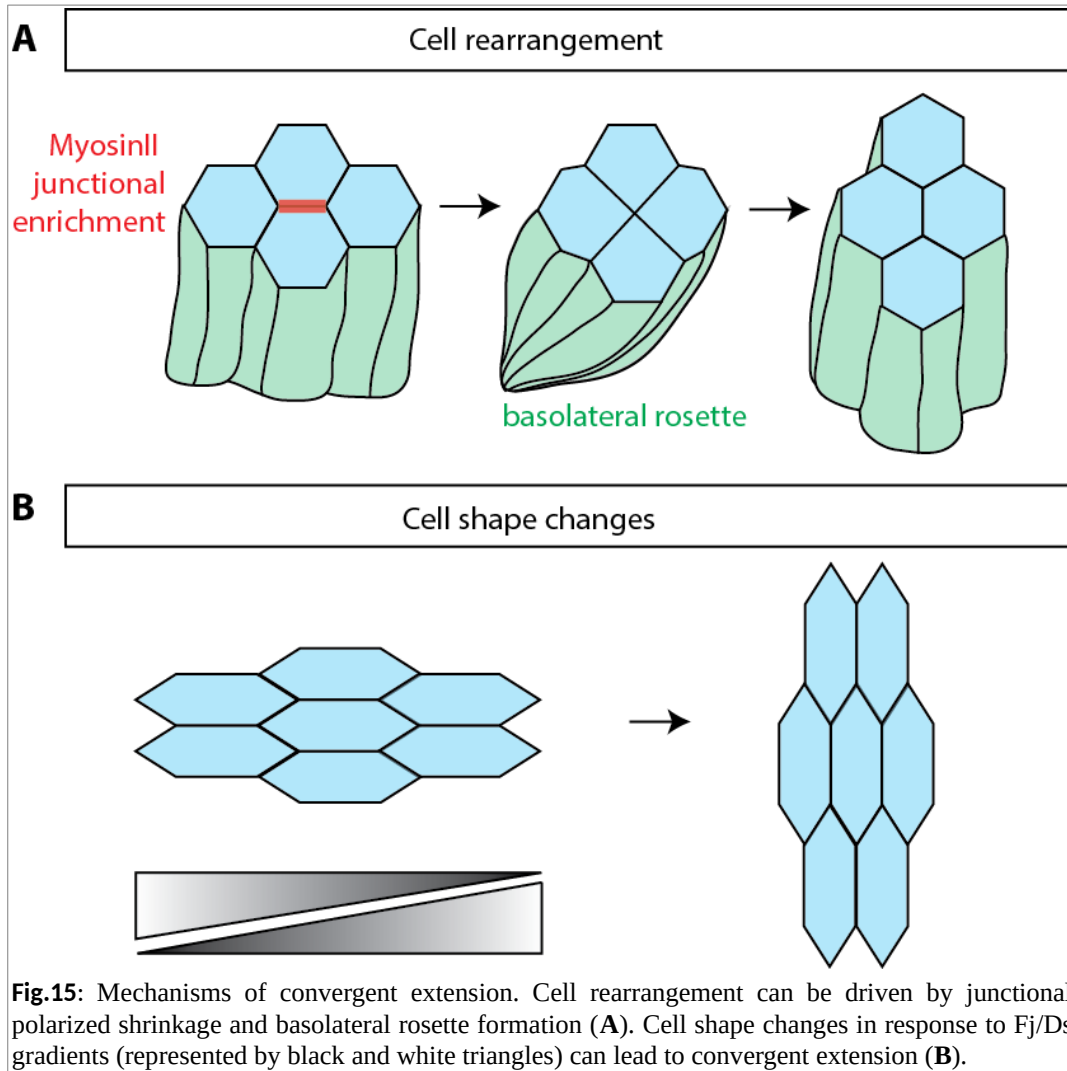
3) Active convergent extension

Convergent extension is a process which is intrinsically based on planar polarity. While the tissue stretches in a preferential direction, it compresses along the perpendicular direction. Its mechanisms have thus to rely somehow on planar polarized cues. Many of the mechanisms driving convergent extension have been identified in studies of *Drosophila* germband extension. During germband extension, junctions that are perpendicular to the orientation of tissue stretching preferentially shrink, disappear and give rise to the formation of new junctions oriented along the orientation of tissue stretching⁶⁷ (Figure 15A). This process, called cell rearrangement or T1 transition, enables cell neighbor exchange and a global redistribution of cells towards a preferential orientation, without total tissue surface variation. Interestingly, cell rearrangements during germband extension are associated with a planar polarization of MyosinII in the tissue, with an enrichment on junctions oriented along the

orientation of tissue shrinkage. This planar polarized enrichment of MyosinII is thought to be the driving force of junction shrinkage, thereby regulating the preferential orientation of cell rearrangements¹³⁴. The source of MyosinII planar polarization in the gastrula is not due to classical core PCP pathway (see A/3 section). It is instead linked with a “code” of genes which are differentially expressed along the antero-posterior axis, forming successive stripes with a given combination of gene expression. Maternal genes (*bicoid*, *nanos* and *torso-like*), gap genes (*knirps*, *hunchback*, *forkhead* and *tailless*) and pair-rule genes (*eve* and *runt*) are all involved in planar polarization of MyosinII⁵⁷. A positional code of overlapping stripes of Toll receptors expression has been shown to act downstream of the pair-rule genes to direct MyosinII planar polarization⁵⁸. The apico-basal polarity protein Bazooka and the protein Slam are downstream actors of this pathway, and are necessary for MyosinII planar polarization. While Bazooka shows an opposite planar polarization to MyosinII, the protein Slam display a similar planar polarization as MyosinII⁵⁷.

While junctional shrinkage is a key mechanism of germband extension, an additional mechanism based on baso-lateral dynamics has been uncovered¹³⁵. Indeed, prior to apical rosette formation (the outcome of junctional shrinkage), cells rosette forms basolaterally as a result of convergent basolateral migration. Cells first rearrange baso-laterally by extending basal protrusions, leading to baso-lateral radial intercalation. This basolateral rearrangement is then propagated apically, and leads to apical rearrangement (Figure 15A). Baso-lateral protrusion formation has also been observed during dorsal intercalation in *C.elegans*¹³⁶. These mechanisms echo a well-known mechanism of convergent extension in mesenchymal tissues, based on polarized intercalation. This process was first observed during *Xenopus* mesoderm convergent extension during gastrulation¹³⁷. In this system polarized intercalation has been linked with polarized emission of protrusions, which are thought to drive intercellular traction forces leading to cell intercalation. Interestingly, mesenchymal tissue convergent extension in vertebrates requires the atypical Wnt pathway¹³⁷, establishing a link between core PCP pathway and convergent extension.

We have seen that convergent extension can emerge from cell neighbor exchanges, but cell shape changes can also drive convergent extension. In the *Drosophila* pupal abdomen, after fusion of the histoblast niches, abdominal cells show a striking change in apical shape aspect ratio⁵⁰. The initial antero-posterior stretched cell shape is converted into a stretched shape along the medio-lateral axis, driving an alignment of the cells along the medio-lateral axis. This process has been shown to depend on Ft/Ds PCP pathway, illustrating convergent extension movements can be regulated by PCP signaling (Figure 15B).



4) Active translocation

We have seen so far that epithelia can change shapes as a result of contraction of polarized and localized pools of acto-myosin networks, independently from their interaction with ECM or other tissues. However, interaction with the ECM and neighboring tissues can also be pivotal for understanding epithelial morphogenesis. The only example involving a tissue-ECM interaction I have mentioned so far is the morphogenesis of the prepupal wing²⁴, in which a connection with the ECM is linked with a “frozen” morphogenetic state, and in which ECM degradation is required to allow tissue deformation (see C1/2/a section). In this section, I will review the importance of the interaction between tissue and ECM for epithelial collective migration.

a) Edge effects and collective migration

Epithelia are highly cohesive structures and display many mechanisms preventing hole formation. Upon wound induction, the creation of free edges is known to induce wound closure processes¹³⁸. One of the mechanisms of wound closure depends on the acquisition of motility of the cells bordering the wound. For example, during wound closure in *Drosophila* pupal epidermis, the cells that line the free edge created by the wound extend long protrusions directed towards the center of the wound¹³⁹. The requirement of integrins in wound re-epithelization suggests that these protrusions underlie migration¹⁴⁰. Interestingly, cells bordering the wound are not the only ones to respond to wounding. In an *in vitro* wound closure assay, it has been shown that multiple rows of cells respond to free edge creation, by emitting so-called “cryptic lamellipodia” along the basal substratum towards the free edges¹⁴¹ (Figure 16). This result suggests that wounding can trigger collective epithelial migration of a few rows of cells bordering the wound edge. Accordingly, in a RNAi screening for actors of wound closure, some targets (like *Mbc*, *Ced-12* or *SCAR*) have been identified as necessary for neighboring tissue remodeling independently of wound edge closure¹⁴².

Traction exerted by cells on their basal substratum can be inferred *in vitro*, both by plating cells on micro-pillars¹⁴³, or on gels containing fluorescent beads¹⁴⁴. The displacements of micro-pillars or the beads within the gel are the result of cells traction forces, and the tracking of these displacements can be used to map traction forces within a migrating epithelial cell culture. Interestingly, traction forces are found to be prominently high on the few cell rows bordering the free edges of the culture^{143,144}, supporting the idea of a high migratory activity in the vicinity of the free edge.

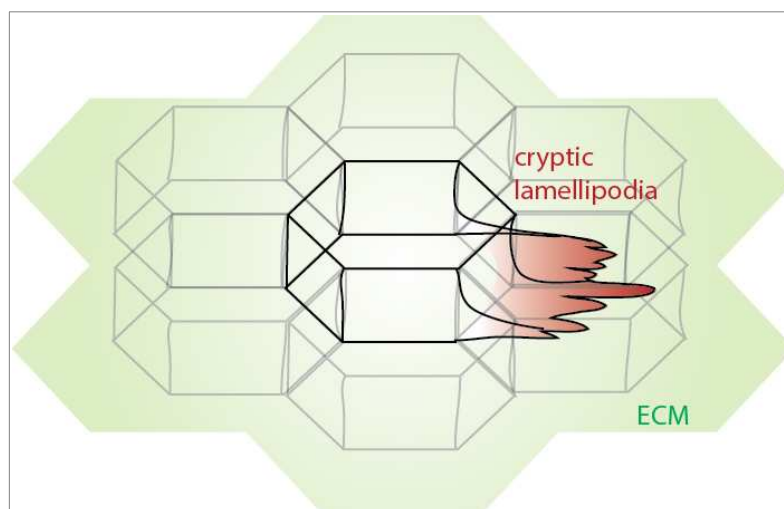
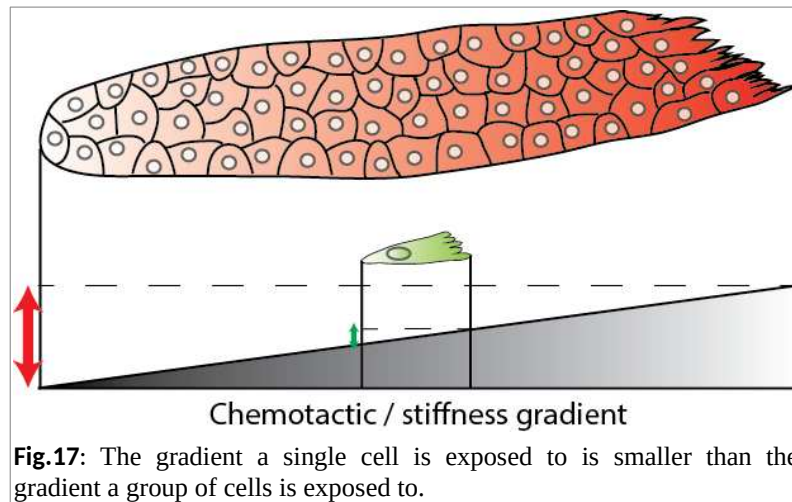


Fig.16: Cryptic lamellipodia can extend below front neighbors and enable crawling within the epithelium.

The mechanism of active migratory edge can be found outside the framework of wound healing and accounts for many events of collective epithelial and epithelio-mesenchymal migration¹⁴⁵. For example, in *Drosophila* ovaries, migration of a small cluster of cells, the border cells, is known to rely on a subdivision of the cluster into actively protruding leaders and passively dragged followers¹⁴⁶. Similarly, during lateral line migration in zebrafish, cells at the front of the lateral line show a clear protrusive and migratory activity, while the trailing edge is composed of cells that passively follow the migrating cells¹⁴⁷. While the activity of the leading edge is a prominent feature of many collective migrations¹⁴⁵, the rear edge has also been reported to elicit active behaviors which not only drive rear retraction, but also provide a rear driving force promoting collective translocation. Indeed, during *Xenopus* cranial neural crest migration, the assembly of a contractile acto-myosin cable at the rear promotes rear retraction and trigger a flow of cells away from the rear, which participates to neural crest translocation¹⁴⁸. In this model system, based on the combination of the activity of the front edge and the rear edge, it was proposed that the migrating cluster of cells behaves as a “super-cell”, whose migration is fully driven by edge effects¹⁴⁹.

b) Emerging properties of migration based on edge-effects

Intercellular cooperativity among cells forming a “super-cell” and migrating as a cohort has been shown to be instrumental for the acquisition of directional migration. The directionality of migration, in single-cells or in collectives, is notably known to be regulated by chemical gradients (this process is called chemotaxis). In theory, the chemical gradient a single-cell can experience is much lower than the gradient that a “super-cell” can experience, predicting that collective chemotaxis would be more efficient as compared to single-cell chemotaxis (Figure 17). Interestingly, when cultured *in vitro*, the directionality of migration of clusters of neural crest cells towards a source of chemoattractant (Sdf1) is higher than that of neural crest cells in isolation¹⁵⁰. Accordingly, intercellular interactions are required for collective chemotaxis towards Sdf1 *in vivo*. It thus appears that the super-cellularity of migrating collectives can lead to a more efficient chemotaxis. Furthermore, it has recently been demonstrated, using zebrafish lateral line as a model system, that collectives of migrating cells can generate, as a result of a spatialized source-and-sink mechanism, their own chemoattractant gradient¹⁵¹. A similar source-and-sink mechanism can be found during *Xenopus* neural crest migration. Indeed, the neighboring placode cells constitute a “source” of chemoattractant for neural crest cells and move away when contacted by the “sink” neural crest cells, leading to a chase-and-run behavior promoting directional movement¹⁵².



Additionally, collectiveness has been shown to promote another form of taxis, named durotaxis. Durotaxis is the ability of cells to migrate towards stiffer substrata¹⁵³. Interestingly, when put in culture as a sheet of cells, human mammary epithelial cells display a tendency to spread towards the stiffer region of a substratum displaying a gradient in stiffness, while single-cells fail to do so¹⁵⁴. This behavior has been shown to involve differential edge behaviors, with traction forces leading to less matrix displacement on the stiff side. Interestingly, this asymmetry is communicated on long range distances across the tissue, leading to a global spreading towards the stiff region. Thus it appears that, similar to a neural crest cluster, a human mammary epithelial cell culture behaves like a “super-cell”, dominated by edge dynamics and propagating edge effects on long range distances.

While the vicinity of free edges appears to play a pivotal role in collective migration, it should be noted that the active behaviors are not necessarily restricted to the few rows of cells lining the free edge. Remarkably, high traction forces have also been found hundreds of microns away from the free edge *in vitro* (even though the intensity of traction decays with the distance from free edge), suggesting that free edge signals can induce active crawling on long-range distances¹⁴⁴. Thus, even if leading edge cells have prominent migratory activity, active behaviors can as well distribute across the migrating cohort.

c) Edge-independent collective migration

Edge effects can drive the translocation of large cohort of cells, but is the classical spatial regionalization between front edge / passive cohort / rear edge necessary for the emergence of collective migration? The *Drosophila* follicular epithelium constitutes a paradigm in the field of collective cell migration to study edge-independent mechanisms, since no subdivision between leaders and followers can be found in this migrating epithelium. Follicular cells all emit protrusions on the front pole at their basal side (comparable to cryptic lamellipodia, Figure 16), and all migrate in a cell-autonomous manner on the basal ECM²⁸ (Figure 18). As a result, the basal surface of the follicular epithelium shows a planar polarized protrusive activity. Interestingly, the basal surface of each migrating cell shows a cortical planar polarization of the cadherin Fat2 and of the receptor tyrosine phosphatase Lar, which both are excluded from the lateral domains, and respectively localize at the front and the back of the cell⁵⁹. Fat2 is required for cell-autonomous rear retraction and Lar for cell-autonomous leading edge protrusive activity. Moreover, Fat2 front localization promotes in a non-cell-autonomous manner the localization of Lar in the neighboring cell. Fat2/Lar planar polarity module is complemented by the semaphorin pathway. Semaphorin-5c indeed localizes at the leading edge, and is required for follicular epithelium collective migration¹⁵⁵.

More than enabling a simple tissue translocation, follicular epithelium migration is necessary for a global elongation of the follicle, which determines the shape of the future egg. Remarkably, follicular epithelium migration takes place on a curved surface, and gives rise to a revolution movement around the germarium¹⁵⁶. During revolution, cells deposit collagen fibrils in a direction which is parallel to their trajectory, building a collagen corset around the germarium. The removal of the collagen matrix completely abrogates germarium elongation. Furthermore, inhibition of migration is associated with defects in collagen parallel fibers deposition and defects in germarium elongation, suggesting that the matrix acts as a corset constraining germarium shape¹⁵⁶.

Interestingly, planar polarity cues guiding cell-based protrusive activity during collective migration have been identified in other systems. During *Drosophila* larval cell migration in the pupa, the larval cells display a collective translocation towards the posterior, which is associated with the emission of lamellipodia on the apical surface, specifically at the front pole⁷⁴ (Figure 18). These lamellipodia are thought to interact with the apical ECM and, as knock-down of the apical ZP protein Piopio leads to migration defects, cells are thought to use the apical ECM as a migration substratum. Although gradients of Fj/Ds are required to guide

the planar polarization the lamellipodia, the Ft/Ds PCP pathway only accounts for the polarization in half of the migrating segment¹⁵⁷. Interestingly, migration using the apical ECM as a substratum might be a conserved mechanism in vertebrates, as a study from 1990 unambiguously showed an interaction between the edge of the spreading ectoderm and the vitelline membrane, the apical matrix surrounding the embryo¹⁵⁸. The mechanism of this migration, nevertheless, remains largely unexplored.

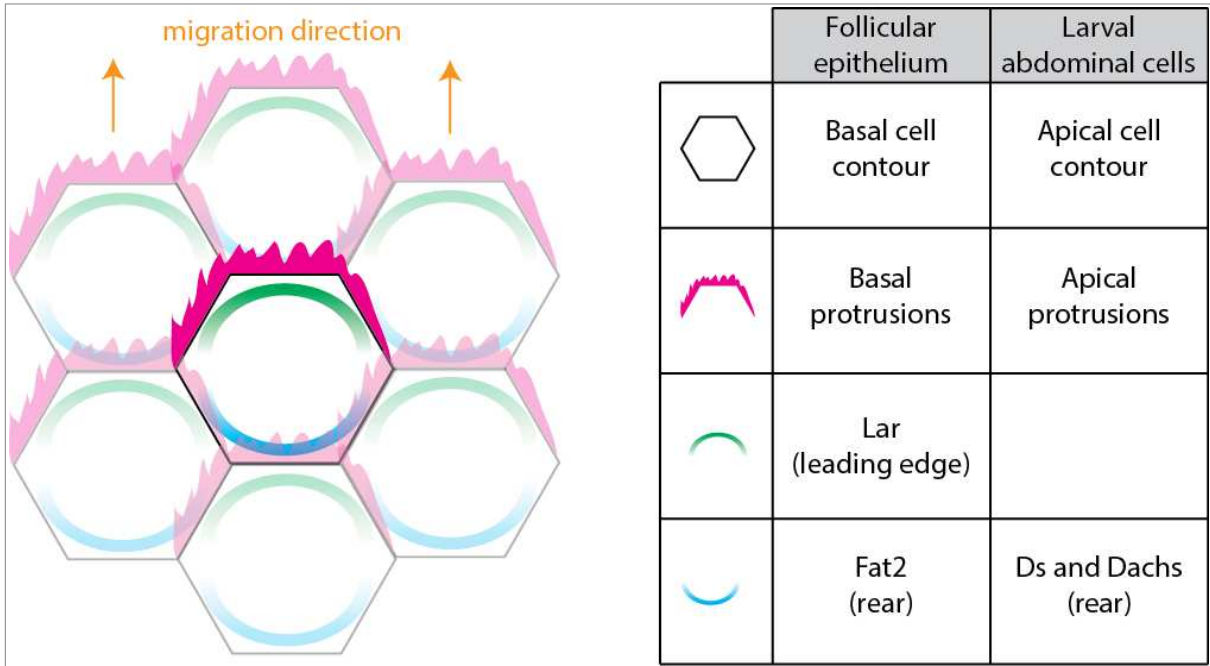


Fig.18: Principle of cell-based crawling. In both *Drosophila* follicular epithelium and larval abdominal cells, all the cells of the migrating cohort emit polarized protrusions and interact with an ECM. As a result, the tissue adopts a tile-like configuration, in which each cell spreads over its front neighbor. Planar polarization pathways provide the directionality of protrusion emission.

In the second part of my thesis, I will show that dorsal thorax cells collectively migrate on the apical ECM using a mechanism based on cell-based emission of polarized protrusions. I will show that core PCP pathway is involved in planar polarization of these apical protrusions, and that the deposition of Dumpy, a ZP protein constituting the apical ECM, is necessary for migration to occur.

C2/ Coupling with neighboring events and morphogenesis

While many active mechanisms can give rise to autonomous deformation of an epithelial domain, epithelial cells, as a result of their mechanical coupling with neighboring epithelial cells or other cell populations, can undergo passive deformations. I will here review cases of passive deformations, by separating cases of tissue surface reduction, tissue surface expansion and stretching, convergent extension and flow.

1) Passive tissue surface reduction

While active contractility is often invoked to account for epithelial surface reduction, a few studies indicate that an epithelial domain can also decrease its surface as a result of interactions with neighboring domains. For example, during *Drosophila* metamorphosis, the larval abdominal cells surface progressively decreases, while histoblast niches expand. Remarkably, larval cell apoptosis preferentially occurs at the contact of the histoblast expanding niches¹³². Additionally, inhibition of histoblast expansion by blocking cell division reduces the rate of apoptosis in the larval cells. It thus appears that histoblast expansion triggers cell death of the neighboring larval cells, leading to the shrinkage of the larval tissue surface. Larval tissue shrinkage is thus partly caused by neighboring tissue expansion. Additionally, an acto-myosin cable is assembled around the larval cells domain during larval tissue surface shrinkage. The increase in circumferential tension associated with this cable could in theory favor larval cell shrinkage. This mechanism has, for example, been proposed to act as a driving force of dorsal closure and amnioserosa tissue shrinkage, providing a ratchet-like mechanism enabling the stabilization of amnioserosa tissue shrinkage⁷³. However, the involvement of this acto-myosin cable in dorsal closure is still debated, as a mutant for *Zasp52*, which does not form an acto-myosin cable, still shows normal dorsal closure dynamics¹⁵⁹.

In the *Drosophila* pupal notum, induction of clonal overgrowth is associated with compression of neighboring cells and an increase in neighboring cell apoptosis probability¹⁶⁰. In this artificial condition, the shrinkage of an epithelial domain (the tissue surrounding the clone) seems to be a consequence of the adjacent overgrowth. Physiological convergent flows of neighboring tissues can also cause tissue contraction, and induce higher apoptosis rate. It is indeed what happens in pupal dorsal thorax, in which convergent flows towards the midline are associated with midline cell crowding and a high rate of delamination. Reduction of the

convergence flows by laser ablation decreased the delamination rate in the midline. These results suggest that midline surface variation depends on the flowing behavior of neighboring regions¹⁶⁰. The mechanisms driving these convergent flows and whether the midline region could have autonomous shrinkage mechanism remains to be explored. Beyond the role of apoptosis in tissue shrinkage, whether tissue cell shape shrinkage and cuboidal-to-columnar transition can be passively caused by active neighboring events remains largely unknown.

In the second part of my thesis, I will study active migration of thorax epithelial cells and show that introduction of a physical obstacle in front of the migrating domain can give rise to tissue compaction. I will also provide evidence that convergent flows towards the midline are dependent on tension of the lateral domains.

2) Passive tissue surface expansion and stretching

While examples of passive tissue surface reduction are relatively rare, many instances of passive epithelial surface expansion (either isotropic expansion or anisotropic stretching) can be found in the literature. I will here review the mechanisms leading to such passive expansions, by (i) presenting the influence of underlying cell populations on the superficial epithelial layer, and by (ii) reviewing the cases of coupling with epithelial active events in the plane of the epithelium.

a) Impact of the underlying layers

First, the deformation of an epithelial layer can be passively caused by active remodeling of the mesenchymal layers that are beneath it. During *Xenopus* epiboly, the deep epidermal layers undergo radial intercalations along the apico-basal axis, leading to a global decrease in the thickness of the mesenchymal tissue and an expansion of its planar surface¹⁶¹ (Figure 20A). This mechanism participates to the isotropic expansion of the superficial layer. Interestingly, mesenchymal radial intercalation has been shown to be caused by short-range chemotaxis as a result of secretion by the superficial layer of the immune-associated complement component C3¹⁶¹. Thus, the superficial epithelial layer sends a signal causing the deep layers to rearrange and to trigger its expansion. Furthermore, the strength of the signal modulates local mesenchymal radial intercalation rate, and hence the amount of expansion of the superficial layer¹⁶¹. This mechanism thus allows converting a pattern of chemoattractant secretion into a pattern of epithelial tissue surface expansion by acting on an underlying cell population.

A similar mechanism of tissue remodeling can be found during zebrafish epiboly¹⁶². In this system, the deep layers undergo similar radial intercalation dynamics. However, even if these radial intercalations should in theory favor both superficial layer expansion and yolk dome formation, they are dispensable for both these events to occur¹⁶². On the contrary, the decrease in surface tension imposed by the superficial layer is a driving force for both deep cell layer radial intercalations and yolk doming (Figure 20C).

We can thus conclude that *Xenopus* and zebrafish epibolies constitute two comparable systems, in which superficial layer spreading is coordinated with deep layer radial dynamics. However, while deep layer dynamics were shown to be an active process and hypothesized to drive superficial layer expansion in *Xenopus*, the study of zebrafish epiboly tends to advocate for an active spreading of the superficial layer, triggering the intercalations in the deep layers. Further work is required to see if these two opposed views can be reconciled. Notably, it would be interesting to study whether C3 chemotaxis is required for radial intercalation in zebrafish.

Finally, another example of underlying constraint can be found during *Drosophila* ovary elongation. In this system, the inner cyst is covered by a superficial epithelial layer. It is hypothesized that the pressure resulting from the growth of the inner cyst could be a major driving force of superficial epithelial layer expansion. Growth pressure of the inner cyst is indeed sufficient to explain superficial epithelia spreading *in silico*¹⁶³. This mechanism can be compared to the swelling of a balloon: when blowing into a balloon, its area extends as a result of the increase of internal pressure.

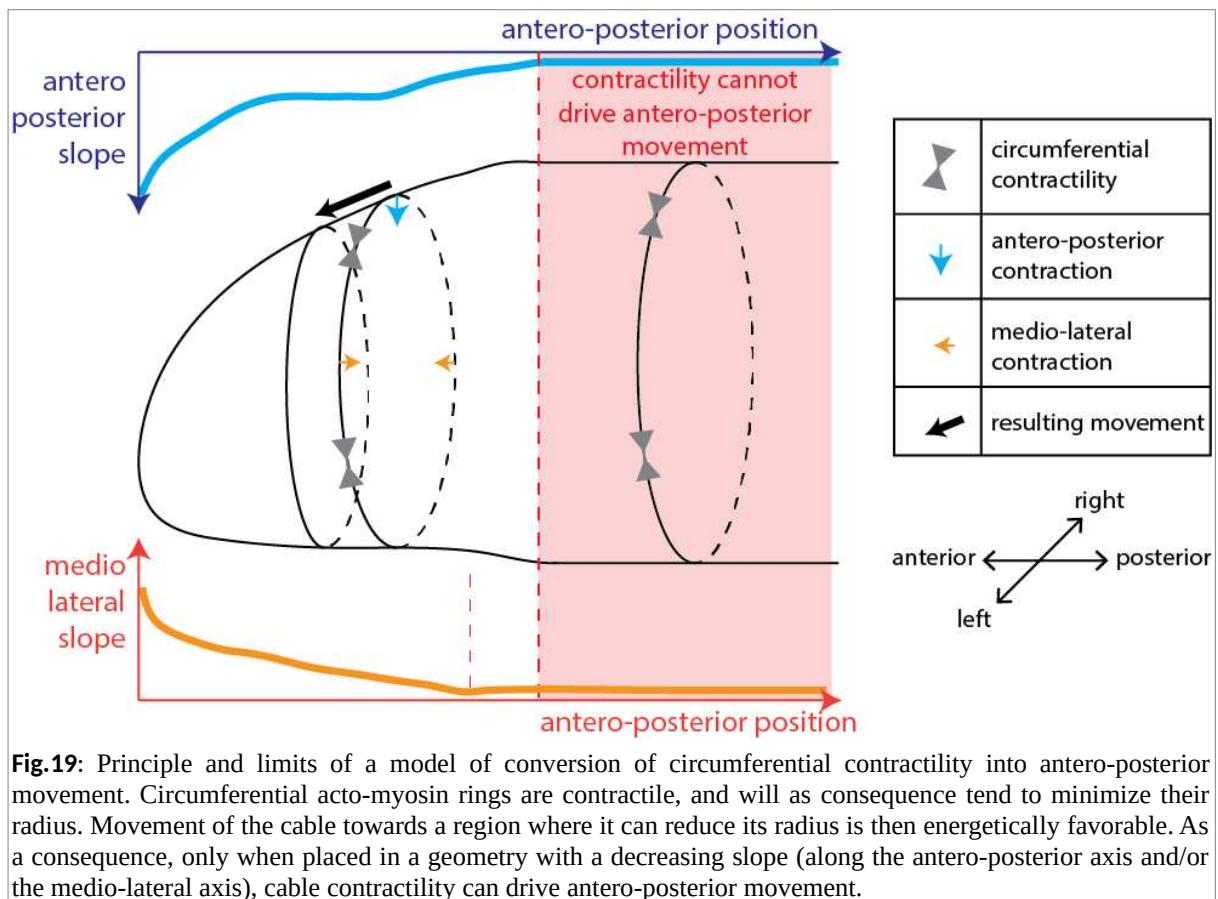
b) Intra-epithelium coupling

While the influence of underlying cell populations on superficial epithelium expansion is still a debated issue, the influence of an epithelial domain on its planar epithelial neighborhood has been shown in many systems. Indeed, epithelial cells are mechanically coupled in the plane of the tissue, as a result of the inter-cellular adhesion network (more details can be found in A/2/ a section). Hence, the active deformation of an epithelial domain can in theory lead to the stretching of the neighboring epithelial domains. I will here review different cases of such intra-epithelium coupling, by separating them based on the type of active mechanism (either (i) the active shrinkage of a tissue domain or (ii) the contraction of a supra-cellular ring) which causes the coupling.

First, the active shrinkage of an epithelial domain has been shown to be able to trigger the stretching of the neighboring epithelial regions. For instance, during *Drosophila* metamorphosis, the constriction of the proximal part of the wing, called the hinge, triggers the stretching of the wing blade⁵⁴ (Figure 20F). This phenomenon is accompanied by the building up of anisotropic tension across the wing blade, driving cell shape changes and cell rearrangements¹⁶⁴. Disconnecting the wing hinge from the wing blade by laser ablation inhibits blade extension and deformation⁵⁴. Interestingly, the distal part of the wing blade is strongly attached to the apical ECM. This anchorage is necessary to prevent wing blade collapse upon hinge contraction¹⁶⁵. Notably, the extracellular protein Dumpy is necessary for this anchorage. Thus, a combination of coupling with a proximal contraction and distal anchoring to the matrix underlies wing blade stretching. Other examples of stretching as a result of a coupling with a neighboring epithelial surface shrinkage can be found during *Drosophila* dorsal closure (Figure 20G). In this system, the epithelium surrounding the amnioserosa stretches and finally fuses, in synchronization with amnioserosa shrinkage and elimination. As amnioserosa shrinkage is an active process, it is likely actively participating to neighboring tissue spreading¹⁶⁶. Similarly, we can envision that larval abdominal cells shrinkage and elimination during *Drosophila* metamorphosis could provide a driving force for histoblast niche expansion⁸⁹ (Figure 20G).

Second, the presence of a contractile supra-cellular acto-myosin ring at the edge of an epithelial domain can as well lead to its isotropic spreading or anisotropic stretching. A first example can be found during wound healing in *Drosophila* pupal epidermis (Figure 20D). After wounding, a supra-cellular cable assembles around the wound. The circumferential tension of this acto-myosin cable, combined with the force provided by tissue fusion at the edge of the wound, is thought to actively participate to wound closure in a purse-string mechanism⁶⁸. Interestingly, neighboring tissue flow is thought to be at least partially driven by the active contraction of the acto-myosin cable⁶⁸. A similar association between neighboring tissue spreading and acto-myosin cable purse-string mechanism can be found during *Drosophila* dorsal closure⁷³ (more details about dorsal closure can be found in C2/1 section). Thus, the circumferential tension of an acto-myosin ring present within the plane of the epithelium can lead to neighboring tissue stretching. What is more, similar acto-myosin rings can also surround tubular or spheroid organs or organisms, and lead to the spreading of epithelial tissue over a curved surface. An example of such a scenario can be found during head involution of *Drosophila* embryo¹¹⁸ (Figure 20E). Head involution is associated with prominent epithelial stretching and flows. Remarkably, many circumferential acto-myosin

cables can be found across the spreading tissue, surrounding the tubular shape of the embryo. A mechanism based on conversion of circumferential contraction of these rings into radial pulling (due to the curvature of the embryo) efficiently models the spreading associated with head involution¹¹⁸ (Figure 19). A comparable example of an edge acto-myosin ring driving neighboring tissue stretching can be found during zebrafish epiboly (Figure 20B). In this context, the enveloping cell layer shows a prominent spreading, which is associated with the presence of a contractile band of acto-myosin in the yolk bordering the enveloping cell layer¹⁶⁷. However, unlike the case of *Drosophila* head involution, a mechanism based on conversion of circumferential contraction of this ring into radial pulling (due to the curvature of the embryo) does not fit with the fact that flattened embryos still show ring translocation. An alternative mechanism account for zebrafish epiboly. The constant radial acto-myosin flows across the ring can transmit a radial contraction force that efficiently account for ring advancement¹⁶⁷. Thus, flowing pulling forces of the yolk acto-myosin ring actively participate in enveloping cell layer spreading.



In the second part of my thesis, I will show that posterior thorax tissue passively flows and stretches as a result of a pulling force exerted by the active migration of the anterior thorax.

3) Passive convergent extension

We have seen that active events can promote stretching of an epithelium domain in a preferential direction, without triggering a prominent contraction in the perpendicular direction (note that during *Drosophila* head involution the prominent antero-posterior stretching is to some extent accompanied by circumferential contraction). Active events can yet also drive both anisotropic stretching and contraction along the perpendicular direction, hence triggering convergent extension. As for tissue stretching, convergent extension can be driven by edge effects. For instance, sea urchin archenteron undergoes a convergent extension which is dependent on the migratory behavior of the secondary mesenchyme cells present at its tip¹⁶⁸ (Figure 20I). A model of passive rearrangement in response to the traction forces imposed by the active migration of secondary mesenchyme cells efficiently mimics archenteron convergent extension¹⁶⁹. This model could also apply to vessel elongation in mouse⁹¹ (Figure 20I), or trachea extension in *Drosophila*¹⁷⁰. In these systems, tip cells have been shown to actively migrate and are hypothesized to provide traction forces that could favor cell intercalation driving tubular convergent extension. Active invagination can also provide active forces favoring convergent extension. This phenomenon has been well described during *Drosophila* germband extension. The front edge of the germband is bordered by the endoderm, which undergoes an active invagination in synchronization with germband extension. Interestingly, the front edge of the germband displays a gradient in cell shape elongation indicating it could be stretched by the invaginating region¹⁷¹ (Figure 20J). Inhibiting endoderm invagination not only prevents cell stretching¹⁷¹, but also leads to less polarized junction growth after apical rosette formation¹⁷². Thus, endoderm invagination provides a long-range mechanical effect that not only stretches the germband, but also favors its shrinkage along the perpendicular direction. It should be noted that even in the absence of invagination, rearrangements still occur in germband, leading to a lesser extent to its convergent extension. In this context, tissue compression can be observed at the edge of the germband, indicating that intrinsic processes leading to germband convergent extension still occur without endoderm invagination, even at the expense on local cell compaction. As a result, we can conclude that germband extension and endoderm invagination are synchronized and mechanically coupled events, but that convergent extension only partly depends on endoderm invagination¹⁷².

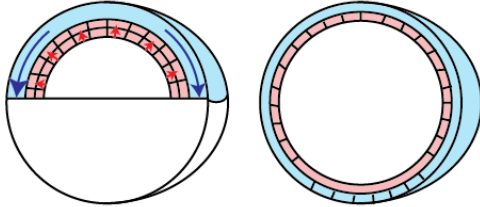
Finally, a surface constraint applied by a non-epithelial population can also lead to convergent extension. During *C.elegans* embryogenesis, the embryo undergoes a final stage of axis elongation. Interestingly, muscle contraction has been shown to be necessary for this elongation to occur¹³⁶. First, muscle activity promotes the formation of hemi-desmosomes in the epidermis, which are necessary for correct elongation¹⁷³. Moreover, the formation of a circumferential array of actin fibers in the extending epidermal cells is also dependent on muscle activity¹⁷⁴. The formation of this actin supra-cellular corset is associated with a polarization of tissue stiffness, which is higher circumferentially than radially. This anisotropy of stiffness is thought to be crucial for *C.elegans* convergent extension, by providing a polarized resistance to deformation¹⁷⁴ (Figure 20H). Additionally, muscle activity also triggers the formation of a similar microtubule corset¹⁷⁵. This microtubule network is mainly involved in tissue convergent extension by enabling the transport of adherens junction components towards the apical domain¹⁷⁵.

4) Graphical summary of part C2/: Typology of tissue surface changes as a result of coupling with adjacent tissues (Figure 20)

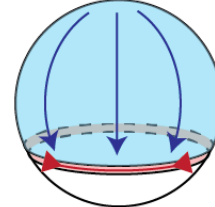
Fig.20: Typology of tissue surface changes as a result of coupling with adjacent tissues. Driving forces are indicated in red, and the effects they have on epithelial tissues are represented in blue. Forces constraining shape changes are indicated in green.

Active radial intercalation of deep mesenchymal layers participates to the spreading of the superficial epithelial layer in *Xenopus* gastrula (A). A contractile acto-myosin ring present in the yolk participates to the enveloping cell layer expansion in zebrafish gastrula (B). The decrease of surface tension and the active spreading of the enveloping cell layer drives deep layer radial intercalation and yolk doming in zebrafish gastrula (C). The purse-string contraction of an acto-myosin cable surrounding a wound drives neighboring tissue expansion during wound healing in *Drosophila* pupal epidermis (D). Contractile acto-myosin cables sliding over a curved surface triggers the displacement and the stretching of neighboring epithelium in *Drosophila* embryo (E). The active constriction of wing hinge, coupled with a distal attachment of the wing blade to the rigid apical ECM, allows the stretching of wing blade in *Drosophila* pupa (F). Contraction and cell death in the amnioserosa (or in larval abdominal cells) participate to neighboring epithelium stretching during *Drosophila* dorsal closure (G). Muscle activity drives the assembly of a polarized actin molecular corset in *C.elegans* epidermis, leading to its convergent extension and axis extension of the animal (H). Actively migrating tip cells provide traction forces leading to sea urchin archenteron and mouse sprouting vessel convergent extension (I). Active invagination of the endoderm participates to germband convergent extension in *Drosophila* (J).

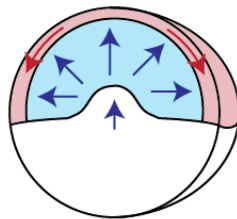
Isotropic expansion
A Surface coupling

 Epiboly
(*Xenopus* gastrula)

B Edge coupling

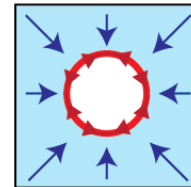
 Epiboly
(zebrafish gastrula)

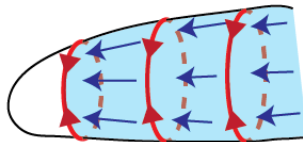
 Contraction of an
acto-myosin ring

C Underlying mesenchyme radial intercalation

 Doming and deep layers intercalation
(zebrafish gastrula)

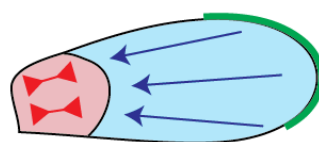
 Enveloping cell layer
decrease of surface
tension and active
spreading

D

 Wound closure
(*Drosophila* pupa)

 Contraction of an
acto-myosin ring

Anisotropic stretching
E

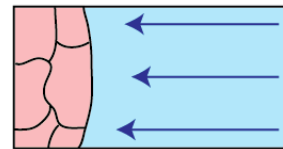
 Head involution
(*Drosophila* embryo)

 Acto-myosin
contraction

F
Edge coupling

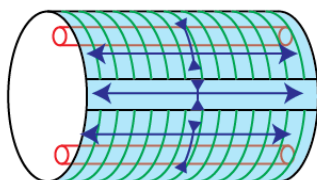
 Wing blade stretching
(*Drosophila* pupa)

 Contraction
of the hinge

 Distal attachment
to the matrix

G

 Dorsal closure / abdomen spreading
(*Drosophila* embryo & pupa)

 Contraction and death of the
amnioserosa (or of the larval
abdominal tissue)

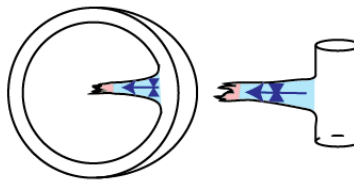
Convergent extension
H
Surface coupling

 Axis extension
(*C.elegans* embryo)


Muscle activity

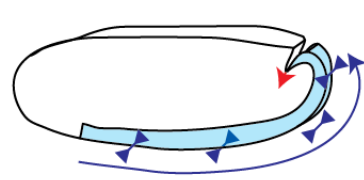
 Actin molecular
corset

I
Edge coupling

 Sea urchin archenteron /
mouse vessel sprouting


Migratory force of the tip cells

J

 Germband extension
(*Drosophila* gastrula)


Active invagination of the endodermis

	Active region		Active flow, radial intercalation or invagination		Resulting flow		Resistive structure (extracellular matrix or actin corset)
	Region undergoing coupling effects		Active contraction		Resulting extension		
					Resulting compression		

5) Passive translocation and swirling

While active mechanisms are required for single-cells to translocate, not every cell necessarily actively participates to migration within a migrating epithelium. Remarkably, many models of collective migration are based on a division of labor within the migrating population, with active behaviors restricted to the edge of the population. As result, “followers” cells translocate as result of coupling with “leader” cells. When coupled with rear retraction, leader cell migration can lead to the translation of a follower cohort, like during *Drosophila* polar cell migration or during *Xenopus* cranial neural crest migration (more details can be found in C1/4/a section). Interestingly, when coupled with rear inertia, leader cells migration can give rise to convergent extension (see C2/3 section) or linear stretching like for example during lateral line migration in zebrafish¹⁴⁷.

In addition to simple linear translations, localized active processes can give rise to complex swirling flows of the neighboring epithelium (Figure 21). These swirling behaviors are highly reminiscent of hydrodynamic flows. Such a behavior is particularly well described during *Drosophila* gastrulation¹⁰⁸. In this context, the presumptive mesoderm organizes as an anisotropic domain with a long axis (x) and a short axis (y), and anisotropically constricts along its short axis (y), to give rise to the formation of a groove, which is oriented along the (x) axis. Interestingly, the active mesoderm anisotropic shrinkage gives rise to surrounding tissue swirling, in a plane defined by the axis which is perpendicular to the groove (y) and the apico-basal axis (z). The swirling of the cytoplasm propagate from one cell to another without being attenuated by plasma membranes¹⁰⁸. This swirling participates to tissue folding by triggering an apical flow towards the site of invagination (see B/2/b section). Note the polarity of this swirling event (Figure 21A): apical mesoderm contraction occurs preferentially along the axis perpendicular to the groove (y), thus, this contraction along a preferential axis (y) can give rise to cytoplasmic swirling flows along the plane (x,z), leading to a linear translation along (y).

Interestingly, swirling patterns within the plane of the tissue (x,y) have been very recently associated with a localized tissue contraction during chicken gastrulation¹⁷⁶ (Figure 21B). Like in *Drosophila*, the contracting region is anisotropic and forms an arc with a long axis (x) and the associated perpendicular axis (y). But contrary to *Drosophila* gastrulation, the contraction is occurring along the long axis (x). This contraction thus gives rise to swirling patterns that are located in the plane of the tissue (x,y), and leads to a stereotypical flowing and deformation pattern. This configuration directly echoes the recent discovery of swirling

patterns in *Xenopus* and chicken neural crest¹⁴⁸. Indeed, the active anisotropic contraction of the rear of neural crest population has been linked with swirling patterns (Figure 21C).

Local contraction is not the only process that can give rise to neighboring tissue swirling. Surface coupling with an underlying migrating population can also give rise to in-plane swirling patterns (Figure 21D). Indeed, during zebrafish gastrulation, a stripe of prechordal plate cells migrate beneath the spreading ectoderm. The direction of ectoderm and prechordal plate cell spreading are opposed. The migrating prechordal plate cells exert friction forces on the ectoderm they migrate on, leading to a localized pulling force, which is the center of emerging swirling within the plane of the ectoderm (x,y) ¹⁷⁷.

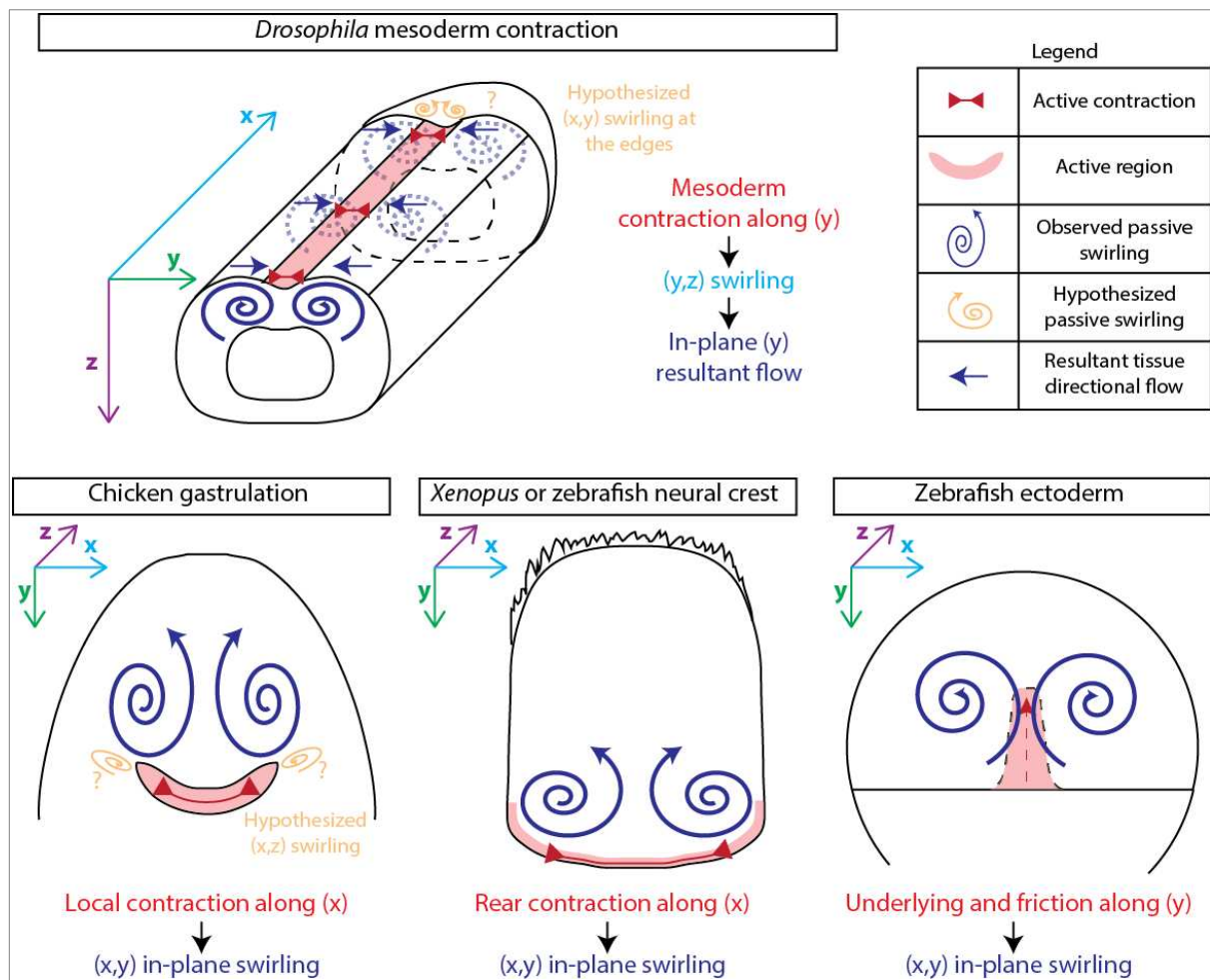


Fig.21: From local and anisotropic forces to global hydrodynamic swirling.

Note that by comparing *Drosophila* and chicken gastrulations, we propose that additional swirling movements might be observable (represented in orange): In-plane swirling at the edge of the constricting mesoderm in *Drosophila*, and (x,z) swirling at the edge of the constricting domain (this latter swirling movement might even participate to local invagination, as hypothesized in *Drosophila*).

The shape and the possibility of the tissue hydrodynamic behaviors described above depend on the fluidity of the epithelial tissue. In a similar way to inert materials, a propensity to behave more as a fluid or as a solid at mesoscopic scales can be defined for an epithelium. Interestingly, the fluidity of the tissue displaying swirling patterns in chicken gastrula has been shown to be enhanced by cell division¹⁷⁸. In this tissue indeed, divisions lead to an intercalation of the neighbors during cytokinesis, and thus to a cell rearrangement. This so-called cell division mediated rearrangements increase tissue fluidity, hence favoring the emergence of swirling behaviors¹⁷⁸. Interestingly, cell division also appear to regulate mesenchymal fluidity during zebrafish epiboly, thus favoring epithelial spreading¹⁷⁹. Thus, tissues can regulate their intrinsic rheological properties, to allow or restrict hydrodynamic behaviors.

While intrinsic factors can modulate tissue rheology, the interaction with the ECM can be key to locally reduce tissue fluidity and restrict the coupling with neighboring events. During gastrulation of *Tribolium* and *Drosophila*, it has indeed been shown that a ventral attachment to the vitelline membrane is required to prevent ectopic flows caused by adjacent contractile events⁷. This attachment to the ECM was shown to involve integrin. Thus, local ECM attachment can provide anchoring points that restrict coupling with active neighboring morphogenetic events.

C3/ Graphical summary of part C/: Typology of the mechanisms leading to in-plane epithelial morphogenesis (Figure 22)

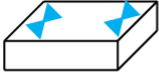
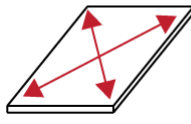


	Active mechanism	Passive mechanism
Surface reduction 	<p>Lateral tension decrease Cuboidal-to-columnar transition of <i>Drosophila</i> wing disc and mouse neural plate</p> <p>Apical constriction Cuboidal-to-columnar transition of ascidian endoderm and mouse neural plate, <i>Drosophila</i> amnioserosa shrinkage</p> <p>Cell delamination <i>Drosophila</i> amnioserosa and abdominal larval tissue</p> <p>Cell volume decrease <i>Drosophila</i> amnioserosa</p>	<p>External pushing force In <i>Drosophila</i>, cable contraction around amnioserosa, pushing of the expanding niche on larval abdominal cells</p> <p>Apoptosis induction <i>Drosophila</i> abdomen, and thoracic midline</p>
Surface expansion and stretching 	<p>Lateral tension increase Columnar-to-cuboidal transitions of <i>Drosophila</i> follicular epithelium and wing/leg prepupal discs</p> <p>Cell division/integration Expansion of mouse blood vessel, <i>Drosophila</i> histoblast niches and <i>Xenopus</i> mucociliary epithelium</p>	<p>Influence of underlying tissues <i>Xenopus</i> epiboly and radial intercalation, and zebrafish epiboly and softening of underlying mesenchyme, growth pressure of the inner cyst in <i>Drosophila</i> ovary</p> <p>Coupling with an active edge Contractile rings during <i>Drosophila</i> wound closure and head involution, and during zebrafish epiboly</p> <p>Coupling with a contracting region <i>Drosophila</i> wing blade extension and hinge constriction, dorsal closure and expansion of neighboring tissue, histoblast niches expansion and larval cells contraction</p>
Convergent extension 	<p>Rearrangement by junctional shrinkage <i>Drosophila</i> germband extension</p> <p>Rearrangement by basolateral motility <i>Drosophila</i> germband extension, <i>C.elegans</i> dorsal intercalation, mesenchymal intercalation in <i>Xenopus</i></p> <p>Cell shape changes <i>Drosophila</i> abdomen</p>	<p>Coupling with an active edge <i>Drosophila</i> germband extension and endodermis invagination, tip cells migration and elongation of mouse vessel, <i>Drosophila</i> trachea and sea urchin archenteron</p> <p>Inter-tissue stress Muscle contractility and <i>C.elegans</i> axis extension</p>
Flowing 	<p>Active edges migration Wound closure in <i>Drosophila</i> pupa, border cell migration in <i>Drosophila</i> ovary, <i>Xenopus</i> neural crest migration, zebrafish lateral line migration, <i>in vitro</i> epithelial migration, tip cells migration in mouse blood vessels and <i>Drosophila</i> trachea, migration of the leading edge of the spreading ectoderm in chicken gastrula</p> <p>Cell-based crawling <i>Drosophila</i> follicular epithelium and abdominal larval cells migration</p>	<p>Traction by leading edge cells Wound closure in <i>Drosophila</i> pupa, border cell migration in <i>Drosophila</i> ovary, <i>Xenopus</i> neural crest migration, zebrafish lateral line migration, <i>in vitro</i> epithelial migration, tip cells migration in mouse blood vessels and <i>Drosophila</i> trachea, migration of the leading edge of the spreading ectoderm in chicken gastrula</p> <p>Hydrodynamic response to neighboring active contraction Swirling behaviors in <i>Drosophila</i> mesoderm invagination, chicken gastrulation and <i>Xenopus</i> and zebrafish neural crest rear contraction</p> <p>Hydrodynamic response to friction from an underlying migrating population Swirling of zebrafish ectoderm resulting from the migration of the underlying prechordal cells</p>

Fig 22: Typology of mechanisms leading to in-plane epithelial morphogenesis. All the examples presented in section C (C1/ and C2/) are summarized depending on the type of morphological changes they illustrate, and on the mechanisms underlying deformation (either active or passive, indicated in grey).

Part1: Analysis of neck invagination dynamics

Contraction of a curved acto-myosin cable and a supra-cellular basal acto-myosin network is associated with epithelial folding

Part1: Analysis of neck invagination dynamics

Contraction of a curved acto-myosin cable and a supra-cellular basal acto-myosin network is associated with epithelial folding

Context

During development, epithelial sheet folding allows the emergence of complex organisms and organs 3D shapes. Many mechanisms accounting for epithelial fold formation have already been discovered. One of the most commonplace mechanisms of fold formation is based on cell apical constriction^{101,94,95,96,97}. Indeed, the shrinkage of cell apical area perpendicularly to the fold axis can promote tissue bending. Alternative mechanisms of tissue bending also exist. They are based on basal cell surface expansion⁷⁵, cell apoptosis⁷⁶, epithelial-to-mesenchymal transition⁷⁷, apico-basal active shrinkage^{75,25} or adherens junction repositioning⁷⁸. Supra-cellular acto-myosin cables can also play a role in epithelial folding. First, the presence of circular acto-myosin cable within the plane of the tissue has been linked with pit formation^{76,116,117}. In these contexts, the circumferential tension of an acto-myosin cable is thought to provide pushing forces triggering the invagination of the tissue it surrounds. Linear acto-myosin cables are also associated with epithelial folding in *Drosophila* gastrula, leading to the formation of shallow and transient grooves at the interface between parasegments¹²⁰. In this context, MyosinII contractility has been identified as necessary for folding, and genetic regulators of parasegment grooves depth have been identified¹²⁰. However, the mechanism linking inter-parasegment interface contractility and folding remains obscure, and is hypothesized to mainly rely on lateral tension increase¹²⁰.

Summary

Drosophila adults show a prominent fold separating the head from the thorax, forming the neck of the animal. Interestingly, this invagination is absent at the beginning of metamorphosis. Using confocal timelapse imaging, we here describe for the first time the epithelial folding of dorsal epidermis leading to *Drosophila* neck formation during

metamorphosis. We show that a linear supra-cellular acto-myosin cable is present at the leading edge of invagination. Using laser ablation, we show that this cable displays high contractility specifically during folding. We moreover highlight the fact that this cable gets more and more curved in the direction parallel to the fold axis during neck tissue bending phase. Additionally, we describe the assembly of a contractile network of actin bundles at the basal surface of the bending region. By inducing local disruption of MyosinII contractility in the neck region, we manage to modulate neck invagination speed. Interestingly, during invagination, the tissue neighboring the acto-myosin cable does not constrict perpendicularly to the fold axis, but constricts along the direction parallel to the fold axis. Taken together, our data suggests that circumferential tension of a curved acto-myosin cable and a supra-cellular acto-myosin basal network may actively participate to neck folding.

Results

Presumptive neck region gradually bends during metamorphosis

At the beginning of pupal development, the head-to-thorax boundary of *Drosophila* is globally flat, whereas the adult shows a deep fold between head and thorax compartments, forming the neck of the animal (Figure 1A). The dynamics and mechanisms leading to the formation of this prominent invagination were unexplored. By performing time-lapse confocal imaging of pupae expressing Ecad::3XGFP as a marker of cell outlines, we have described at the tissue-scale and with a sub-micrometric resolution the dynamics of neck bending during metamorphosis (Figure 1B). We have followed the invaginating tissue up to 50µm below the initial tissue plane. This high depth coverage allowed us to follow the progressive indentation of the tissue and the fold deepening from 18hAPF (hours after puparium formation) to 23.5hAPF. Based on the detection of apical plane in our movies (see C/3 and C/7 sections in Material & Methods), we could quantitatively describe the fact that the presumptive neck tissue remains in the same plane at the beginning of metamorphosis and starts to gradually bend around 20hAPF (Figures 1C-F). Notably, the deepening of the leading edge of invagination and the indentation of the neck gradually and persistently increase with time (Figures 1C-E). We also found that neck indentation and leading edge deepening speeds are highly correlated in time (Figure 1F).

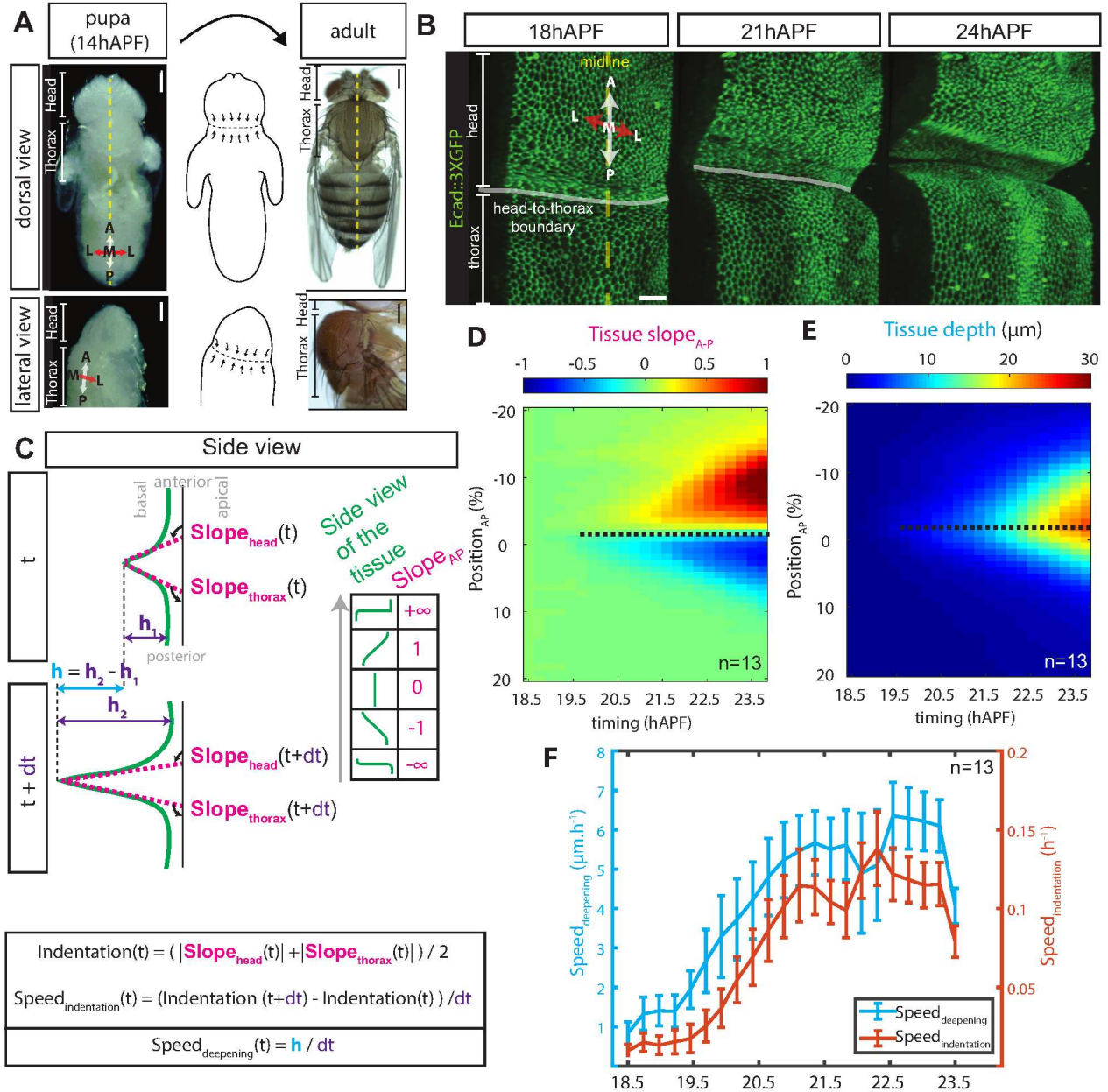


Fig.1. Presumptive neck region gradually bends during metamorphosis. Head and thorax epidermis is almost flat at the beginning of metamorphosis (14hAPF), while it is highly invaginated in the adult, scale bars: 150μm (**A**). Time-lapse imaging using Ecad::3XGFP as a marker reveals that neck invagination progressively bends from 20hAPF. Yellow dashed line highlights the position of the midline, white lines highlight the position of the head-to-thorax boundary, scale bar: 30μm (**B**). Extraction of the slope along the antero-posterior (A-P) axis of the apical plane of the tissue ($Slope_{AP}$). Extraction of the depth of the leading edge of invagination (h_1 and h_2). Calculation of neck indentation (Indentation) based on maximal slopes on the head and the thorax sides ($Slope_{head}$ and $Slope_{thorax}$). Calculation of speeds of neck indentation and of leading edge deepening (Speed_{indentation} and Speed_{deepening}, **C**). Average kymograph of A-P slopes of the tissue reveals neck indentation dynamics (**D**). Average kymograph of depth of the tissue reveals neck fold progressive deepening (**E**). Average curves of neck indentation speed and leading edge deepening speed. Note the high correlation between the two speeds (Pearson correlation of the mean values = 0.95, **F**).

[(D) and (E)] Black dashed lines highlight invagination leading edge location, calculated based on the average kymograph of depth (E). [(D), (E) and (F)] n: number of analyzed animals.

A : Anterior, P : Posterior, M : Medial, L : Lateral.

Bending region constricts along the direction parallel to the fold axis

The most classical model for epithelial fold formation is based on apical constriction of a subset of cells perpendicularly to the fold axis, that triggers bending of the tissue in the middle of the constricting region^{101,94,95,96,97}. The consequence of a bending mechanism based on apical constriction is that tissue maximal bending should be found in a region showing apical constriction in the direction perpendicular to the fold axis^{180,181} (Figure 2A). Moreover, flows directed perpendicularly to the fold axis and directed towards the fold should occur^{180,181,108} (Figure 2A). We thus reasoned that if neck invagination was simply due to apical constriction, we should find that neck leading edge should be located in the middle of a region showing antero-posterior (A-P) constriction, and that A-P flows towards the invagination leading edge should be observed. We have thus used Ecad::3XGFP cell contours labelling to track tissue displacements and infer tissue deformations in the neck region. Surprisingly, we found that bending leading edge does not coincide with a region showing A-P constriction. It rather corresponds to a boundary between an anterior region that constricts along the A-P axis and a posterior region that mildly elongates along the A-P axis (Figure 2B). The region of A-P constriction in the head side does not spatially correspond to the furrowing region, but rather corresponds to one side of the folding region and its surrounding (compare Figures 2B with Figures 1D-E). Additionally, the whole invaginating region coherently moves towards the anterior, without showing convergent A-P flows towards the invagination leading edge (Figure 2C). Taken together, this data suggests that a model simply based on apical constriction is unlikely to account for neck invagination.

On the other hand, bending region is associated with medio-lateral (M-L) compression and flows towards the midline (Figure 2D-F). Both M-L flows and M-L compression are maximal directly next to the invagination leading edge and they also temporally correlate with neck invagination onset (compare Figures 2E-F with Figures 1D-E). These observations suggest that leading edge M-L contraction might actively contribute to neck folding. These considerations prompted us to investigate more in depth the structure of neck invagination leading edge.

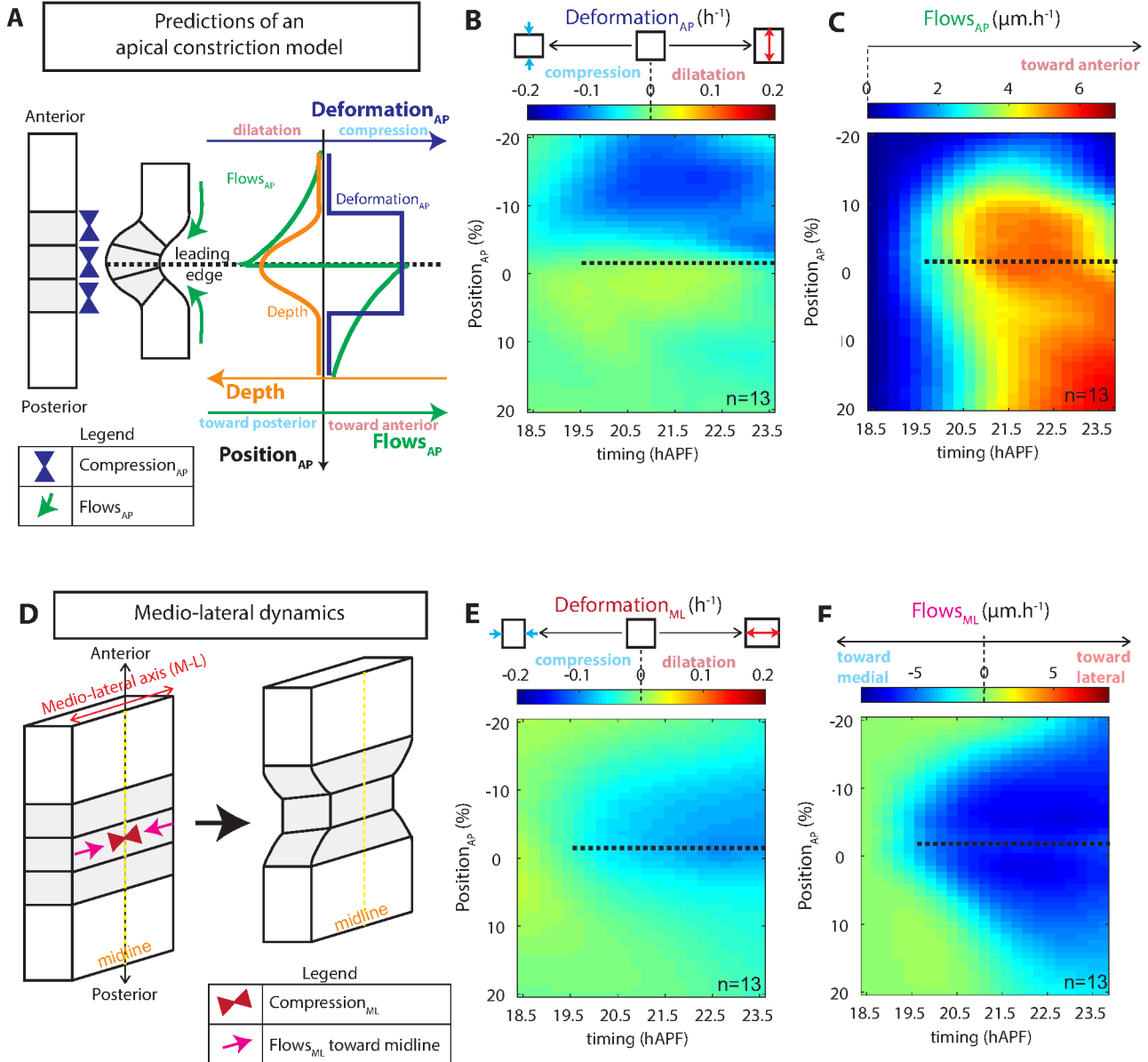


Fig.2. Bending region constricts along the direction parallel to the fold axis. If apical constriction was the main driving force of neck folding, neck invagination leading edge should be at the center of a region undergoing apical antero-posterior (A-P) constriction, and A-P flows toward the site of invagination should occur (**A**). The average kymograph of A-P deformations reveals that the leading edge of invagination is on the contrary associated with local A-P stretching (**B**). The average kymograph of displacements along the A-P axis reveals that the region neighboring the leading edge is globally moving toward the anterior (**C**). Tissue deformation and displacement also occur along the medio-lateral (M-L) axis (**D**). The average kymograph of M-L deformations reveals that the leading edge is the center of M-L tissue compression, note the similarity of patterns with Figures 1D-E (**E**). The average kymograph of displacements along the M-L axis reveals that the leading edge is the center of flows directed toward the midline, note the similarity of patterns with Figures 1D-E (**F**).

[(**A**), (**B**), (**C**), (**E**) and (**F**)] black dashed lines highlight invagination leading edge location, calculated based on the average kymograph of depth (Figure 1E).

n: number of analyzed animals.

Neck invagination is associated with a contractile acto-myosin cable

Sagittal views of neck invaginating region along the A-P axis revealed a pointed apical leading edge of invagination (see Reslices in Figure 3A). At the scale of the tissue, this edge corresponds to a very localized linear apical leading edge, composed of aligned cell-to-cell junctions (white lines in Figure 1A). By imaging live reporters of MyosinII (squash::GFP, Figure 3A), of F-actin (utrophin::GFP, Figure 3C) and by performing immunostaining against phospho-MyosinII (Figure 3B-B'), we could show that a supra-cellular acto-myosin cable is present at the apical leading edge of neck invagination.

Such long and rectilinear supra-cellular acto-myosin cables are known to be present at boundaries between territories of different genetic identities at the level of the adherens junctions network^{182,69}. Using immunostaining for segment identity Hox genes (*Antennapedia* and *Deformed*¹⁸³), we found that the neck acto-myosin cable is present at the boundary between head and thorax homeotic domains (Figure 3E). Boundary acto-myosin cables can be composed of enrichment of MyosinII of only one of the two developmental compartments they delimit, like in *Drosophila* salivary glands¹¹⁶. On the contrary, as revealed by a mosaic expression of MyosinII reporters, neck cable is composed of apical MyosinII cortical enrichment from both head and thorax cells (Figure 3D), with comparable enrichments on the head and on the thorax sides (Figure 3D'). One function associated with boundary acto-myosin cables is to prevent cell mixing between the two facing territories. Linear tension along boundary cables is pivotal to fulfil this function^{182,69}. By using laser ablation to estimate tension/friction ratio, we were able to show that junctions belonging to the cable display higher tension/friction ratios than neighboring junctions prior to invagination. Interestingly, tension/friction ratio at the cable increases during the phase of invagination (Figure 3F). Increase in tension/friction ratio along the cable thus coincides with neck bending onset.

Taken together, this data shows that an apical boundary acto-myosin cable is present at the leading edge of neck invagination, and displays a higher tension/friction ratio during bending phase. Comparable acto-myosin cables are associated with folding of the inter-parasegment boundaries of *Drosophila* embryo¹²⁰. However, the mechanism linking interface tension and folding in this context remains unclear. By which mechanism and to what extent could the contractility of a boundary cable lead to interface folding in the context of neck invagination?

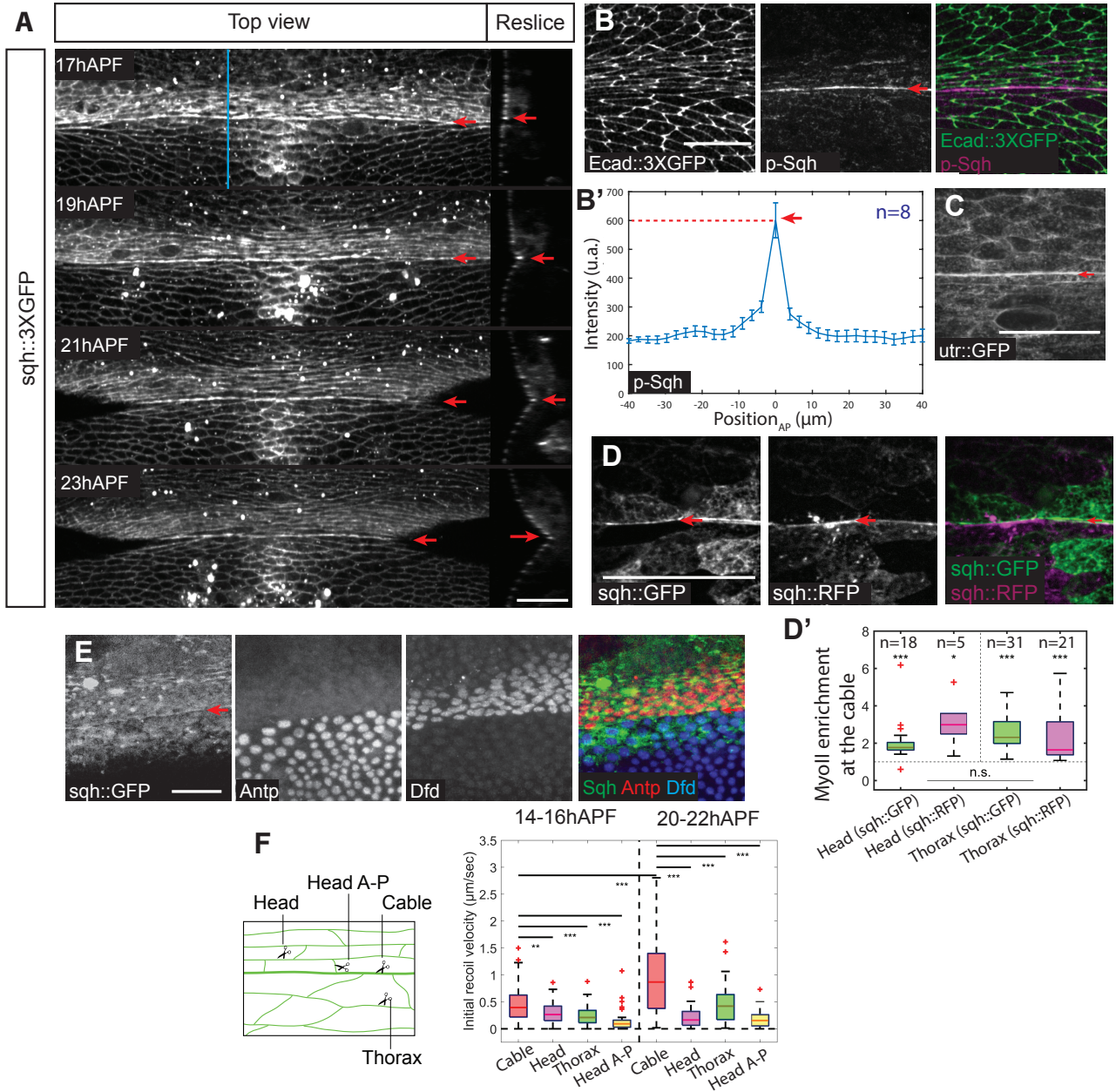


Fig.3. Neck invagination is associated with a contractile acto-myosin cable. Neck invagination leading edge is marked by a linear enrichment in MyosinII, labelled by *sqh::3XGFP*, blue line represents the region used for reslicing (**A**). Neck MyosinII cable is marked by an enrichment in activated MyosinII, labelled by anti-phospho-Squash (p-Sqh) immunostaining (**B**). This enrichment corresponds to a 2 to 3-fold increase in cortical p-Sqh levels, error bars represent standard error to the mean, n: number of analyzed stainings (**B'**). F-actin, labelled with utrophin::GFP, is also enriched in the MyosinII cable (**C**). Mosaic expression of *sqh::GFP* and *sqh::RFP* reveals that the cable is composed of MyosinII cortical enrichment of both head and thorax cells (**D**). Quantification of MyosinII enrichment at the cable, on the head and thorax sides, n: number of analyzed junctions. T-tests have been performed to assess whether mean of each distribution is different from 1 (**p-value<0.001, *p-value<0.05), and a Welch test has been performed to compare pooled head with pooled thorax enrichments measurements (n.s. p-value<0.05 (p-value=0.77), **D'**). The acto-myosin cable is located at the precise boundary between *Antennapedia* and *Deformed* homeotic expression domains (**E**). Recoil velocities after ablation are higher in the cable than in neighbouring junctions (either in junctions in the head or in the thorax which are parallel to the cable, or in junctions in the head that are perpendicular to the cable), and recoil velocities after ablation in the cable are higher during invagination (20-22hAPF) than prior to invagination (14-16hAPF). Welch tests have been performed to compare distribution means (**p-value<0.001, *p-value<0.1, **F**).

[(A), (B), (B'), (C), (D) and (E)] red arrows indicate head-to-thorax boundary acto-myosin cable location. Scale bars : 25μm.

Neck acto-myosin cable is curved and could act as a “tissue-scale cytokinetic ring”

Due to the global morphology of the pupa, the boundary between head and thorax domains is medio-laterally curved, at least on its lateral tips (Figure 4A). Mounting procedure for dorsal epidermis imaging includes a step in which a coverslip is placed on the dorsal region of the pupa, locally flattening the tissue (Figure 4A, pink region). As a consequence, tissue M-L curvature is expected to be artificially reduced in the timelapse movies we have acquired. Nevertheless, we were able to detect a small M-L bending on the lateral edges of the imaged field prior to invagination (Figure 4B-C). Interestingly, the leading edge of invagination gets more and more curved along the M-L axis while invagination proceeds (Figure 4C). Thus, the contractile acto-myosin cable present at the leading edge of invagination, which is initially only medio-laterally curved on its lateral tips, gets more and more circular while neck bending proceeds.

We propose that due to its curved geometry, the contraction of neck cable could participate in neck bending. A comparable bending mechanism is well described at a very different scale, during cell cytokinesis: as a result of its circular geometry, the circumferential tension of the cytokinetic ring conveys an inward resultant force that leads to cell membrane bending, and eventually to the separation of the cytoplasms of the two daughter cells¹¹⁹ (Figure 4D). We thus propose that neck cable could function as a “tissue-scale cytokinetic ring”. Contraction of the curved neck cable might convey an inward resultant force, leading to neck tissue bending and eventually separating head and thorax tissues (Figure 4D).

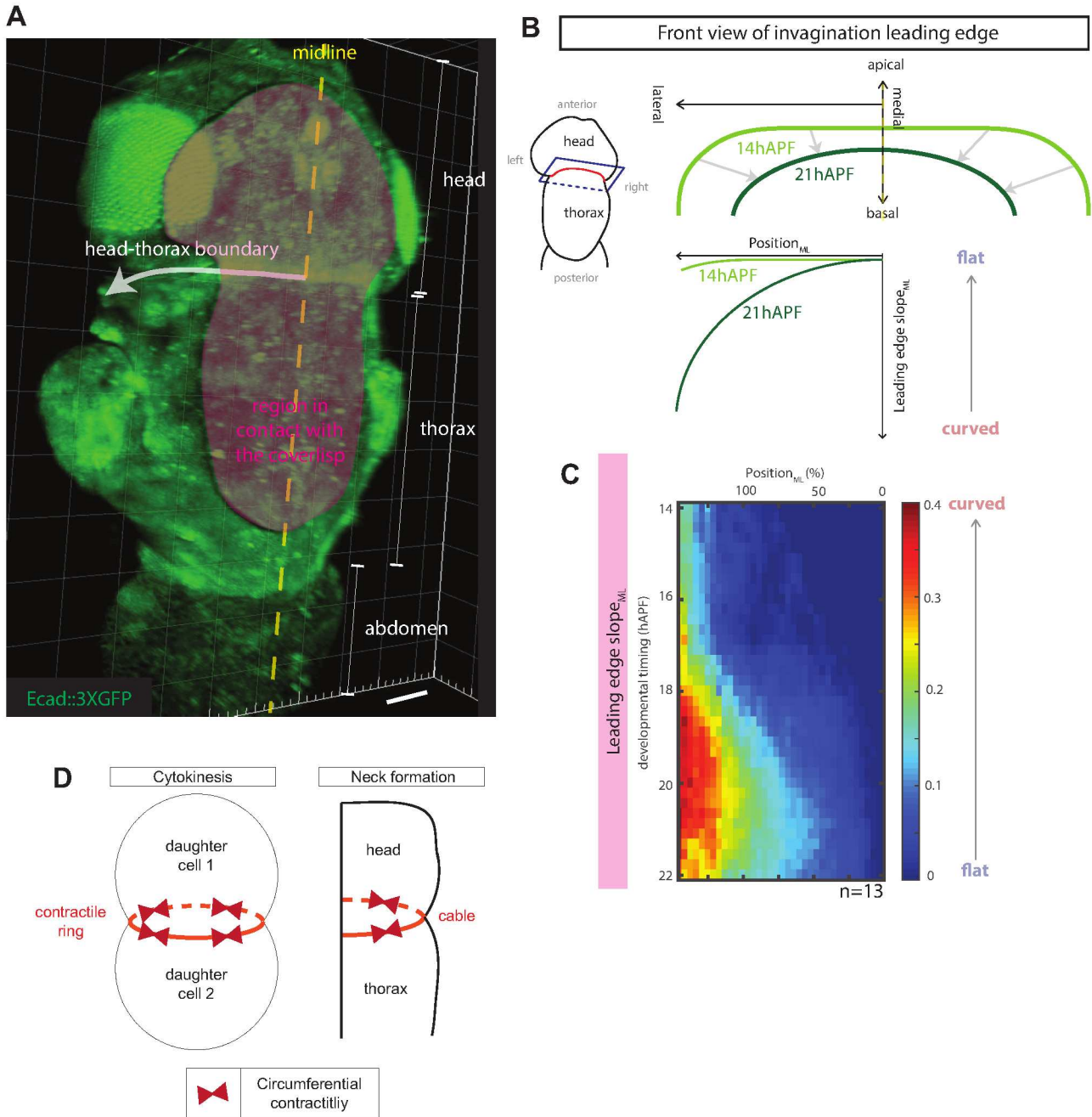


Fig.4: Neck acto-myosin cable is curved and could act as a «tissue-scale cytokinetic ring». A global overview of pupal epidermis at 14hAPF reveals a geometry marked by M-L curvature on the sides. Note that our mounting procedure creates an artificial flattening of the medial region due to the contact between the tissue and a flat coverslip (pink region, **A**). Detection of the position of the leading edge of neck invagination enables to measure leading edge M-L slope evolution in time (**B**). Average kymograph of leading M-L slope, n: number of analyzed animals. Note that the leading edge gets more and more bent along the M-L axis, and that initially flattened medial regions get progressively bent as well, n: number of analyzed animals (**C**). During cytokinesis, the circumferential contractility of the contractile ring promotes deep bending of the cell membrane, and separation of the cytoplasms of the two daughter cells. In a comparable way, we propose that the circumferential tension along the curved boundary cable could convey bending force during *Drosophila* neck formation (**D**).

A basal contractile supra-cellular network is present in neck folding region

While apical contractility has often been shown to be critical to account for epithelial invagination, basal tension release has recently been identified as another possible mechanism of epithelial folding⁷⁵. We thus investigated whether we could identify acto-myosin structures on the basal surface of the invaginating neck cells. Interestingly, we have discovered the presence of a supra-cellular network made of parallel actin bundles on the basal surface of neck region (Figure 5A). The assembly of this basal network correlates with invagination onset (Figure 5A'-A''). Moreover, phospho-MyosinII localizes on this basal network, indicating that it could be contractile (Figure 5B). Using rectangular laser ablation spanning many cell diameters, we have found that this basal actin network stores tension along the M-L axis (Figure 5C). We have performed such laser ablations on the basal and the apical surfaces of neck region, for successive stages of neck bending (from 15hAPF to 23hAPF). Interestingly, both apical and basal tension/friction ratios increase in time (Figures 5D-D'). Furthermore, basal and apical tension/friction ratio correlate both with neck deepening and indentation speeds (compare Figure 1F and Figures 5D-D'), and with basal network assembly (compare Figure 5A'' and Figures 5D-D'). Note that basal and apical tension/friction increase and basal network assembly precede by approximately 2h neck invagination onset. Taken together, this data shows that, contrary to what was described in other bending contexts^{75,184}, neck basal tension does not decrease during invagination, but on the contrary increases in a similar fashion as apical tension.

As apical and basal tension/friction ratios are of comparable amplitudes, we wanted to test whether apical and basal tensions could be interdependent. To do so, we have performed pairs of successive ablations. In a first set of experiments (BA_{experiment}, Figure 5F), ablation on neck basal surface was performed, quickly followed by an ablation of neck apical surface in the same region. In a second set of experiments, ablation on apical surface was performed first, followed by an ablation on the basal surface (AB_{experiment}, Figure 5E). These experiments were performed for successive stages of neck bending, from 15hAPF to 23hAPF. Interestingly, both apical and basal recoils are unaffected by previous ablation, showing that apical and basal cytoskeleton networks are mechanically uncoupled on short time scales (Figures 5F-F'). What is more, we could show that basal tension/friction ratio tends to always be superior to apical tension/friction ratio (Figure 5F''). Taken together, this data shows that neck basal actin network develops a M-L tension which is mechanically uncoupled from apical tension field at short time scales. We hypothesize that the tension of neck basal supra-cellular furrow might promote neck formation by a “tissue-scale cytokinetic furrow” mechanism, in a similar way to (and/or in combination with) the apical acto-myosin boundary cable.

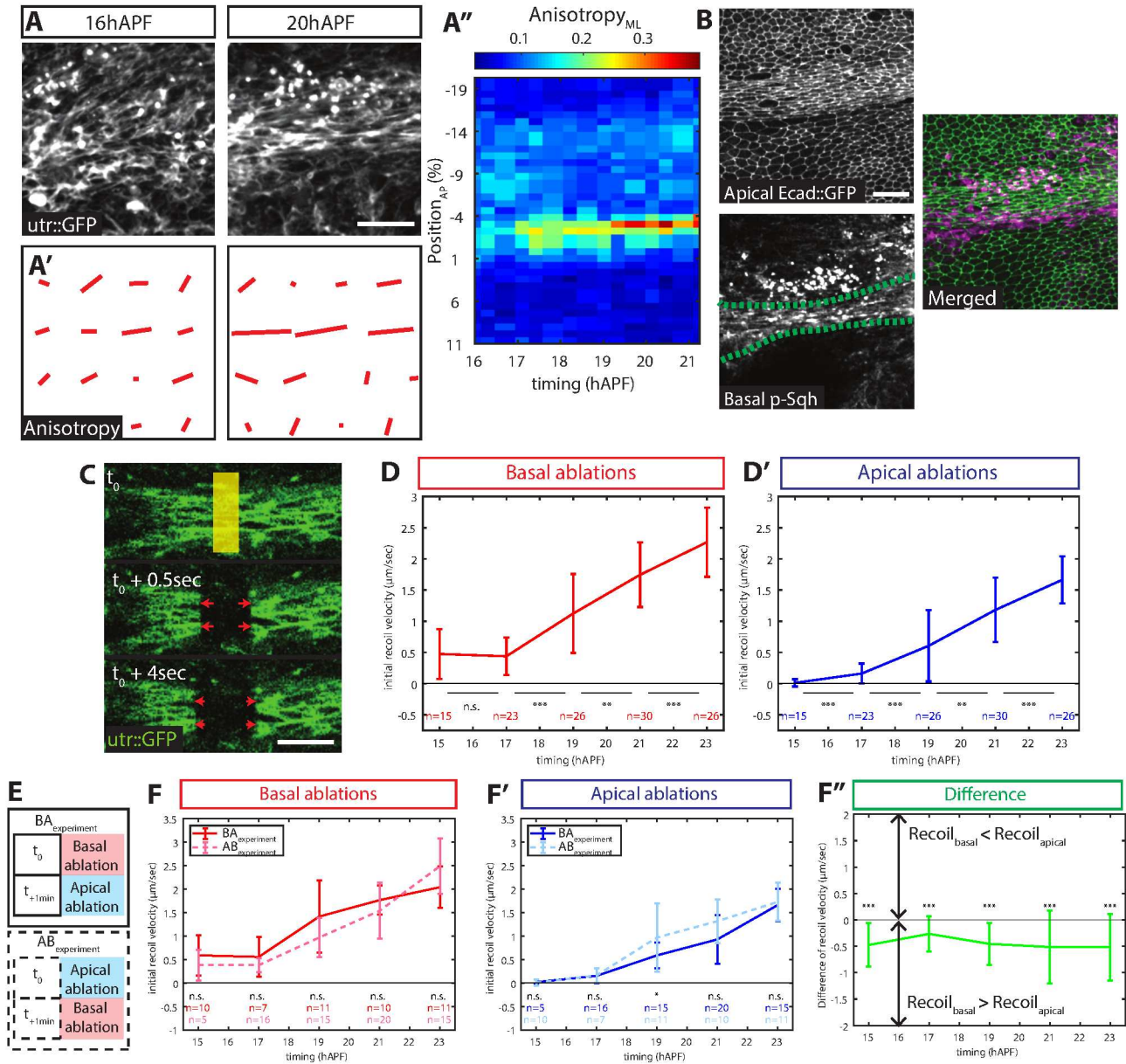


Fig.5: A basal contractile supra-cellular network is present in neck folding region. Basal actin fibers which are labelled with utrophin::GFP (utr::GFP) progressively align along M-L axis to form a supracellular band of parallel basal fibers in the neck region (**A**). 2D Fourier analysis enables the quantification of basal fibers local anisotropy tensors (**A'**). Extraction of M-L component of anisotropy tensors and averaging along the M-L axis enables the mapping of M-L anisotropy of basal fibers in time. A representative map is here shown. From 17hAPF to 20hAPF, prior to invagination onset, basal actin fibers get more and more parallel and aligned along M-L axis specifically in neck invagination region (**A''**). Immunostaining against phospho-Squash (p-Sqh) at 18hAPF, showing localisation of p-Sqh in neck basal actin network, green dashed lines delimitate the boundaries of neck basal network (**B**). Laser ablation of neck basal network triggers M-L recoil (**C**). Basal ablations and apical ablations trigger increasing recoils in time from 17hAPF to 23hAPF. Welch tests have been performed to compare successive time points and test for a significant variation of the means (**D**, **D'**). Successive ablations on basal then apical side (BA_{experiment}), or on apical then basal side (AB_{experiment}) have been performed (**E**). Basal ablations trigger recoils whether or not they were preceded by an apical ablation (**F**). Similarly, apical ablations trigger recoils whether or not they were preceded by a basal ablation (**F'**). While basal and apical recoils show similar trends in time, basal recoils tend to always be higher than apical recoils, t-tests have been performed to test whether distribution means were significantly different from zero (**F''**).

[(A), (B) and (C)] Scale bars: 25 μm . [(D), (D'), (F) and (F')] n: number of analyzed ablations. [(F) and (F')] Welch tests have been performed to compare, for each timing, recoils on a given side (apical or basal) obtained from BA_{experiment} or from AB_{experiment}.

Modulation of MyosinII contractility regulates neck invagination speed

Neck invagination region is associated with supra-cellular acto-myosin structures that could participate to neck folding. In order to functionally test the requirement of MyosinII-dependent contractility in neck invagination, we have built a *Dfd::GAL4* fly line. *Dfd::GAL4* enables to specifically induce RNAi in the most posterior domain of the head, which both borders the apical acto-myosin cable and encompass most of the regions showing basal contractile fibers (Figure 6A). We have used RNAi against MyosinII kinase *Rok* or against MyosinII regulatory subunit *sqh* to downregulate MyosinII contractility in the *Dfd*-expressing domain (*Dfd>Rok^{RNAi}* and *Dfd>sqh^{RNAi}*). Complementary, we have used RNAi against *Mbs*, a regulatory subunit of MyosinII targeted by MyosinII phosphatase, to upregulate MyosinII contractility (*Dfd>Mbs^{RNAi}*). RNAi induction was controlled in time using the GAL4/GAL80ts system¹⁸⁵.

Using immunostaining against phospho-MyosinII, we have shows that MyosinII phosphorylation was almost completely suppressed in the *Dfd*-expressing domain in *Dfd>Rok^{RNAi}* and *Dfd>sqh^{RNAi}*, both apically and basally (Figure 6B-B'). Interestingly, we can notice that phospho-MyosinII enrichment at the boundary cable is still present on the thorax side in *Dfd>Rok^{RNAi}* and *Dfd>sqh^{RNAi}* (Figure 6B). Thus, only one half of the acto-myosin enrichment at the cable is removed in these conditions (Figure 6B'). Additionally, phospho-MyosinII levels are increased in *Dfd>Mbs^{RNAi}*, both apically and basally (Figure 6B-B'). We can thus conclude that MyosinII phosphorylation is highly affected in *Dfd>Rok^{RNAi}*, *Dfd>sqh^{RNAi}* and *Dfd>Mbs^{RNAi}*.

We have assessed whether apical tension was affected in *Dfd>Rok^{RNAi}*, *Dfd>sqh^{RNAi}* and *Dfd>Mbs^{RNAi}*. Using single junction ablation, we have estimated the tension/friction ratio of the junctions belonging to the boundary cable or belonging to the *Dfd*-expressing domain in *Dfd>Rok^{RNAi}*, *Dfd>sqh^{RNAi}* and *Dfd>Mbs^{RNAi}* (Figure 6C). Interestingly, we found that tension/friction ratio was decreased in the cable in *Dfd>Rok^{RNAi}* and *Dfd>sqh^{RNAi}*, and increased in *Dfd>Mbs^{RNAi}* (Figure 6C). We can thus conclude that decreasing MyosinII contractility in the neck region leads to a decrease in tension/friction ratio, while increasing MyosinII contractility in the neck region leads to an increase in tension/friction ratio.

When comparing *Dfd>Rok^{RNAi}* and *Dfd>sqh^{RNAi}* with the control, the decrease of phospho-MyosinII enrichment at the cable appears to be comparable with the decrease of cable recoil after ablation (Figure 6D). However, in *Dfd>Mbs^{RNAi}*, the increase of cable recoil velocity after ablation appears modest as compared to the amount of increase in phospho-MyosinII

enrichment in the cable (Figure 6D). This result suggests that junction tension non linearly depends on phospho-MyosinII cortical level. We propose that (i) a saturation effect or (ii) high friction due to the coupling with the apical ECM could explain why high phospho-MyosinII enrichment observed in $Dfd>Mbs^{RNAi}$ only causes a modest increase in cable recoil after ablation as compared to the control.

Finally, we have described neck invagination dynamics in $Dfd>Rok^{RNAi}$, $Dfd>sqh^{RNAi}$ and $Dfd>Mbs^{RNAi}$. While invagination still takes place in $Dfd>Rok^{RNAi}$ and $Dfd>sqh^{RNAi}$, deepening of the invagination leading edge and tissue indentation are delayed (Figures 7A-C). A decrease of MyosinII contractility in the neck thus leads to invagination defects. What is more, in $Dfd>Mbs^{RNAi}$, deepening of the invagination leading edge and tissue indentation is premature and faster (Figures 7A-C). Invagination speed is thus increased when increasing MyosinII contractility in the neck. Taken together, these results show that local MyosinII contractility levels regulate neck invagination speed.

Additionally, we have analyzed neck tissue displacements and deformations in $Dfd>Rok^{RNAi}$, $Dfd>sqh^{RNAi}$ and $Dfd>Mbs^{RNAi}$. Tissue in the head next to the leading edge stretches more along the A-P axis in $Dfd>Rok^{RNAi}$ and $Dfd>sqh^{RNAi}$ than in the control, and contracts more along the A-P axis in $Dfd>Mbs^{RNAi}$ (compare Figures 2B and 8A). The increase in A-P contractility in $Dfd>Mbs^{RNAi}$, however, is not restricted to the domain in which RNAi against *Mbs* was induced, suggesting that this increased contraction is more likely a consequence of higher invagination speed than its cause (Figure 8A). M-L flows, on the other hand, were reduced in $Dfd>Rok^{RNAi}$ and $Dfd>sqh^{RNAi}$, and precocious in $Dfd>Mbs^{RNAi}$ (compare Figures 2F and 8B). We propose that this changes in M-L flows may be the consequence of the changes in M-L contractility of the leading edge acto-myosin cable (Figure 8C).

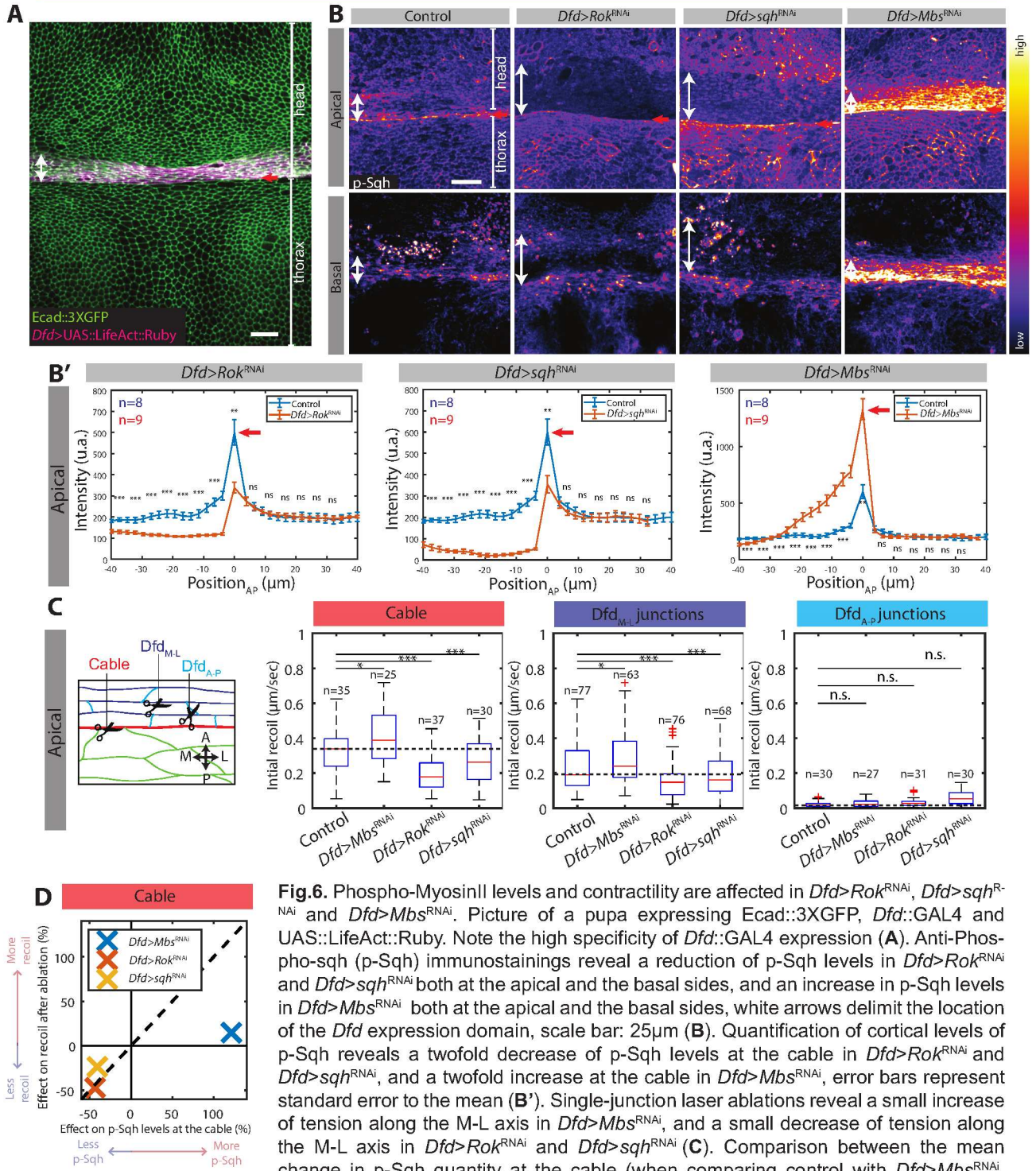


Fig.6. Phospho-MyosinII levels and contractility are affected in $Dfd>Rok^{RNAi}$, $Dfd>sqh^{RNAi}$ and $Dfd>Mbs^{RNAi}$. Picture of a pupa expressing Ecad::3XGFP, $Dfd::GAL4$ and UAS::LifeAct::Ruby. Note the high specificity of $Dfd::GAL4$ expression (**A**). Anti-Phospho-sqh (p-Sqh) immunostainings reveal a reduction of p-Sqh levels in $Dfd>Rok^{RNAi}$ and $Dfd>sqh^{RNAi}$ both at the apical and the basal sides, and an increase in p-Sqh levels in $Dfd>Mbs^{RNAi}$ both at the apical and the basal sides, white arrows delimit the location of the Dfd expression domain, scale bar: 25μm (**B**). Quantification of cortical levels of p-Sqh reveals a twofold decrease of p-Sqh levels at the cable in $Dfd>Rok^{RNAi}$ and $Dfd>sqh^{RNAi}$, and a twofold increase at the cable in $Dfd>Mbs^{RNAi}$, error bars represent standard error to the mean (**B'**). Single-junction laser ablations reveal a small increase of tension along the M-L axis in $Dfd>Mbs^{RNAi}$, and a small decrease of tension along the M-L axis in $Dfd>Rok^{RNAi}$ and $Dfd>sqh^{RNAi}$ (**C**). Comparison between the mean change in p-Sqh quantity at the cable (when comparing control with $Dfd>Mbs^{RNAi}$, $Dfd>Rok^{RNAi}$ and $Dfd>sqh^{RNAi}$) and the mean change in cable recoil after ablation (when comparing control with $Dfd>Mbs^{RNAi}$, $Dfd>Rok^{RNAi}$ and $Dfd>sqh^{RNAi}$), dashed line represents the expected relationship in the case of a proportionality between the two effects (**D**).

[(A), (B) and (B')] Red arrows indicate head-to-thorax boundary acto-myosin cable location. [(B') and (C)] Welch tests have been performed to compare control and RNAi means. n: number of analyzed stainings or number of analyzed laser ablations.

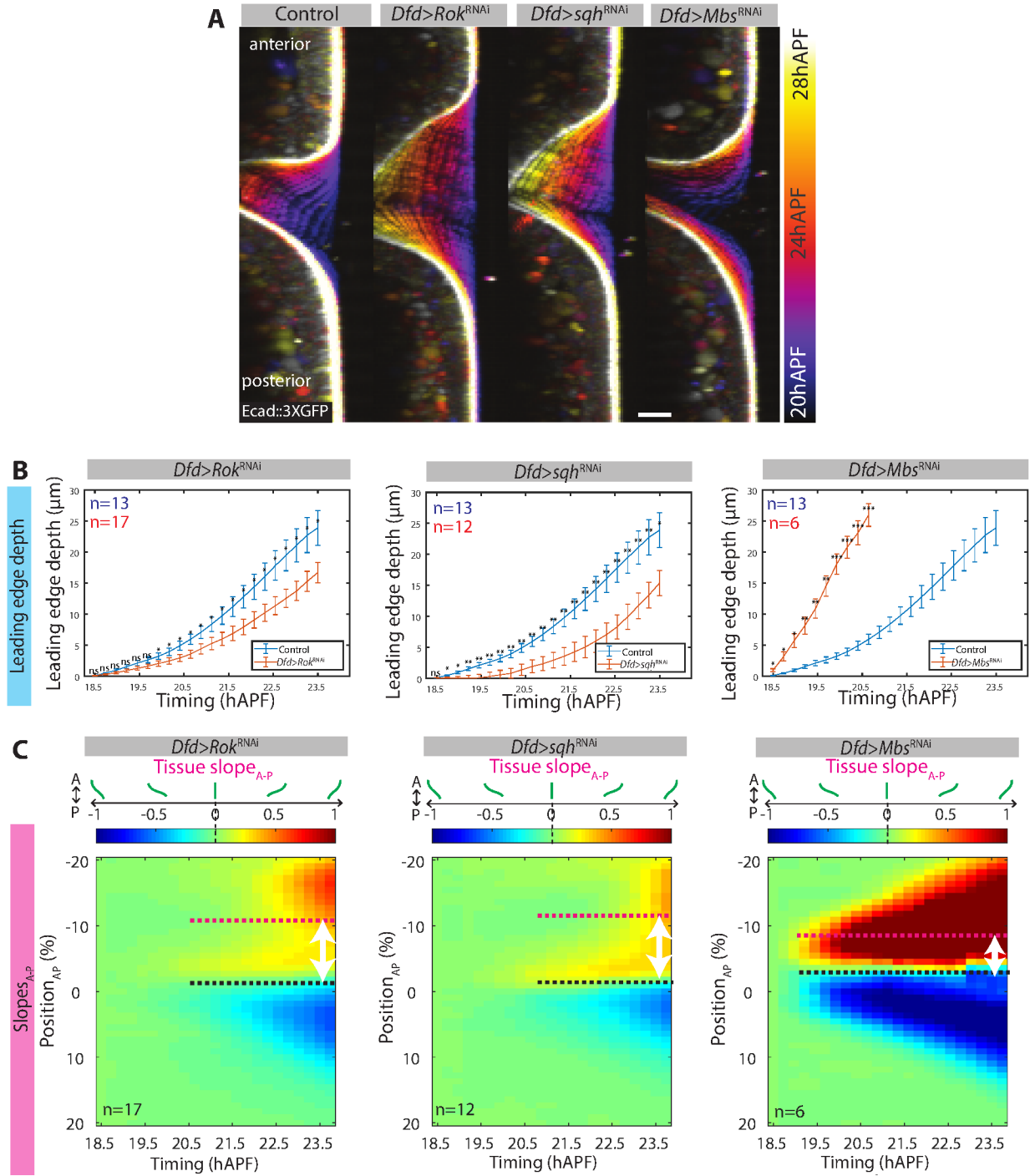


Fig.7. Neck invagination dynamics is affected in $Dfd>Rok^{RNAi}$, $Dfd>sqh^{RNAi}$ and $Dfd>Mbs^{RNAi}$. Sagittal views (along the midline) of neck invagination region projected in time of representative animals, illustrating the fact that neck invagination is delayed and slower in $Dfd>Rok^{RNAi}$ and $Dfd>sqh^{RNAi}$, and precocious and faster in $Dfd>Mbs^{RNAi}$, scale bar: 25 μm (A). Mean curves of the evolution of the depth of leading edge invagination in time reveal an invagination delay in $Dfd>Rok^{RNAi}$ and $Dfd>sqh^{RNAi}$, and a premature and faster deepening in $Dfd>Mbs^{RNAi}$, error bars represent standard error to the mean, Welch tests have been performed at each time point to test for an increase in depth in $Dfd>Mbs^{RNAi}$, and for a decrease in depth in $Dfd>Rok^{RNAi}$ and $Dfd>sqh^{RNAi}$ (B). Average kymographs of A-P slopes reveal a decrease in speed of neck indentation in $Dfd>Rok^{RNAi}$ and $Dfd>sqh^{RNAi}$, and a faster indentation in $Dfd>Mbs^{RNAi}$, black dashed lines represent the position of neck invagination leading edge, pink dashed line represent the anterior limit of $Dfd::GAL4$ expression domain, white arrows represent Dfd expression domain (C).

[(B) and (C)] n: number of analyzed animals.

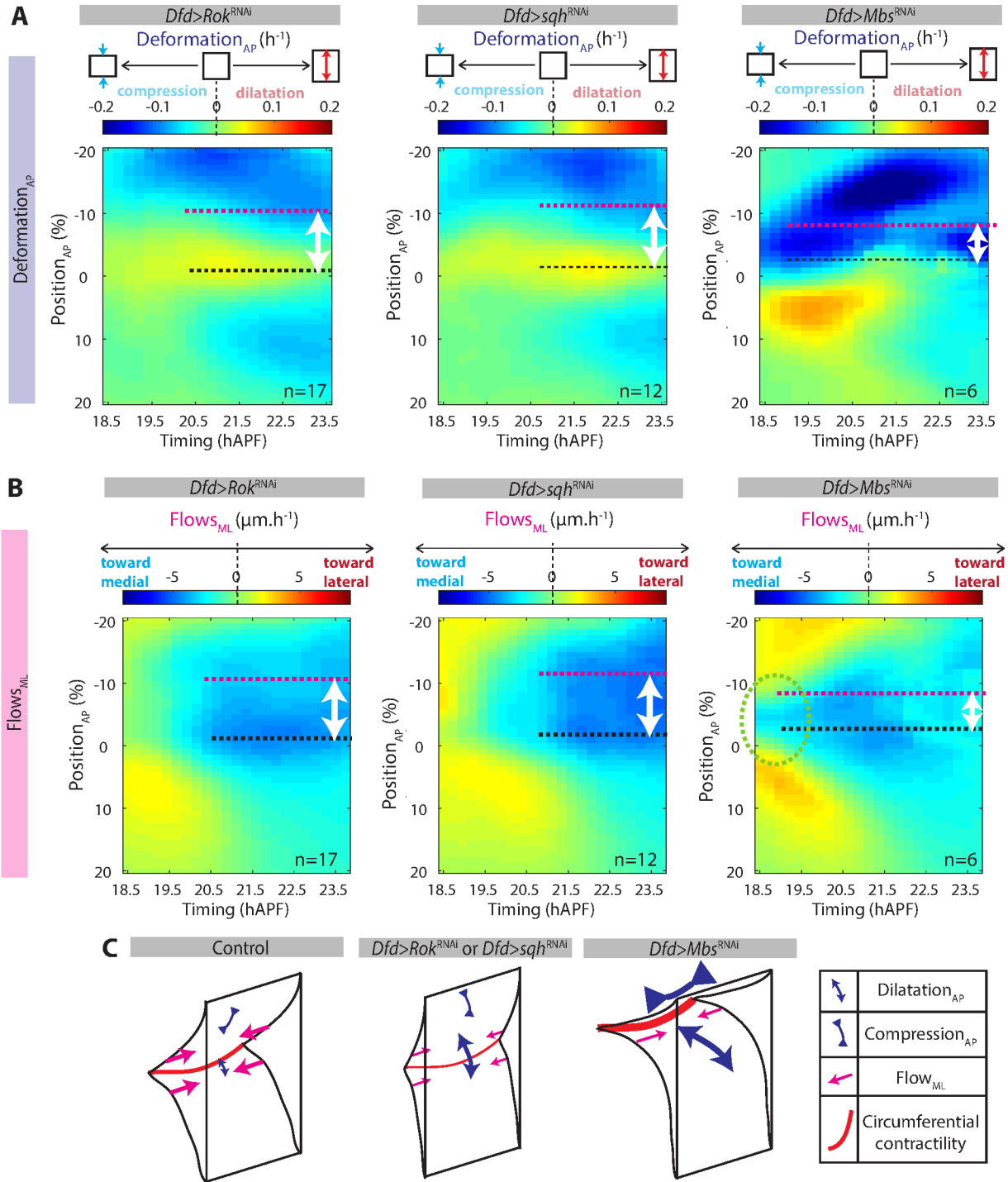


Fig.8. Tissue deformations and flows patterns are affected in *Dfd>Rok^{RNAi}*, *Dfd>sqh^{RNAi}* and *Dfd>Mbs^{RNAi}*. Average kymographs of A-P deformations reveal local A-P stretching next to the leading edge in *Dfd>Rok^{RNAi}* and *Dfd>sqh^{RNAi}*, and reveal higher A-P stretching in the thorax and higher A-P contraction in the head in *Dfd>Mbs^{RNAi}*. Note that increased A-P contraction in *Dfd>Mbs^{RNAi}* can be observed outside the region of expression of *Dfd* (A). Average kymographs of M-L speeds reveal a reduction of M-L flows in *Dfd>Rok^{RNAi}* and *Dfd>sqh^{RNAi}*, and precocious M-L flows in *Dfd>Mbs^{RNAi}* (green dashed circle, B). Schematic recapitulation of *Dfd>Rok^{RNAi}*, *Dfd>sqh^{RNAi}* and *Dfd>Mbs^{RNAi}* phenotypes (C).

[(A) and (B)] black dashed lines represent the position of neck invagination leading edge, pink dashed line represent the anterior limit of *Dfd::GAL4* expression domain, white arrows represent *Dfd* expression domain. n: number of analyzed animals.

Discussion

Association between interface contractility and tissue invagination

We have here provided the first detailed description of neck fold formation during *Drosophila* metamorphosis. Interestingly, neck invagination leading edge is marked by the presence of a prominent supra-cellular junctional acto-myosin cable. This cable is located at the boundary between head and thorax compartments, and display increasing tension/friction ratios during neck tissue bending. Such boundary acto-myosin cables have been recently shown to regulate the final depth of grooves formed at the interface between parasegments in *Drosophila* embryo¹²⁰. In concordance with these results, we have found that locally decreasing or increasing neck MyosinII contractility at the head-thorax interface respectively leads to a decrease or an increase in neck invagination speed. Thus, our results strengthen the idea that increased contractility at the interface between two development compartments can actively participate to fold formation. The position of neck acto-myosin cable at the leading edge of invagination throughout the whole bending phase further suggests an active role of the boundary apical acto-myosin cable in neck fold formation.

Nevertheless, even if its speed is affected, neck invagination still proceeds in *Dfd>Rok^{RNAi}* and *Dfd>sqh^{RNAi}*. This might be due to the fact that *Dfd::GAL4* only allows to disrupt MyosinII contractility in the region that borders head-to-thorax boundary on the head side. In fact, we have shown that head-to-thorax boundary acto-myosin cable is composed of cortical MyosinII enrichment of both head and thorax sides. Accordingly, in *Dfd>Rok^{RNAi}*, *Dfd>sqh^{RNAi}* and *Dfd>Mbs^{RNAi}*, the cortical enrichment of the acto-myosin cable on the thorax side is not affected. Thus, this non-affected MyosinII enrichment in the thorax side may be enough to promote neck folding in *Dfd>Rok^{RNAi}* and *Dfd>sqh^{RNAi}*, although with a reduced speed.

Interestingly, *tsh::GAL4* is expressed in cells bordering the cable on the thorax side (data not shown). *tsh::GAL4* could thus be used to disrupt MyosinII contractility on the thorax side of head-thorax interface. We thus propose to complement *Dfd>Rok^{RNAi}*, *Dfd>sqh^{RNAi}* and *Dfd>Mbs^{RNAi}* experiments by studying neck invagination dynamics in *tsh>Rok^{RNAi}*, *tsh>sqh^{RNAi}* and *tsh>Mbs^{RNAi}*. A decreased invagination speed in *tsh>Rok^{RNAi}* and *tsh>sqh^{RNAi}* and an increased invagination speed in *tsh>Mbs^{RNAi}* would further show the importance of interface contractility in neck folding. What is more, *Dfd::GAL4* and *tsh::GAL4* could be combined, in

order to affect at the same time both head and thorax MyosinII contractility. This latter experiment could enable to test whether neck invagination can be fully inhibited by disrupting interface contractility on both head and thorax sides.

Boundary acto-myosin cable and invagination: Towards a model of a “tissue-scale cytokinetic ring”?

In *Drosophila*, circular acto-myosin cables surrounding the trachea¹⁸⁶, the salivary glands¹¹⁶ or clones aberrantly expressing transcription factors¹¹⁷ have been linked with epithelial pit formation. Note that all these cables are present within the plane of the tissue. In these contexts, the tension along the cable and the propensity of the cable to decrease its radius have been linked with pit formation. The circular geometry of the cable is pivotal for transforming circumferential tension into bending force, as linear cables cannot lead to fold formation and only trigger the formation of straight boundaries according to the study of Bielmair & colleagues¹¹⁷. However, linear cables have been associated with fold formation at the interface between parasegments in *Drosophila* embryo¹²⁰. As a consequence, the mechanism linking acto-myosin cable contractility and parasegment grooves formation remains obscure. As for the case of clones aberrantly expressing transcription factors¹¹⁷, an increase in lateral contractility is thus hypothesized to mainly drive tissue bending at inter-parasegment boundaries, but this mechanism appears insufficient as regards the depth of the folds¹²⁰.

In a comparable way to parasegment folds, a linear cable is associated with neck fold formation. However, we here provide evidence that neck cable is curved along the M-L axis, and gets more and more circular while neck invagination proceeds. Moreover, we show that during neck invagination, head-thorax interface constricts in the direction parallel to the fold axis, and display high convergent flows towards the midline. Based on these observations, we hypothesize that neck cable circumferential contractility could actively participate in neck morphogenesis. We argue that neck cable circularity may be pivotal to convert cable contractility into a bending force. This hypothesized bending mechanism is inspired from the studies of cell cytokinesis: Indeed, during this process (which happens at very different spatial and temporal scales), the contractility of a cytokinetic ring surrounding the cell leads to membrane bending. We thus propose that neck cable could function as a “tissue-scale cytokinetic ring”. The curved acto-myosin cable contractility could then be converted into a tissue bending force participating to neck formation. This “tissue-scale cytokinetic ring”

mechanism could be extrapolated to other systems showing an association between tensile interfaces and groove formation, like *Drosophila* inter-parasegment boundaries¹²⁰, *Drosophila* cephalic furrow formation¹⁸⁷ or vertebrate hindbrain rhombomeres boundaries¹⁸⁸.

Study of the quantitative contributions of cellular processes (rearrangements, delaminations, divisions and cell shape changes) to M-L contraction next to the cable would be precious to more deeply understand how neck acto-myosin cable could drive neck folding. In the present study, the quantitative analysis of tissue deformation in the neck region that we have here performed is based on PIV. However, the use of Ecad::3XGFP as a marker for cell contours allows cell segmentation and tracking in the neck region during folding. However, this analysis remains challenging: the high curvature of the tissue and the small apical size of cells in neck region challenge current automatic segmentation tools, which produce high error rates when trying to segment neck region cell contours. Designing specific segmentation tools based on 3D analysis of Ecad::3XGFP signal might be helpful to segment cell contours, correct segmentation errors and track cells in neck invagination movies in a manageable amount of time.

Finally, we believe that integration of our assumptions in an *in silico* model would be useful to test the plausibility and the coherence of a “tissue-scale cytokinetic ring” model. 2D models can efficiently model the role of apical constriction in epithelial bending^{180,181}, but they ignore the possible contributions of dynamics along the fold axis. Thus, 3D models are required to study the role of neck cable circumferential tension in neck folding. The 3D vertex model that was used to model linear flat boundary tension could be used as a starting point¹¹⁷, but it takes as an initial state a flat tissue. This model should thus be complemented by implementing a curved manifold as an initial state. The 3D model used to recapitulate *Drosophila* leg disc folding⁷⁶ could as well be well suited to model neck invagination dynamics, as it takes as an initial state a curved epithelium. Finally, models used for recapitulating the effect of cytokinetic ring contractility on cell membrane invagination could also be a source of inspiration¹¹⁹.

Proposition of an experiment to test the validity of “tissue-scale cytokinetic ring” mechanism

Pupae are naturally dorsally flattened, and display higher lateral curvature. This dorsal flattening is exacerbated in our mounting set-up, as a coverslip is placed on dorsal thorax tissues and further flattens dorsal tissue (Figure 4A). One prediction of a “tissue-scale cytokinetic ring” model would be that regions showing low initial curvature should invaginate later than bent regions (Figure 9A). Preliminary analysis of neck leading edge invagination deepening dynamics suggest that it is the case, with medial flattened regions invaginating later than curved lateral regions (Figure 9B).

We propose that an experiment based on pupa initial geometry disruption could enable to directly test the validity of a “tissue-scale cytokinetic ring” mechanism (Figure 9C). The pressure imposed by the coverslip put on the pupa prior to imaging can be controlled, and has been standardized in the present study. We propose to vary mounting pressure (from an almost null pressure to extreme dorso-ventral squeezing of the pupa), in order to test the influence of initial tissue geometry on invagination dynamics (Figure 9C). We expect to observe a correlation between the amount of mounting pressure put on neck tissue and neck invagination delay. Besides, in the present study, our mounting is centered on the midline, and left and right halves of the animal undergo equivalent mounting pressures. We propose to tilt pupae on one side, in order to obtain different mounting pressures on each hemi-pupa. In this condition, we predict that the pressured half should invaginate later than the unpressured half. Finally, pupae could be squeezed along the left-right axis, in order to increase medial tissue curvature (Figure 9C). We expect in this condition that invagination in medial neck region should be precocious. Taken together, these experiments could enable to shed light on the importance of animal geometry in morphogenesis, and strengthen the credibility of a “tissue-scale cytokinetic ring” mechanism.

Basal tension increase and neck invagination

We interestingly report the assembly of a contractile basal network made of parallel actin bundles. While invagination has been reported to be associated with basal tension relaxation^{75,184}, we here show that it is on the contrary associated with basal tension building up. Indeed, both the assembly and the increase in tension/friction ratio of neck basal network correlate with invagination dynamics. These observations suggest that neck basal network could actively participate to neck bending.

It would be interesting to quantify the effect of downregulation of neck basal tension on neck invagination dynamics. However, we do not have identified yet a genetic condition in which basal tension is altered. Basal tension is however likely to be altered in *Dfd>Rok^{RNAi}*, *Dfd>sqh^{RNAi}* and *Dfd>Mbs^{RNAi}*, as in these conditions, phospho-MyosinII levels are altered in the basal network. We however have not assessed whether basal tension was altered in *Dfd>Rok^{RNAi}*, *Dfd>sqh^{RNAi}* and *Dfd>Mbs^{RNAi}*. This could be achieved by using UAS::LifeAct::Ruby as a reporter to perform laser ablation on the basal surface of the *Dfd* expression domain in *Dfd>Rok^{RNAi}*, *Dfd>sqh^{RNAi}* and *Dfd>Mbs^{RNAi}*. These experiments could help us interpreting the decrease in invagination speed observed in these genetic contexts, that we for the moment mainly attribute to apical tension disruption. Second, identifying specific regulators of basal actin network assembly would be precious to specifically disrupt basal tension field and study its impact on invagination dynamic. In concordance with previous studies⁷⁵, preliminary data obtained by Floris Bosveld in our team suggests that integrity of the basal ECM and the protein Dystrophin (*dys*) are required for the assembly of a comparable basal actin network at the boundary between scutum and scutellum in dorsal thorax. Using RNAi against *dys* or preventing basal ECM assembly in the neck region by knocking down *collagenIV* (named *viking* in flies) expression could be two approaches that might enable to specifically prevent neck basal actin network assembly.

We have besides showed in neck region that basal and apical tension fields, although showing similar tension/friction ratios, are mechanically uncoupled at short time scales. Additionally, we have observed that basal tension/friction ratio tends to be higher than apical tension/friction ratio. Interestingly, in the scutum-scutellum boundary region in dorsal thorax, a basal network comparable to neck basal network assembles (data not shown). Interestingly, I have observed that in this region, basal tension/friction ratio tends also to be higher than apical tension/friction ratio (data not shown). It would be interesting to study whether this apical/basal asymmetry in tension/friction ratios has any morphogenetic relevance, in neck region or in scutum-scutellum boundary region.

Assessing the role of additional mechanisms during neck invagination

Apical constriction is a widespread mechanism promoting epithelial bending. We have here shown that neck invagination leading edge is not clearly associated with neighboring tissue constriction perpendicularly to the fold axis. Based on this observation, we have concluded that a simple model based on apical constriction cannot efficiently account for neck invagination dynamics. However, we have not directly measured cell apical area deformation in the neck region. Segmentation of cell contours and cell tracking would be required to directly claim that cells located at the neighborhood of the leading edge of invagination do not undergo constriction along the A-P axis.

Alternative bending mechanisms based on apico-basal active shrinkage⁷⁵, adherens junction repositioning⁷⁸ or apico-basal apoptotic forces⁷⁶ can account for epithelial folding. We have noticed that these bending mechanisms based on apico-basal dynamics are systematically found in folds forming in columnar epithelia^{76,75,25,78}. In these contexts, the thickness of the tissue is comparable or bigger than the diameter of the fold (Figure 9F). We hypothesize that due to simple geometrical constraints, mechanisms based on apico-basal dynamics may have poor explanatory power in systems in which the diameter of the created fold is much higher than tissue thickness (Figure^{introduction} 4). However, *Drosophila* neck invagination show a much lower tissue thickness/fold diameter ratio (Figure 9E). We thus conclude that neck invagination is unlikely to mainly rely on apico-basal dynamics. Nevertheless, we do not rule out that apico-basal dynamics could participate in neck folding. In fact, mainly prior to neck invagination onset, and to a lesser extent during invagination, many cells delaminate in neck region (data not shown). Whether apoptotic or EMT apico-basal forces could participate to neck invagination dynamic is thus still an open question. Genetically preventing apoptosis in neck region, by for example overexpressing *p35*, could help tackling this issue. On the other hand, the analysis of neck tissue thickness and neck cell 3D shape during invagination could help assessing whether neck bending could partly rely on local apico-basal shrinkage or adherens junction repositioning.

Finally, the idea that a pushing force from neighboring tissue can trigger buckling is a common hypothesis⁹⁵, but its relevance *in vivo* is still unclear. Our data indicates that neck invagination is accompanied by a directional flow of neck and neighboring thorax region towards the anterior (Figure 2C). One could thus envision that thorax flow could provide a pushing force sufficient to promote neck buckling. In the second part of my thesis, I will

experimentally test this hypothesis, by analyzing early neck invagination dynamics in genetic contexts in which anterior thorax flow is highly reduced. I will show that thorax active migration does not contribute to the initial bending of the neck. However, my findings do not rule out that late bending of the neck might depend on thorax flow pushing force.

What is triggering neck invagination onset?

Head-to-thorax boundary cable appears to be a potential central actor in neck folding. However, this cable is already present prior to invagination, and already display a higher tension/friction ratio than neighboring junctions prior to invagination. How comes neck cable does not trigger invagination earlier than 20hAPF? We have shown that neck cable displays higher tension/friction during neck invagination. This increase in tension/friction ratio may control neck invagination onset. The signals temporally regulating this increase in tension/friction ratio are however unknown.

One explanation for this change in tension/friction ratio might be that the friction imposed by the apical ECM on the tissue decreases just prior to invagination onset. In fact, while neck tissue closely interacts with the apical ECM prior to invagination, we have obtained preliminary data showing that neck epidermis locally detaches from the apical ECM during invagination (Figure 9D). We thus propose that this detachment from the apical ECM may promote a decrease in friction undergone by the tissue, thus triggering an increase in neck cable tension/friction ratio. This increase might in turn control the timing of neck invagination onset. In order to test this hypothesis, neck invagination dynamics could be analyzed in a context of local disruption of the interaction between the tissue and the apical ECM. To do so, RNAi against the apical ECM proteins *Dumpy*, *piopio*, *pot*, and against integrin complex components could be used.

In conclusion, we propose that *Drosophila* neck folding may represent a valuable new model system to study epithelial folding *in vivo*. The present study, complemented with further studies of neck invagination dynamics, may shed light of new mechanisms and physical models accounting for deep fold formation within an epithelial tissue.

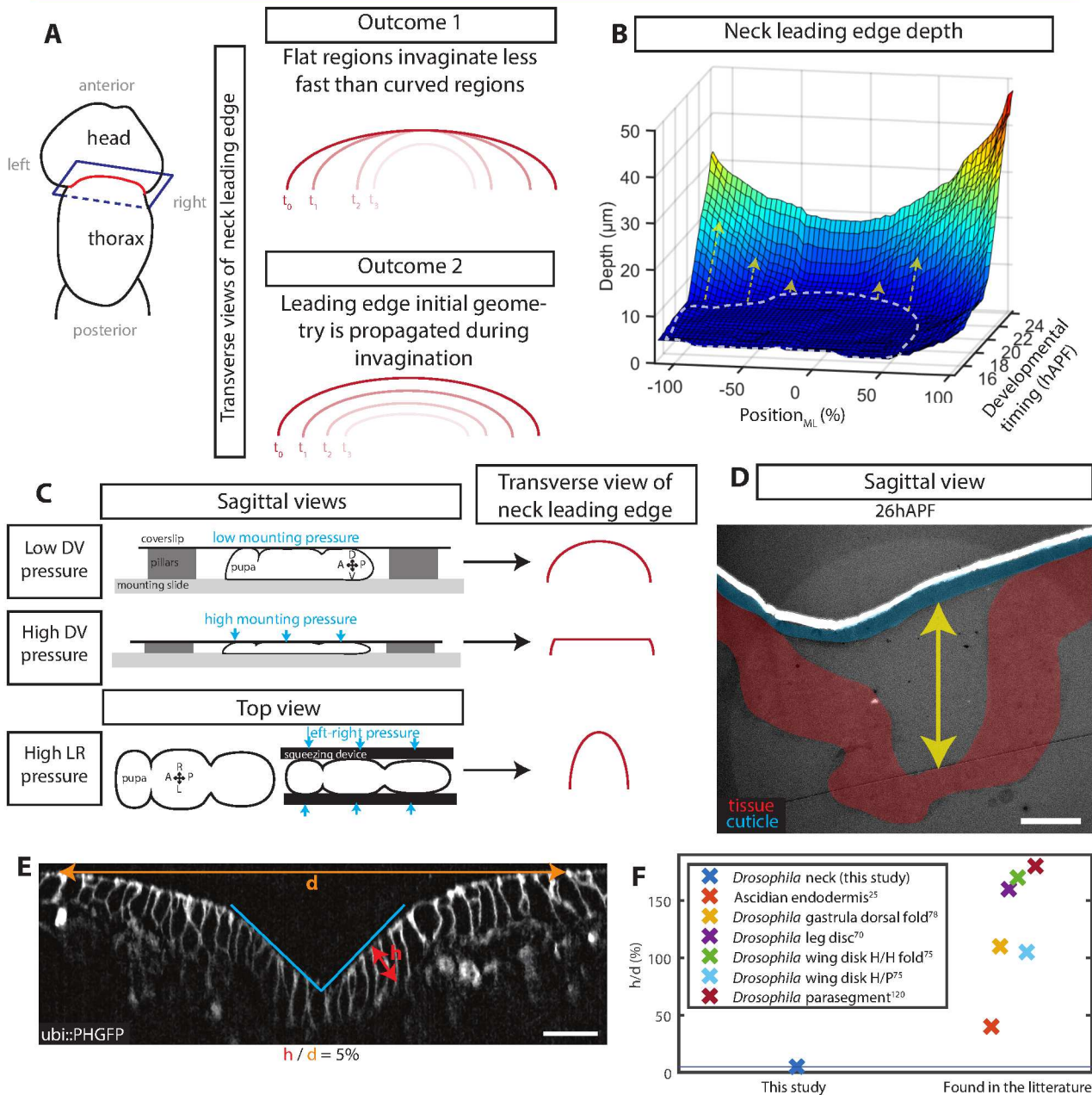


Fig.9. Possible outcomes of leading edge deepening as regard to its initial geometry. Outcome1: Flat regions invaginates less fast than medio-laterally curved regions, and leading edge initial M-L flattening progressively disappears. Outcome2: The initial geometry of neck invagination leading edge is conserved during invagination. We propose that Outcome1 may be compatible with a «tissue-scale cytokinetic ring» mechanism, whereas Outcome2 may be more compatible with classical models based on apical constriction or on apico-basal dynamics (A). 3D representation of the evolution of the depth of the leading edge of invagination in time and along the M-L axis. Data extracted from a representative animal. Note that the initially flattened region (circled with a white dashed line), deepens later than the lateral regions. Note as well the lateral-to-medial propagation of M-L curvature (B). Initial neck curvature could be artificially modulated by putting more or less dorso-ventral pressure on the animal using our imaging set-up, or by creating a device enabling to squeeze the pupa along its left-right axis. The obtained leading edge geometry are depicted in red. A: Anterior, P: Posterior, D: Dorsal, V: Ventral, L: Left, R: Right (C). Electron microscopy image of a sagittal slice of neck region at 26hAPF. Note the local detachment and the distance between the tissue and the cuticle (yellow arrow), scale bar: 20 μm (D). Side view at 23hAPF of neck invagination region labelled with the membrane marker PH::GFP, scale bar: 15 μm , note the low ratio between tissue thickness (h) and diameter of folding (d , E). Estimation of the ratio between tissue thickness and diameter of folding in *Drosophila* neck invagination (5%), and various other invaginations that rely on apico-basal intrinsic forces, note that *Drosophila* neck h/d ratio is at least 8 times smaller than in other folds. Respective references: this study, ²⁵, ⁷⁸, ⁷⁰, ⁷⁵, ⁷⁵, ¹²⁰. H/H fold: hinge-hinge fold (depending on basal tension relaxation⁷⁵), H/P fold: hinge/pouch fold (depending on lateral tension increase⁷⁵, F).

Part2: Analysis of anterior thorax flows

Collective cell migration on the apical extracellular matrix participates to thorax morphogenesis

Part2: Analysis of anterior thorax flows

Collective cell migration on the apical extracellular matrix participates to thorax morphogenesis

Context

The morphogenesis of an epithelium is driven by specific behaviors of the cells it is composed of. Cell shape changes, cell rearrangements, cell divisions, cell delaminations and cell translocation all synergize to give rise to tissue-scale flows and deformations¹⁸⁹. Within an epithelium, cells are mechanically coupled with their neighbors through a network of adherens junctions. The contractility of the acto-myosin networks associated with the adherens junction has been identified as a major actor of morphogenesis¹⁹⁰, by driving both cell shape changes⁷⁹, cell rearrangements⁶⁷ and cell delaminations¹⁹¹. When patterned and polarized across the epithelium as a result of patterned expression of transcription factors and planar polarity pathways, acto-myosin contractility can give rise to tissue-scale deformations^{192,68}. Furthermore, the contractility of an epithelial region can trigger the passive flowing and deformation of neighboring epithelial regions, as a result of long-range mechanical coupling^{171,54,193}.

An epithelial cell is not only mechanically coupled with neighboring cells, but also interacts with extracellular matrices (ECM). The interaction between epithelial cells and the ECM can provide fixed anchor points restricting long-range mechanical coupling within the tissue^{5,7}, but can also underlie epithelial cells collective migration¹⁹⁴. Collective migration can first underlie global tissue translocation. Moreover, migration of a subset of cells can give rise to neighboring tissue stretching, like in zebrafish lateral line¹⁴⁷ of mouse sprouting vessels⁹¹.

Drosophila dorsal thorax epidermis is a well-characterized model system for studying epithelial morphogenesis^{45,189}. The morphogenesis of this tissue has been quantified using live-imaging and cell tracking^{45,189}. Genetic regulation of dorsal thorax morphogenesis has been mostly studied in the posterior domain of dorsal thorax, called scutellum. Notably, Ft/Ds pathway is necessary for correct scutellum morphogenesis⁴⁵. However, the anterior thorax domain also deforms during development, and is marked by a prominent flow towards the anterior⁴⁵. The mechanisms underlying anterior thorax flow and deformation, however, are unclear. Interestingly, we have shown in part 1 that head-to-thorax interface actively

invaginates during morphogenesis. Thus, this active morphogenetic event happening at the edge of anterior thorax could provide a pulling force driving thorax flow. Besides, collective cell migration or tissue active deformation might as well autonomously drive thorax flow.

Summary

We here study the genetic, cellular and mechanical bases of *Drosophila* dorsal thorax flow during metamorphosis, by combining genetics, laser ablation and live-imaging. First, we quantitatively assess the effect of head-to-thorax interface invagination on thorax flow. We interestingly discover that thorax flow is only locally dependent on neck folding. Similarly, we show that anterior thorax flow only locally depends on the coupling with posterior thorax and lateral flanking regions. These observations suggest that intrinsic active mechanisms drive most of thorax flow. Indeed, we provide evidence that thorax cells use the apical ECM as a substratum for collective migration. Both core PCP pathway, the transcription factor *stripe* and the apically deposited protein Dumpy regulate thorax cell collective migration. Finally, we provide evidence that the migration of the anterior thorax provides a pulling force driving posterior thorax flow. Taken together, our study shows that collective cell migration in the anterior dorsal thorax is a driving force of thorax flows, and actively participate to thorax morphogenesis.

Results

Characterization of *Drosophila* dorsal thorax flow

Live-imaging of pupae expressing the cell contours marker Ecad::3XGFP was used to record dorsal thorax morphogenesis from 13hAPF to 38hAPF, with 15min time resolution and a sub-micrometric resolution (Figure 1A). Displacement fields were quantified using Particle Image Velocimetry (PIV, Figure 1B), and averaged along the medio-lateral (M-L) axis for each time point in a region of interest ($\text{Position}_{\text{AP}}=0\text{-}160\%$, $\text{Position}_{\text{ML}}=0\text{-}100\%$, Figure 1B). The obtained average velocity vectors were projected onto the antero-posterior (A-P) axis to get A-P velocity values, or onto the M-L axis to get M-L velocity values. The obtained A-P velocity values can then be visualized in an “A-P velocity kymograph” (see C/3-5 sections of Material & Methods, Figure 3B’). This plot quantifies the evolution with time of the distribution of A-P velocities along the A-P axis. Similarly, the M-L velocity kymograph

shows the evolution with time of the distribution of M-L velocities along the A-P axis (Figure 1E). Spatial and temporal registration of animals allowed the comparison of A-P and M-L velocity kymographs between different animals (see C/4 section of Material & Methods), and the calculation of average A-P and M-L velocity kymographs (Figures 1C, 1E) and of the associated standard variation kymographs (Figures 1D, 1F).

Thorax flows towards the anterior starts at 19hAPF, and are marked by an acceleration phase from 19hAPF to 24hAPF, and a deceleration phase from 24hAPF to 35hAPF (Figure 1C). Interestingly, thorax A-P velocity is patterned along the A-P axis. From 19hAPF to 35hAPF, A-P velocities decrease from $\text{Position}_{\text{AP}}=25\%$ to $\text{Position}_{\text{AP}}=140\%$ and increase from $\text{Position}_{\text{AP}}=0\%$ to $\text{Position}_{\text{AP}}=25\%$. The spatio-temporal pattern of A-P velocities is reproducible from an animal to another, as revealed by the low standard deviation of A-P velocities among the imaged animals (Figure 1D).

A pattern of M-L velocities can also be observed (Figure 1E), although M-L velocities are globally smaller than A-P velocities, indicating that thorax flows are mainly directed towards the anterior. Nevertheless, from 14hAPF to 20hAPF, thorax cells flow towards the lateral regions, especially next to the head-to-thorax boundary ($\text{Position}_{\text{AP}}=0-25\%$) and in the scutellum ($\text{Position}_{\text{AP}}=125-160\%$). From 20hAPF to 35hAPF, thorax cells displacement tends to be directed towards the midline ($\text{Position}_{\text{AP}}=0-140\%$). The spatio-temporal pattern of M-L velocities is reproducible from an animal to another, as revealed by the low standard deviation of M-L velocities among the imaged animals (Figure 1F).

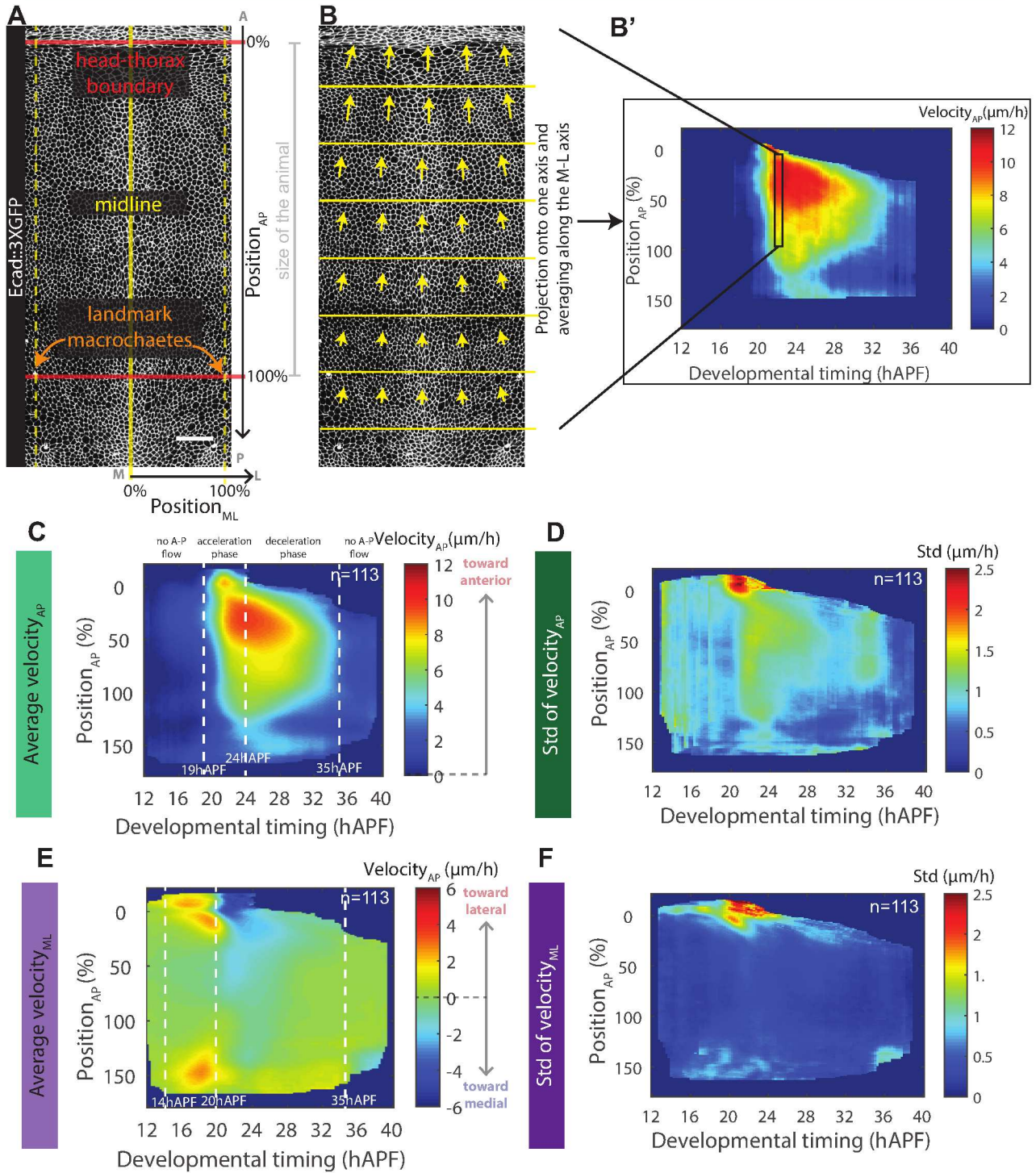


Fig.1. Thorax flow shows a reproducible pattern. Picture of dorsal thorax at 18hAPF, labelled with *Ecad::3XGFP*, and illustration of the location of the spatial landmarks used for registration (**A**). Illustration of PIV calculation, yellow arrows represent velocity vectors, note that the real PIV box used in this study is smaller than in the illustration (16X0.322 μ m, **B**). To generate velocity kymographs, for each time-point, velocity vectors were averaged along the M-L axis and projected either onto the A-P or onto the M-L axis, leading to the obtention of a column of velocities along the A-P axis for one time-point. When concatenating these columns for all analyzed time points, we can build a velocity kymograph (**B'**). Average kymograph of A-P velocity (**C**), and its associated standard deviation kymograph (**D**). Average kymograph of M-L velocity (**E**), and its associated standard deviation map (**F**).

A: Anterior, P: Posterior, M: Medial, L: Lateral, n: number of analyzed animals, Std: standard deviation.

The presence of velocity gradients across the tissue implies the existence of patterned tissue deformation during thorax flow. We have thus analyzed tissue deformation during thorax flow based on our PIV analysis. In concordance to displacement patterns, we have found that the anterior thorax tissue stretches ($\text{Position}_{\text{AP}}=25\text{-}140\%$) and locally contracts ($\text{Position}_{\text{AP}}=0\text{-}25\%$) along the A-P axis (Figure 2A), while it globally contracts along the M-L axis ($\text{Position}_{\text{AP}}=0\text{-}140\%$, Figure 2C). What is more, A-P and M-L deformations are reproducible from an animal to another, as revealed by the low standard deviations among imaged animals (Figures 2B, 2D).

Taken together, these data show that anterior thorax flow and deformation are spatio-temporally patterned. These patterns can be quantitatively described using PIV, and are reproducible from an animal to another.

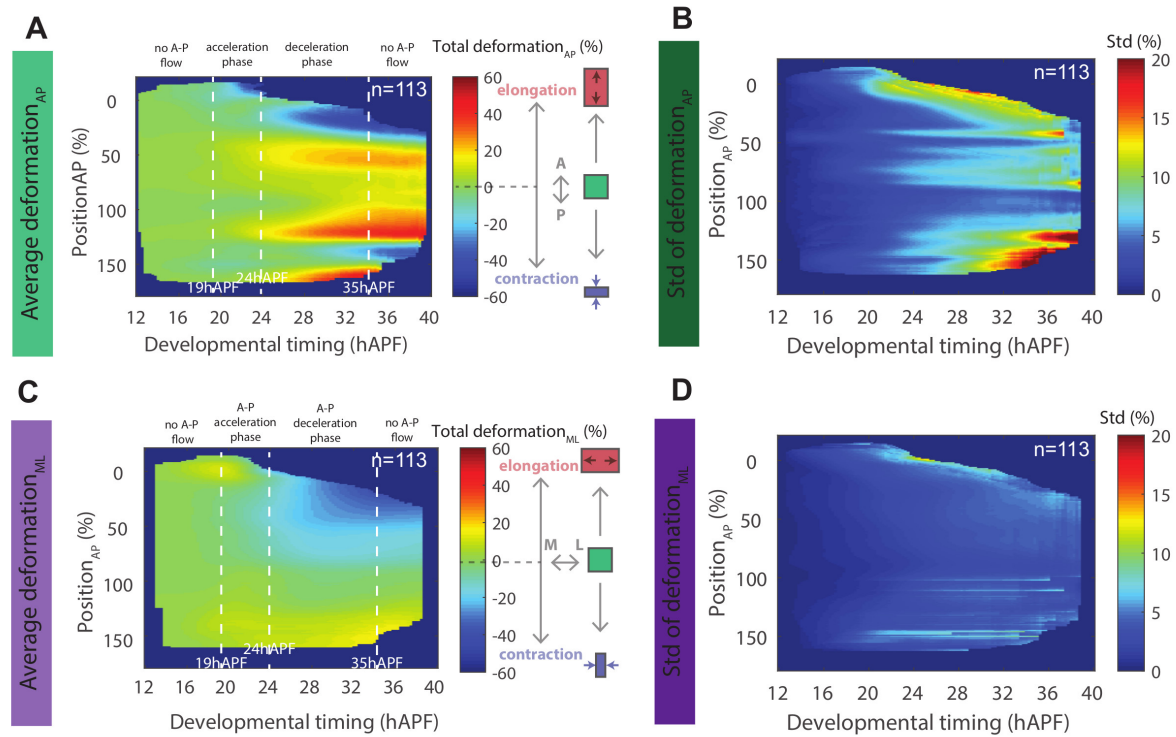


Fig.2 : Thorax tissue deforms while flowing. Average kymograph of cumulative A-P deformation (A), and its associated standard deviation kymograph (B). Average kymograph of cumulative M-L deformation (C), and its associated standard deviation kymograph (D).

n: number of analyzed animals, Std: standard deviation.

Thorax flow is only anteriorly coupled with head-to-thorax interface invagination

The anterior edge of the dorsal thorax is bordered by the epidermis of the head segment. We have shown in part1 that the head-to-thorax interface actively invaginates, starting at 20hAPF (Figure_{part1} 1B). By performing imaging of pupae expressing the cell contours marker *Ecad::3XGFP*, we were able to image initial neck bending together with anterior thorax flow (Figure 3A). Interestingly, both neck indentation speed and neck leading edge deepening speed highly correlate with anterior thorax cells A-P velocity (Figure 3B-D). Such a synchrony led us to the hypothesis that neck invagination may provide a pulling force driving thorax flows dynamics. Under this assumption, disrupting neck invagination should have an impact on thorax flows dynamics.

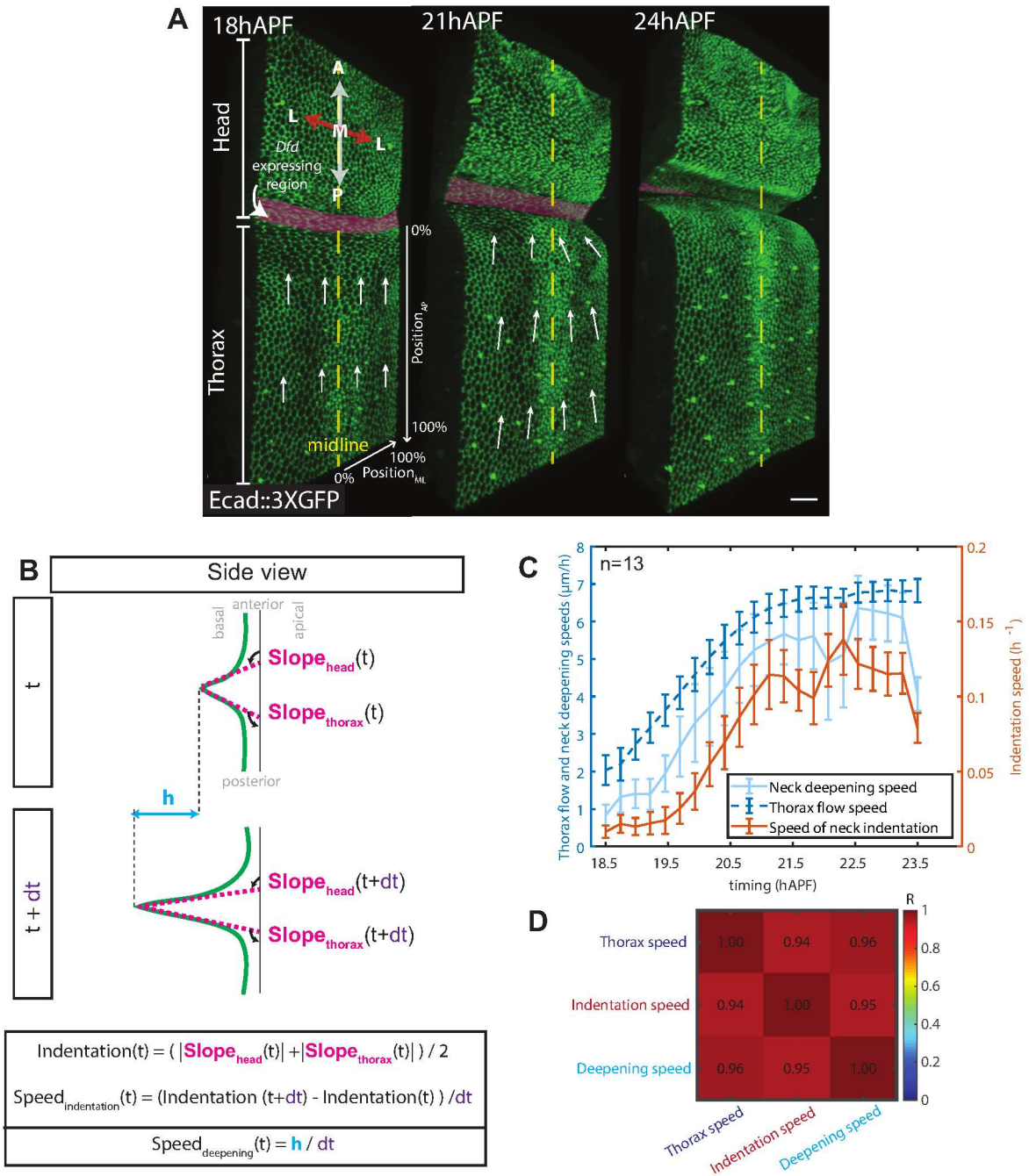


Fig.3. Thorax flow is coordinated with neck invagination. Timelapse imaging using Ecad::3XGFP as a marker reveals that thorax flow toward the anterior is synchronized with progressive neck invagination, scale bar: 30 μm . White arrows represent displacement vectors between each frame (A). Extraction of maximal slopes along the antero-posterior axis of the apical plane of neck region. Extraction of the depth of the leading edge of invagination. Calculation of neck indentation based on maximal slopes on the head and the thorax sides. Calculation of speeds of neck indentation and of neck leading edge deepening (B). Average curves of neck indentation speed, neck leading edge deepening speed and anterior thorax flow (averaged for Position_{AP}=0-25%), error bars represent standard error to the mean (C). Correlation matrix of thorax speed, neck indentation speed and neck leading edge deepening speed (D).

A: Anterior, P: Posterior, M: Medial, L: Lateral, n: number of analyzed animals.

In order to test the influence of neck invagination on thorax flow, we have used laser ablation to mechanically uncouple neck and thorax tissues. Repeated ablation of the neck region was performed prior to invagination, and repeated from 18hPF to 35APF every 3h, in order to kill neck cells and to prevent wound closure (Ablation_{neck}, Figure 4A). We have noticed that cells located next to the wound (Position_{AP}=0-10%, Figures 4B) are immobilized, likely due to wound healing processes trying to close the wound invoked by the ablation. As a result, this immobilized anterior thorax edge represents a physical linear obstacle for tissue flows. Interestingly, even if it faces the immobilized edge, tissue located at Position_{AP}=10-25% still moves towards the anterior (Figures 4A-B). When compared to the control, Ablation_{neck} shows decreased A-P velocities only next to the ablation site (Position_{AP}=0-25%) from 18h to 20hAPF, and shows a gradient of A-P velocities decrease from 20hAPF to 35hAPF, reaching Position_{AP} up to 120% (Figure 4C). In concordance with this patterned decrease in A-P velocities, higher A-P compression rates are observed next to the ablation site (Position_{AP}=0-25%) from 18h to 20hAPF, and more posteriorly (Position_{AP}=25-120%) from 20hAPF to 35hAPF (Figure 4D). Accordingly, cells located next to the ablation site show very high A-P compaction (red dashed rectangles, Figures 4A-A'). We can thus conclude that thorax flow can still partially occur when thorax tissue is mechanically uncoupled from neck invagination, and when its anterior edge is artificially immobilized. As the decrease in A-P velocity for Position_{AP}>50% are in average of 25%, we conclude that the pulling force associated with neck invagination is mostly dispensable for thorax flow in the posterior thorax. Nevertheless, whether the long-range partial decrease of A-P velocities observed in Ablation_{neck} can be attributed to (i) the absence of neck invagination or to (ii) the introduction of a physical obstacle at the anterior edge of the thorax is unclear.

In order to distinguish between these two possibilities, we have quantified thorax flow in a context of less severe inhibition of neck invagination. We have shown in part1 that neck invagination leading edge deepening speed is delayed in *Dfd>Rok^{RNAi}* and *Dfd>sqh^{RNAi}*, and is precocious and faster in *Dfd>Mbs^{RNAi}* (Figure_{part1} 7B): These three genetic conditions are thus well-suited to quantify the impact of defects in neck invagination dynamics on thorax flows without introducing a physical obstacle at the anterior edge of the thorax, thus complementing neck repeated ablation experiment.

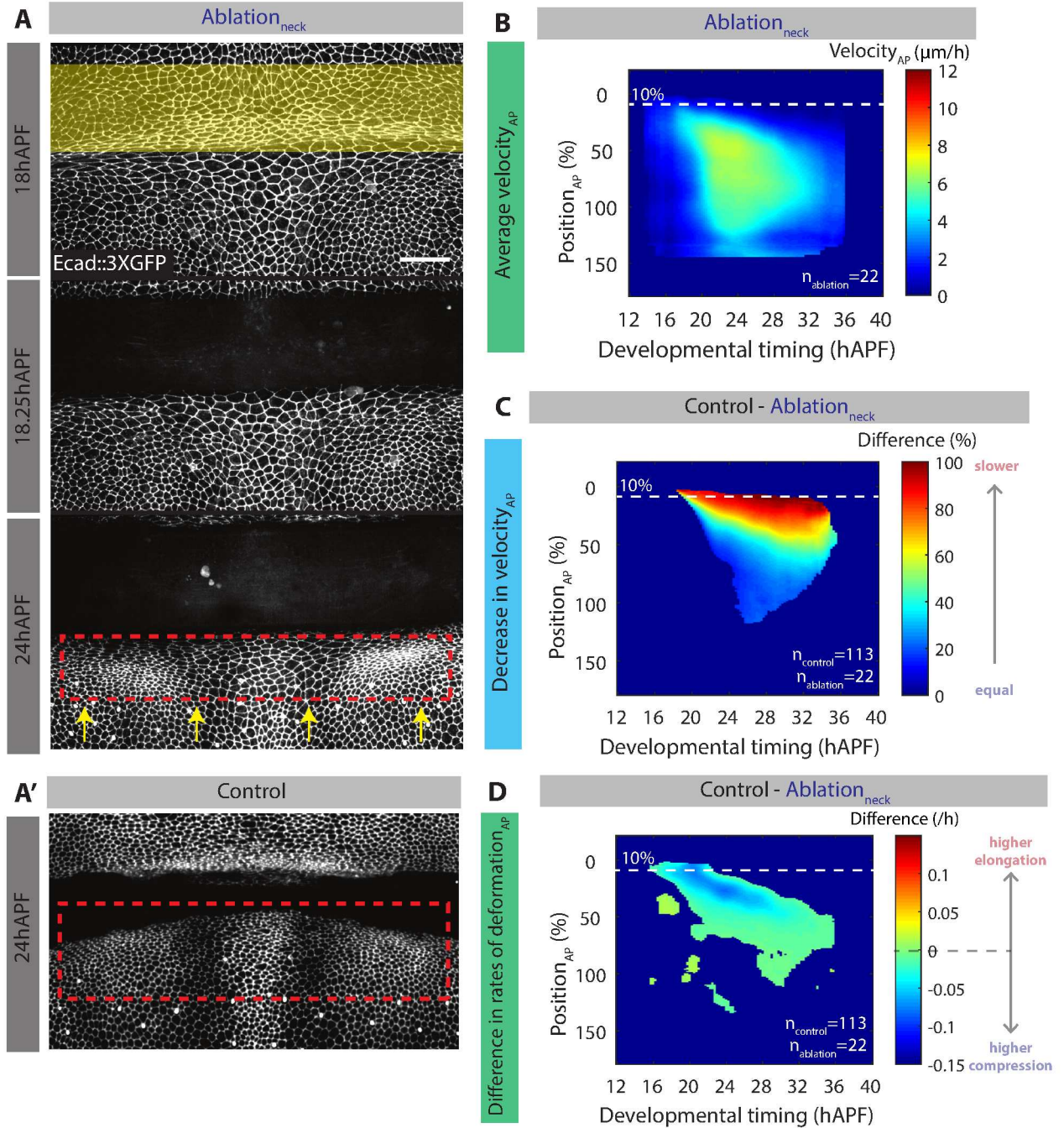


Fig.4: Repeated neck ablation does not abrogate thorax flow. Neck region was ablated around 18hAPF, and ablation was repeated every 3 hours, yellow region corresponds to the ablated region. This treatment leads to the immobilisation of the cells neighbouring the wound, yet thorax tissue still flows toward the anterior, yellow arrows represents thorax cells displacement, red dashed rectangle highlights the region of high cell A-P compaction (**A**). Picture of a control pupa, red dashed rectangle highlights the same region as in Figure A. Note that cells in the red dashed rectangle region are more compacted along the A-P axis in Neck_{ablation} when compared to the control (**A'**). Average A-P velocity kymograph of Neck_{ablation} (**B**). Kymograph of difference in A-P velocity between control and Neck_{ablation} (**C**). Kymograph of difference in A-P deformation rate between control and Neck_{ablation} (**D**).

$n_{control}/n_{ablation}$: number of animals in the control/Ablation_{neck} sample.

In $Dfd>Rok^{RNAi}$ and $Dfd>sqh^{RNAi}$, A-P velocities are reduced of approximately 40% as compared to the control in the region adjacent to the neck ($Position_{AP}=0-25\%$, Figures 5A, 5C). However, A-P velocity are globally unaffected for $Position_{AP}$ superior to 25% prior to 25hAPF. In concordance with these flow defects, higher compression rates can be observed for $Position_{AP}=0-25\%$ in $Dfd>Rok^{RNAi}$ and $Dfd>sqh^{RNAi}$ (Figures 5B, 5D). Furthermore, segmentation of cell contours in this region revealed a higher cell aspect ratio and an apical cell shape anisotropy oriented more in parallel to the M-L axis in $Dfd>Rok^{RNAi}$ at 24hAPF (Figures 6A, 6C and 6D). Taken together, these results show that neck invagination speed decrease in $Dfd>Rok^{RNAi}$ and $Dfd>sqh^{RNAi}$ triggers a local flow speed reduction next to the invaginating region, without globally affecting thorax flows for $Position_{AP}>25\%$. This patterned decrease in flows speed triggers cell compaction along the A-P axis, leading to local tissue compression for $Position_{AP}=0-25\%$. We can thus conclude that posterior regions are flowing independently of neck invagination pulling, as their A-P velocity is unaffected when decreasing neck invagination speed.

In $Dfd>Mbs^{RNAi}$, A-P velocities are increased of approximately 20% as compared to the control in the region adjacent to the neck ($Position_{AP}=0-25\%$) from 20hAPF to 23hAPF (Figures 4E). However, A-P velocity are globally unaffected for $Position_{AP}$ superior to 25% and after 23hAPF. In concordance with these flow defects, higher elongation rates can be observed for $Position_{AP}=0-25\%$ from 20hAPF to 23hAPF in $Dfd>Mbs^{RNAi}$ (Figures 4F). Furthermore, segmentation of cell contours revealed a lower cell aspect ratio and an apical cell shape anisotropy oriented more in parallel to the M-L axis in $Dfd>Mbs^{RNAi}$ at 22hAPF (Figures 5E-F). Taken together, these results show that neck invagination speed increase in $Dfd>Mbs^{RNAi}$ trigger a local flow speed increase next to the invaginating region from 20hAPF to 23hAPF, without globally affecting thorax flows for $Position_{AP}>25\%$. This patterned increase in flows speed triggers cell elongation along the A-P axis, leading to local tissue elongation for $Position_{AP}=0-25\%$.

Taken together, the analyses of $Dfd>Rok^{RNAi}$, $Dfd>sqh^{RNAi}$, $Dfd>Mbs^{RNAi}$ and $Neck_{ablation}$ show that neck invagination and thorax flow are locally coupled ($Position_{AP}=0-25\%$), and that neck invagination is likely providing a pulling force locally elongating cells along the A-P axis in this region. More posterior regions are, however, at least mostly flowing independently of neck invagination pulling.

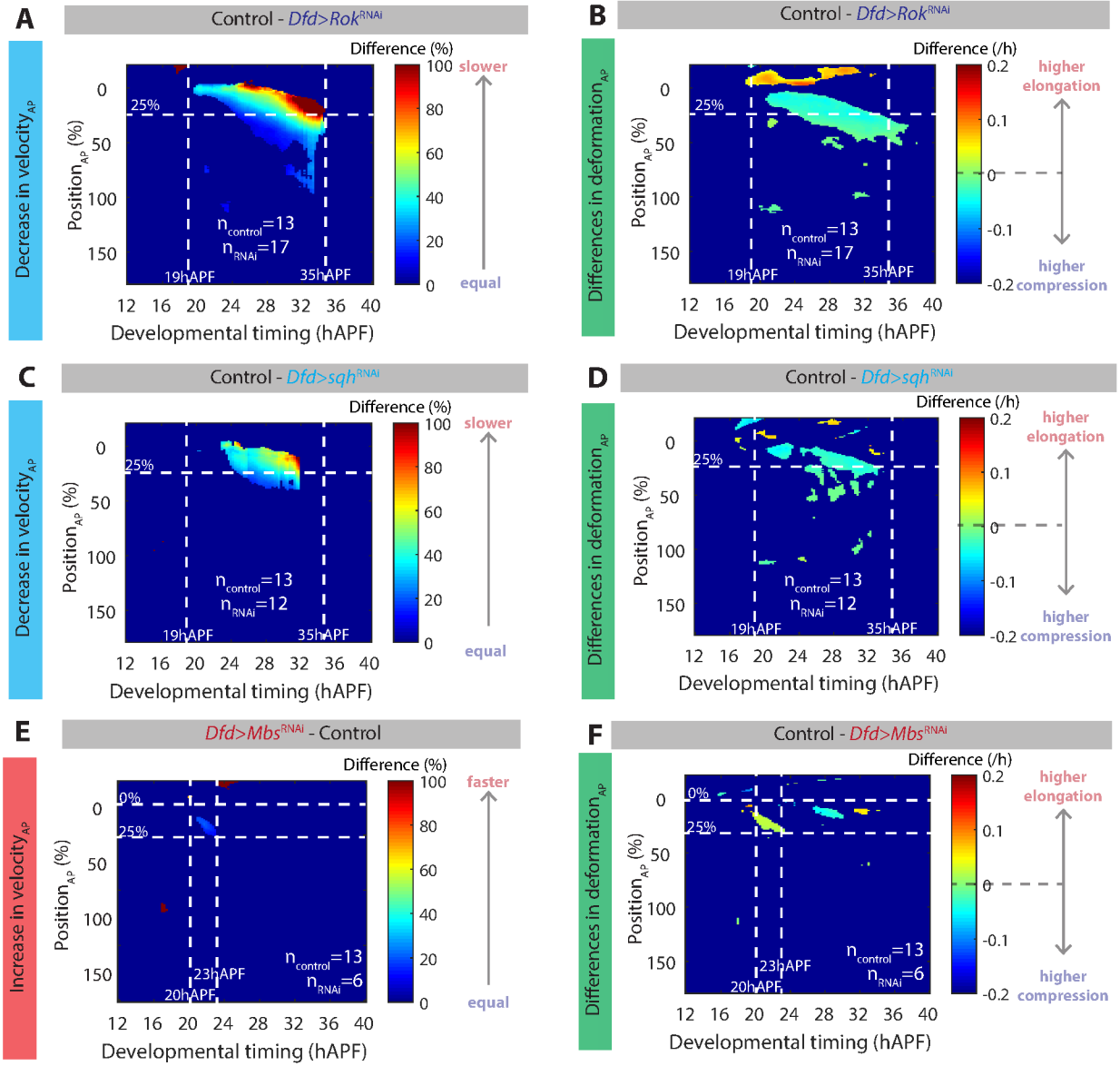


Fig.5: Defects in neck invagination speed trigger local displacements and tissue deformations changes in the anterior thorax. Kymographs of differences in A-P velocity between control and *Dfd>Rok*^{RNAi} (A), *Dfd>sqh*^{RNAi} (C) and *Dfd>Mbs*^{RNAi}, note that no reduction of A-P velocity was detected in *Dfd>Mbs*^{RNAi} and only increase in A-P velocities are shown (E). Kymographs of differences in tissue A-P deformations in *Dfd>Rok*^{RNAi} (B), *Dfd>sqh*^{RNAi} (D) and *Dfd>Mbs*^{RNAi} (F).

n_{control}/n_{RNAi}: number of analyzed animals in the control/RNAi sample.

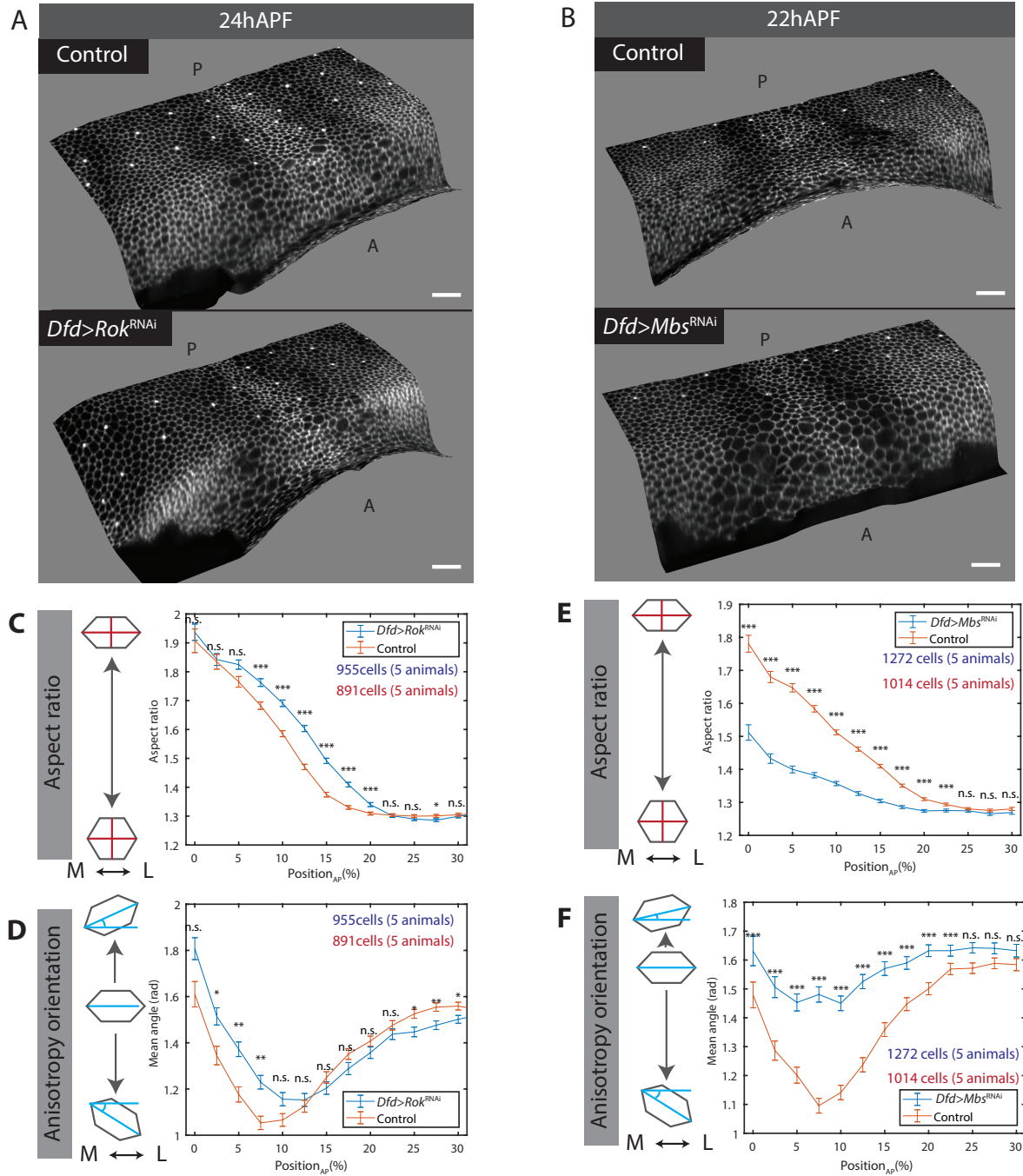


Fig.6: Defects in neck invagination speed trigger local cell shape changes in the thorax. 3D representation of cells labelled with Ecad::3XGFP in control and *Dfd>Rok^{RNAi}* at 24hAPF (**A**), and control and *Dfd>Mbs^{RNAi}* at 22hAPF, scale bars: 30μm (**B**). Quantification based on segmentation of cell contours of cell aspect ratio and cell shape anisotropy orientation in control and *Dfd>Rok^{RNAi}* at 24hAPF (**C**, **D**), and in control and *Dfd>Mbs^{RNAi}* at 22hAPF (**E**, **F**).

[(C), (D), (E) and (F)] Error bars represent standard error to the mean. Welch tests have been performed for each A-P position to compare the control and RNAi samples means.

Thorax A-P flow is mostly autonomous

Having established that thorax displacement is only anteriorly coupled with neck invagination, we wondered whether thorax flow, rather than stemming from an anterior pulling force, could stem from a posterior pushing force¹⁴⁸. In order to test this hypothesis, we performed repeated laser ablations in the posterior thorax (Ablation_{posterior}). Like in Ablation_{neck}, we noticed that cells next to the wound are immobilized in Ablation_{posterior} (Position_{AP}=90-100%, Figure 7A), likely due to wound healing processes trying to close the wound invoked by the ablation. Interestingly, in Ablation_{posterior}, A-P velocity is unaffected for Position_{AP}=0-50%, and a gradient of decrease in A-P velocity is observed for Position_{AP}=50-100% (Figure 7A). Accordingly, higher A-P elongation rates are observed in Ablation_{posterior} for Position_{AP}=50-100% (Figure 7B), and cells in this region show higher A-P elongation (Figure 7C). These results show that anterior thorax flow (Position_{AP}=0-50%) is independent from coupling with posterior thorax. Furthermore, we have combined the anterior and posterior ablations (Ablation_{neck+posterior}). The effect of this double ablation on A-P velocities equals to the sum of the effects of the two ablations performed in isolation (compare Figures 7D and 7E). Interestingly, more than half of thorax flow towards the anterior is still observed in Ablation_{neck+posterior} (Position_{AP}=25-75% before 30hAPF, Figure 7D, pink dashed region), even in anterior and posterior edges are immobilized. Therefore, A-P thorax flow is mostly independent from an anterior pulling force and a posterior pushing force.

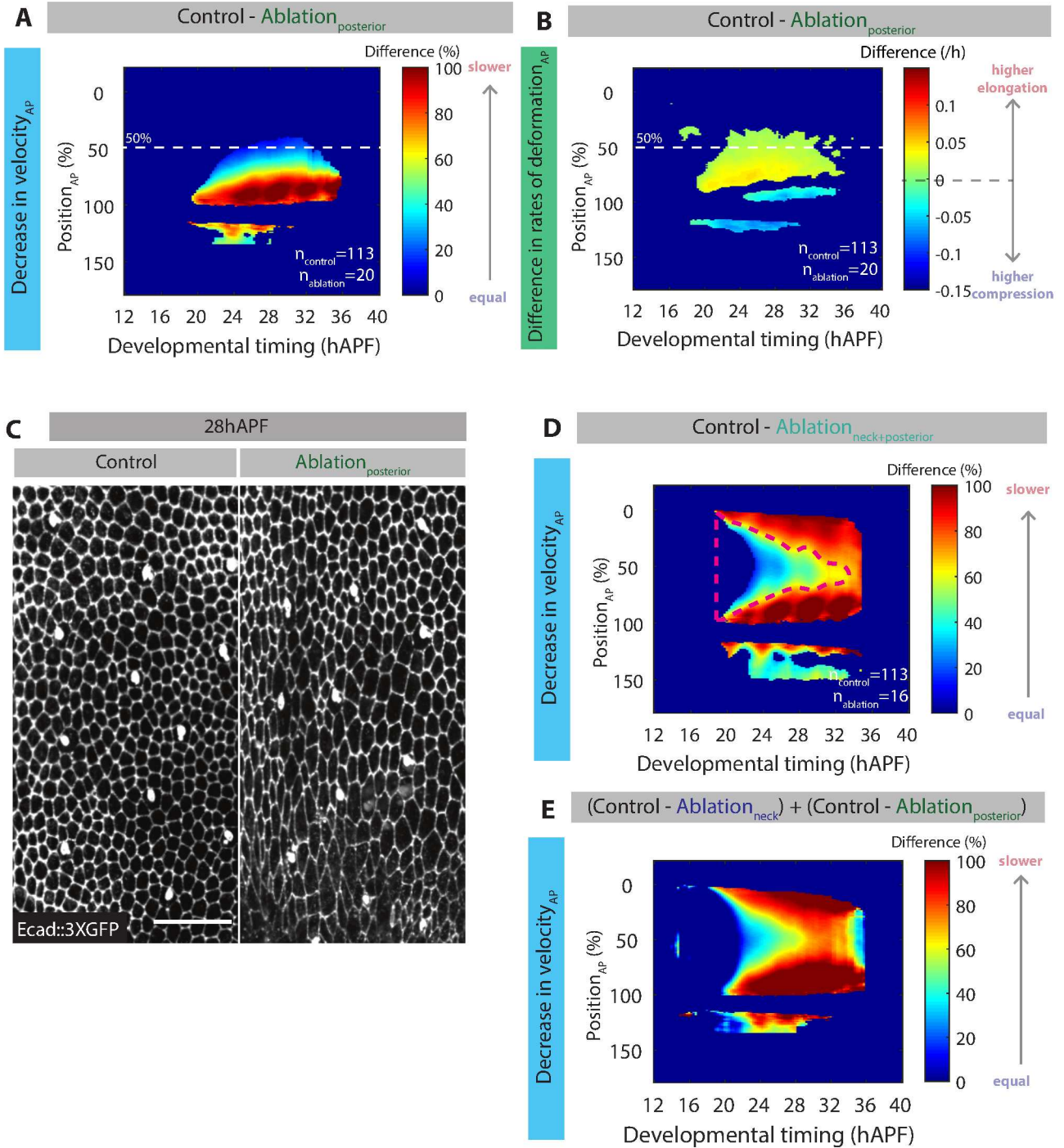


Fig.7: Repeated posterior thorax ablation only locally affects thorax flow. Kymograph of difference in A-P velocity between control and Ablation_{posterior} (A). Kymograph of difference in A-P deformation rate between control and Ablation_{posterior} (B). Tissue stretching due to the asymmetry of A-P velocity between anterior tissue and posterior tissue immobilized by the wound triggers high cell apical A-P stretching next to the ablation site which can be visualized using Ecad::3XGFP marker, scale bar: 25μm, regions of comparable coordinates are here shown (Position_{AP}=50-100%, C). Kymograph of difference in A-P velocity between control and Ablation_{neck+posterior}, pink dashed line outlines the region still showing flow toward the anterior (D), Sum of the kymograph of (i) difference in A-P velocity between control and Ablation_{neck} (Figure 6C) and (ii) the kymograph of difference in A-P velocity between control and of Ablation_{posterior} (Figure 7A). Note the close resemblance with Figure D (E).

n_{control}: number of animals in the control sample, n_{ablation}: number of animals in the ablation sample.

Finally, we have tested whether thorax flow might be dependent on flanking lateral tissues ($\text{Position}_{\text{ML}} > 75\%$). Our analyses of M-L thorax flows demonstrated a small flux of lateral cells towards the midline (Figure 1E) and accordingly a convergent extension occurring in the medial thorax domain (Figures 2A and 2C). Although the magnitude of this M-L flow is small and unlikely to contribute significantly to the A-P flow, we nevertheless tested whether the lateral domains could provide a squeezing force driving thorax cells to flow towards the anterior. Downregulation of *Rok* or *Mbs* expression, using the lateral driver *mirr::GAL4* (*mirr>Rok^{RNAi}* and *mirr>Mbs^{RNAi}*, Figure 8A), resulted in changes in M-L flow dynamics (Figures 8B-D). In *mirr>Rok^{RNAi}*, thorax displacement orientation is displaced towards the midline (compare Figures 8B and 8C, Figure 8E), triggering M-L compaction of the medial tissue, which is maximal in the midline region (compare Figure 8F and 8G). On the contrary, in *mirr>Mbs^{RNAi}* thorax cell displacement is slightly displaced towards the lateral sides (compare Figure 8B and 8D, Figure 8E), and a small M-L elongation of the medial tissue was observed (compare Figure 8F and 8H). Despite these changes in M-L flows, both *mirr>Rok^{RNAi}* and *mirr>Mbs^{RNAi}* did not impair flows velocity along the A-P axis (Figure 9), showing that, respectively, down and up regulation of MyosinII contractility in the lateral domain does not impact on A-P flow. Thus, lateral contractility is required for medial domain deformation along M-L axis, yet is dispensable for A-P flows. These findings further corroborate the notion that thorax A-P flow constitutes an active and autonomous process.

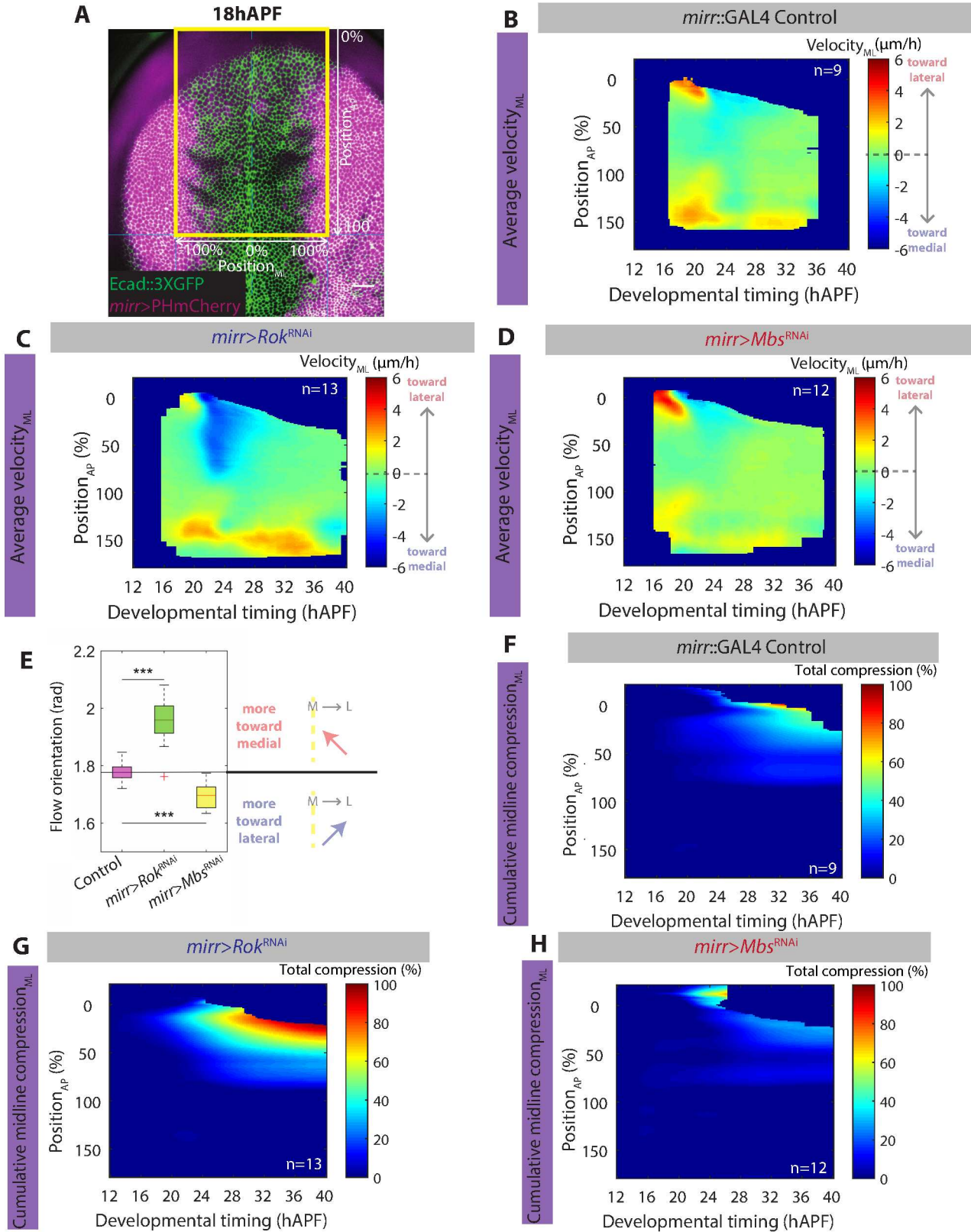


Fig.8: Lateral domains contractility regulates thorax flow along the M-L axis. *mirr::GAL4* is specifically expressed in the lateral domains (A). Average kymographs of M-L velocity for the control sample (expressing *mirr::GAL4*, B), *mirr>Rok^{RNAi}* (C) and *mirr>Mbs^{RNAi}* (D). Distribution of global orientation of thorax flow 18hAPF to 30hAPF in control, *mirr>Rok^{RNAi}* and *mirr>Mbs^{RNAi}*, ANOVA tests for circular data have been performed to compare control with RNAi samples (E). Average kymographs of cumulative M-L compression on the midline region (Position_{ML}=0-50%) for the control sample (F), *mirr>Rok^{RNAi}* (G) and *mirr>Mbs^{RNAi}* (H).

n: number of analyzed animals

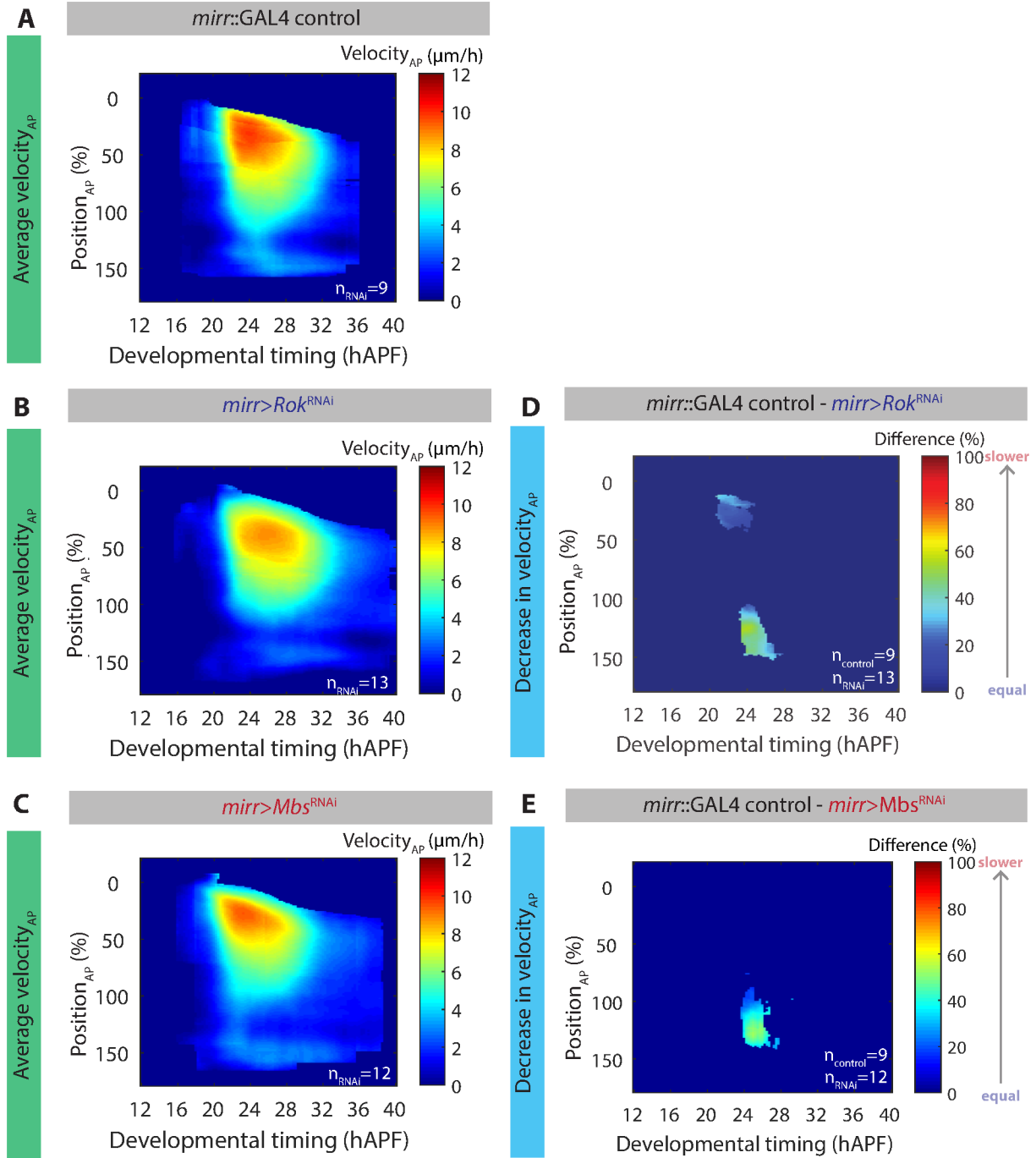


Fig.9: Lateral domains contractility does not affect thorax flow along the A-P axis. Average kymographs of A-P velocity for the control sample (A), *mirr>Rok^{RNAi}* (B) and *mirr>Mbs^{RNAi}* (C). Significant difference in A-P velocity between control and *mirr>Rok^{RNAi}* (D) and between control and *mirr>Mbs^{RNAi}* (E). Note the very mild and localized effect of *mirr>Rok^{RNAi}* and *mirr>Mbs^{RNAi}* on A-P flows.

$n_{control}$: number of animals in the control sample, n_{RNAi} : number of animals in the RNAi sample.

Interaction with the apical ECM is necessary for thorax flow

To enable active and collective tissue displacement, epithelial cells can not only interact with neighboring epithelial cells, but also with their extracellular environment¹⁹⁵, with cells either migrating on another tissue layer^{196,177}, on the apical⁷⁴ or on the basal ECM¹⁹⁷. To identify the substratum used by thorax cells to migrate, we have analyzed these three possibilities.

First, *Drosophila* dorsal epidermis tissue constitutes a mono-layered epithelium and no additional epithelial or mesenchymal tissue layers are present underneath or above it. The basal surface of the dorsal epidermis is mainly in contact with the hemolymph, a viscous internal milieu that is unlikely to serve as a migration substratum. However, lateral indirect flight muscles are locally in contact with the basal surface of the epidermis and could constitute a substratum for its migration. To test the role of indirect flight muscles in epidermis morphogenesis, we have laser-ablated them prior to thorax flow (Ablation_{muscles}), and have recorded epidermis morphogenesis. No defect of thorax flow was detectable in Ablation_{muscles} (Figure 10A), ruling out the hypothesis of a migration of epidermal cells on lateral indirect flight muscles.

Second, we have analyzed whether thorax cells could use the basal ECM as a substratum. If cells migrate on their basal surface, they must propagate their motion across their cell body to trigger an apical movement. Under the assumption of a basal migration, we thus reasoned that basal sides of the cells should point towards the direction of apical motion and pull the cell from basal to apical, while a mechanism involving a transmission of basal motion through a pushing force from basal to apical seems unlikely (Figure 10D). Using a mosaic expression of LifeAct::Ruby to mark cell bodies in small cell patches, we assessed 3D cell shape at 25hAPF (Figure 10B). Surprisingly, all the basal domains of anterior thorax cells (Position_{AP}=0-120%) point in the opposite direction of thorax apical flow (Figure 10C). This result suggests that thorax cells are unlikely to migrate on the basal ECM.

Finally, the thorax epidermis is apically covered by the pupal cuticle. Imaging ChtVisTomato, a live reporter of apical matrix chitin¹⁹⁸, and LifeAct::GFP as a reporter for the epidermal cells (Figure 10E), we noticed that the medial thorax (Position_{AP}=10-110%, Position_{ML}=0-125%) remains in close contact with the chitin-rich layer of the cuticle in the anterior domain during thorax flow, while the posterior tissue (Position_{AP}=110-160%) and the lateral tissues (Position_{ML}=180-250%) progressively move away from the chitin-rich layer of the cuticle (Figures 10F-H). Thus, the apical ECM could represent a substratum for the migration of thorax cells in at least most of our region of interest (Position_{AP}=10-110%, Position_{ML}=0-100%).

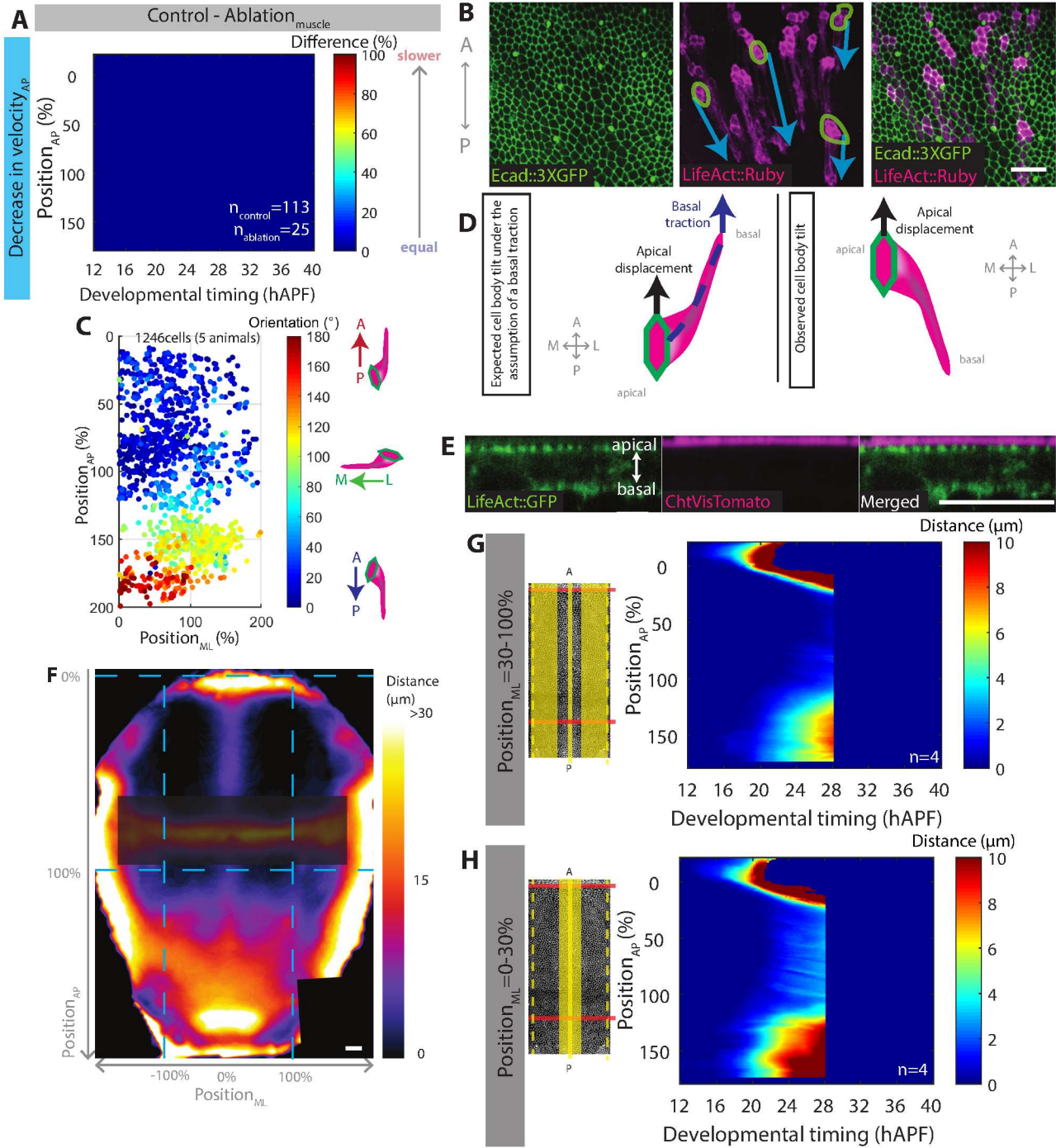


Fig.10: Thorax cells are more likely to use apical than basal ECM for migration. Average kymograph showing no difference in A-P velocity between control and muscle-ablated pupae (**A**). Maximum projection of a hyperstack covering the whole thickness of the tissue in which cells are mosaically labelled with LifeAct::Ruby reveals cell body tilt pattern, green circles outline apical cell domain, and dashed arrows represent cell body tilt (**B**). Map of orientation of cell body tilt, note that the the region of interest (Position_{AP}=0-125%, Position_{ML}=0-125%) only contains cells pointing toward the posterior (**C**). Basal migration is likely to trigger a cell body tilt in the same direction as apical flow, in order to propagate basal traction to the adherens junction level through the cell body. However, we observe a cell body tilt in the opposite direction (**D**). Sagittal view of anterior thorax tissue at 28hAPF. ChtVisTomato, a live reporter of chitin, labels chitin-rich layer of the pupal cuticle, while LifeAct::GFP labels the tissue (**E**). Distance between apical tissue surface labelled with LifeAct::GFP and basal surface of the chitin-rich layer of the cuticle labelled with ChtVisTomato at 28hAPF, blue dashed lines represent spatial landmarks, dark rectangle corresponds to a region marked by an artificial fold induced by mounting (artificial folds have been filtered out for analysis, **F**). Average kymographs showing the distance between tissue and the chitin-rich layer of the cuticle for Position_{ML}=30-100% (**G**), and for Position_{ML}=0-30% (**H**).

[(A), (D) and (E)] Scale bars: 25μm. [(F) and (G)] n: number of analyzed animals.

To test whether the apical ECM is required for thorax flow, we developed an *ex vivo* system enabling the usage of pharmacological treatments. In brief, pupae are dorsally glued on a glass, put in S2 medium, ventral tissues are dissected out and internal organs and trachea are removed (Figure 11A). Upon addition of ecdysone in the medium, thorax cells show collective displacement for approximately 10 hours, albeit with a reduced velocity as compared to *in vivo* flows (Figure 11B). To test whether apical ECM is required for the flow to occur, we incubated explants with a mix of chitinase and N-actetylglucosamidase (hereafter called “chitinase mix”) which is known to digest chitin in the cuticle in similar *ex vivo* set-ups used for pupal wings culture¹⁹⁹. Interestingly, thorax flow velocity decreased 2-to-3 fold when the tissue was cultured in 17mU/mL chitinase mix, while thorax flow was completely abrogated in 100mU/mL chitinase mix, and the tissue detached from the cuticle (Figure 11C, D).

Taken together, our data indicate that thorax cells adhere to the apical ECM and most likely use it as a substratum for migration.

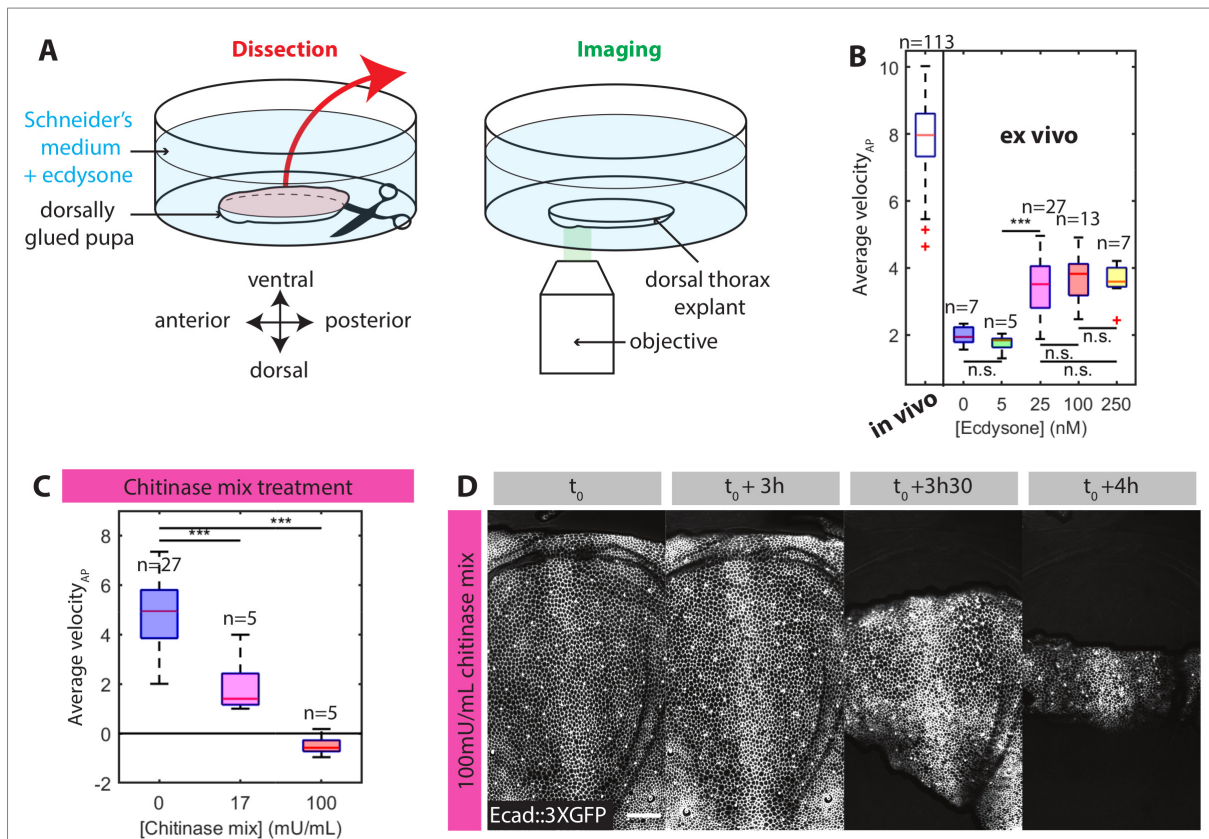


Fig.11 : The apical ECM is required for thorax flows *ex vivo*. Dorsal thorax explants are dissected in Schneider's medium supplemented with ecdysone and imaged (**A**). Average A-P velocity of explants exposed to different ecdysone concentrations, and corresponding A-P velocity *in vivo* (**B**). Average flow speed of explants exposed to different chitinase/N-acetylglucosamidase mix concentrations. Ecdysone concentration was set to 25nM (**C**). Representative detachment and collapse phenotype of the explants exposed to [chitinase mix] 100mU/mL, scale bar: 25μm (**D**).

[(**B**) and (**C**)] A-P velocities were averaged for the first 8h of incubation for a region of interest (Position_{AP}=0-100%, Position_{ML}=0-100%). Time-points showing tissue detachment have been filtered out. [(**B**) and (**C**)] Welch tests have been performed to compare means for given concentrations.

Dorsal thorax cells interact with the apical ECM using adhesive polarized apical protrusions

The polarized emission of protrusions can promote cell migration¹⁹⁷. We thus aimed at identifying whether thorax cells were emitting polarized protrusions while they flow. By imaging clones of cells expressing LifeAct::Ruby in a background of Ecad::GFP3X expression, we found that thorax cells display apical protrusions above the adherens junction domain (Figure 12A). These protrusions mainly look like filopodia and lamellipodia, and are very dynamic (with dynamics in the range of tens of seconds). Interestingly, apical protrusions are enriched at the anterior side of the cells and are almost absent at the posterior side of the cells (Figure 12A). By performing a polar analysis of the spreading of the LifeAct::Ruby signal outside the outline of the cells labelled with Ecad::3XGFP, we can derive a vector indicating the direction and the intensity of protrusion polarity (see C/11 section in Material & Methods). The higher the amplitude of the vector, the longer and more polarized the protrusions are (Figures 12A, blue arrow). This polar analysis can also be performed by analyzing the cortical intensity of LifeAct::Ruby, which provides the direction and the intensity of polarity of apical actin levels. Interestingly, both spreading and actin levels polarity scores show a pattern across the tissue at 25hAPF, with anterior thorax cells showing longer and more polarized protrusions than posterior thorax cells (Figure 12B-C). Interestingly, protrusion polarity field at 25hAPF strongly resembles thorax flow velocity field at 25hAPF (compare Figure 12B-C and Figure 12D). We also mapped protrusions polarity at 19hAPF (at the beginning of the acceleration phase) and at 29hAPF (during late deceleration phase). Noticeably, spreading polarity strongly correlates with thorax flow velocity at 19, 24 and 29hAPF (Figures 12E-E’'). We can thus conclude that thoracic cells show apical protrusive activity that is polarized towards the direction of thorax flow, and that the intensity of this polarized protrusive activity shows a pattern across the tissue that correlates with the velocity pattern. These data strongly suggest that apical protrusion could promote thorax cell migration on the apical ECM.

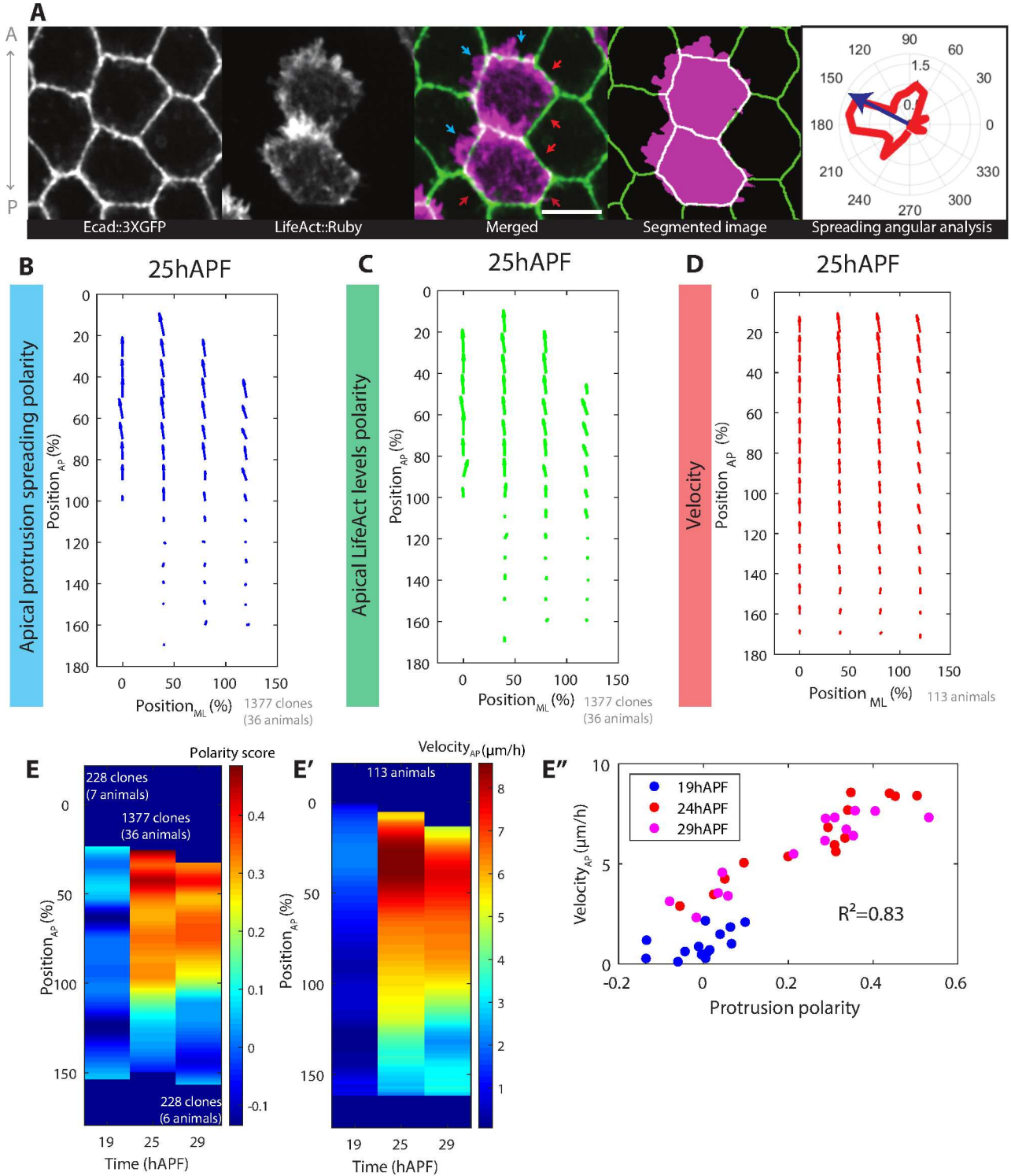


Fig.12: Polarized apical protrusive activity is patterned across dorsal thorax. Detection of adherens junction plane using Ecad::GFP3X and projection of the apical domain of the cells reveal the presence of apical protrusions at the front (blue arrows) but not at the back (red arrows) of anterior thorax cells. Segmentation of Ecad::GFP3X and LifeAct::Ruby signals enable the extraction of the angular distribution of spreading of actin beyond adherens junction outlines, and of a polarity vector of spreading (blue arrow), scale bar: 5μm (**A**). Quantification of polarity of apical protrusion spreading over Ecad::3XGFP contours at 25hAPF (**B**), of polarity of apical cortical LifeAct::Ruby levels at 25hAPF (**C**) and of thorax flow velocity (**D**). Kymograph of A-P component of spreading polarity (**E**) and kymograph of A-P velocity (**E'**) reveal a high correlation both in time and in space between protrusion polarity and A-P velocity, when plotting A-P velocity and A-P polarity scores averaged for A-P forks of 10% (**E''**).

We reasoned that if these apical protrusions were used by the cells to exert forces on the ECM and allow migration, they should be mechanically coupled to the ECM. To experimentally assess mechanical coupling between the apical domain of thorax cells and the apical ECM, we have designed an assay based on recoil after laser ablation in the adherens junction network. We have used pupae expressing Ecad::3XGFP and a mosaic labelling of LifeAct::Ruby to be able to visualize both adherens junctions and apical protrusions. We have performed ablation at the anterior of cells labelled with LifeAct::Ruby, at the level of the adherens junction network, in order to trigger a recoil of the cells towards the posterior without damaging labelled apical protrusions. We reasoned that if the apical protrusions are strongly attached to the apical ECM, apical protrusions should stretch upon recoil of the adherens junction network. Indeed, we observed that anterior protrusions stretch upon recoil in the anterior thorax (Figures 13A, 13C-D). Interestingly, laser ablations performed at the back of the cells triggers a recoil towards the anterior, but did not induce any stretching of the posterior protrusions (Figures 13B, 13C-D). Taken together, these results show that cells of the anterior thorax are anchored to the apical ECM, and that this anchoring is specifically located at the anterior pole of the cell. This result further suggests that thorax cells migrate on the apical ECM using polarized adhesive protrusions.

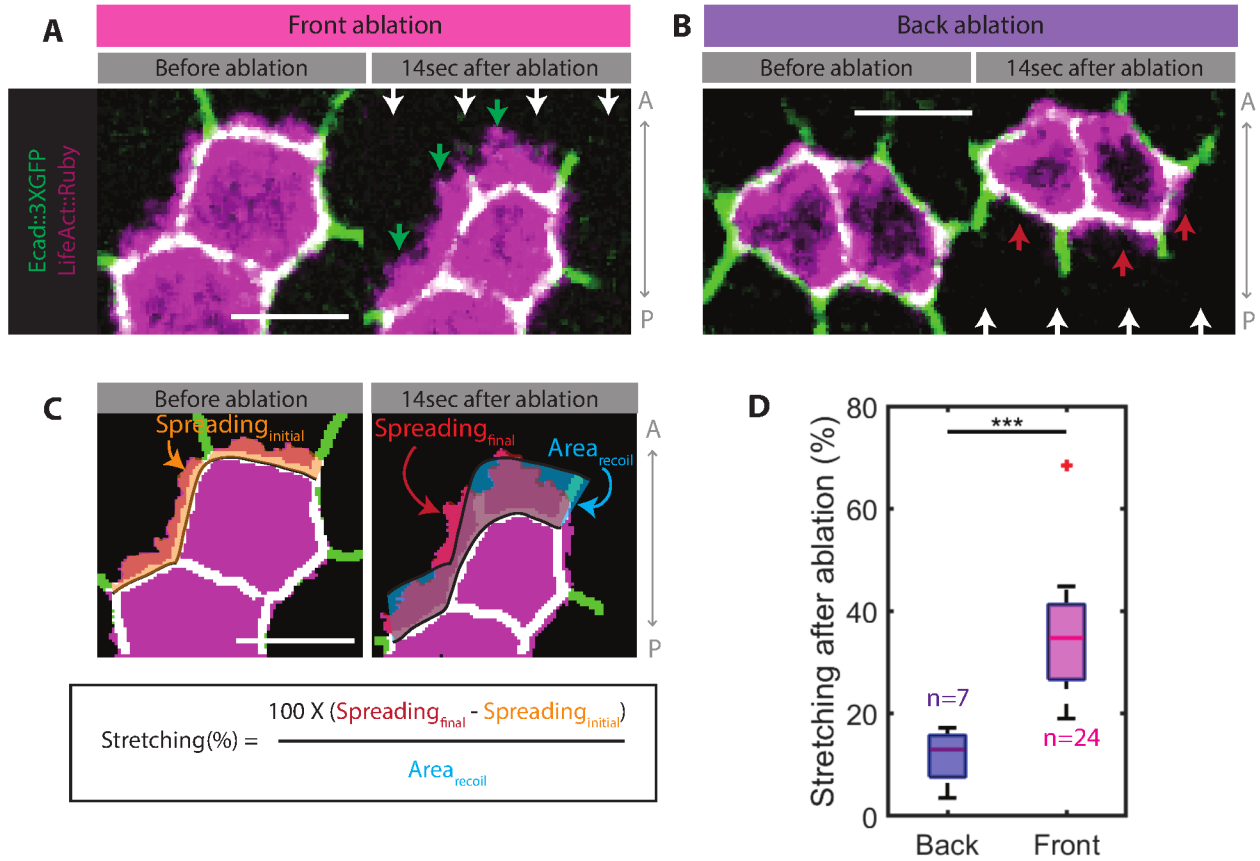


Fig.13: Cells are anchored to the apical ECM in a polarized manner. Ablation in the plane of the adherens junction network have been performed in front of clones of cells expressing LifeAct::Ruby, in a background of Ecad::3XGFP expression, inducing a backward recoil of the cells, and triggering a stretching of the apical protrusions (**A**). Ablations at the back of clones have also been performed, inducing a forward recoil of the cells, and triggering very low stretching of the apical domain (**B**). Quantification of stretching of protrusions after ablation (**C**). Stretching after front and back ablations performed in the anterior thorax ($\text{Position}_{\text{Ap}}=0-50\%$), a Welch test has been performed to compare mean stretching of front and back ablations, n: number of ablations (**D**).

[(A) and (B)] White arrows represent adherens junctions recoil after ablation, green arrows point at highly stretched protrusions, red arrows point at the very lowly stretched protrusions. [(A), (B) and (C)] Scale bars: $5\mu\text{m}$.

Core PCP pathway is locally required for migration and apical protrusions polarity

If polarized protrusions underlie thorax cells migration, disrupting their polarity should trigger defects in thorax flows. Polarization of protrusion emission is known to be regulated by planar polarity pathways activity^{59,74}. We have thus investigated the impact of planar polarity pathways on thorax flows and on apical protrusion emission. Planar polarity is well studied in *Drosophila* epidermis, and is known to rely on two major pathways: Ft/Ds pathway and core PCP pathway (fly orthologous of the atypical Wnt pathway)³⁶.

We have first studied the impact of Ft/Ds pathway, as this pathway is responsible for collective migration on the apical ECM in *Drosophila* larval abdominal cells⁷⁴. RNAi against *fat* or *dachsous* using *Act::GAL4* (*Act>ds^{RNAi}* and *Act>fat^{RNAi}*), or global overexpression of *four-jointed* (*Act>fj^{up}*, which triggers a flattening of Fj gradient and hence disrupts Ft/Ds pathway) only give rise to minor defects in thorax flow along the A-P axis (Figures 14A, 14C, 14E). Moreover, these small effects are mainly restricted to the edges of the migrating domain. Therefore, we can conclude that Ft/Ds pathway is not required for A-P thorax flow. Accordingly, planar cell polarity in the thorax does not appear as majorly disrupted in *Act>ds^{RNAi}*, *Act>fat^{RNAi}* and *Act>fj^{up}*, as microchaetes precursors are almost normally polarized along the A-P axis in these conditions (Figures 14G-I).

Supplementary data 1: Effect on Ft/Ds pathway on M-L flows

Disruption of *fat* and *dachsous* expression has been reported to disrupt tissue contraction along the M-L axis in a specific region of the posterior thorax from 17hAPF to 21hAPF⁴⁵. Accordingly, we have found a localized increase in flow towards the lateral sides in the same posterior thorax region (Position_{AP}=100-150%) from 18hAPF to 24hAPF in *Act>ds^{RNAi}*, *Act>fat^{RNAi}* and *Act>fj^{up}* (Figures 14B, 14D, 14F). Additionally, we have discovered a similar excess of flow towards the lateral sides from 17hAPF to 24hAPF in the anterior edge of the thorax (Position_{AP}=0-50%), next to the neck invagination site (Figures 14B, 14D, 14F).

However, unlike in the posterior thorax, the excess of flow towards the lateral sides in the anterior thorax is followed by an excess of flow towards the midline from 24hAPF to 35hAPF in *Act>ds^{RNAi}* and *Act>fat^{RNAi}* (Figures 14B, 14D, 14F). We hypothesize that this latter effect may be the consequence of neck M-L contraction during invagination. We thus propose that Ft/Ds pathway, in addition to its known role in promoting contraction⁴⁵ and global alignment⁵⁰, might be important to locally buffer M-L tissue flows by providing a resistive force to external contraction.

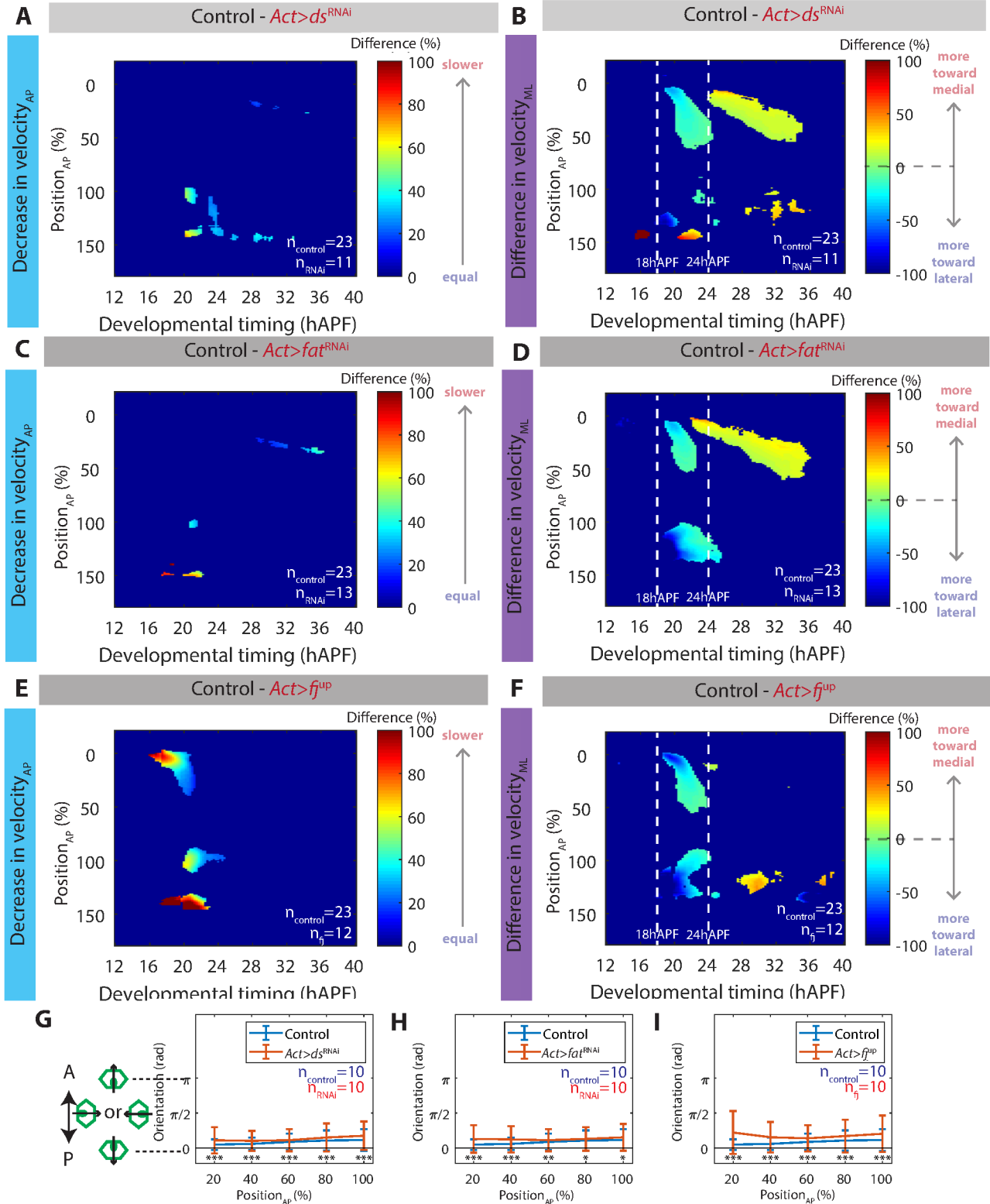


Fig.14: Ft/ds pathway is not required for A-P thorax flow, but locally buffers M-L flows. Average kymographs of difference in A-P velocity between control and *Act>ds^{RNAi}* (A), *Act>fat^{RNAi}* (B) and *Act>fj^{up}* (C). Average kymographs of difference in M-L velocity between control and *Act>ds^{RNAi}* (D), *Act>fat^{RNAi}* (E) and *Act>fj^{up}* (F). Orientation of microchaetes at 24h-28hAPF in *Act>ds^{RNAi}* (G), *Act>fat^{RNAi}* (H) and *Act>fj^{up}* (I).

[(G) to (I)] Error bars represent standard variation. Kolmogorov-Smirnov tests have been performed for each A-P position to test for a difference in orientation distribution between samples.

n_{control}/n_{RNAi}/n_{fj}: number of analyzed animals in the control/RNAi/*Act>fj^{up}* sample.

Next, we have assessed the role of the core PCP pathway in the polarization of apical protrusions and thorax cell flows. Dishevelled (Dsh) is a key actor of core PCP pathway, which is required for planar cell polarity in dorsal thorax. We hence investigated whether polarized apical protrusive activity was disrupted in *dsh¹* mutants. Interestingly, polarity scores of spreading of apical protrusions are globally lower in *dsh¹* than in the wild type, especially in the posterior thorax (compare Figure 12B and 15B). To distinguish between a loss of polarization or a randomization of the main axis of polarization, we have analyzed the variation of standard deviation of orientation of polarization as a function of the amplitude of polarization (Figure 15C). As expected for the wild type, polarity scores of low amplitude display random orientation. But when comparing wild type and *dsh¹*, it appeared that orientation of polarization tends to be more random in *dsh¹*, even for polarity scores of higher amplitudes (Figure 15C). Moreover, randomization of orientation is particularly prominent in the posterior thorax (Position_{AP}=50-100%, Figures 15D-D'). Taken together, this data indicates that the polarity of apical protrusive activity is more random in *dsh¹* than in the wild type.

Supplementary data 2: Rescue of *dsh¹* planar polarity defects

Dsh is known to be a pivotal regulator of planar polarity in the thorax before 20hAPF, as *dsh¹* triggers random orientation of the first division of microchaetes precursors before 20hAPF³⁵. Accordingly, we have found that microchaetes precursors show random orientations at 24hAPF (Figure 15A). However, we have as well discovered that microchaetes progressively realign during the migration phase, so that only mild microchaetes orientation defects can be observed at 32hAPF and 36hAPF (Figure 15A). We thus conclude that additional planar polarity cues may correct initial *dsh¹* planar cell polarity defects, and that thorax migration itself might participate in planar polarity defects correction (as tissue deformation is known to realign PCP orientation in the wing⁵⁴).

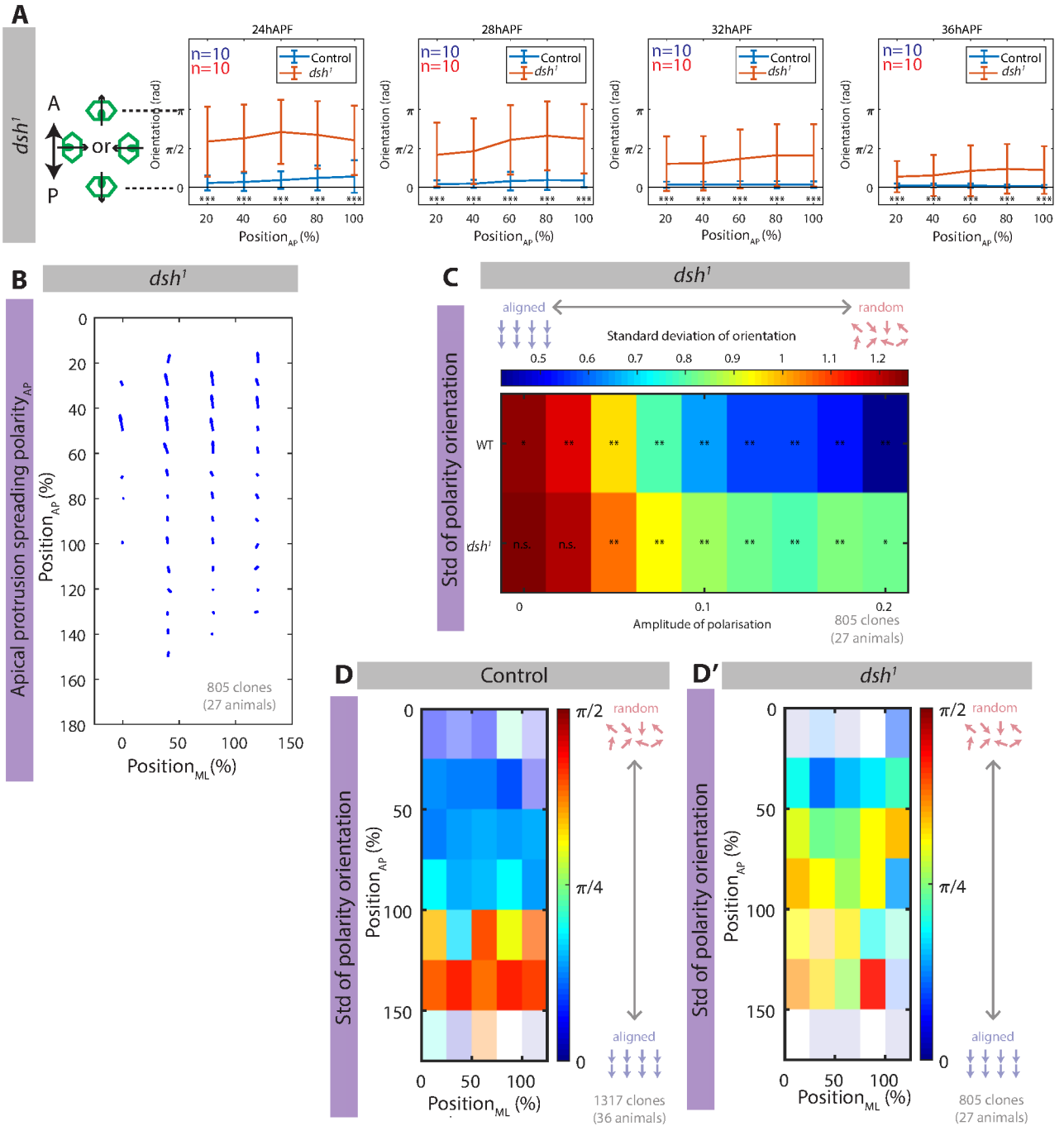


Fig.15: *Dishevelled* is required for proper planar polarization of apical protrusions. Orientation of microchaete at 24hAPF, 28hAPF, 32hAPF and 36hAPF in *dsh¹* mutant background, error bars represent standard deviation, Kolmogorov-Smirnov tests have been performed for each A-P position to test for a difference in orientation distribution between control and *dsh¹* samples (**A**). Average vectors of polarity of spreading of apical protrusions in *dsh¹* at 25hAPF (**B**). Plot of standard deviation of orientation of spreading polarity against amplitude of spreading polarity in control and *dsh¹* samples, note that orientations are more variable in *dsh¹* than in the wild type for equivalent amplitudes. For each fork of amplitude, a Rao's spacing test has been performed to test for non-uniformity (non-randomness) of polarity orientation distribution (**C**). Map of standard deviation of orientation of spreading polarity at 25hAPF in control (**D**) and in *dsh¹* (**D'**).

[(D) and (D')] Polarity scores with amplitude inferior to 0.02 have been filtered out, and standard deviation adapted to circular data was calculated for each spatial box.

n: number of analyzed animals. Std: standard deviation adapted to circular data.

As protrusions are less polarized in *dsh*¹, we expect that thorax migration should be disrupted in *dsh*¹. Indeed, imaging of *dsh*¹ mutant thorax flows revealed a patterned reduction of A-P velocity, with a maximal defect in the posterior thorax (Position_{AP}=50-115%) from 19 to 24hAPF (compare Figures 1C and 16A, Figure 16B). Accordingly, deformation pattern is altered in *dsh*¹ (compare Figures 2A and 16C). Interestingly, protrusion polarity and thorax velocity at 25hAPF still correlates in *dsh*¹ (Figures 16D-E). This strongly suggests that defects of protrusion polarization in *dsh*¹ is the cause of the observed thorax flow defects.

To further analyze the role of core PCP in thorax flow, we have analyzed thorax flows in additional core PCP pathway mutants. First, RNAi against *starry night* using *Act::GAL4* (*Act>stan*^{RNAi}) phenocopies both microchaetes orientation, thorax flow and deformation defects of *dsh*¹ (Figures 17A-C). Second, the overexpression of *Spiny leg* is known to lead to the reversal of microchaetes polarization in the adult⁴⁹. Accordingly, global overexpression of *Spiny leg* using *Act::GAL4* (*Act>Sple*^{up}) leads to the reversal of microchaetes orientation specifically in the posterior thorax (Position_{AP}=60-100%), which is mostly kept from 24hAPF to 36hAPF (Figure 18A). Interestingly, thorax flow is highly affected in the posterior thorax (Position_{AP}=50-150%) from 18hAPF to 28hAPF (Figure 18B), even resulting in a reversal of flow direction from 19 to 23hAPF (Figure 18C). As a result of the opposed migration directions of the anterior and the posterior thorax regions, high tissue A-P stretching can be observed in the middle of the thorax (Position_{AP}=30-80%, compare Figures 2A and 18D). Finally, the overexpression of *prickle* is known to affect the orientation of microchaetes specifically in the most anterior region of thorax in the adult⁴⁹. Accordingly, global overexpression of *pk* using *Act::GAL4* (*Act>pk*^{up}) leads to defects of microchaetes orientation which are maximal in the most anterior region of the thorax (Figure 19A). Interestingly, thorax flow defects occur specifically in the same anterior region (Figure 19B). As a result of the decreased A-P velocity of the anterior thorax, tissue A-P compression occurs next to the slowed down region (compare Figures 2A and Figure 19C). Taken together, this data shows that a pattern of defect in planar polarity leads to a similar pattern of thorax flow defects.

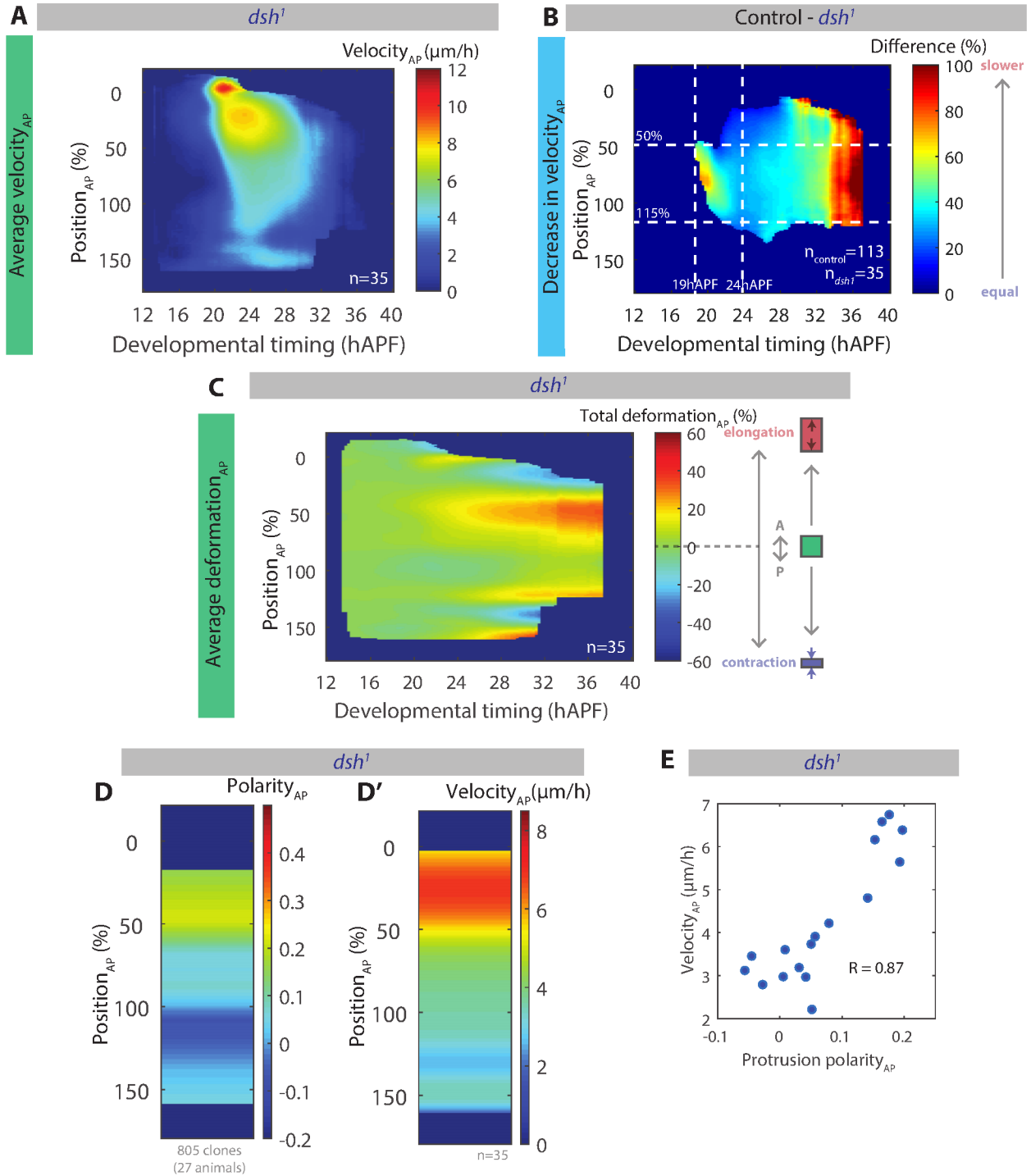


Fig.16: *Dishevelled* regulates A-P velocity and A-P deformation patterns. Average kymograph of A-P velocity of *dsh¹* mutants (A). Average kymograph of difference in A-P velocity between control and *dsh¹* (B). Average kymograph of cumulative A-P deformations in *dsh¹* (C). A-P gradients at 25hAPF in *dsh¹* mutants of A-P component of polarity of protrusion spreading (D) and of A-P component of thorax flow velocity (D'). Correlation plot of A-P polarity of protrusion spreading and thorax A-P velocity after averaging them for forks of A-P position of 10% (E).

$n_{\text{control}}/n_{\text{dsh1}}$: number of analyzed animals in the control/*dsh¹* sample.

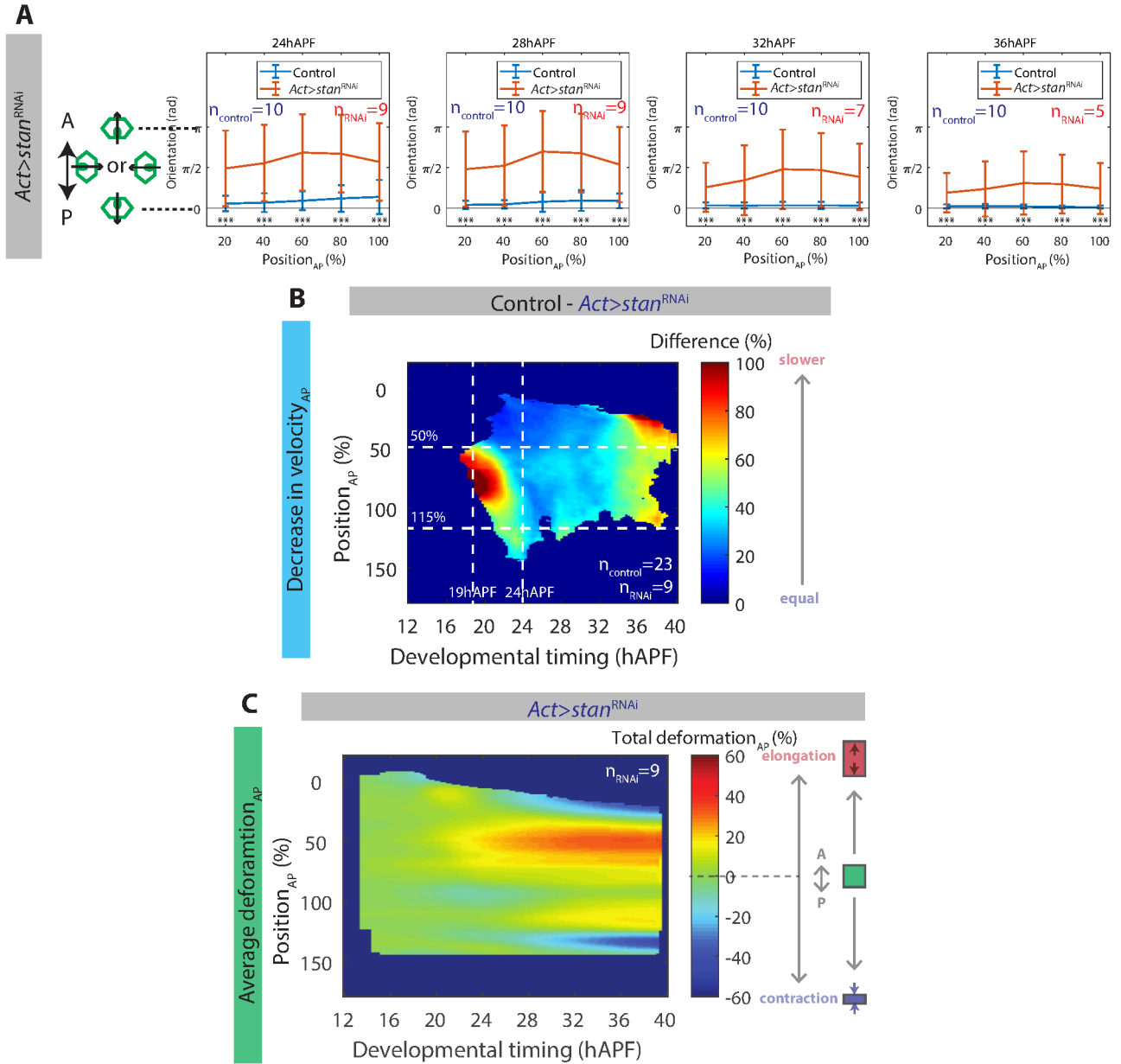


Fig.17: *Act>stan^{RNAi}* phenocopies *dsh1* planar polarity, flow and deformation phenotypes. Orientation of microchaete at 24hAPF, 28hAPF, 32hAPF and 36hAPF in *Act>stan^{RNAi}*, error bars represent standard deviation, Kolmogorov-Smirnov tests have been performed for each A-P position to test for a difference in orientation distribution between control and *Act>stan^{RNAi}* samples (**A**). Average kymograph of difference in A-P velocity between control and *Act>stan^{RNAi}* (**B**). Average kymograph of cumulative deformation along the A-P axis in *Act>stan^{RNAi}* (**C**).

$n_{\text{control}}/n_{\text{RNAi}}$: number of analyzed animals in the control/*Act>stan^{RNAi}* sample.

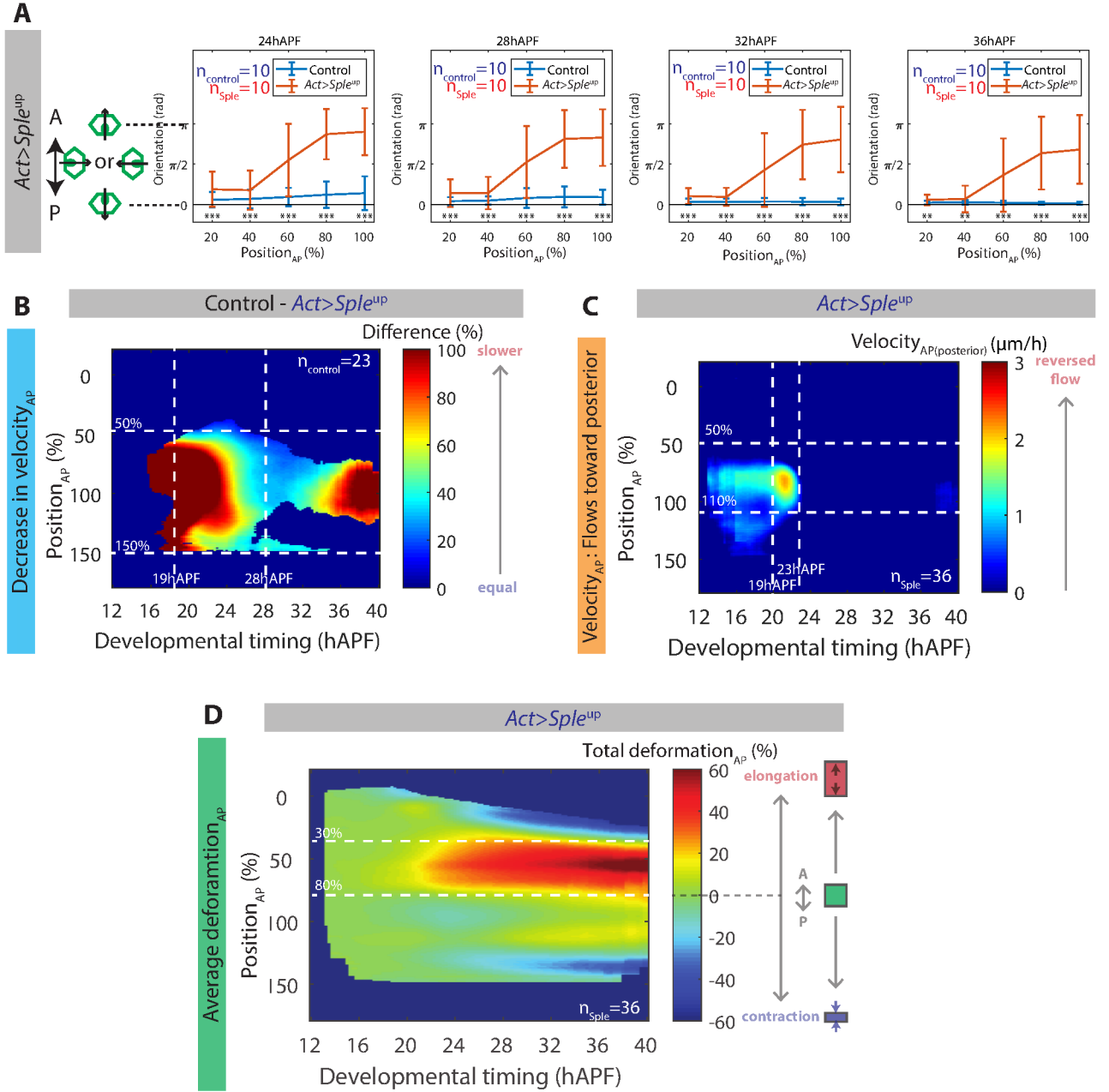


Fig.18: Overexpression of *Sple* triggers planar polarity reversal in the posterior thorax, and accordingly affect thorax flow and deformation. Orientation of microchaete at 24hAPF, 28hAPF, 32hAPF and 36hAPF in *Act>Sple^{up}*, error bars represent standard variation, Kolmogorov-Smirnov tests have been performed for each A-P position to test for a difference in orientation distribution between control and *Act>Sple^{up}* samples (A). Average kymograph of difference in A-P velocity between control and *Act>Sple^{up}* (B). Average kymograph of A-P velocity directed toward the posterior (in the reversed direction as compared to wild type flows) in *Act>Sple^{up}* (C). Average kymograph of cumulative deformation along the A-P axis in *Act>Sple^{up}*, note the high stretching deriving from opposite migration directions (D).

$n_{\text{control}}/n_{\text{Sple}^{\text{up}}}$: number of analyzed animals in the control/*Act>Sple^{up}* sample.

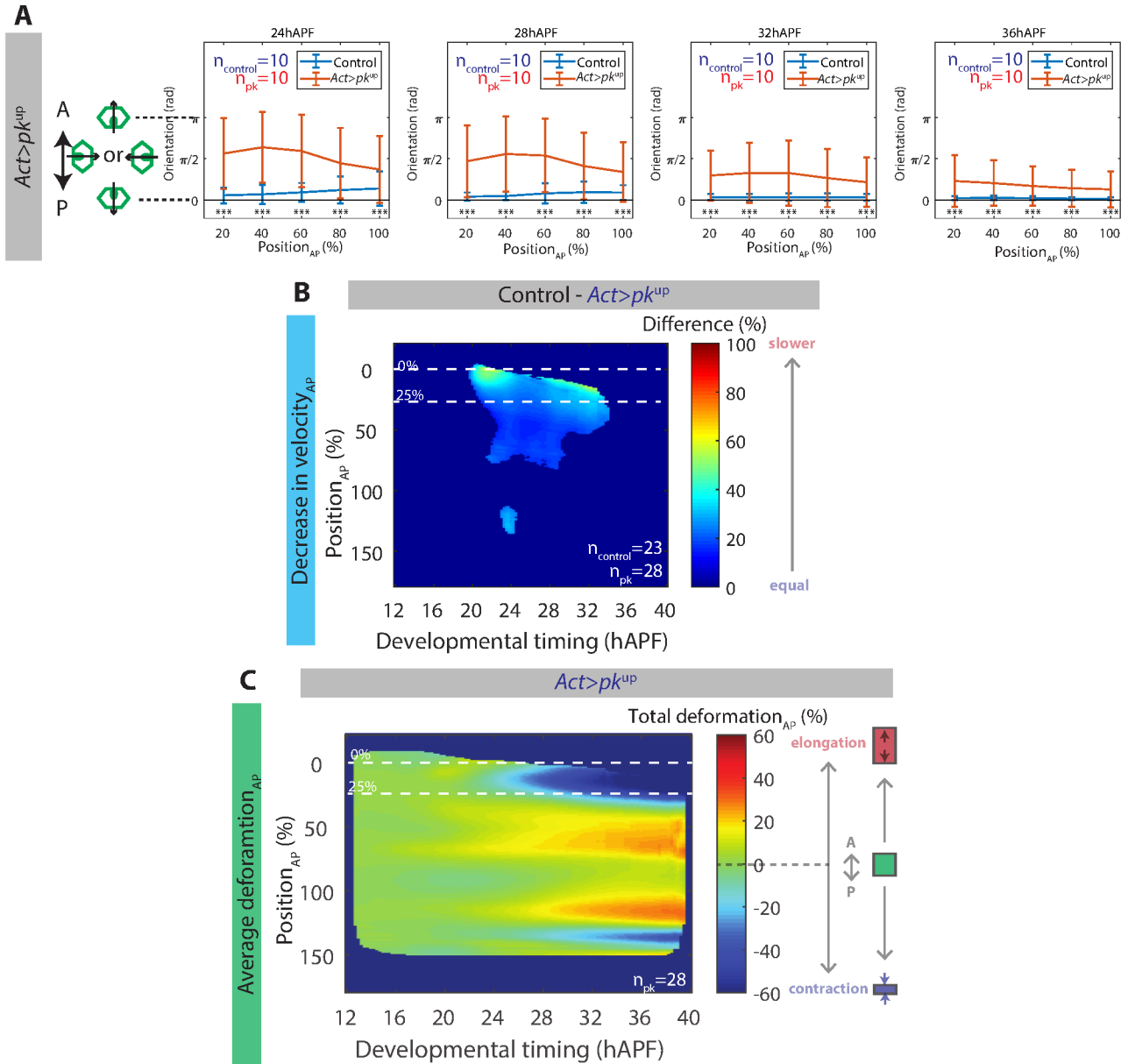


Fig.19: Overexpression of *pk* triggers planar polarity defects in the anterior thorax, and accordingly affect thorax flow and deformation. Orientation of microchaete at 24hAPF, 28hAPF, 32hAPF and 36hAPF in *Act>pk^{up}*, error bars represent standard variation, Kolmogorov-Smirnov tests have been performed for each A-P position to test for a difference in orientation distribution between control and *Act>pk^{up}* samples (**A**). Average kymograph of difference in A-P velocity between control and *Act>pk^{up}* (**B**). Average kymograph of cumulative deformation along the A-P axis in *Act>pk^{up}*, note the high compaction deriving from the slowing down of the anterior thorax (**D**).

$n_{\text{control}}/n_{\text{pk}}$: number of analyzed animals in the control/*Act>pk^{up}* sample.

***Stripe* regulates thorax flow and protrusion polarity in synergy with core PCP pathway**

In all the core PCP pathway disruption conditions that we have analyzed, thorax flow can be highly affected in the posterior domain ($\text{Position}_{\text{AP}}=50\text{-}150\%$) and in the most anterior domain ($\text{Position}_{\text{AP}}=0\text{-}20\%$) of the thorax. The flow of the rest of the anterior thorax ($\text{Position}_{\text{AP}}=20\text{-}50\%$), on the contrary, appears overall robust to core PCP disruptions. *Stripe* (Sr) is a transcription factor which is known to have a patterned expression in the thorax. More precisely, Sr expression is maximal in the region which is robust to core PCP disruptions (Figures 20A-B). This observation prompted us to test the role of *sr* in thorax flow using a viable hypomorphic *sr* allele (sr^l). Interestingly, thorax flows are reduced in sr^l mutant, particularly for $\text{Position}_{\text{AP}}=20\text{-}50\%$ (Figure 20D). While thorax flows show an A-P velocity gradient in the control (Figure 1C), A-P velocity gradient is reduced in sr^l : Anterior thorax cells indeed all migrate with an almost homogeneous A-P velocity in sr^l ($\text{Position}_{\text{AP}}=20\text{-}50\%$, compare Figures 1C and 20C). This effect is phenocopied when globally inducing RNAi against *stripe* using *Act::GAL4* (*Act>sr^{RNAi}*, compare Figures 20C and 20E). In concordance with the reduction of the gradient of A-P velocity, A-P deformations are reduced in sr^l in the anterior thorax ($\text{Position}_{\text{AP}}=0\text{-}50\%$, compare Figures 2A and 20F). Thus, we can conclude that the expression of *stripe* is necessary for anterior thorax migration and deformation.

The defects in thorax flows in sr^l prompted us to investigate the pattern of polarity of apical protrusions in this mutant condition. Almost no defects of microchaetes planar polarization can be observed in sr^l (Figure 21A), suggesting that sr^l is unlikely to control the polarization of apical protrusions. Surprisingly, however, polarity of apical protrusion spreading is reduced in sr^l (compare Figures 12B and 21B). Unlike in dsh^l , the reduction of polarity scores cannot be mainly attributed to a randomization of the main orientation of polarization, as sr^l shows comparable variability of orientations of spreading polarity as the wild type for similar amplitudes (compare Figures 15C and 21C). We thus conclude that sr^l mutation causes a reduction of intensity of polarization of protrusive activity, without changing its main orientation. Besides, similarly as in the wild type and dsh^l conditions, polarity of spreading of the apical protrusions and migration velocity correlate in sr^l (Figures 21D-E), further suggesting a direct link between the intensity of polarized protrusive activity and migration velocity.

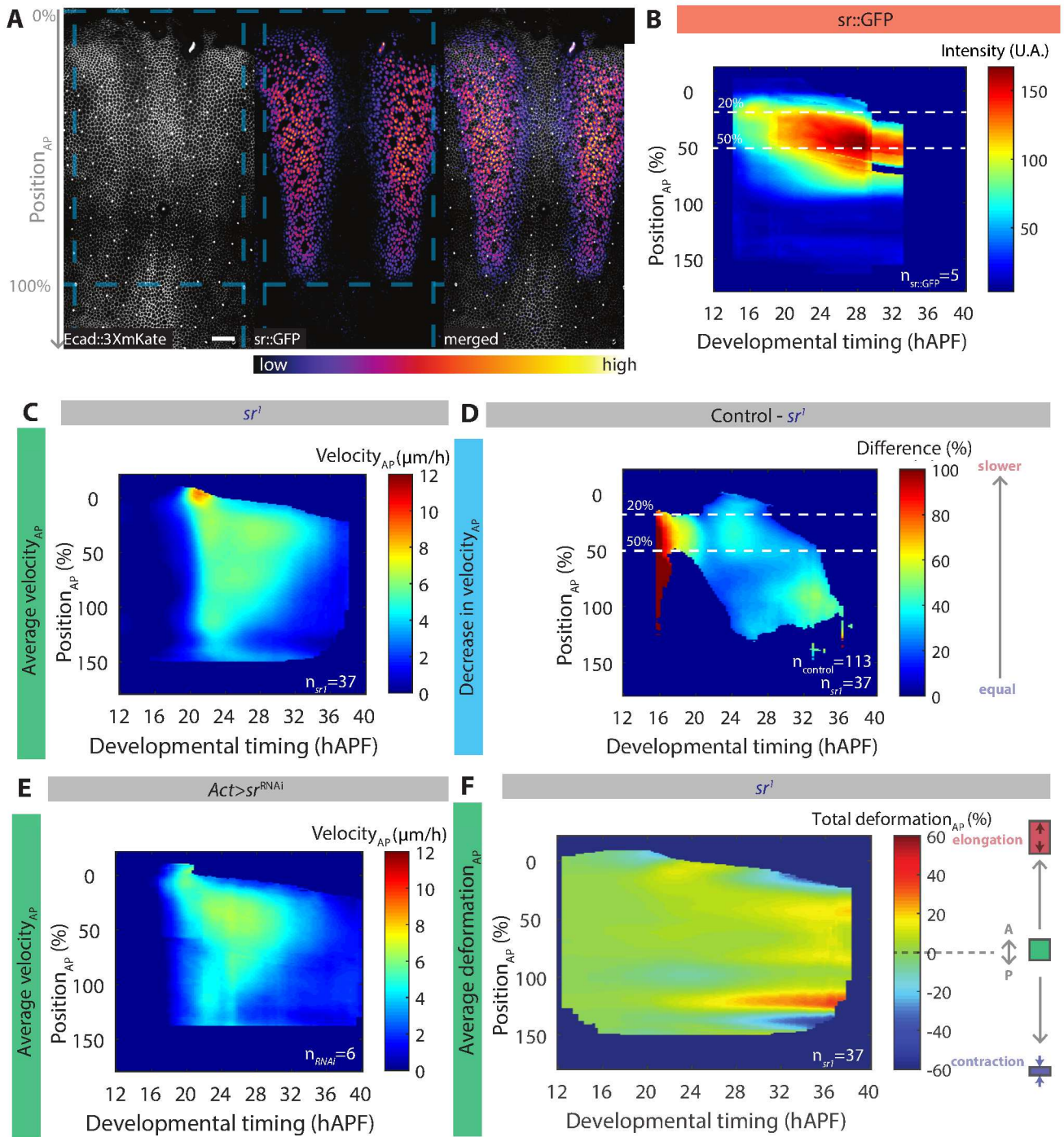


Fig.20: *Stripe* regulates A-P flows and A-P deformations in the anterior thorax. Picture of a pupae expressing *sr::GFP* and *Ecad::3XmKate* at 25hAPF, revealing the patterned expression of *sr*, blue dashed lines represent spatial landmarks (head-to-thorax boundary and landmark macrochaetes), scale bar: 25μm (**A**). Average kymograph of *sr::GFP* levels (**B**). Average kymograph of A-P velocity in *sr*¹ (**C**) and in *Act>sr^{RNAi}* (**E**). Kymograph of difference in A-P velocity between control and *sr*¹ mutants (**D**). Average kymograph of cumulative A-P deformation in *sr*¹, note the global decrease in elongation in the anterior thorax (**F**).

n_{control}/n_{sr::GFP}/n_{sr¹}/n_{RNAi}: number of analyzed animals in the control/*sr::GFP*/*sr*¹/*Act>sr^{RNAi}* sample.

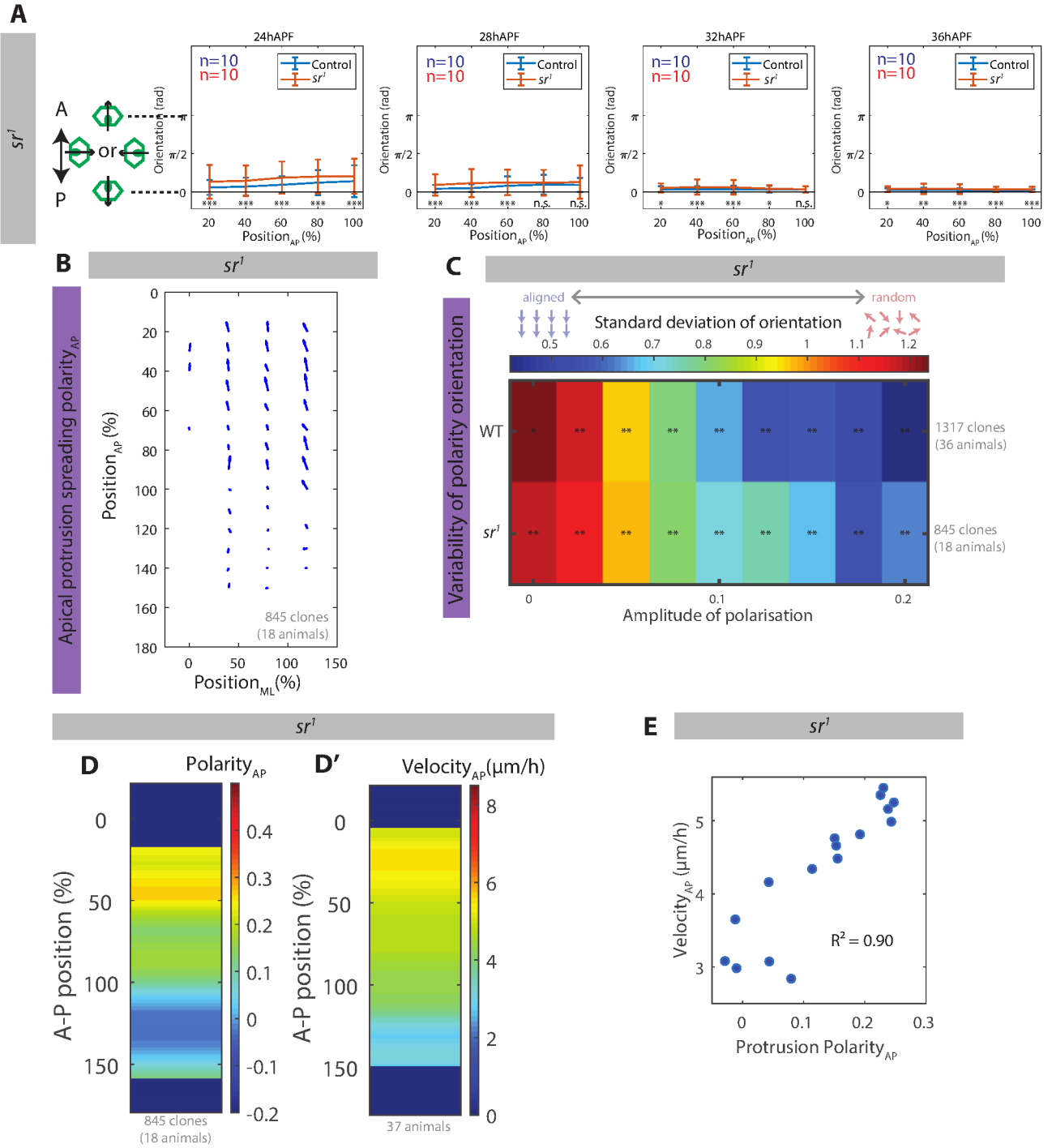


Fig. 21: *Stripe* regulates polarized apical protrusions emission. Orientation of microchaetes at 24hAPF, 28hAPF, 32hAPF and 36hAPF in sr^1 mutant background, error bars represent standard variation, Kolmogorov-Smirnov tests have been performed for each A-P position to test for a difference in orientation distribution between control and sr^1 samples (**A**). Average vectors of apical protrusions spreading polarity in sr^1 at 25hAPF (**B**). Plot of standard deviation of orientation of spreading polarity against amplitude of spreading polarity in control and sr^1 samples, note that orientations are similarly variable in sr^1 and in the wild type for equivalent amplitudes. For each fork of amplitude, a Rao's spacing test has been performed to test for non-uniformity (non-randomness) of polarity orientation distribution (**C**). A-P gradients at 25hAPF in sr^1 mutants of the A-P component of protrusion spreading polarity (**D**) and of the A-P component of thorax flow velocity (**D'**). Correlation plot of protrusion A-P polarity and A-P velocity after averaging them for forks of A-P position of 10% (**E**).

As both *stripe* and core PCP pathway are involved in the regulation of polarized protrusive activity, we investigated whether *stripe* and core PCP pathway could interact, by combining *sr¹* mutation with *dsh¹* mutation. Interestingly, while *sr¹* almost shows no microchaetes planar cell polarity defects (Figure 21A), microchaetes orientation defects are enhanced in *dsh¹sr¹* double mutant when compared to *dsh¹* mutant (Figure 22A). This enhancement of microchaetes polarity defects is phenocopied when globally inducing both RNAi against *stan* and RNAi against *sr* using *Act::GAL4* (*Act>stan^{RNAi}sr^{RNAi}*, Figure 22B). Moreover, apical protrusions spreading polarity at 25hAPF is severely reduced in *dsh¹sr¹* double mutant (compare Figures 12B and 22C). When comparing the A-P gradients of spreading polarity of control, *dsh¹*, *sr¹* and *dsh¹sr¹* (Figure 22D), it appears that the effect of *dsh¹sr¹* on spreading polarity is equal to the sum of the effects of *dsh¹* and *sr¹* on spreading polarity (Figure 22E). Moreover, spreading polarity orientation is more random in *dsh¹sr¹* than in control, *sr¹* and even *dsh¹* samples (Figures 22F, compare Figures 15D-D' and 22G). We thus conclude that *sr¹* and core PCP pathway act in parallel in regulating the polarization of apical protrusive activity.

As *stripe* and core PCP pathway synergize to regulate polarized apical protrusive activity, we wanted to test whether they synergize as well to regulate thorax flows. Remarkably, thorax flows are severely reduced in *dsh¹sr¹* (compare Figure 1C and 23A, Figure 23B). The effects of *dsh¹sr¹* of thorax flows is approximately equal to the sum of the effects of *dsh¹* and *sr¹* on thorax flows (compare Figures 23B and 23C). These defects are phenocopied in *Act>stan^{RNAi}sr^{RNAi}* (compare Figures 23B and 23D). In concordance with severe reduction of thorax flows, A-P deformations are decreased in *dsh¹sr¹* (compare Figures 2A and 23E). Finally, apical protrusion spreading polarity and thorax velocity are both very low in *dsh¹sr¹* (Figures 23F-F'), further validating the direct link between spreading polarity and migration velocity.

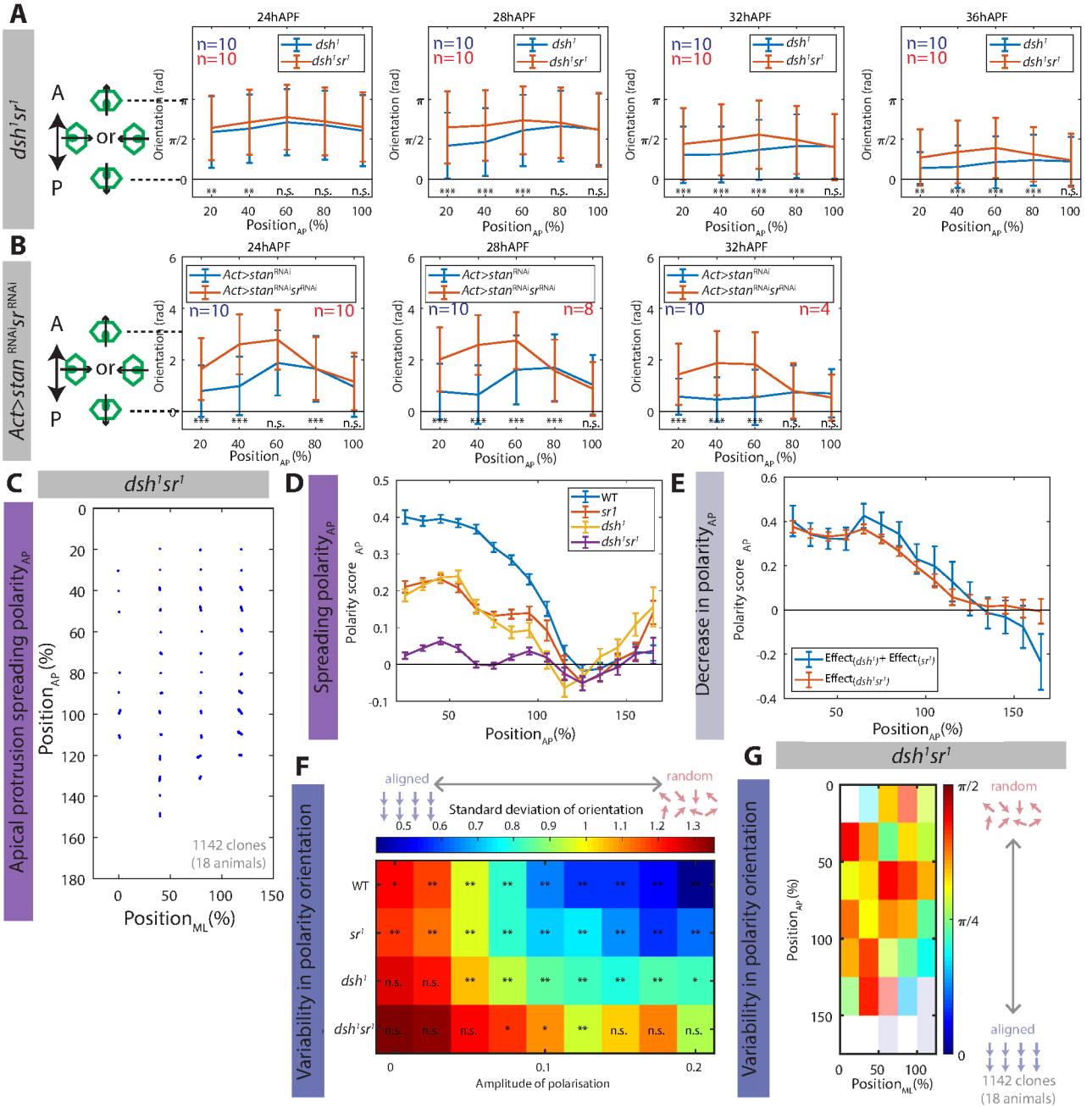


Fig.22: Stripe and core PCP pathway synergize to regulate polarized protrusion emission. Orientation of microchaetes at 24hAPF, 28hAPF, 32hAPF and 36hAPF in *dsh¹sr¹* and *dsh¹* (A) and in *Act>stan^{RNAi}sr^{RNAi}* and *Act>stan^{RNAi}* (B). Average vectors of polarity of spreading of apical protrusions in *dsh¹sr¹* at 25hAPF (C). A-P gradient of A-P component of spreading polarity at 25hAPF of wild type, *sr¹*, *dsh¹* and *dsh¹sr¹* (D). Comparison between the decreases in spreading polarity caused by *dsh¹sr¹* and the sum of the decreases in spreading polarity of *dsh¹* and of *sr¹*, note that the effect of *dsh¹sr¹* appears to be equal to the sum of the effects of *dsh¹* and *sr¹* (E). Plot of standard deviation of orientation of spreading polarity against amplitude of spreading polarity in control, *dsh¹*, *sr¹* and *dsh¹sr¹* samples. For each fork of amplitude, a Rao's spacing test has been performed to test for non-uniformity (non-randomness) of polarity orientation distribution. Note that orientations of *dsh¹sr¹* are more random than in the other conditions for similar polarity amplitudes (F). Map of standard deviation of spreading polarity at 25hAPF in *dsh¹sr¹*, spreading polarity scores with amplitude inferior to 0.02 have been filtered out, and standard deviation adapted to circular data was calculated for each spatial box (G).

[(A) and (B)] Error bars represent standard variation. Kolmogorov-Smirnov tests have been performed for each A-P position to test for a difference in orientation distribution between samples.

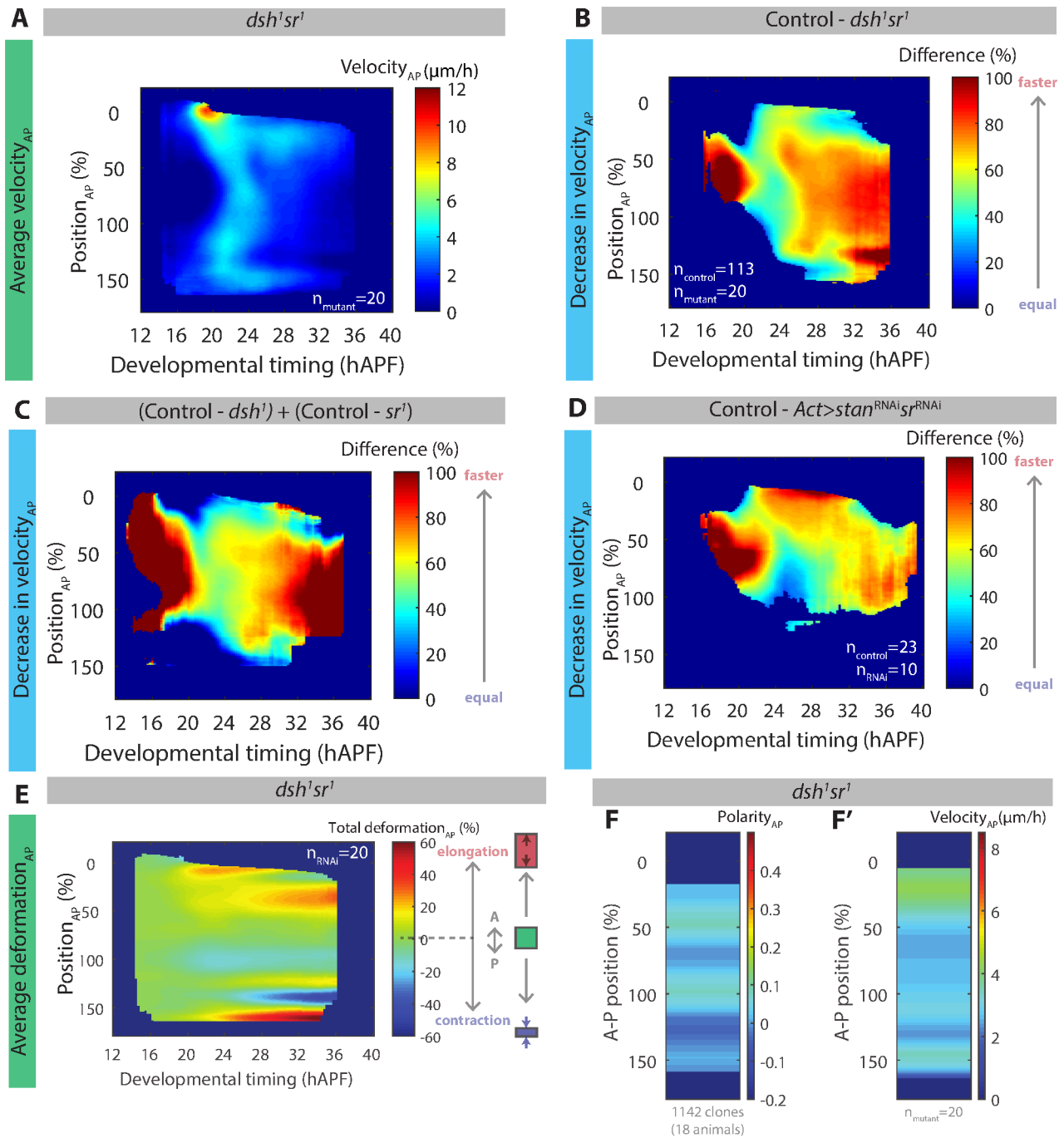


Fig.23: Thorax flow is almost completely inhibited in *dsh'sr'* double mutant. Average kymograph of A-P velocity of *dsh'sr'* (A). Kymographs of differences in A-P velocity between control and *dsh'sr'* (B). Sum of the effects of *dsh'* and *sr'* on A-P velocity, note the close resemblance with Figure B (C). Kymographs of differences in A-P velocity between control and *Act>stan^{RNAi}sr^{RNAi}*, note the close resemblance with Figure B (D). Average kymograph of cumulative A-P deformation in *dsh'sr'* (E). A-P gradients at 25hAPF in *dsh'sr'* double mutants of A-P component of polarity of protrusion A-P spreading (F) and of A-P velocity (F').

$n_{\text{control}}/n_{\text{mutant}}/n_{\text{RNAi}}$: number of analyzed animals in the control sample/*dsh'sr'*/*Act>stan^{RNAi}sr^{RNAi}*.

To further show the synergy between *stripe* and core PCP pathway in regulating thorax flows, we have as well combined global induction of RNAi against *sr* and overexpression of *pk* using *Act::GAL4* (*Act>pk^{up}sr^{RNAi}*). In a similar way to the comparison of *dsh^lsr^l* and *dsh^l* (Figure 22A), microchaetes orientation defects show an increase in *Act>pk^{up}sr^{RNAi}* when compared with *Act>pk^{up}* (Figure 24A). Moreover, thorax flows were severely disrupted in the anterior thorax in *Act>pk^{up}sr^{RNAi}* ($\text{Position}_{\text{AP}}=0\text{-}50\%$, Figure 24B), even reproducibly displaying flows towards the reverse direction as in the control (orange dashed ellipse in Figure 24C). The effect of *Act>pk^{up}sr^{RNAi}* on thorax flows appears to be even higher than the sum of the effects of *Act>pk^{up}* and *Act>sr^{RNAi}* on thorax flows (compare Figures 24B and 24D). In concordance with the severe defects in flows in the anterior region, anterior thorax shows defects in elongation in *Act>pk^{up}sr^{RNAi}* (compare Figures 2A and 24E).

Taken together, this data shows that *sr* and core PCP pathway synergistically regulate the polarization pattern of apical protrusive activity, and hence regulate thorax flows pattern.

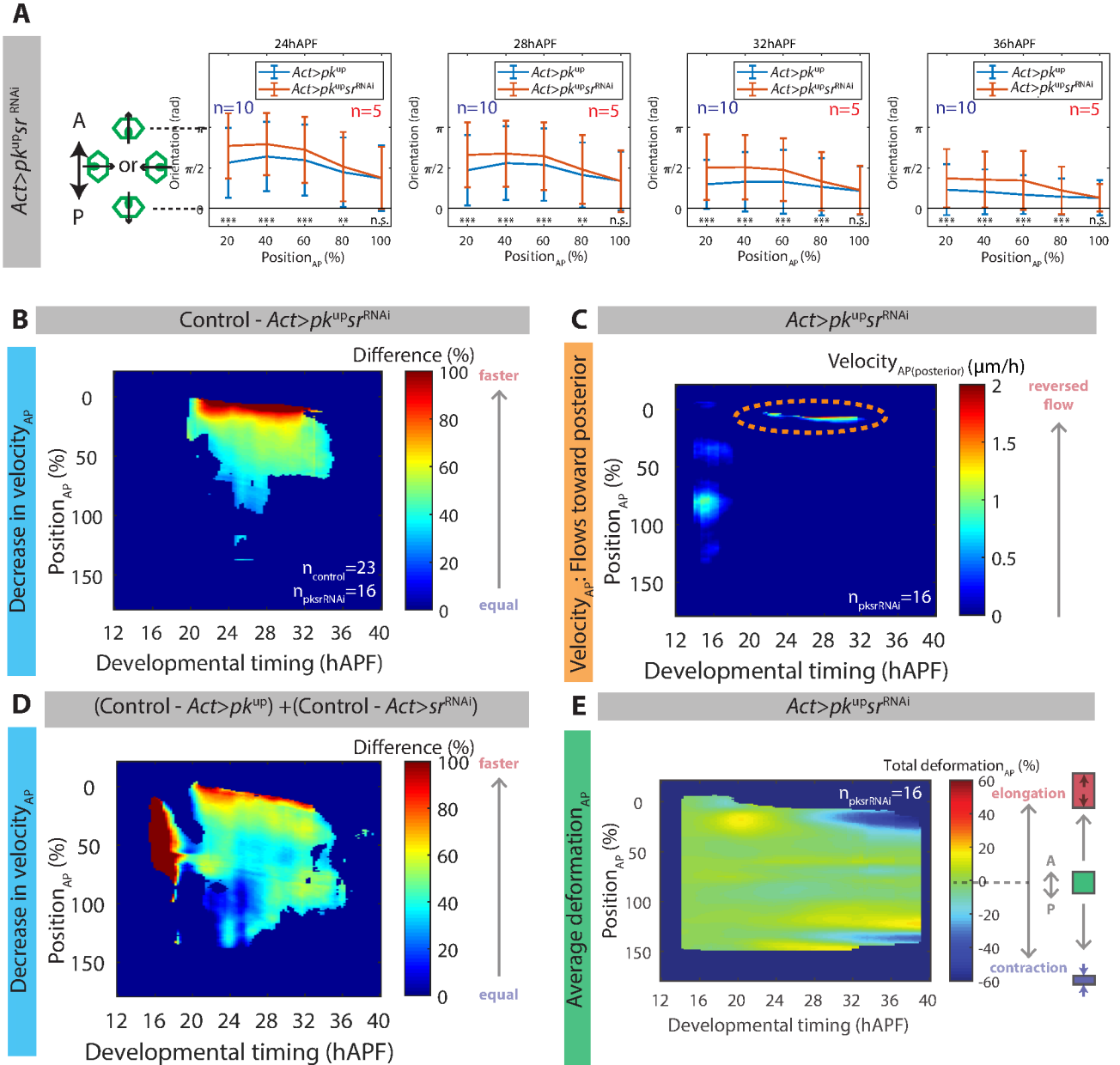


Fig.24: The combination of RNAi against *sr* and *pk* overexpression highlights the cross-talk between *sr* and core PCP pathway. Orientation of microchaetes at 24hAPF, 28hAPF, 32hAPF and 36hAPF in *Act>pk^{up}sr^{RNAi}*, error bars represent standard variation, Kolmogorov-Smirnov tests have been performed for each A-P position to test for a difference in orientation distribution between *Act>pk^{up}* and *Act>pk^{up}sr^{RNAi}* samples (A). Kymographs representing the differences in A-P velocity between control and *Act>pk^{up}sr^{RNAi}* (B). Average kymograph of A-P velocity of flows directed toward the posterior (in the reversed direction as compared to wild type flows) in *Act>pk^{up}sr^{RNAi}* (C). Sum of the effects of *Act>pk^{up}* and *Act>sr^{RNAi}* on A-P velocity, note the close resemblance with Figure B (D). Average kymograph of cumulative A-P deformation in *Act>pk^{up}sr^{RNAi}*, note the defect in elongation in the anterior thorax (E).

$n_{\text{control}}/n_{\text{pk}^{\text{up}}\text{sr}^{\text{RNAi}}}$: number of analyzed animals in control/*Act>pk^{up}sr^{RNAi}* sample.

Dumpy deposition pattern correlates with migration velocity pattern, and is partly regulated by *stripe*

Knowing that thorax cells are mechanically coupled with the apical ECM and that the protrusive activity in the thorax is required for A-P flow, we next aimed at identifying the molecular mechanism by which the cells adhere to the apical ECM. A good candidate for mediating this interaction is the protein Dumpy (Dpy). Dpy is a transmembrane protein exported to the apical membrane which is thought to be cleaved and to be liberated in the apical ECM²⁰⁰, and is known to be determinant in mediating tissue-cuticle interaction during *Drosophila* appendages morphogenesis⁵. We first performed the imaging of the fluorescently labelled Dpy::YFP, combined with the cell contours marker Ecad::3XmKate, in order to correlate Dpy::YFP levels with thorax flows velocities. We quantified the intensity of Dpy::YFP signal above the adherens junctions plane across space and over the whole time of thorax flow. Interestingly, apical Dpy::YFP signal increases over time everywhere in the tissue (Figures 25A-B), and forms a fixed network that overall does not follow cell movements (Figure 25C). By repeating bleaching of Dpy::YFP signal every 2 hours and extracting local Dpy::YFP deposition pattern, we have discovered high similarity between successive deposition patterns (Figures 25D-E), suggesting that Dpy::YFP could bind previously deposited Dpy, and thus form pillars made of successive deposition layers. In order to extract the rate of apical deposition of Dpy::YFP in time and in space, we have isolated the increase in apical Dpy::YFP signal for every time interval, enabling us to generate a map of apical Dpy deposition rate (Figure 25F). Interestingly, Dpy deposition rate correlates with tissue velocity (Figure 25G-H).

The region marked by high Dpy deposition coincides with *Sr* expression region (compare Figures 20A and 25A), and the accumulation of *sr*::GFP signal in time correlates with Dpy apical accumulation in time (compare Figures 20B and 25B). We thus hypothesized that *sr* could regulate Dpy deposition. Indeed, we found that in *sr^l*, Dpy deposition rate is twice lower than in the wild type (Figures 25F, 26A). Interestingly, the decrease in Dpy deposition rate in *sr^l* correlates with the decrease in migration velocity in *sr^l* (Figures 26B-D). Moreover, clonal overexpression of *sr* triggers an increase in apically deposited Dpy::YFP (Figures 26E-F). Taken together, this data shows that *sr* partly controls Dpy deposition, and that different *sr* expression levels could enable different Dpy deposition rates, converting a gradient of patterned transcription factor into a gradient of apical ECM deposition.

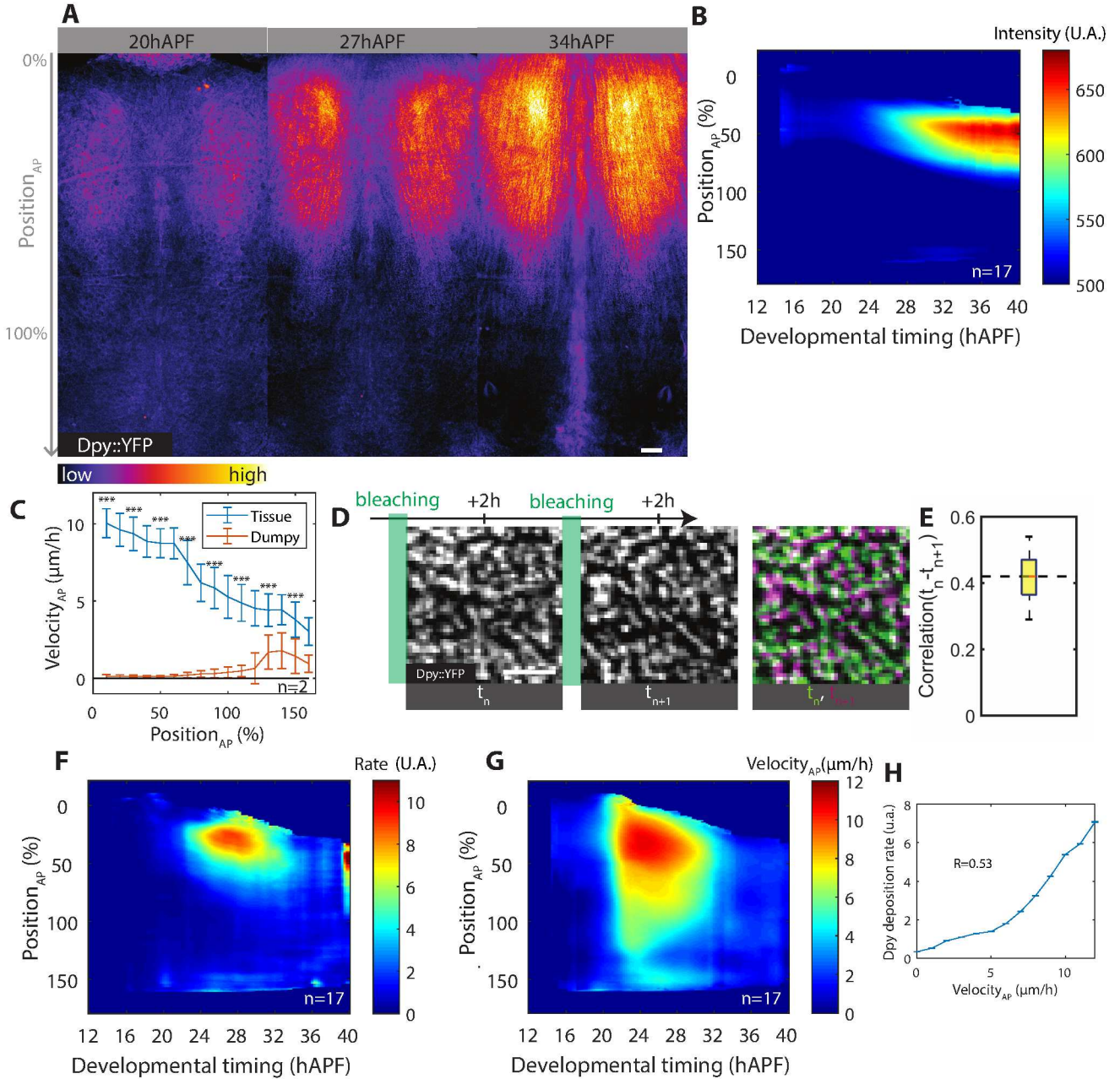


Fig.25: Dpy::YFP deposition rate pattern correlates with thorax A-P velocity pattern. Projection of Dpy::YFP signal above the adherens junction plane reveals that Dpy::YFP apically accumulates during thorax flows, scale bar: 25μm. **(A)** Average kymograph showing total Dpy::YFP apical levels **(B)**. High spatial resolution movie with 30min time intervals and tracking of Dpy::YFP fibers and Ecad::3XmKate cell contours movement reveals that Dpy::YFP overall stay fixed while tissue flows, error bars represent standard deviation **(C)**. Systematic global bleaching of Dpy::YFP every 2hours for 16hours reveals that Dpy::YFP tends to be deposited in a locally fixed pattern **(D)**. Correlation between Dpy::YFP local deposition pattern 2h after bleaching and local deposition pattern 2h after the next bleaching round. Correlation between local successive deposition patterns was calculated for 6 time intervals of a region delimited by Position_{AP}=20-50% and Position_{ML}=0-100% in the two hemithoraxes of 2 animals **(E)**. Average kymograph showing the estimation of Dpy::YFP tissue-scale deposition rate **(F)**, and average A-P velocity kymograph obtained by tracking Ecad::3XmKate in the same animals **(G)**. Relationship between A-P velocity and Dpy deposition rate, data extracted from the kymographs in Figure F and G, error bars represent standard error to the mean of data binned for 1μm/h A-P velocity intervals, R: Pearson correlation **(H)**.

n: number of analyzed animals.

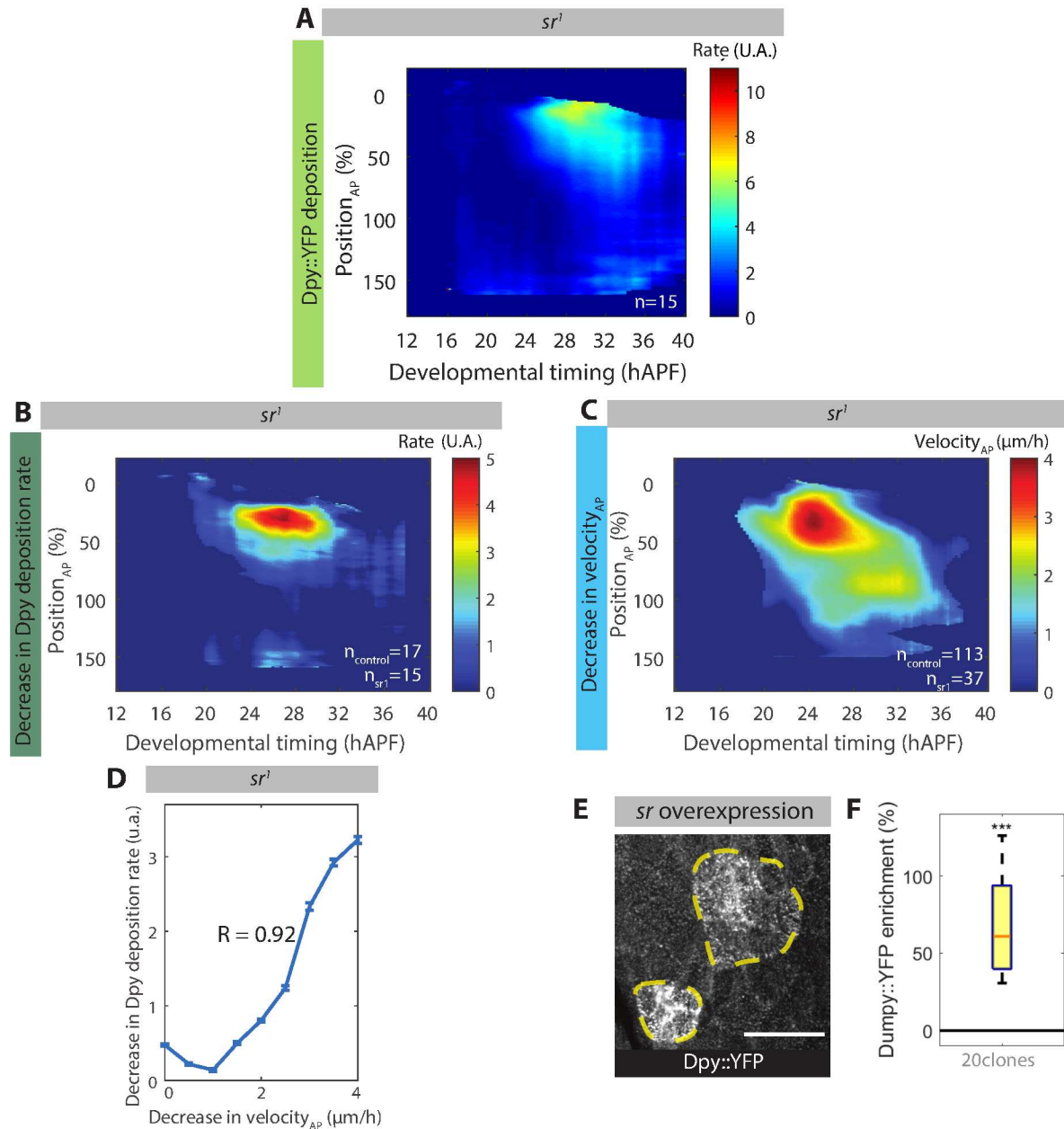


Fig.26: *Stripe* controls Dpy deposition pattern. Average kymograph showing Dpy::YFP deposition rate, note a twofold decrease as compared to control deposition rate (**A**). Average kymographs showing the decrease in Dpy::YFP deposition rate between control and sr^1 (**B**), and the decrease of speed between control and sr^1 (**C**). A high correlation can be found between the effect of sr^1 on Dpy deposition rate and on A-P velocity, data extracted from the kymographs in Figure B and C, error bars represent standard error to the mean of data binned for 0.5 μm/h speed intervals (**D**). Clonal overexpression of sr trigger higher Dpy::YFP deposition, yellow dashed region delineate clones overexpressing sr , scale bar: 15 μm (**E**). The increase of Dpy::YFP levels in clones overexpressing sr vary from 40% to 140%, a t-test has been performed to test whether the average increase is different from zero (**F**).

Dpy expression is necessary for most of the thorax flow to occur

The correlation between Dpy deposition rate and thorax flow velocity, and the fact that Dpy deposition rate defects correlate with thorax flow velocity defects in *sr¹* prompted us to functionally assess the role of Dpy in thorax migration. A global induction of RNAi against Dpy using *Act::GAL4* (*Act>Dpy^{RNAi}*) leads to the complete abrogation of Dpy::YFP apical accumulation (data not shown), and phenocopies the severe thorax deformations attributed to muscle pulling in the *Dpy^{vortex}* mutants²⁰¹, with dynamics of formation of thoracic vortices that are consistent with published timing of muscle pulling²⁰² (26-30hAPF, Figures 27 A-B). In *Act>Dpy^{RNAi}*, A-P flows are severely reduced (Figure 28A), but whether this reduction in A-P velocity is attributable to a role of Dpy in migration or to muscle pulling and vortex formation is unclear. To assess the role of Dpy independently from its role in resisting muscle pulling forces, we have ablated the lateral indirect flight muscles, prior to migration onset and have analyzed thorax flow. Muscle ablation did not affect thoracic flows in a wild type background (Figure 10A), and prevented vortex formation in *Act>Dpy^{RNAi}* pupae (Figures 27C-D). Interestingly, thoracic flows were severely reduced in muscle-ablated *Act>Dpy^{RNAi}* pupae (compare Figures 28B and 28B', Figure 28C). We thus conclude that *Dpy* expression is indispensable for most of the thorax flow to occur. Hence, we hypothesize that the effect of *sr¹* of thorax flows could also be due the fact that Dpy deposition rate is reduced in this mutant condition.

Moreover, tissue elongation and compression are severely reduced in muscle-ablated *Act>Dpy^{RNAi}* pupae (compare Figures 2A and 28D), showing that thorax deformation is dependent on cell interaction with the apical ECM through Dpy.

Supplementary data 3: Dpy is necessary in the posterior thorax to prevent scutellum collapse.

We have also noticed that in *Act>Dpy^{RNAi}*, an A-P collapse of the scutellum and a precocious global displacement occur (Figure 28C'). This phenotype can be phenocopied by inducing RNAi against *Dpy* specifically in the scutellum using a GAL4 driver specific for this region (*Scut>Dpy^{RNAi}*, Figure 29B), and leads to defects in adult scutella aspect ratio (Figure 29C). Interestingly, Dpy::YFP is apically enriched at the posterior margin of the scutellum (Figure 29A). We thus propose that scutellum morphogenesis could be very similar to pupal wing extension: a distal margin anchoring to the cuticle mediated by Dpy may prevent in both cases the tissue from collapsing and may allow its elongation⁵ (Figure 29E).

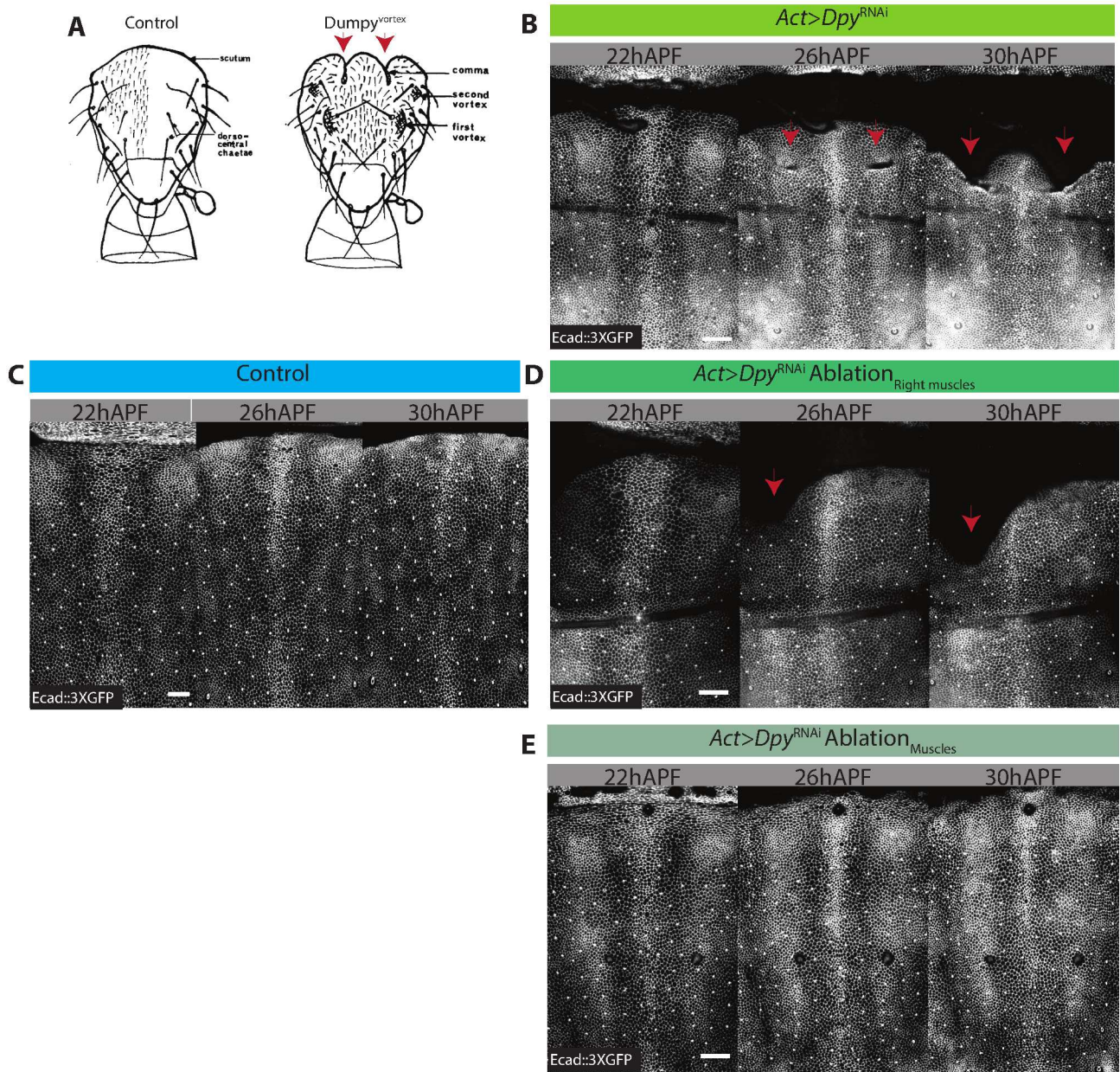


Fig.27: Muscle laser ablation prevents vortex formation in *Act>Dpy^{RNAi}*. *Dpy* mutations of the vortex class trigger high epidermal deformation at muscle insertion sites, which are visible in the adult, adapted from Metcalfe, Genetics (1970, **A**). *Act>Dpy^{RNAi}* triggers vortex formation starting around 25hAPF (**B**), which is never observed in the control (**C**). Muscles laser ablation inhibit vortex formation, either when performed on one side of the thorax (**D**) or on both sides (**E**).

[(A) to (C)] red arrows point at vortex formation site. Scale bars: 40µm.

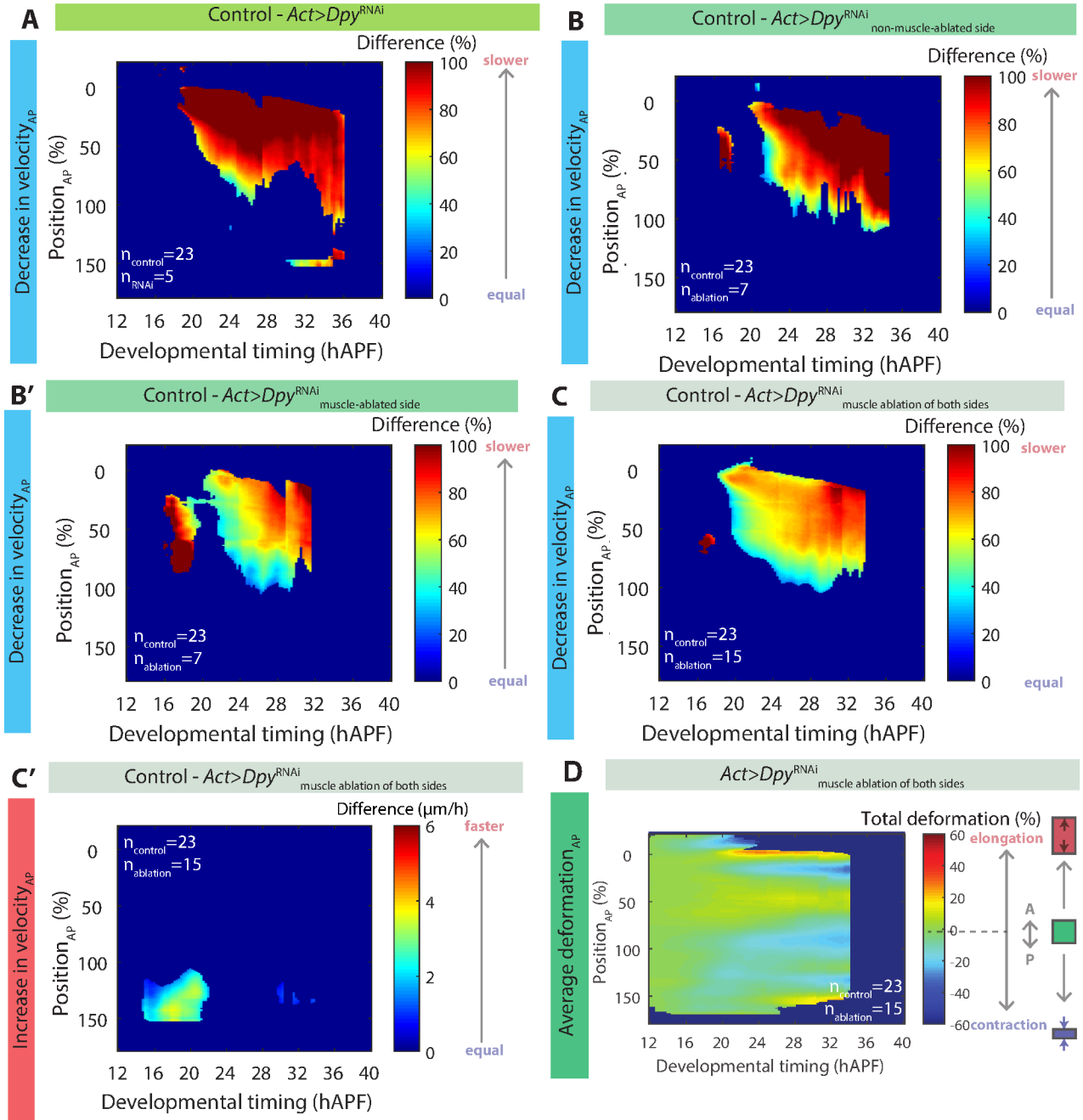


Fig.28: *Dpy* expression is necessary for most of thorax flow to occur. Average kymographs showing decrease in A-P velocity between control and *Act>Dpy^{RNAi}* pupae without muscle ablation (A), non-ablated side of *Act>Dpy^{RNAi}* pupae which were muscle-ablated on one side (B), ablated side of *Act>Dpy^{RNAi}* pupae which were muscle-ablated on one side (B'), and *Act>Dpy^{RNAi}* pupae which were muscle ablated on both sides (C). Average kymograph showing a local increase in A-P velocity comparing control and *Act>Dpy^{RNAi}* which were muscle ablated on both sides (C'). Average kymograph of A-P cumulative deformation in *Act>Dpy^{RNAi}* muscle ablation on both sides (D).

$n_{\text{control}}/n_{\text{RNAi}}/n_{\text{ablation}}$: number of analyzed animal in the control/RNAi/ablation sample.

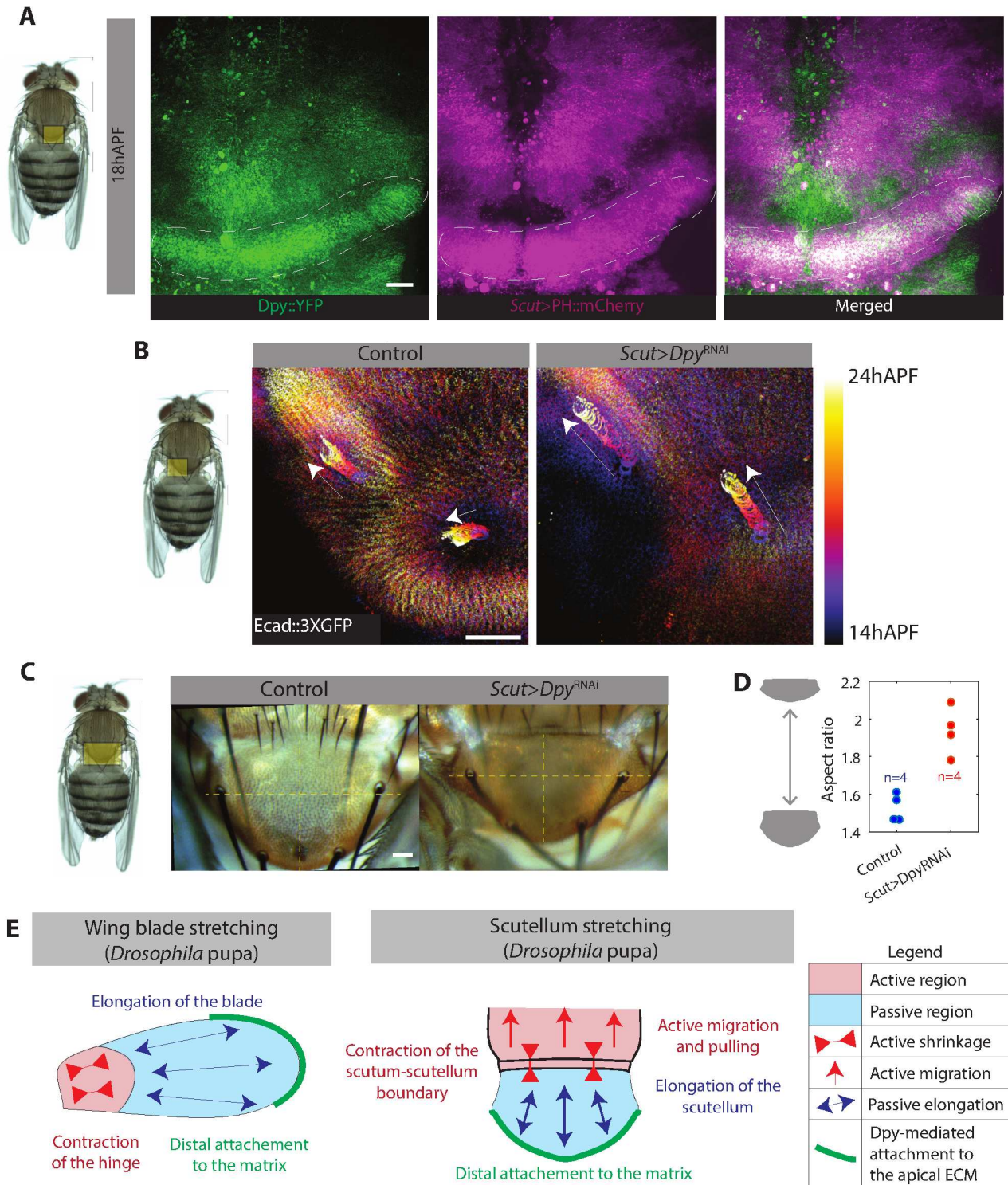


Fig.29: *Dpy* expression in the scutellum is required for preventing scutellum collapse. *Dpy*::YFP is enriched in the posterior edge of the scutellum at 18hAPF (white dashed regions). Expression of a scutellum GAL4 driver overlaps with *Dpy*::YFP posterior enrichment region (A). Time-projection of scutellum region labelled with *Ecad*::3XGFP in the control in *Scut*>*Dpy*^{RNAi} reveals a scutellum antero-posterior collapse in *Scut*>*Dpy*^{RNAi}, white arrows represent macrochaete displacement from 14hAPF to 24hAPF (B). Adult scutellum of control and *Scut*>*Dpy*^{RNAi} (C). Quantification of adult scutellum aspect ratio in control and *Scut*>*Dpy*^{RNAi} (D). Comparison of wing blade and scutellum extension mechanisms (E).

[(A) to (C)] Scale bars: 25µm. The yellow region on the adult highlights the imaged region.

Finally, Papillote (Pot) and Piopio (Pio) are proteins known to regulate tissue-apical ECM interaction⁶. Like Dpy, they contain a ZP domain and are found apically in the pupal wing⁶. Interestingly, induction of RNAi against *pot* using *Act::GAL4* (*Act>pot^{RNAi}*) leads to a reduction of thorax flow (Figure 30A). The decrease in A-P velocity is maximal in *Act>pot^{RNAi}* in the posterior tissue (Position_{AP}=50-150%) from 18hAPF to 22hAPF and in the most anterior thorax (Position_{AP}=0-25%) from 18 to 35hAPF (white dashed regions in Figure 30A). Interestingly, these spatio-temporal regions coincide with regions in which A-P velocity is mildly affected in *Act>Dpy^{RNAi}* Muscle ablation (white dashed regions in Figure 30B) and in which Dpy::YFP deposition rate is low (white dashed regions in Figure 30C). We can thus conclude that early migration of the posterior thorax depends on *pot* and not on *Dpy*. Thus, while *Dpy* is the main matrix constituent regulating thorax migration, *pot* may contribute to tissue-matrix interaction and regulate thorax migration in a complementary manner. We hypothesize that other ZP proteins, like Pio, which is deposited in a complementary tissue pattern as Dpy (Figure 30C), might similarly contribute to thorax migration.

Thorax migration is dispensable for early neck invagination

While neck invagination does only locally influence thorax flows, we can hypothesize that thorax active migration might provide a pushing force participating in neck invagination. To test this hypothesis, we have analyzed neck invagination dynamics in two contexts showing highly reduced anterior thorax migration speeds: *Act>Dpy^{RNAi}* MuscleAblated and *Act>pk^{up}*. In these two contexts, even if initial anterior thorax migration is abrogated, neck invagination proceeds with normal leading edge deepening dynamics from 19hAPF to 22.5hAPF (Figures 31A-B). Nevertheless, in both *Act>Dpy^{RNAi}* MuscleAblated and *Act>pk^{up}*, the tissue gets locally more stretched than in the control in the neighborhood of the invaginating region (Position_{AP}=0-10%, Figures 31C-E). Thus, early neck invagination is not abrogated by loss of thorax migration, likely due to the elongation of cells neighboring the invagination. As a result, we can conclude that thorax migration is not necessary for early neck invagination but is critical to ensure the correct dynamics of cell at the interface between neck and thorax.

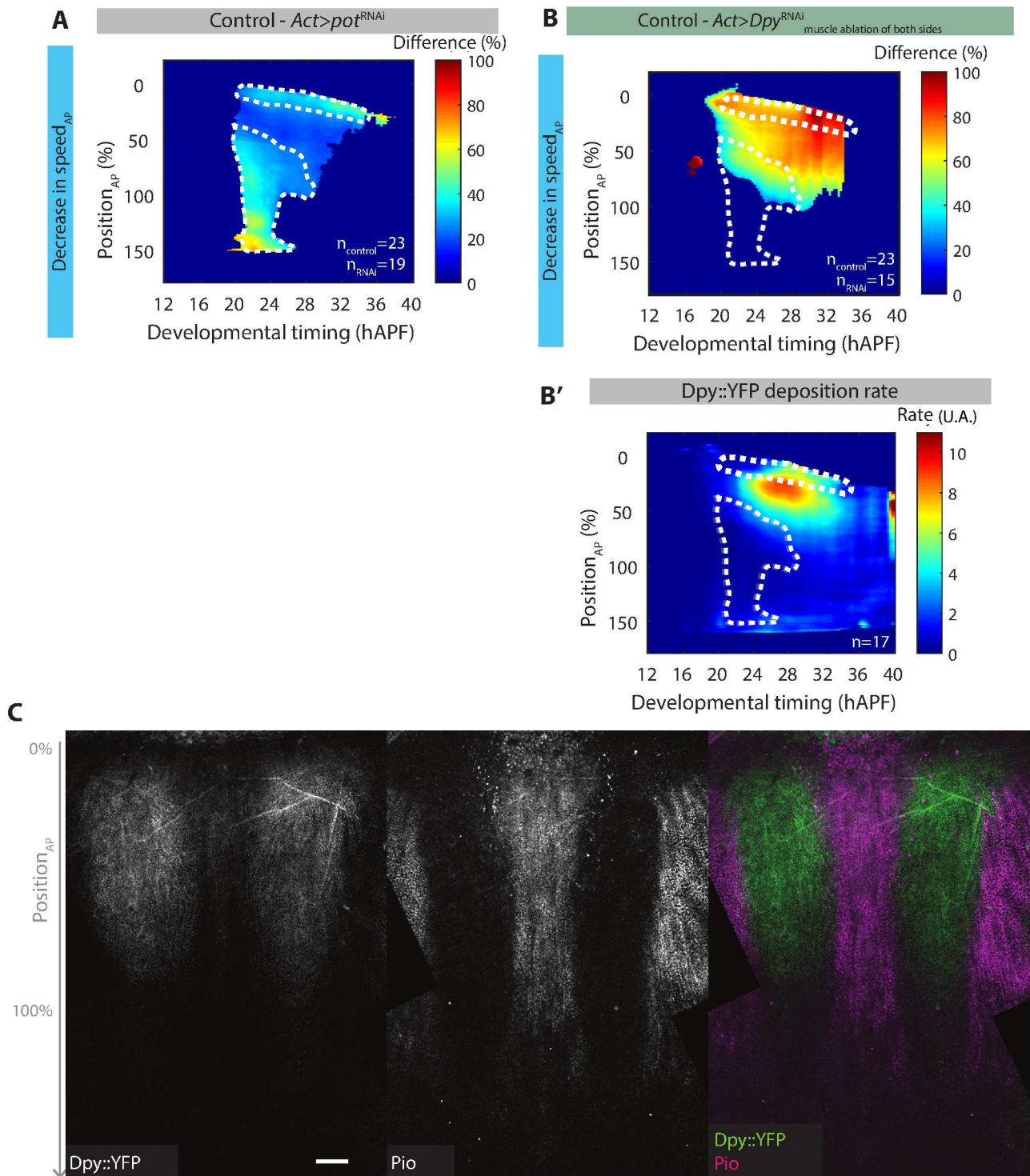


Fig.30: A combination of patterns of apically located ZP domain proteins may contribute to thorax migration. Average difference in A-P velocity between control and *Act>pot^{RNAi}* (**A**). Average difference in A-P velocity between control and muscle-ablated *Act>Dpy^{RNAi}* (**B**) and average *Dpy::YFP* deposition rate (**B'**). Immunostaining against Pio reveals an apical Pio deposition with a complementary pattern to *Dpy::YFP* at 25hAPF, scale bar 25µm (**C**).

[(B) and (B')] Similar kymographs as in Figure 28D and Figure 25F. The point of these figures is to highlight the complementarity between the regions of *Act>pot^{RNAi}* maximal effect (white dashed lines) and the regions of *Act>Dpy^{RNAi}* maximal effect and of maximal *Dpy::YFP* deposition.

$n_{\text{control}}/n_{\text{RNAi}}/n$: number of analyzed animals in the control/RNAi/*Dpy::YFP* sample.

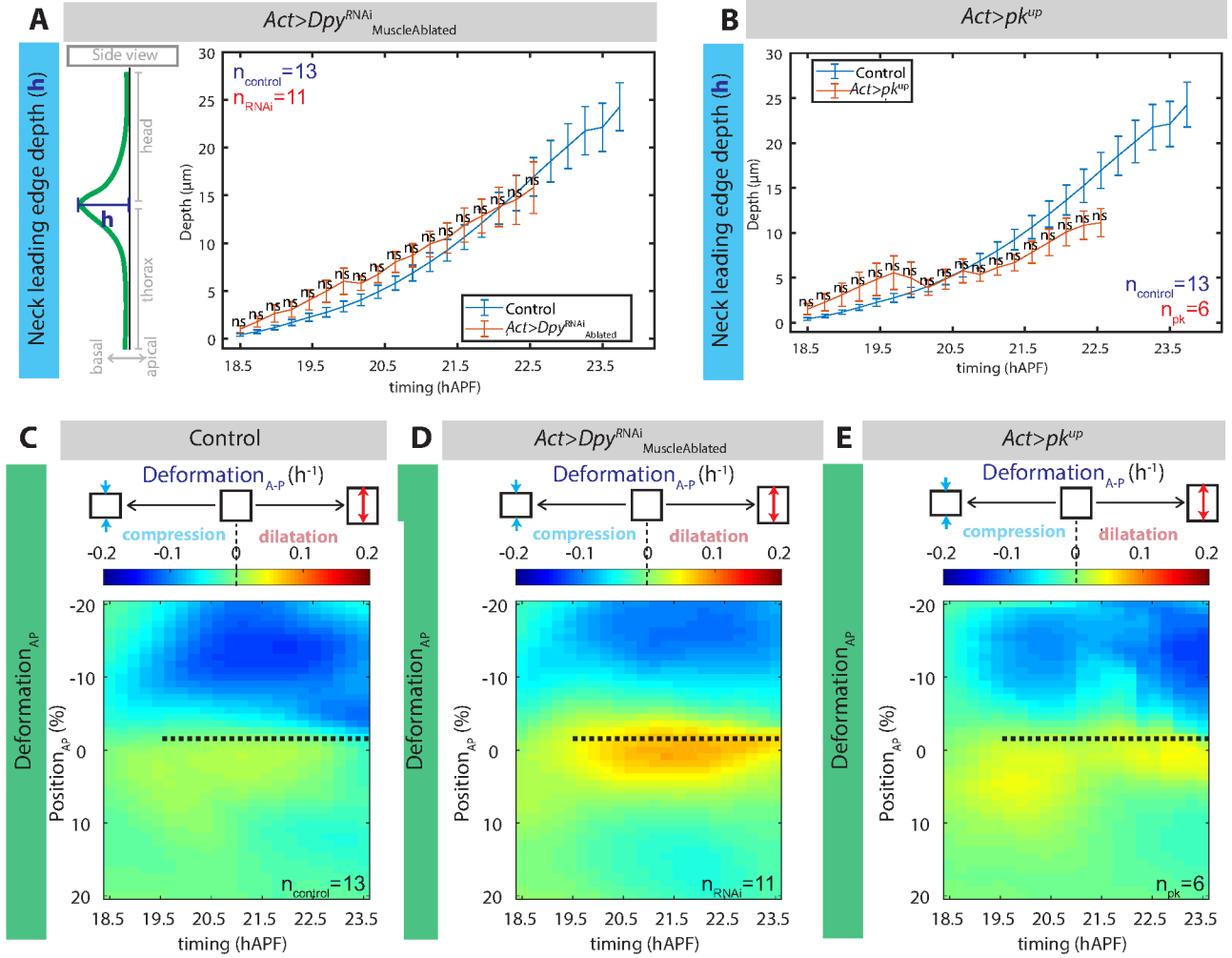


Fig.31: Thorax migration is not required for early neck invagination. Curves of average depth of neck leading edge in control and *Act>Dpy^{RNAi} MuscleAblated* (A), and in control and *Act>pk^{up}* (B). Kymographs of A-P deformation of control sample (C), of *Act>Dpy^{RNAi} MuscleAblated* (D) and of *Act>pk^{up}* (E).

[(A) and (B)] Welch tests have been performed to compare control and *Act>Dpy^{RNAi} MuscleAblated* or *Act>pk^{up}* mean leading edge depths (n.s: p-value>0.05). [(C) to (E)] Black dashed lines represent mean leading edge position.
 $n_{\text{control}}/n_{\text{RNAi}}/n_{\text{pk}}$: number of analyzed animals in the control/RNAi/*Act>pk^{up}* samples.

Posterior thorax (Position_{AP}=50-150%) flow is dependent on anterior thorax (Position_{AP}=0-50%) flow pulling from 22hAPF to 35hAPF

We have previously found that the migration of the anterior thorax (Position_{AP}=0-50%) is not affected by posterior thorax laser ablation. Thus, anterior thorax migration is independent from long-range interaction of posterior thorax. Here, we would like to explore whether the posterior thorax movements could be influenced by anterior thorax traction.

Several pieces of evidence indicate that posterior thorax flow may be influenced by an anterior thorax pulling force. First, in both *Act>Sple^{up}*, *dsh^l* and *Act>stan^{RNAi}*, A-P velocities are highly reduced in posterior thorax (Position_{AP}=50-150%) from 18hAPF to 22hAPF (with A-P velocity decreases superior to 60%), but strikingly gradually comes back to speeds comparable to the control from 22hAPF to 35hAPF (with A-P velocity decreases inferior to 40%, white dashed region in Figures 32A-F). Similarly, in *Act>pot^{RNAi}*, A-P velocities in the posterior thorax are more reduced from 18hAPF to 22hAPF than after 24hAPF (Figures 32G-F). These first observations suggest that posterior thorax could switch from an active migration from 18hAPF to 22hAPF to a more and more passive flow after 22hAPF. Following this hypothesis, reduction of anterior thorax speeds is expected to trigger posterior thorax flow reduction from 22hAPF to 35hAPF. Interestingly, this is precisely what happens in *sr^l* mutant. In *sr^l* tissue, anterior thorax speed is decreased by a factor of two (Figure 33A), and even if *sr::GFP* is not expressed in the posterior thorax (Figure 33C), posterior thorax speed is decreased from 22hAPF to 35hAPF (Figure 33B), suggesting that reduced anterior thorax migration could cause posterior thorax flow defects. To further investigate the interaction between anterior thorax and posterior thorax flows, we have combined RNAi against *sr* and overexpression of *Sple* using *Act::GAL4 (Act>Sple^{up}sr^{RNAi})*. In this context, posterior thorax shows similar flow defects to *Act>Sple^{up}* from 18hAPF to 22hAPF, but show increased flow defects from 24hAPF to 35hAPF (compare Figure 32A and 33D, compare Figure 32D and 33E). This result further suggests that the migration of the posterior domain in *Act>Sple^{up}* from 24hAPF to 35hAPF depends on normal anterior thorax migration.

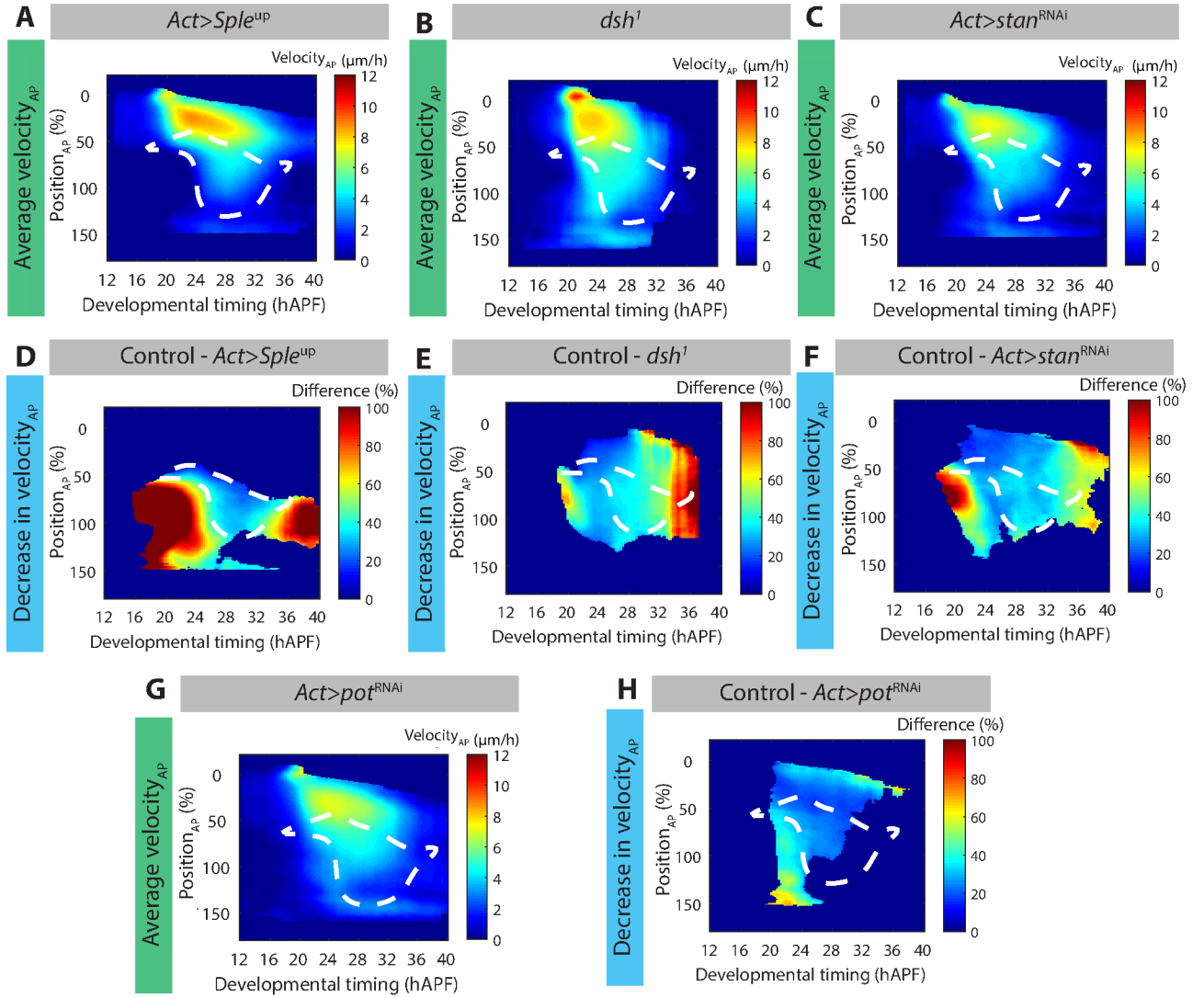


Fig.32: Posterior thorax displacement is robust to core PCP and *pot* genetic disruptions from 24hAPF to 35hAPF. Average kymographs of A-P velocity of $Act>Sple^{up}$ (A), dsh^1 (B), $Act>stan^{RNAi}$ (C) and $Act>pot^{RNAi}$ (G). Kymographs of difference in A-P velocity between the control and $Act>Sple^{up}$ (D), dsh^1 (E), $Act>stan^{RNAi}$ (F) and $Act>pot^{RNAi}$ (H).

[(A) to (H)] White dashed region represents the posterior region showing robust displacement patterns, calculated using (D) with a threshold of 50%. Note that all these kymographs have already been presented previously, the only point of this panel is to highlight the common region in the posterior thorax that shows displacements patterns that are robust to genetic disruptions.

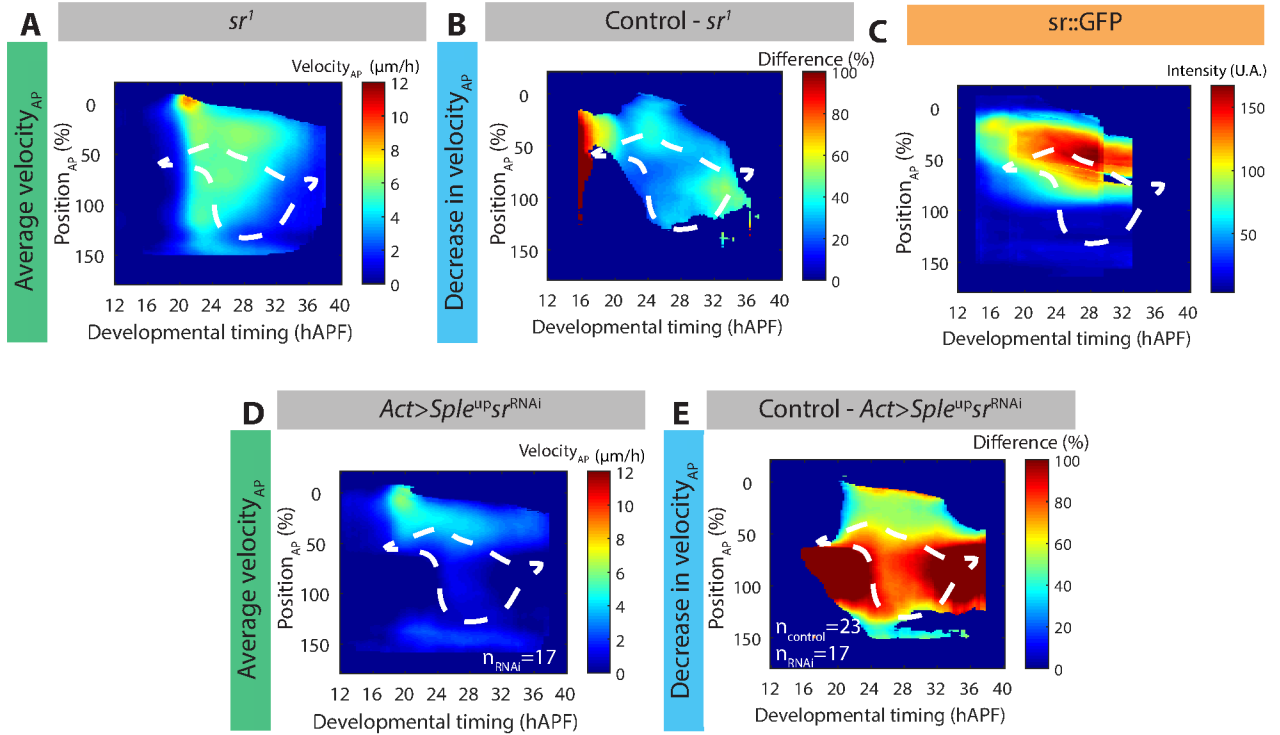


Fig.33: Posterior thorax displacement from 24hAPF to 35hAPF is affected by anterior thorax migration defects. Average kymograph of A-P velocity of sr^1 (A). Kymograph of difference in A-P velocity between the control and sr^1 (B). Average kymograph of $sr::GFP$ levels (C). Average kymograph of A-P velocity of $Act>SpIe^{up}sr^{RNAi}$ (D). Kymograph of difference in A-P velocity between the control and $Act>SpIe^{up}sr^{RNAi}$ (E).

[(A) to (E)] White dashed region represents the same region as in Figure 32C. [(A) to (C)] Note that all these kymographs have already been presented previously, the only point of this panel is to highlight that the region that shows displacements patterns that are robust to core PCP genetic disruptions (Figure 32) overlaps with the region that shows displacements patterns that are affected by sr expression disruption but express low or null levels of $sr::GFP$.

$n_{control}/n_{RNAi}$: number of analyzed animals in the control/ $Act>SpIe^{up}sr^{RNAi}$ sample.

To further test the hypothesis of a long-range influence of anterior thorax migration on posterior thorax flow, we have imaged thorax flow while performing a linear large ablation in the middle of the thorax, at equidistance between head-to-thorax boundary and landmarks macrochaetes (Ablation_{Thorax50%}, Figure 34A). Ablation was repeated every 3 hours in order to prevent wound closure and reestablishment of mechanical coupling between the anterior and the posterior domains. As a result, in Ablation_{Thorax50%} condition, posterior thorax is mechanically isolated from anterior thorax. The initial flow of posterior thorax is only locally disrupted by the wound (from 19hAPF to 22hAPF, Figures 34B-C). However, the decrease of A-P velocity of the posterior domain increases and rapidly propagates posteriorly from 22h to 26hAPF. This culminates with a severally decreased posterior flow from 26hAPF to 35hAPF (Figures 34B-C). Ablation_{Thorax50%} condition thus provides evidence that the posterior thorax flows depends on the connection between posterior and anterior thorax from 24hAPF to 35hAPF. Last, we have tested whether redirection of abnormally oriented flows in *Act>Sple^{up}* was dependent on anterior thorax traction. Hence, we have combined *Act>Sple^{up}* with repeated laser ablation in the middle of the thorax (Ablation_{Thorax50%}*Act>Sple^{up}*). In this condition, posterior thorax flow redirection is efficiently abrogated (Figures 34D-E). Taken together, our data indicate that posterior thorax flow is autonomous from 18hAPF to 22hAPF and then become dependent on its coupling with anterior thorax migration from 22hAPF to 35hAPF.

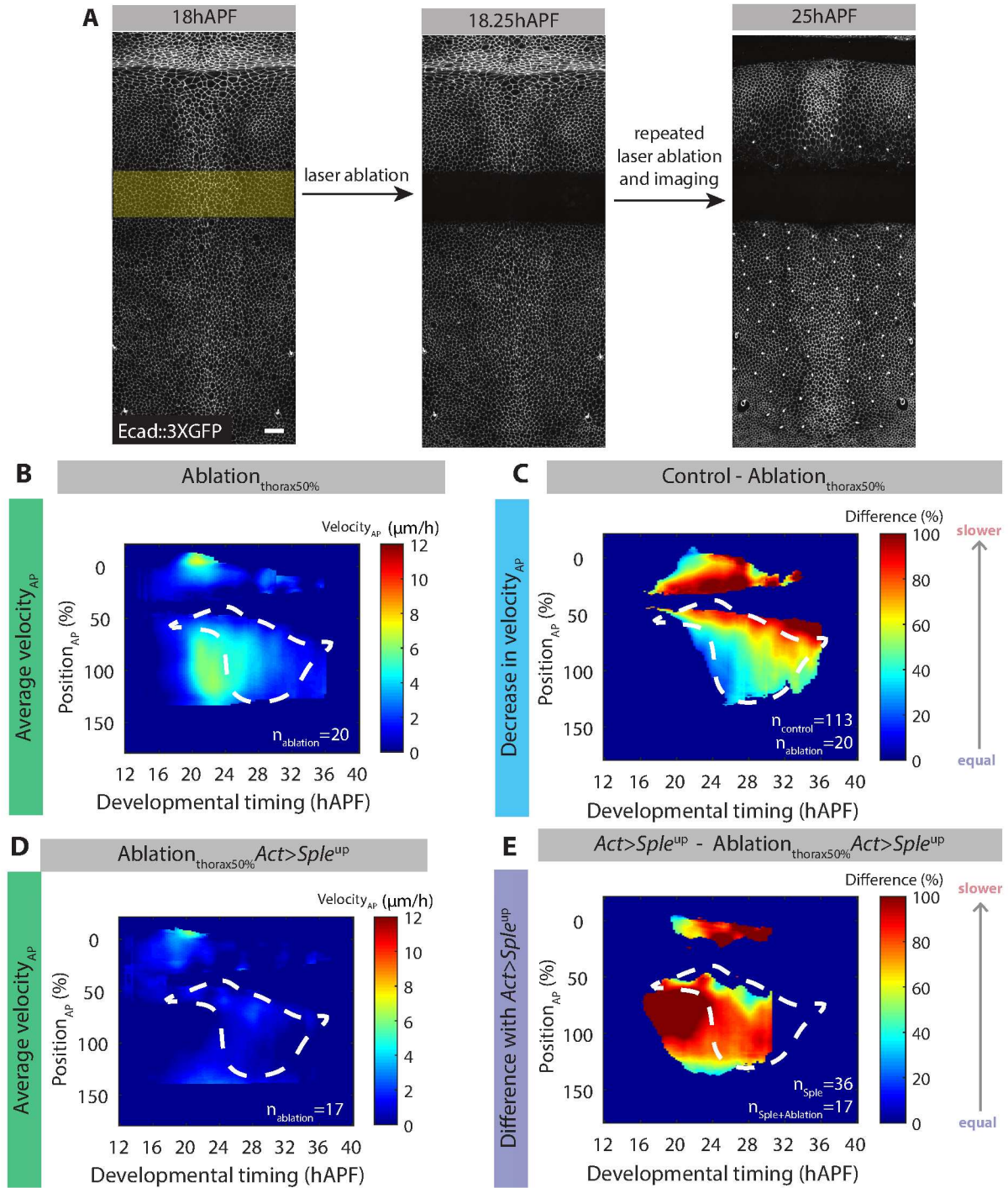


Fig.34: Posterior thorax is advected by anterior thorax from 24hAPF to 35hAPF. Repeated laser ablation in the middle of the thorax (Ablation_{thorax50%}) mechanically isolates anterior and posterior thorax domains, scale bar: 25μm. **(A).** Average kymograph of A-P velocity of Ablation_{thorax50%} **(B).** Kymograph of difference in A-P velocity between the control and Ablation_{thorax50%} **(C).** Average kymograph of A-P velocity of Ablation_{thorax50%} Act>Sp1e^{up} **(D).** Kymograph of difference in A-P velocity between the Act>Sp1e^{up} and Ablation_{thorax50%} Act>Sp1e^{up}, note the almost complete abrogation of thorax flow toward the anterior in the posterior thorax **(E).**

[(B) to (E)] White dashed region represents the region calculated in Figure 32C. Note the overlap between this region and the region showing defects when performing Ablation_{thorax50%}.

n_{control}/n_{ablation}/n_{Sp1e}/n_{Sp1e+Ab1ation}: number of analyzed animals in the control, Ablation_{thorax50%}, Act>Sp1e^{up} and Ablation_{thorax50%} Act>Sp1e^{up} samples.

Discussion

A cell-based crawling on the apical ECM

A cell-based mechanism of collective migration

We have here provided evidence that thorax cells collectively migrate during metamorphosis. This collective migration, like in *Drosophila* follicular epithelium⁵⁹ or larval abdominal cells⁷⁴, is based on a cell-autonomous emission of polarized protrusions, regulated at the tissue-scale by planar polarity cues (Figure^{Introduction} 18). Thorax cells migration is however dependent on distinct planar polarity pathways than follicular cells migration, which depends on a *fat2/lar* basal planar polarity pathway⁵⁹, and than larval abdominal cells migration, which depends on Ft/Ds pathway⁷⁴. Distinctively, migration of thorax cells depends on the core PCP pathway, and is largely independent from Ft/Ds pathway. Our results thus highlight the diversity of planar polarity pathways able to convey collective epithelial migrations based on cell-autonomous crawling.

A migration on the apical ECM

While collective migration often happens as a result of the interaction of a tissue with a basal substratum (either a basal ECM or an underlying cell population), we show that thorax cells migrate on the apical ECM. We provide evidence that apical crawling is achieved by adhesive apical polarized protrusions and by the deposition of the apical ECM protein Dpy. This result echoes the studies carried out in *Drosophila* larval abdominal cells^{74,157}. In this system, apical polarized lamellipodia are observed, and the ZP protein Piopio is necessary for collective movements. In the present study, we additionally show that apical protrusions mechanically interact with the apical ECM. This was achieved by (i) developing a novel assay based on laser ablation and by (ii) showing that the disruption of the apical protrusive activity systematically leads to migration defects. Taken together, our results establish that cells can use the apical ECM as a substratum for crawling.

Many recent studies point at the importance of apical ECM for morphogenesis^{5,24,7,203}. Adhesion to the apical ECM has been shown to create local fixed anchor points to resist neighboring tissue deformations, preventing *Drosophila* wing blade from collapsing upon wing hinge contraction⁵, and spatially restricting flows triggered by mesoderm invagination in *Tribolium* and *Drosophila*⁷. In these contexts, the interaction with the apical ECM provides a patterned constraint that direct morphogenesis and allow a local stabilization of tissue shape. Moreover, apical ECM degradation in *Drosophila* prepupal wing²⁴ is required for the initiation of tissue deformation, further showing that the adhesion to the apical ECM inhibits tissue deformation. On the contrary, we here show that a dynamic interaction with the apical ECM gives rise to highly persistent and reproducible migration and deformation patterns. Thus, more than providing a static anchor, we propose that the apical ECM could as well favor cell and tissue deformation in the context of tissue migration.

Perspectives: Study the regulation of apical protrusive activity

We show that protrusion polarity is decreased in *sr^l* mutant tissue (Figure 21B). While *sr^l* mutation affects the polarization of apical protrusions, no important planar polarity defect of microchaetes can be observed in *sr^l* mutant (Figure 21A). Thus, the decrease of apical protrusion scores in *sr^l* is unlikely to arise from a lack of epithelial planar polarity information. We therefore propose that loss of *sr* function might rather derive from a global decrease of protrusive activity or of protrusions length. As *sr^l* reduces the level of Dumpy and loss of Dumpy prevents migration, we would like to test whether Dpy regulates protrusion activity. To do so, we will quantify protrusive activity by generating clones of cells expressing the actin reporter LifeAct::Ruby and the dsRNA against *Dpy*. Defects of apical protrusions emission in these clones would indicate that Dpy deposition is required for correct apical protrusive activity. Note that muscles should beforehand be laser ablated in this condition, in order to observe the effect of *Dpy* on protrusive activity independently on muscle pulling. Additionally, we have recently built a construct that we have named LifeAct_{Reverso}, which allows to generate mosaic labelling of actin in a context of global RNAi induction using *Act::GAL4* (Figure 35A). LifeAct_{Reverso} could thus be used to quantify protrusion polarity in a context of global induction of RNAi against Dpy (*Act>Dpy^{RNAi}*).

We have provided evidence that apical protrusion polarity is reduced in *dsh^l* (Figure 15B). To further test whether PCP polarity regulates the orientation of the protrusion, we will quantify the polarity of apical protrusive activity in *Act>Sple^{up}* or *Act>pk^{up}*. In these two genetic conditions, the migration orientations are locally highly affected or even reversed (Figures 18A, 19A). Thus, if PCP regulates migration direction by orienting apical protrusions, we predict a similar defects of apical protrusion polarity in *Act>Sple^{up}* or *Act>pk^{up}*. To test this, we will make use of the LifeAct_{Reverso} construct, to quantify protrusions polarity in *Act>Sple^{up}* and *Act>pk^{up}* backgrounds.

In order to gain further mechanistic insight into thorax migration, it would be interesting to screen for downstream regulators of apical protrusive activity. Cytoskeletal regulators, as actin nucleators or RhoGEFs, are potential regulators of apical protrusions dynamics. Interestingly, the formin Daam, the actin nucleator Arp3 and the Rho GEF Mbc localize in the apical protrusions (Figures 35B, 35D, 35F), and RNAi against *Daam* (*Act>Daam^{RNAi}*), against *Arp2* (*Act>Arp2^{RNAi}*) and against *Mbc* (*Act>Mbc^{RNAi}*) give rise to weak and patterned, yet reproducible decreases of migration A-P velocity (Figure 35C, 35E, 35G). Therefore, it would be important to determine apical protrusion polarity in these three contexts and determine whether the observed patterned of protrusion polarity defects correlate with the pattern of migration defects. Additionally, it would be interesting to extend the screen for other cytoskeletal regulators and cell-ECM adhesion proteins, like integrins.

Finally, our analysis of protrusion polarity and magnitude could be complemented by analysis of the dynamics of protrusions. Extraction of half-life of protrusions, heterogeneity in protrusion length or motility of single protrusion would be precious information. These measurements, would require the segmentation and the tracking of protrusions in time. Segmentation of such small and dynamic structures remains challenging with our current imaging set-up, and require the development of new image analysis tools. Performing the analyses in the future might provide additional information to understand how protrusive activity is regulated in time and to better characterize the mechanisms of protrusion polarization.

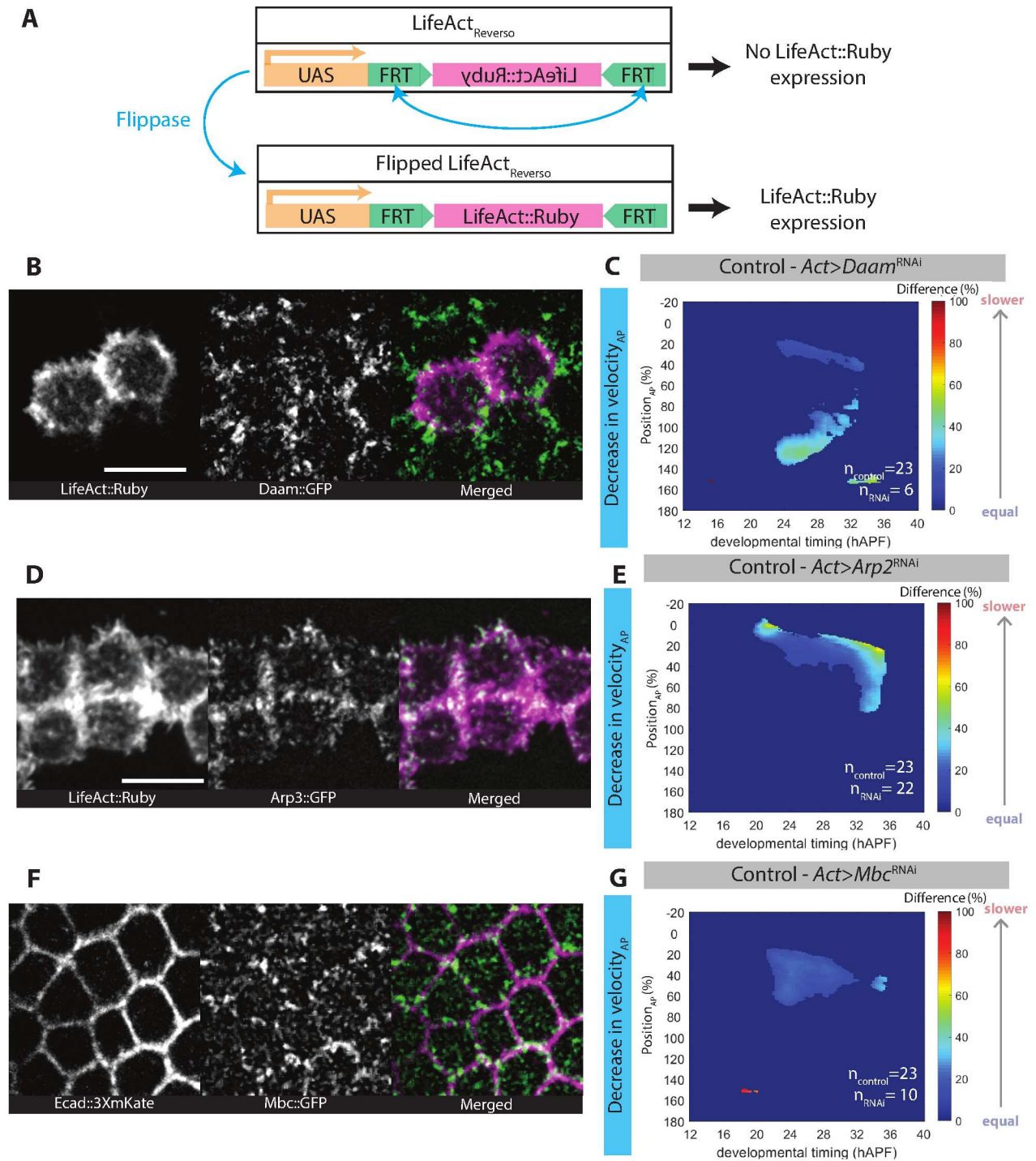


Fig.35: Functioning of LifeAct^{Reverso} construct: when flipped, LifeAct::Ruby sequence is de-reversed and can be transcribed using the UAS/GAL4 system (**A**). Apical projection above the adherens junction plane reveals the presence of Daam::GFP in the apical protrusions (**B**). Kymograph of difference in A-P velocity between control and *Act>Daam^{RNAi}* (**C**). Clonally expressed UAS>Arp3::GFP localizes in the apical protrusions (**D**). Kymograph of difference in A-P velocity between control and *Act>Arp2^{RNAi}* (**E**). Mbc::GFP localizes in the apical protrusions (**F**). Kymograph of difference in A-P velocity between control and *Act>Mbc^{RNAi}* (**G**).

[(B), (D) and (F)] Scale bars: 5µm.

$n_{\text{control}}/n_{\text{RNAi}}$: number of analyzed animals in the control/RNAi samples.

Role of Dpy in thorax migration

We have shown that *Dpy* expression is necessary for thorax cells to migrate. Remarkably, migration speed correlates with *Dpy*::YFP apical deposition rate. Mechanistically interpreting the role of *Dpy* in thorax migration remains nevertheless challenging. *Dpy* is a transmembrane protein, which contains a furin cleavage site in its extracellular domain²⁰⁴. It can therefore be cleaved and liberated into the extracellular space. As the carboxy-terminal ZP domain of *Dpy* may allow homotypic interaction, or heterotypic interaction with other apical matrix constituents containing ZP domains²⁰⁴, cleaved *Dpy* could act as a substratum for migration, while uncleaved *Dpy* could act as a receptor mediating adhesion to the substratum (playing similar roles as integrins). Our results indicate that at least part of *Dpy* is cleaved, as cells move, while *Dpy*::YFP globally does not follow cell movements in the anterior thorax. Thus, *Dpy* is a constituent of the apical ECM. How much uncleaved *Dpy* can be found at the apical membrane of thorax cells remains to be determined. We are currently building a fly line expressing a version of *Dpy* tagged with YFP on its extracellular domain, and by mKate on its cytoplasmic domain. Imaging of this construct could reveal the proportion of cleaved/uncleaved *Dpy*. This would be a first step in gaining more insight into the mechanistic role of *Dpy* in thorax cells migration. Moreover, we are building a fly line in which ZP domain is removed from *Dpy* sequence. Characterizing thorax flow in this mutant may shed light on the importance of the potential linkage between *Dpy* and the apical ECM through its ZP domain.

Perspectives: Study stronger mutant backgrounds

In the present study, we have used *dsh*¹ and *sr*¹ hypomorphic alleles to respectively show the implication of core PCP pathway and of *sr* in thorax flow and apical protrusive polarization. Although we have phenocopied *dsh*¹ and *sr*¹ A-P velocity decrease phenotypes using respectively RNAi against *stan* or against *sr*, we do not exclude the possibility that stronger phenotypes could be obtained by studying stronger loss-of-function alleles. Notably, we hypothesize that *Dpy*::YFP deposition rate decrease might be higher in stronger *sr* down-regulation contexts.

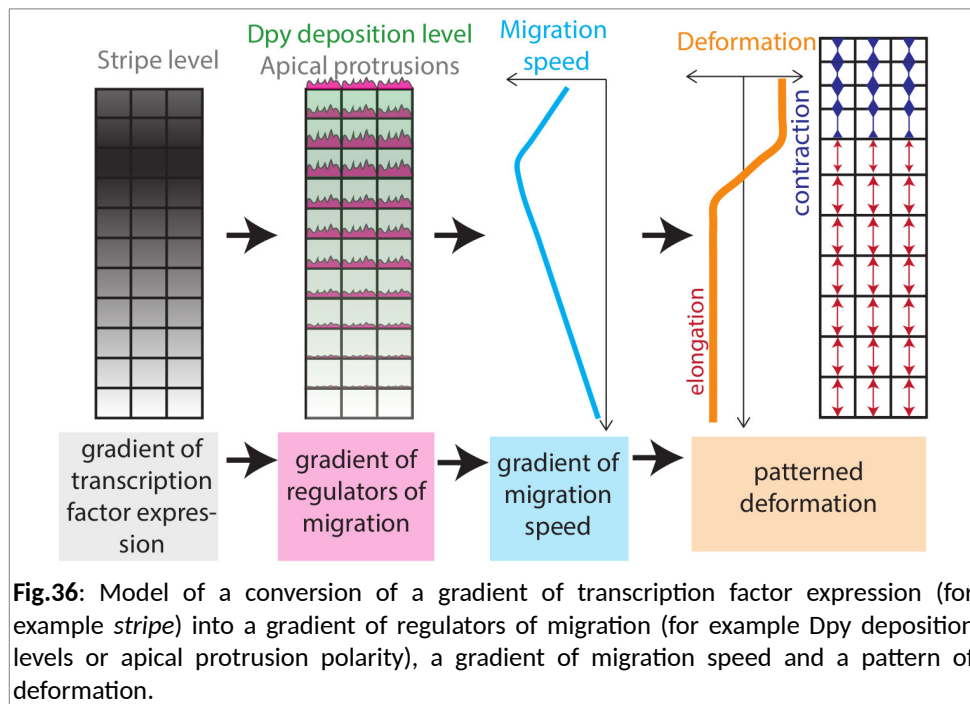
Hence, we will study thorax flow in the heterozygote *dsh*_{v26}/*dsh*¹ background, which shows stronger planar cell polarity defects than *dsh*¹ homozygotes males. We will as well estimate to what extent RNAi against *sr* leads to a decrease in *sr*::GFP signal, and we will try to induce RNAi against *sr* earlier to obtain stronger downregulation of *sr* expression.

Tissue deformation by collective cell migration

All the genetic conditions altering thorax flow migration pattern (dsh^l , $Act>stan^{RNAi}$, $Act>Sple^{up}$, $Act>pk^{up}$, sr^l , $dsh^l sr^l$, $Act>pk^{up} sr^{RNAi}$ and $Act>Dpy^{RNAi}$) show altered deformation patterns (compares Figure 2A with Figures 16C, 17C, 18D, 19C, 20F, 23E, 24E and 28D). In particular, ectopic elongation is observed in $Act>Sple^{up}$ (compare Figures 2A and 18D), and deformation is overall highly reduced in $Act>Dpy^{RNAi}$ (compare Figures 2A and 28D). We can thus conclude that collective migration not only contributes to thorax flows, but is also necessary for correct thorax deformation.

Classically, tissue deformation can be accounted for by a patterned sequence of acto-myosin contractility, apoptosis and cell division^{192,190}. The subdivision of the tissue into domains marked by specific patterns of transcription factors expression is key to account for the spatiality of these events. We here provide an additional model accounting for tissue deformation, based on collective cell migration. We thus propose that patterning information can as well be converted into patterns of expression of regulators of cell migration, leading to differential migration speeds, and eventually tissue deformation (Figure 36). Thus, expression of migration regulators could ensure a dual function: enabling collective cell translocation, but also deforming the tissue.

Furthermore, due to epithelial cohesion, the migrating domain can exert pulling forces that participate to the non-migratile neighboring regions deformations (in the present study, actively migrating anterior thorax pulls on the posterior thorax to trigger its movement). Thus, active migration can induce deformation of the migrating domain, but also of its surroundings.



Tissue-scale mechanical coupling

It has been shown and often hypothesized that neighboring morphogenetic events can influence each other, even on large scales. For example, endoderm invagination is known to contribute to germband extension^{172,205}. This integrated view first highlights the importance of considering the neighborhood of a morphogenetic region to fully understand the driving forces behind its deformation. It also accounts for the importance of the synchronization between adjacent morphogenetic modules: divergent dynamics can indeed cause tissue stress at the boundary between two morphogenetic modules.

We here quantitatively describe the coupling between neck invagination and thorax migration in four different contexts. (i) When decreasing neck invagination speed (*Dfd>Rok^{RNAi}* and *Dfd>sqh^{RNAi}*), we observed that the anterior tip of thorax migrating domain flows more slowly and compacts along the A-P axis. (ii) When increasing neck invagination speed (*Dfd>Mbs^{RNAi}*), we observed that the anterior tip of the thorax shows increased flow and elongates along the A-P. (iii) When laser ablating neck region and forcing thorax anterior tip to remain immobile (Ablation_{neck}), we observed high A-P compaction in the anterior thorax and effects in thorax flow that propagate throughout the thorax, yet with only mild effects in the posterior thorax. (iv) When genetically reducing anterior thorax migration (*Act>Dpy^{RNAi}* and *Act>pk^{up}*), we observed that neck invagination triggers tissue stretching at the anterior tip of the thorax. Taken together, these results show that neck invagination provide a local pulling force that can elongate cells of the anterior tip of the thorax domain. Moreover, correct dynamics of neck invagination is required to prevent cell compaction along the A-P axis at the anterior tip of the thorax.

Nevertheless, the spatial range of mechanical coupling between neck invagination and thorax migration is limited. Indeed, (i) thorax still considerably flows in a context of neck ablation (Ablation_{neck}), (ii) genetic disruption leading to mild neck invagination speed defects (*Dfd>Rok^{RNAi}*, *Dfd>sqh^{RNAi}* and *Dfd>Mbs^{RNAi}*) does not affect posterior thorax migration velocity, and (iii) initial neck invagination speed is not affected by anterior thorax migration defects (*Act>Dpy^{RNAi}* and *Act>pk^{up}*). Taken together, these results suggest that synchronization between neck invagination and thorax flow can only be partly explained by mechanical coupling. Hence, what could be the complementary mechanisms leading to the synchronization between neck invagination and thorax migration? We hypothesize that hormonal signals, like ecdysone signaling, might provide a systemic signal that could synchronize the onset of both neck invagination and thorax migration. Study of the impact of hormones on neck invagination and thorax migration dynamics and onset might thus shed light on the mechanisms leading to the synchronization between these two active morphogenetic events.

Even if we have observed that early neck invagination is not affected by severe thorax migration inhibition, whether later neck invagination phases depend on thorax migration is still an open question. Indeed, we have not yet performed imaging of neck invagination with high z coverage in *Act>Dpy^{RNAi}* and *Act>pk^{up}*, and have only followed neck invagination leading edge deepening till 22.5hAPF in these

conditions. Thus, imaging neck invagination deep dynamics in these conditions could reveal a potential contribution of thorax migration pushing force to neck folding.

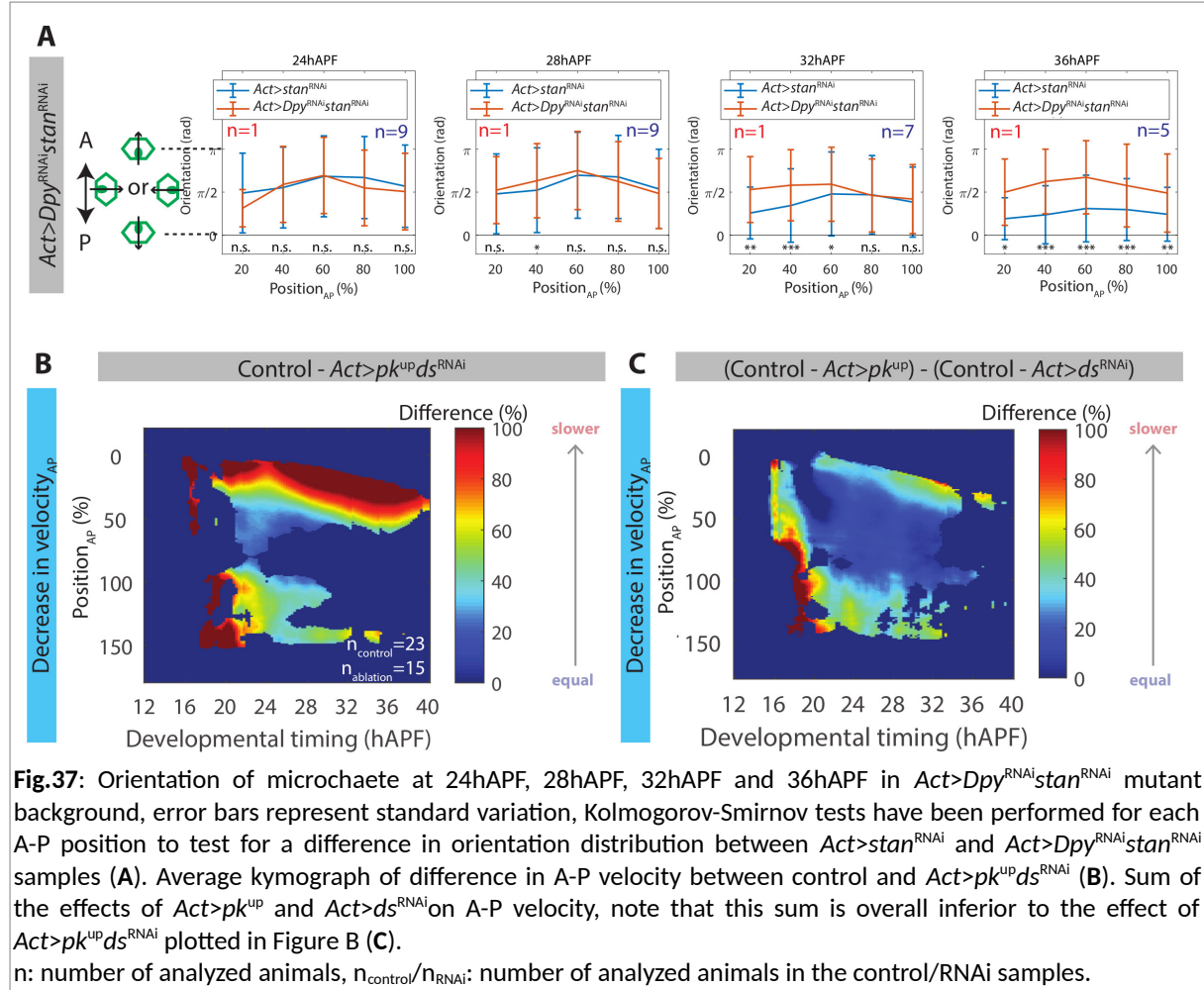
Planar cell polarity and patterning information

Drosophila epidermis is a fundamental model for the identification of genes involved in planar cell polarity³⁷. Even if core PCP pathway and Ft/Ds pathways are key regulators of apical planar polarity, the existence of additional planar polarity cues has often been hypothesized^{48,56}. In the wing for example, even when knocking down both core PCP and Ft/Ds pathways, trichomes orientation is not random and point towards the veins⁴⁸. We here show that the patterned transcription factor *stripe* provides planar polarization cues orienting both apical protrusions and microchaetes when core PCP is disrupted. Thus, planar polarity in the pupal epidermis may also results from the integration of transcription factors expression patterns. This idea echoes the planar polarization of MyosinII in *Drosophila* gastrula. MyosinII is independent from core PCP pathway but results from the expression of patterning genes in overlapping stripes⁵⁷.

Moreover, in *dsh*¹ mutant, we have observed a progressive rescue of microchaetes planar polarity defects in the tissue from 20hAPF to 36hAPF (Supplementary data 2). Whether thorax flow itself is required for such planar polarity correction remains to be tested. Preliminary results indicate that *Dpy* is required for microchaetes polarity rescue: induction of RNAi against *Dpy* and *stan* using *Act::GAL4*, combined with muscle laser ablation (*Act>Dpy^{RNAi}stan^{RNAi}*) triggers an absence of rescue of microchaetes planar polarity defects (Figure 37A). It thus appears that active migration could be pivotal to correct planar polarity defects in dorsal thorax. Nevertheless, *Dpy* could as well act on microchaetes reorientation independently on its role on cell migration.

More generally, we propose that dorsal thorax could be an interesting model system to complement the study of planar cell polarity in the wing and in the eye. Migration patterns appear to be a dynamic output of planar cell polarity. To further precise planar cell polarity dynamics and regulation, it would be interesting to spatio-temporally map polarity of core PCP and Ft/Ds pathways, using *Stbm::EYFP* and *Ds::EGFP* as reporters, as done in the wing⁴⁸. Describing planar polarity fields in wild type and mutant conditions would be precious to dissect planar polarization mechanisms in dorsal thorax. In addition, we have shown that Ft/Ds pathway disruption does not impact a lot thorax migration and microchaetes polarity. It would however be interesting to combine Ft/Ds disruption with core PCP disruptions, to test for interactions between Ft/Ds and core PCP pathway in dorsal thorax. Interestingly for example, we have found that migration defects due to overexpression of *pk* are increased when combined with RNAi against *ds* (Figures 37B-C).

As a conclusion, dorsal thorax appears to be an interesting model system to further characterize planar polarity pathways and their cross-talks with morphogenesis and migration.



Part3: Analysis of matrix motion *in vivo*

Low deformation of the apical extracellular matrix is associated with persistent migration *in vivo*

Part3: Analysis of matrix motion *in vivo*

Low deformation of the apical extracellular matrix is associated with persistent migration *in vivo*

Context

Studying the mechanical properties of the extracellular matrix (ECM) is pivotal for understanding development and cancer: *in vitro*, it has indeed been shown that fundamental processes like cell differentiation^{206,207} cell survival and division²⁰⁸ and cell migration^{209,210} (both as regards its speed and its direction) can be controlled by the stiffness of the culture substratum. On the other hand, ECM changes of stiffness and architecture are observed in both developmental contexts¹⁵⁶ and cancer^{211,212}. Understanding the impact of ECM mechanics on *in vivo* tissue biology could thus provide interesting insight into development and cancer mechanisms.

During cell migration, cells exert traction forces on their substratum to translocate. Understanding how traction forces distribute among a population of collectively migrating cells is of particular interest to gain insight into collective cell migration mechanisms. By plating cells on deformable micro-pillars¹⁴³ or soft gels containing fluorescent beads¹⁴⁴, it is possible to estimate cell traction forces *in vitro*, in single cells or collective migrating cohorts. These *in vitro* devices allow to record the motions of the ECM constituents induced by cell traction, which is one important measurement allowing the calculation of cell traction force exerted on the substratum. Whether it is possible to record ECM constituents motion during migration *in vivo*, however, remains an unexplored issue, but could potentially enable to estimate traction force and ECM mechanical properties *in vivo*.

We have shown in part 2 that dorsal thorax cells use the apical ECM to collectively translocate. The fluorescent reporter Dpy::YFP localizes in the apical ECM, forming steady deposition patterns that can be imaged at a sub-micrometric resolution during migration. Moreover, dorsal thorax cells mechanically interact with the apical ECM through apical polarized protrusions. Dorsal thorax migration thus appears as a suited model system to explore ECM constituents motion *in vivo*, during a process of collective migration.

Summary

Using high resolution live-imaging of Dpy::YFP and cell protrusions dynamics after laser ablation or in a physiological context, we explore the mechanical interaction between dorsal thorax cells and the apical ECM *in vivo*. We provide evidence that all cells of the thorax are mechanically coupled to the apical ECM, and that apical ECM display a pattern in motion across the thorax. Interestingly, regions showing low ECM motion coincide with regions showing high tissue migration persistence. We will as well show that apical ECM motion pattern is altered in *sr^l* mutant. Altogether, our results emphasize on the correlation between low apical ECM motion and dorsal thorax cells migration persistence.

Results

Study of the mechanics of ECM-tissue interface by laser ablation

Stretching after ablation is patterned across the tissue

We have shown in part 2 that mechanical coupling between dorsal thorax cells and the apical ECM can be assessed by laser ablation (Figure_{part2} 13). Our study was focused on the anterior thorax, the thorax region that migrates the fastest. We have here further used this laser-ablation assay to quantify protrusion stretching after ablation across the whole dorsal thorax, performing ablations not only in the anterior thorax but also in the posterior thorax (Figures 1A-B). Interestingly, we have discovered that protrusion stretching after ablation shows a pattern across the thorax (Figure 1C). Ablations performed at the front of the cells trigger high protrusion stretching when performed in the anterior thorax ($\text{Position}_{\text{AP}}=30-90\%$), but low protrusion stretching when performed in the posterior thorax ($\text{Position}_{\text{AP}}=90-130\%$). On the other hand, ablations performed at the back of the cells always trigger very low apical stretching in both anterior and posterior thorax, and may cause slightly higher stretching in the posterior thorax than in the anterior thorax (Figure 1C).

Note that we will hereafter call “anterior thorax” the region defined by $\text{Position}_{\text{AP}}=30-90\%$, and “posterior thorax” the region defined by $\text{Position}_{\text{AP}}=90-150\%$.

The fact that ablation performed at the front of the cells in the anterior thorax triggers high stretching shows that the front of the cells is mechanically coupled to the apical ECM in this region (Figure 1D). However, the fact that apical protrusions do not stretch after ablation in the posterior thorax can lead to three non-exclusive interpretations (Figure 1D): (i) in the posterior thorax, protrusions may not be connected to the apical ECM, or (ii) cells may be weakly attached to the ECM and could disconnect because of the force of the recoil, or (iii) protrusions may be anchored to the ECM, but the recoil could be directly communicated to the ECM and induce ECM recoil.

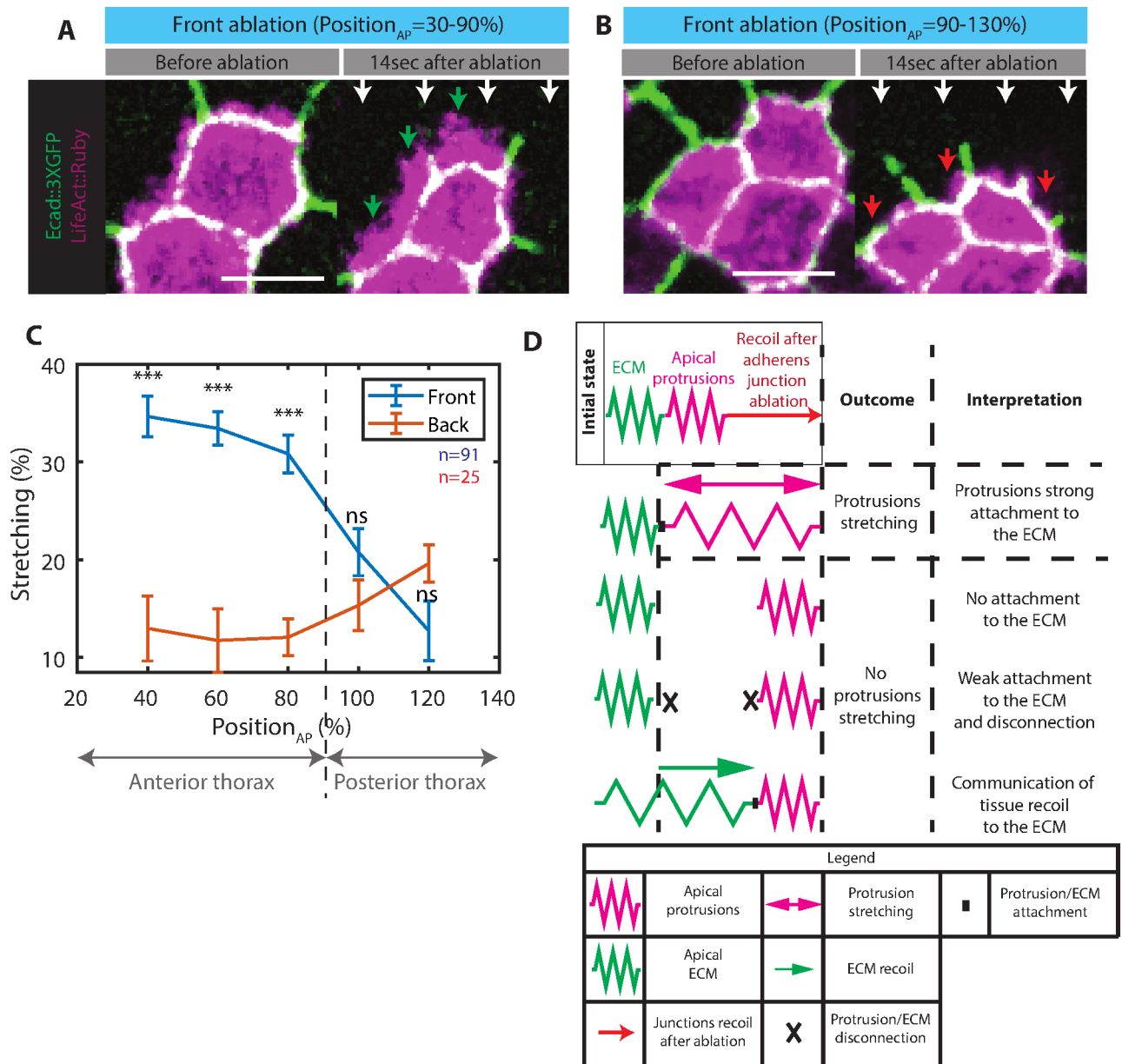


Fig.1: Stretching after ablation is patterned across the tissue. Ablations in the plane of the adherens junction network have been performed in front of clones of cells expressing LifeAct::Ruby, in a background of Ecad::3XGFP expression, inducing a backward recoil of the cells, and triggering a stretching of the apical protrusions when performed in the anterior thorax (**A**) or very low stretching of the apical protrusions when performed in the posterior thorax (**B**). Distribution of stretching after front and back ablations along the A-P axis, Welch tests have been performed to compare means of front and back ablations stretching for a given A-P position, n: number of front ablations (blue) and back ablations (red, **C**). Possible interpretations of protrusion stretching after ablation (**D**).

[(A) and (B)] White arrows represent adherens junctions recoil direction after ablation, green arrows point at highly stretched protrusions, red arrows point at the very lowly stretched protrusions. Scale bars: 5µm.

All thorax cells are mechanically coupled to the apical ECM

In order to test these three hypotheses, we have design an assay to explore the reaction of Dpy::YFP fibers to fast tissue displacements triggered by laser ablation. We have performed circular laser ablation at the level of adherens junctions and have analyzed the impact of the recoil of the tissue on neighboring Dpy::YFP network (Figure 2A). We have beforehand checked that a circular ablation performed on Dpy::YFP network itself does not trigger neighboring Dpy::YFP fibers recoil (Figure 2B), indicating that Dpy network does not store enough tension forces to trigger Dpy::YFP fibers recoil. Remarkably, similar circular laser ablation performed at the level of the adherens junctions triggers both tissue and Dpy::YFP fibers recoils (Figure 2B). We have spatially analyzed how much tissue recoil is transmitted to Dpy::YFP network. Interestingly, tissue and Dpy::YFP fibers recoils closely resemble one another in the posterior thorax, while tissue recoils trigger very little Dpy::YFP fibers recoil in the anterior thorax (Figure 2C). We can thus conclude that in the posterior thorax, adherens junction recoil is transmitted to apical Dpy::YFP fibers, whereas in the anterior thorax, recoil displacement mainly leads to protrusion stretching and trigger low Dpy::YFP fibers recoil.

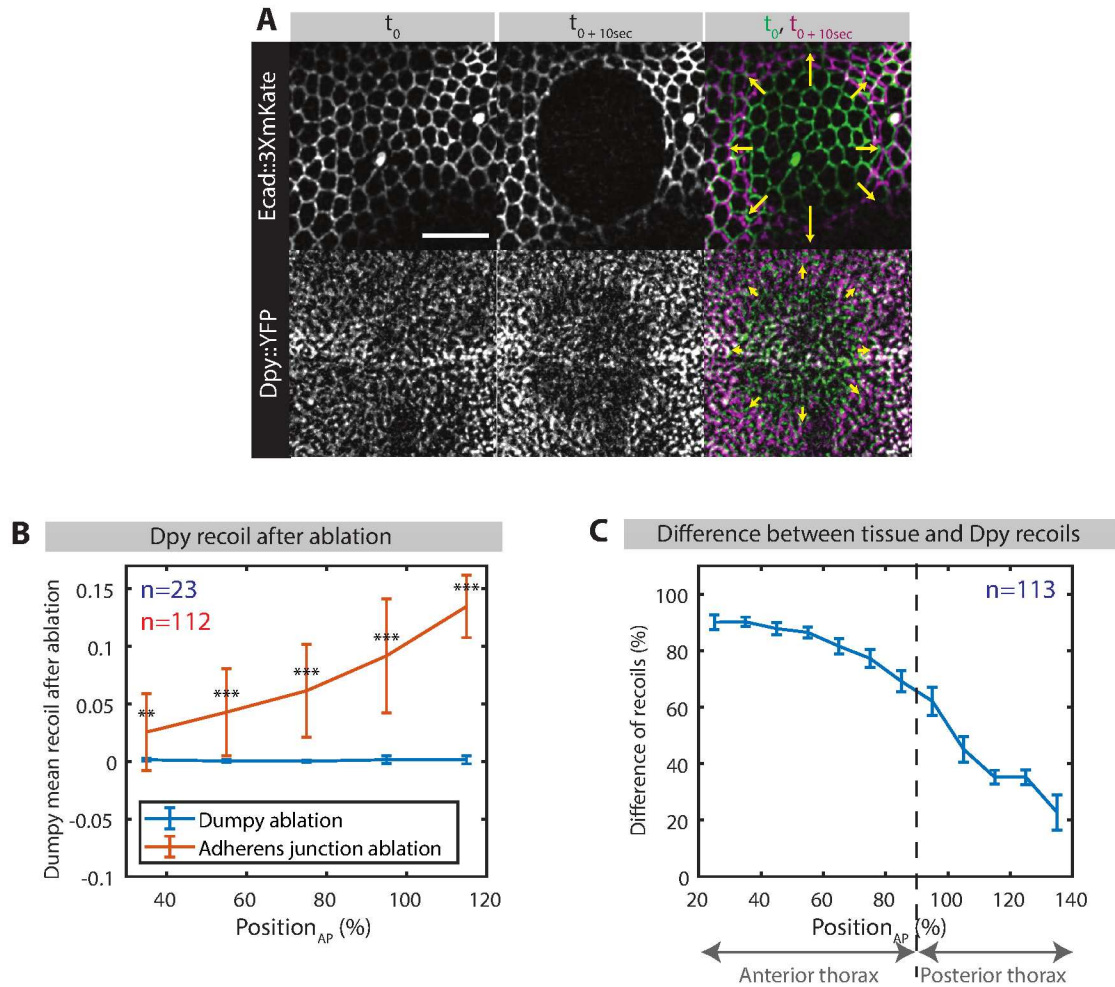


Fig.2: Tissue recoil is almost completely transmitted to proximal Dpy::YFP fibers in the posterior thorax. Example of an outcome of circular ablation at the level of the adherens junction, here triggering both adherens junctions and proximal Dpy::YFP fibers recoils, yellow arrows represent tissue and Dpy::YFP fibers recoils, scale bar: 25 μm , Dpy::YFP signal has been projected from 0.5 to 1 μm above adherens junctions plane (**A**). Mean initial recoil velocity of Dpy::YFP fibers after ablation performed at the level of proximal Dpy layer (data plotted in blue), or at the level of adherens junctions (data plotted in red). Note that ablations performed at the level of proximal Dpy layer reproducibly give a null recoil, error bars represent standard deviation, Welch tests have been performed for each A-P position to test for a difference in means between ablations performed at the level of Dumpy proximal layer and ablations performed at the level of adherens junctions (**B**). A-P gradient of difference of recoil between tissue and Dpy proximal layer, error bars represent standard errors, data has been averaged along the M-L axis (Position_{ML}=0-150%) and binned along the A-P axis (**C**).

[(B) and (C)] n: total number of performed ablations.

The interpretation of Dpy::YFP fibers recoil in the posterior thorax is not straightforward. First, as Dpy contains a transmembrane domain, the Dpy::YFP fibers we have recorded could correspond to a pool of Dpy proteins embedded in the apical membrane of the cells, which is not necessarily connected to the apical ECM (Figure 3A). Second, in the posterior thorax, the distance between the tissue and the chitin-rich layers of the apical ECM is high (Figure_{part2} 10E-G), raising the possibility that posterior cells are disconnected from the apical ECM. However, imaging of Dpy::YFP with a higher z coverage revealed that the posterior thorax is covered by a thick meshwork of Dpy::YFP fibers, which thickness corresponds to the distance between tissue and chitin-rich layer (Figure 3B). In order to test whether posterior tissue is mechanically coupled to distal Dpy::YFP layers, we have once again performed laser ablations in the posterior thorax, but we have this time analyzed the reaction of the Dpy::YFP network on all its thickness. Interestingly, tissue recoil induces a recoil of the distal apical layers of Dpy::YFP network, and we could observe a graded dissipation of Dpy::YFP fibers recoil from the most proximal to the most distal layers (Figure 3C). This result thus shows that posterior thorax tissue and distal ECM layers are mechanically coupled. To further highlight this mechanical coupling, we have analyzed the behavior of fibers labelled by ChtVisTomato after ablation. ChtVisTomato is a chitin reporter that is exported in the apical extracellular space¹⁹⁸. While it normally labels the region of the apical ECM layer that is just above Dpy::YFP network, some fibers labelled with ChtVisTomato can sometimes be found more basally, embedded in the distal Dpy layers. Interestingly, these fibers can show a recoil after tissue ablation (Figure 3D), further indicating a mechanical coupling between the tissue and distal cuticle layers. We can thus conclude that in the posterior thorax, tissue is mechanically coupled with the apical ECM, and that the tissue displacement triggered by laser ablation is transmitted to the ECM and leads to a gradient of ECM recoil of the successive apico-basal layers of Dpy network.

Taken together, our data shows that, even if their protrusions do not systematically stretch after ablation, thorax cells are all mechanically coupled to the apical ECM. Two opposed regimes of mechanical interaction with the apical ECM (and a gradual progression from one regime to the other along the A-P axis) can thus be found. After ablation, for the cells of the anterior thorax, recoil after ablation leads to the deformation of the front apical protrusions and to very low ECM recoil. On the other hand, for the cells of the posterior thorax, recoil after ablation leads to recoil of the apical ECM without deforming apical protrusions.

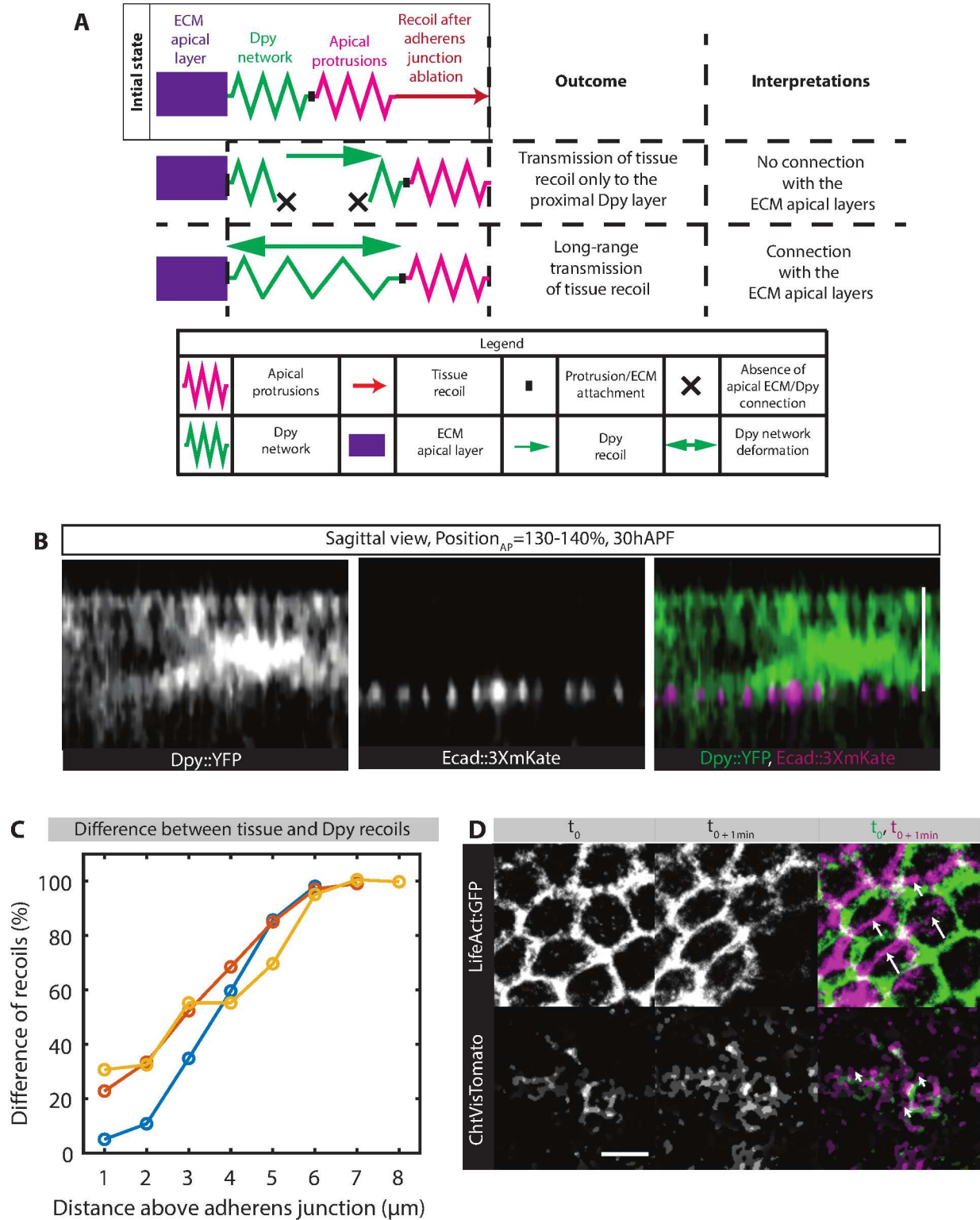


Fig.3: Cells of the posterior thorax are mechanically coupled to the apical ECM. Possible interpretation of proximal Dpy fibers recoil after ablation (**A**). Sagittal view of the posterior tissue of a pupa expressing Ecad::3XmKate and Dpy::YFP, note the high thickness of Dpy::YFP network, scale bar: 15μm (**B**). Difference between tissue and Dpy successive apico-basal layers recoil 1min after ablation at the level of the adherens junction at 25hAPF (**C**). Example of recoil of ChtVisTomato fibers after ablation performed at the level of adherens junctions at 25hAPF, scale bar: 5μm, white arrows represent the recoil of tissue and of chitin fibers, ChtVisTomato signal has been projected from 5 to 6μm above adherens junctions plane (which corresponds to the level of distal Dpy layers, **D**).

Estimation of the proportion of protrusions that are attached to the apical ECM

If we make the hypothesis that all protrusions are attached to the ECM and none of them detach during tissue recoil, tissue displacement triggered by laser ablation should lead to two antagonist mechanisms: protrusion stretching and Dpy proximal layer recoil (Figure 4A, with $\text{Proportion}_{\text{attached protrusions}} = 1$). In agreement with this idea, we have found that, after space averaging, protrusion stretching and difference between tissue and ECM recoil after ablation are very well anti-correlated (Figure 4B). However, the sum of these two scores is not equal to 100%, and we obtained residuals that can reach 55% for low ECM recoils scores (Figure 4C). This residual suggests that our initial assumption that all front protrusions are attached to the ECM is not valid. We thus propose that protrusion population is heterogeneous, with a given proportion ($1 - \text{Proportion}_{\text{attached protrusion}}$) of protrusions showing no or low attachment to the ECM (Figures 4A, 4D). Interestingly, residual between ECM recoil and protrusion stretching is minimal when assuming a proportion of attached protrusions of approximately 40% (Figure 4E). We thus propose that around 60% of apical protrusions are not attached to the ECM and do not participate to stretching of the apical area after ablation.

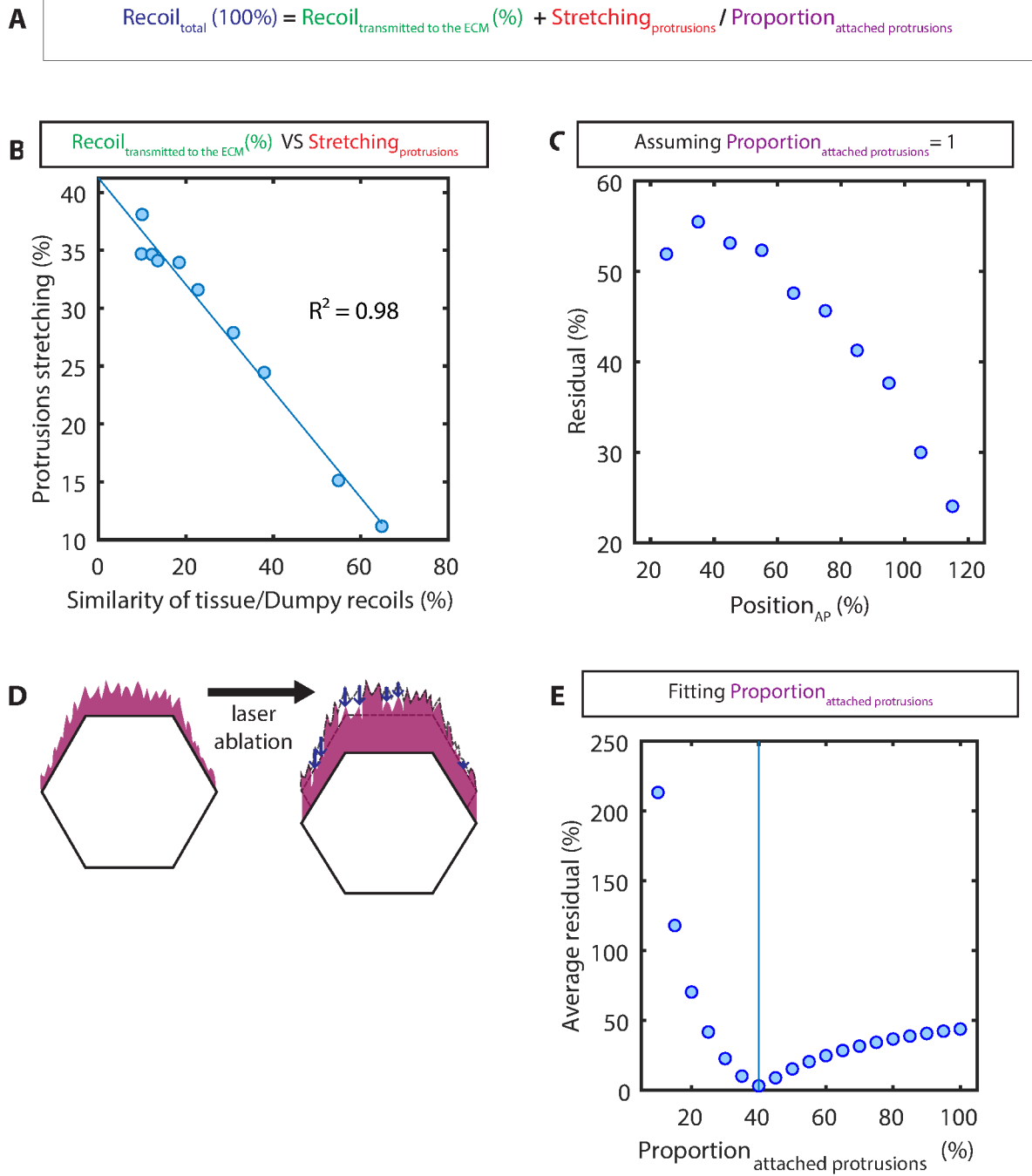


Fig.4: Around 40% of the anterior protrusions are not attached to the ECM in the wild type. Equation describing the distribution of tissue recoil among ECM recoil and protrusion stretching (A). Strong anti-correlation between similarity of tissue/Dumpy recoils ($\text{Recoil}_{\text{transmitted to the ECM}}$) and protrusions stretching ($\text{Stretching}_{\text{protrusions}}$) (B). Deviation from 100% of the sum $\text{Recoil}_{\text{transmitted to the ECM}} + \text{Stretching}_{\text{protrusions}}$, note that we here assume $\text{Proportion}_{\text{attached protrusions}} = 1$ (C). Illustration of heterogeneity of reaction to laser ablation of apical protrusions population. Some protrusions stretch while some other don't (or only partially stretch), blue arrows represent protrusion that do not participate to the apical stretching after ablation (D). Estimation of the $\text{Proportion}_{\text{attached protrusions}}$ that minimizes the average deviation from 100% of the sum $\text{Recoil}_{\text{transmitted to the ECM}} + \text{Stretching}_{\text{protrusions}}$ (E).

[(A), (C) and (E)] Similarity between tissue/Dumpy recoils and protrusion stretching have been averaged along the M-L axis and binned along the A-P axis (overlapping bins of 30% width and 10% spacing).

The gradient of ECM motion after ablation is shifted anteriorly in sr^1 mutant

We have shown in part 2 that sr^1 mutants shows a decreased migration speed (Figure_{part2} 20D), lower protrusion polarity scores (Figure_{part2} 22D) and lower Dpy deposition levels (Figure_{part2} 26A). This mutant background thus offers the possibility to precise the links between Dpy levels, protrusions polarity and behaviors of the ECM and the protrusions after laser ablation. For this reason, we have first investigated the similarities between Dpy proximal layer and tissue recoils after ablation in sr^1 mutant. Interestingly, the region of higher Dpy recoil after ablation is shifted towards the anterior in sr^1 (Figure 5A). We have then mapped protrusions stretching after ablation in sr^1 mutant. In concordance with Dpy/tissue similarities results, the region of smaller protrusion stretching is shifted to a comparable extent towards the anterior (Figure 5B). We can thus conclude that the gradient of apical ECM motion after ablation is shifted in sr^1 , with an expansion towards the anterior of the region of high transmission of recoil to the ECM and of low protrusion stretching after ablation.

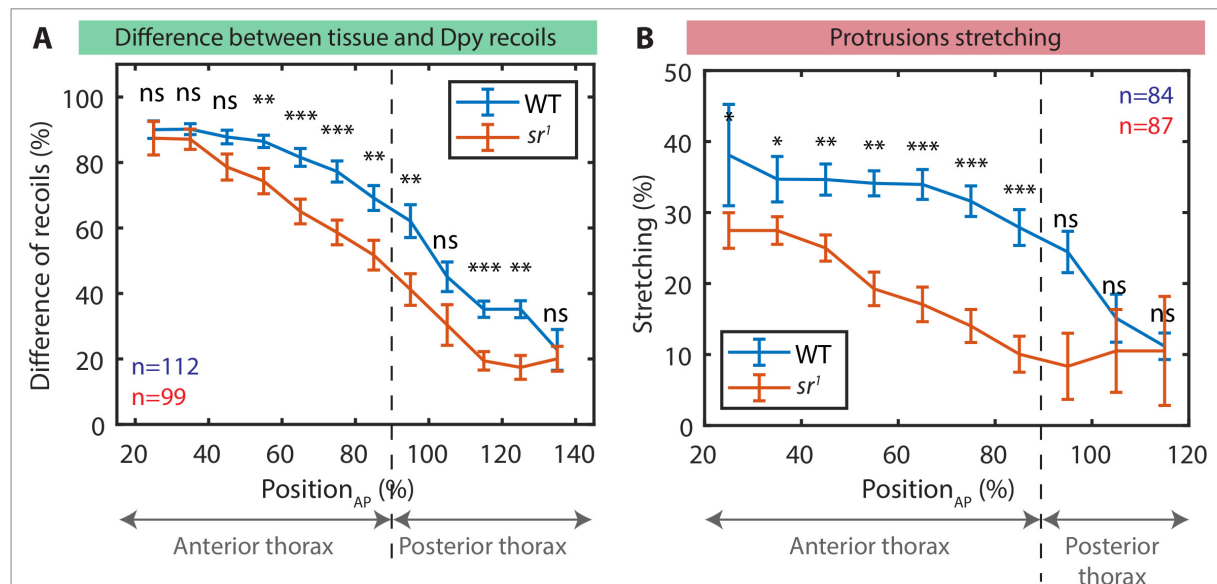


Fig.5: The pattern of ECM motion after ablation is shifted toward the anterior in sr^1 . Difference between tissue and Dpy proximal layer recoil after ablation in sr^1 and wild type conditions (A). Protrusions stretching after ablation in sr^1 and wild type conditions (B).

[(A) and (B)] Data has been averaged along the M-L axis and binned along the A-P axis (overlapping bins of 30% width and 10% spacing). Welch tests have been performed to compare for each A-P position bin control and sr^1 means. n: number of ablations in wild type (blue) and sr^1 (red).

Relationships between migration speed, Dpy deposition rate, protrusion polarity and behaviors of protrusions and ECM after ablation, in control and sr^l

The gradients along the A-P axis of migration A-P velocity, Dpy deposition rate, protrusion A-P polarity, similarity of recoil between ECM and tissue, and protrusion stretching after ablation are all well correlated at 25hAPF, both in wild type and sr^l (Figures 6A-B). This observation prompted us to investigate more in depth the relationship between these values. Interestingly, difference of recoils between ECM and tissue in sr^l follows the same Michaelis-Menten dependence towards Dpy deposition rates as observed in the wild type (Figure 6C). This observation suggests that Dpy deposition rates may be directly linked with ECM motion and protrusion stretching after ablation. Thus, defects of Dpy deposition rate in sr^l might be the cause of the anterior shift of the gradient of ECM motion after ablation.

Besides, for given Dpy deposition rates, protrusion polarity and stretching after ablation appear to be lower in sr^l than in the control (Figures 6D-E). Yet, in sr^l , protrusion polarity and stretching after ablation keeps on showing a similar linear relationship as observed in the wild type (Figure 6F). We thus hypothesize that low protrusions stretching after ablation observed in sr^l may be explained by a lower proportion of attachment of apical protrusions in sr^l background. Using our previous model (Figure 4A), we indeed predict that 30% of front protrusion are attached to the ECM in sr^l background (Figure 6G), against 40% in the wild type (Figure 4E). Thus, sr^l may affect migration by two different ways: first by affecting Dpy deposition rates, and second by decreasing the proportion of protrusions that are attached to the ECM. Interestingly, by correcting stretching scores for the proportion of attachment of the protrusions, we find that protrusion stretching follow the same Michaelis-Menten law of dependency on Dpy deposition rate in the control and in sr^l (Figure 6H). This result further suggests that Dpy deposition rates may regulate the protrusion-stretching/ECM-recoil ratio, while sr^l could affect the proportion of protrusion attachment independently of its role in Dpy deposition. Surprisingly, by correcting protrusion polarity scores by the proportion of attached protrusions, we also get similar law of dependency between Dpy deposition rate and protrusion polarity (Figure 6I). This observation suggests that the proportion of protrusions attachment may be linked with the degree of protrusion polarity. We propose that protrusions that are attached to the ECM could be more concentrated at the front or more elongated in the direction of global polarization, while unattached protrusions could distribute and/or be directed in a less polarized fashion. This assumption could explain why sr^l protrusions show lower polarity scores.

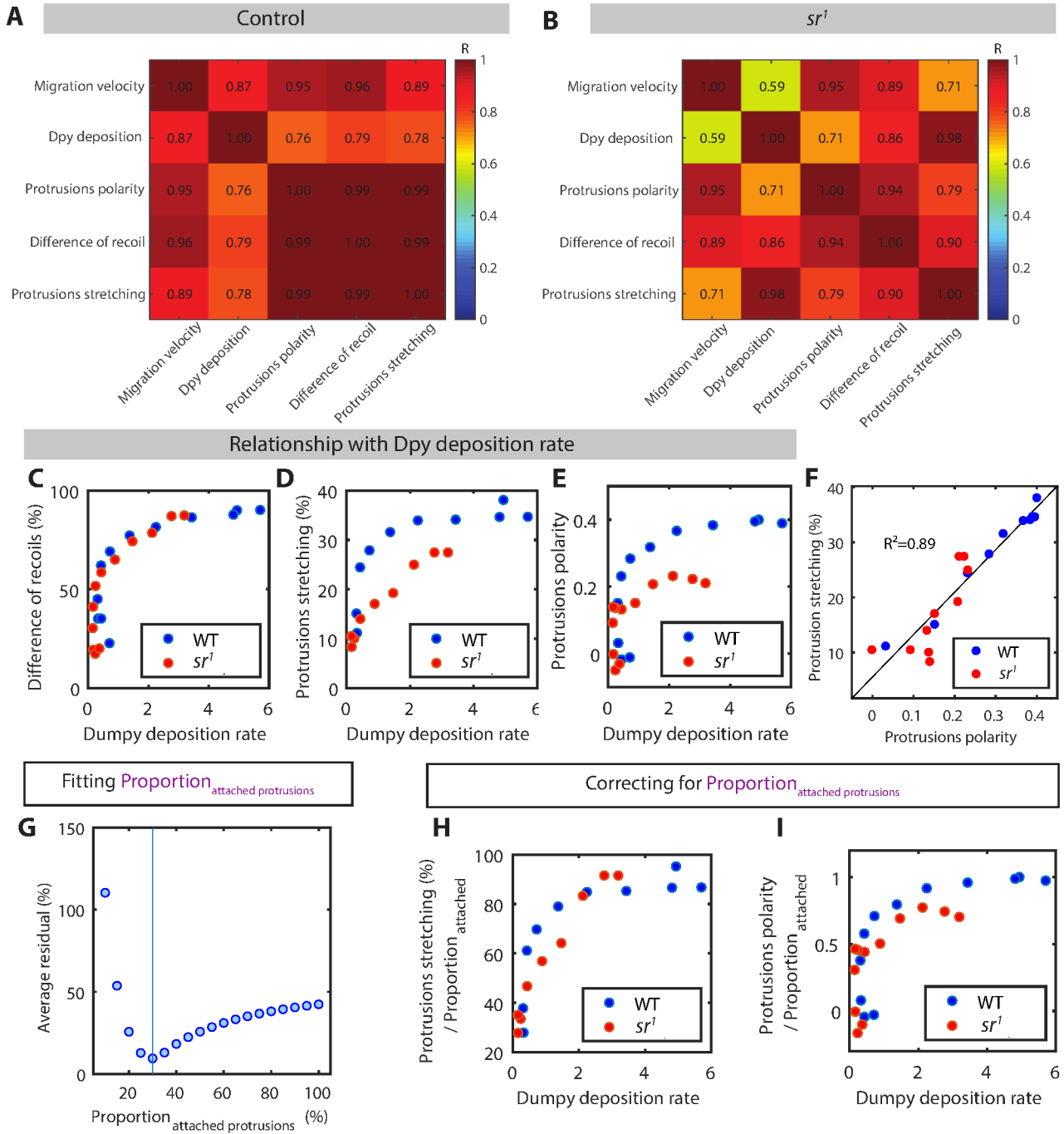


Fig.6: Study of the relationships between migration velocity, Dpy deposition rates, protrusion polarity, difference of recoil between Dpy::YFP and tissue, and protrusion stretching after ablation. Correlation matrix at 25hAPF between migration speed, Dpy deposition rate, protrusion polarity, difference of recoil between Dpy::YFP and tissue, and protrusion stretching after ablation for the control (A), and *sr¹* (B). Relationship, in wild type and *sr¹*, between Dpy deposition rate and difference of recoil between Dpy::YFP and tissue after ablation (C), between Dpy deposition rate and protrusions stretching after ablation (D), and between Dpy deposition rate and protrusions polarity (E). Linear relationship between protrusions polarity and protrusions stretching in *sr¹* and wild type (F). Estimation of the $\text{Proportion}_{\text{attached protrusions}}$ that minimizes the average deviation from 100% of the sum $\text{Recoil}_{\text{transmitted to the ECM}} + \text{Stretching}_{\text{protrusions}}$ (G). Relationship, in wild type and *sr¹*, between Dpy deposition rate and protrusion stretching after ablation divided by $\text{Proportion}_{\text{attached protrusions}}$ (H), and between Dpy deposition rate and protrusions polarity divided by $\text{Proportion}_{\text{attached protrusions}}$ (I).

[(A) to (I)] Data has been averaged along the M-L axis and binned along the A-P axis (overlapping bins of 30% width and 10% spacing). [(A) and (B)] Welch tests have been performed to compare for each A-P position bin control and *sr¹* means. [(H) and (I)] We have used 40% and 30% protrusion attachment for respectively wild type and *sr¹* backgrounds.

Study of ECM-tissue interface mechanics in physiological conditions

Dpy::YFP fibers show local movements of various amplitudes across the thorax

Laser ablation experiments have revealed that motion of ECM after ablation is patterned across the tissue: in the anterior thorax, ECM does not recoil much after ablation, while it does recoil in a similar fashion as the tissue in the posterior thorax. In order to test the relevance of these observations during physiological tissue flow, we have imaged with a high spatio-temporal resolution both cell contours labelled with Ecad::3XmKate and Dpy::YFP fibers. Interestingly, while Dpy network is stable between 30min intervals (Figure_{part2}25C and Figure 7C), we could detect Dpy::YFP local motion within 2min intervals (Figure 7A). By tracking Dpy::YFP fibers local movements, we realized that Dpy fibers were showing rare and small fluctuations in the anterior thorax, while they show faster and more frequent movements in the posterior thorax (Figure 7B). Thus, we can conclude that we can detect and quantify apical ECM components movements during dorsal thorax migration. Moreover, our results highlight a pattern of apical ECM components displacements, with frequent and fast movements in the posterior thorax, and rare and small movements in the anterior thorax.

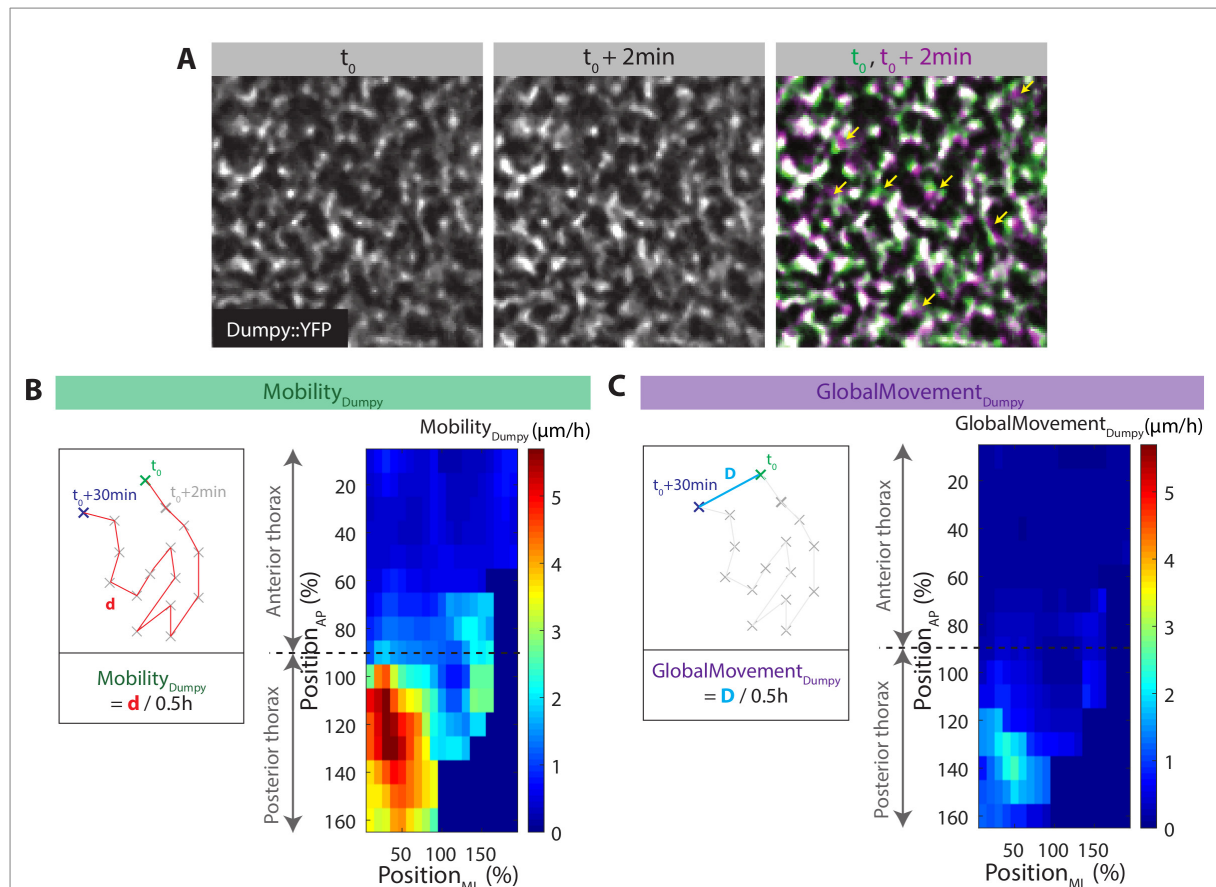


Fig.7: Dpy::YFP fibers show local movements of various amplitudes across the thorax. Pictures of the proximal layer of Dpy::YFP network, showing small movements between t_0 and $t_0+2\text{min}$ (highlighted by yellow arrows), scale bar: 5μm (A). Map of average velocity amplitude of Dpy fibers movements during 2min intervals, here called Mobility_{Dumpy} (B). Map of average velocity amplitude of Dpy fiber movements during 30min intervals, here called GlobalMovement_{Dumpy} (C).

[(B) and (C)] Data extracted from 2 timelapse movies of 30min long with a 2min time resolution. Dpy layer at a distance of 1.2μm-1.5μm from adherens junctions level has been analyzed.

Tissue shows a gradient of motion persistence

While we have characterized a global and persistent movement towards the anterior across the whole dorsal thorax using a 15min time resolution in part 2 (Figure_{part2} 1C), the behavior of cell contours at 2min time intervals during dorsal thorax migration was largely unexplored. We have thus tracked cell contours displacements with a 2min time resolution and a high spatial resolution.

Tracking of cell contours revealed a clear heterogeneity between anterior and posterior thorax. Remarkably, very low fluctuation around global movement was detected in the anterior thorax (Figure 8A). Furthermore, the A-P component of fluctuation around global movement is very low, and almost null in the anterior thorax. These results suggest that almost all cell contours fluctuations towards the A-P axis are canalized towards the main direction of motion in this region. Accordingly, fluctuations around average displacement along M-L axis are higher and more comparable between anterior and posterior thorax. In concordance with these observations, persistence of tissue motion is relatively low in the posterior thorax, and is very high in the anterior thorax, especially along the A-P axis (Figures 8D-F).

Remarkably, tissue motion persistence highly anti-correlates with ECM mobility (Figure 8G). This result could lead to two non-exclusive interpretations: (i) low ECM mobility could be permissive for persistent tissue migration, while ECM mobility could lead to more dissipation of migration energy and favor cell contours random fluctuations, or (ii) cell persistent migration could trigger low ECM movement, while high cell contours fluctuations could trigger high ECM mobility.

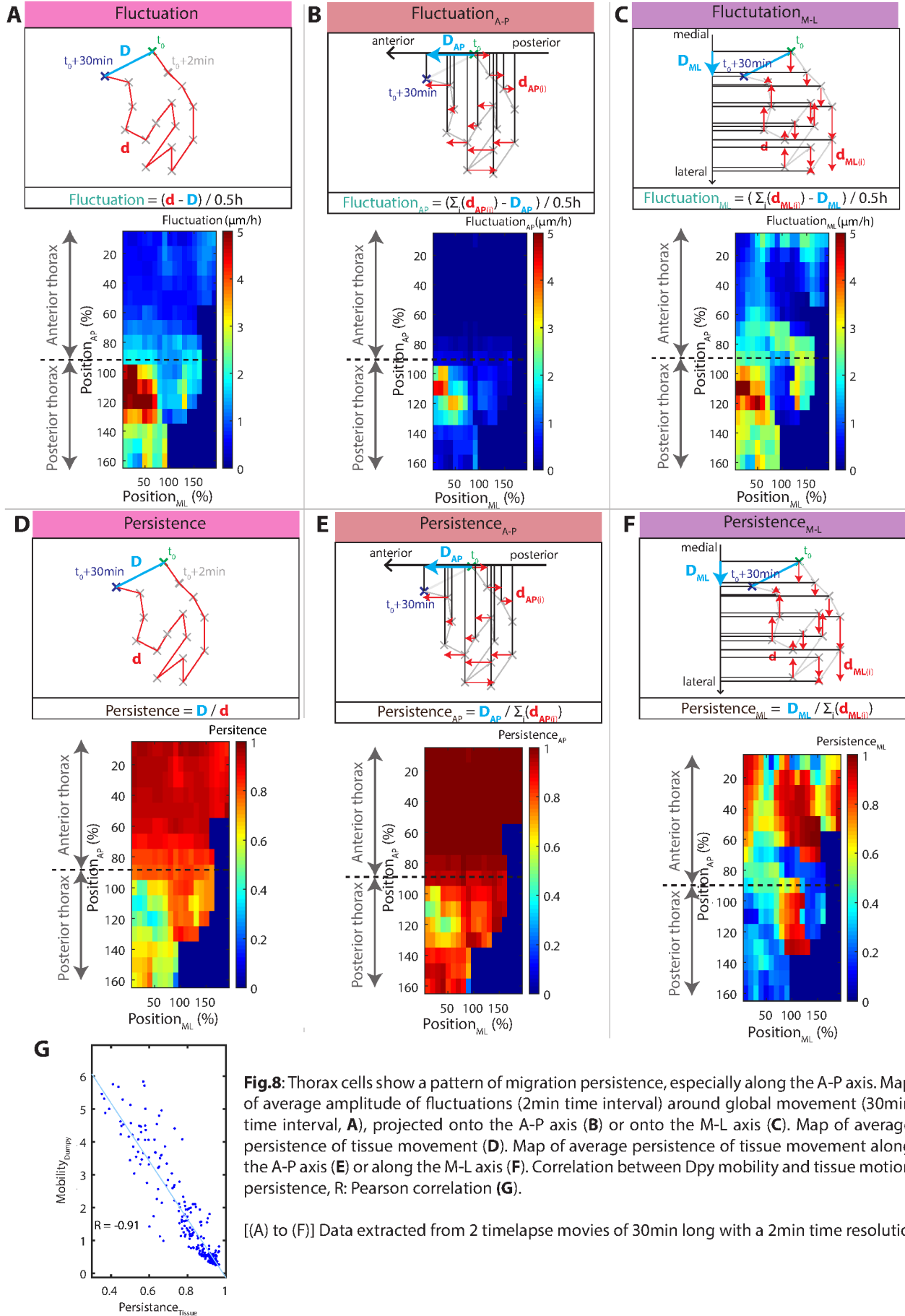


Fig.8: Thorax cells show a pattern of migration persistence, especially along the A-P axis. Map of average amplitude of fluctuations (2min time interval) around global movement (30min time interval, **A**), projected onto the A-P axis (**B**) or onto the M-L axis (**C**). Map of average persistence of tissue movement (**D**). Map of average persistence of tissue movement along the A-P axis (**E**) or along the M-L axis (**F**). Correlation between Dpy mobility and tissue motion persistence, R: Pearson correlation (**G**).

[(A) to (F)] Data extracted from 2 timelapse movies of 30min long with a 2min time resolution.

ECM motion is associated with underlying tissue similar motion

Averaging in time of tissue and Dpy::YFP fibers motions have revealed interesting spatial patterns. To go further, we have directly compared tissue and Dpy::YFP motion fields for each time point across the tissue. Interestingly, we have found that Dpy and tissue local oscillations show high similarities specifically in the posterior thorax (Figure 9A). Moreover, when comparing tissue and Dpy movements with ± 2 min, this similarity was lost (Figures 9B-C). We can as a result conclude that, in physiological conditions in the posterior thorax, cell motion is rapidly and almost completely transmitted to the apical ECM, mirroring the results obtained in laser ablation experiments.

In the anterior thorax however, Dpy fibers remain globally steady while tissue show fast migration speeds towards the anterior, and no straightforward similarity between Dpy and tissue motion fields was detected (Figure 9A). Yet, we wanted to investigate whether the small and rare Dpy fibers movements that we have detected in the anterior thorax could locally correlate with cell contours local motion. For this reason, we have isolated the anterior thorax region, and have analyzed whether local ECM movements could correlate with local cell contour deformations. Interestingly, we have discovered a systematic tendency of the tissue to locally deform so as to follow Dpy fibers movements, both along the A-P and the M-L axes (Figures 9D-E). Indeed, along the A-P axis, Dpy::YFP motion towards the main direction of movement (towards the anterior) is associated with tissue compression, while Dpy::YFP motion towards the opposite of the main direction of movement (towards the posterior) is associated with tissue elongation. Similarly, along the M-L axis, Dpy::YFP motion towards the main direction of movement (towards the midline) is associated with tissue compression, while Dpy::YFP motion towards the opposite of the main direction of movement (towards lateral) is associated with tissue elongation. We thus conclude that even in the region where Dpy network is overall stable, local instabilities of the ECM are associated with local changes in tissue movement and local tissue deformations (Figure 10B).

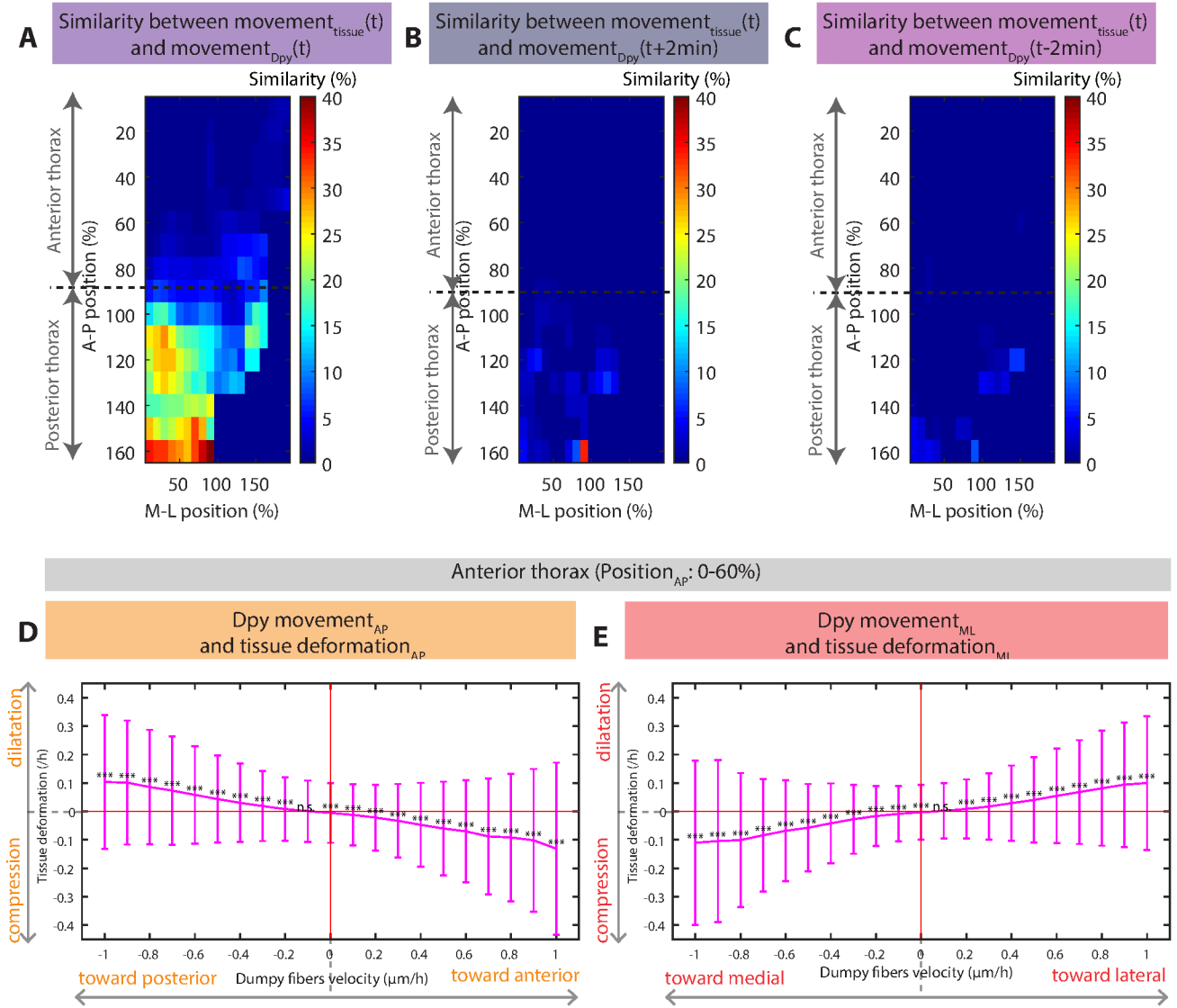


Fig.9: Comparison between cell contours and Dpy::YFP movements reveals similarities between tissue and ECM movements. Map of average similarity between Dpy and tissue movement compared at the same time (**A**), or compared with a lag of +2min for Dpy movement (**B**), or with a lag of -2min for Dpy movement (**C**). Correlation between Dpy movement and tissue deformation along the A-P axis (**D**), or along the M-L axis (**E**).

[(D) and (E)] Only data from the most anterior thorax (Position_{AP}: 0-60%) was used. Error bars represent standard deviations. A T-test has been performed for each Dpy speed fork to test whether tissue deformation mean value was different from 0.

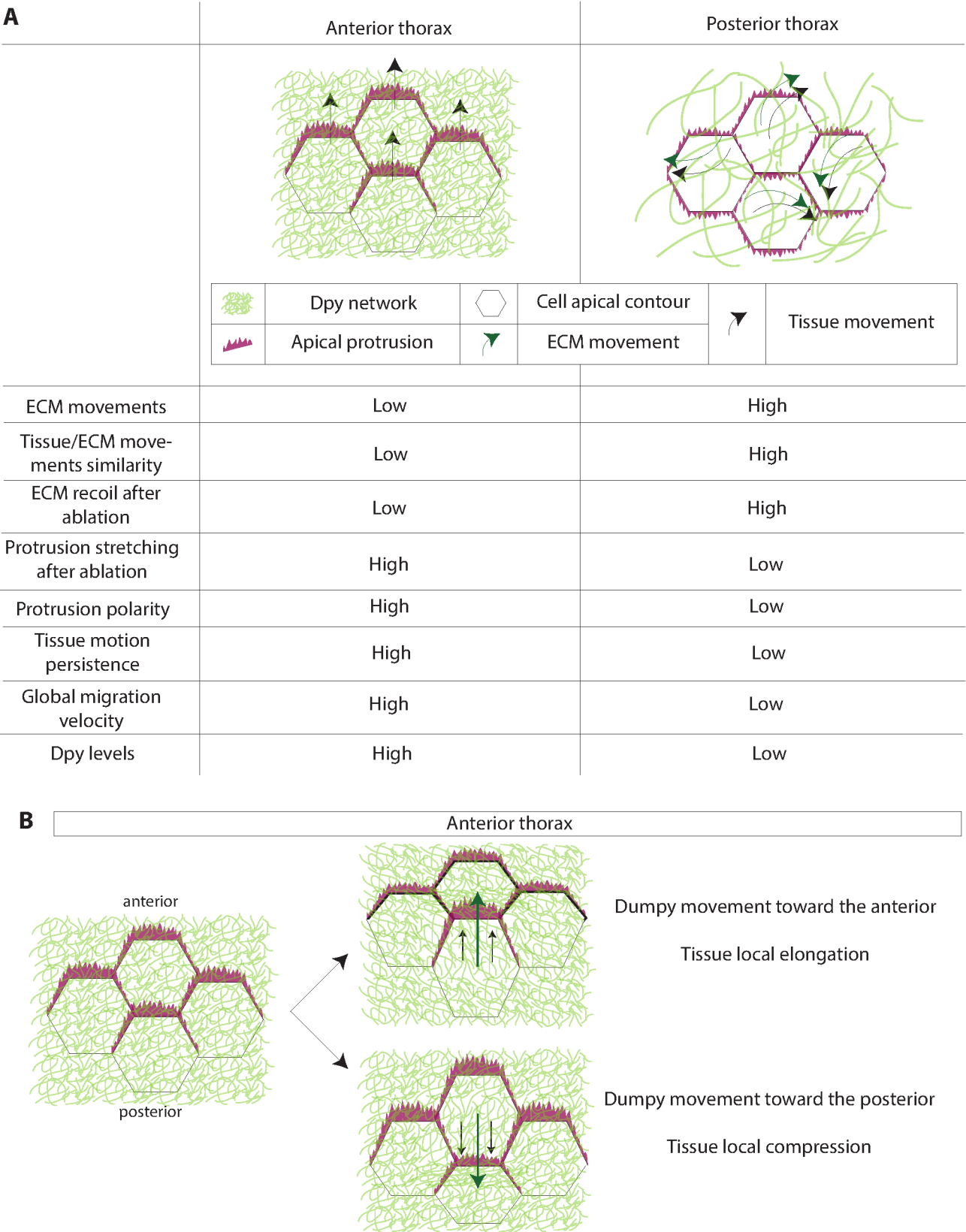


Fig.10: Anterior and posterior thorax show different mechanical regimes of interaction with the ECM (A). ECM instabilities are associated with local tissue deformation in the anterior thorax (B).

Discussion

Taken together, our results highlight the existence of distinct mechanical regimes of interaction with the ECM in the anterior ($\text{Position}_{\text{AP}}=30\text{-}90\%$) and posterior ($\text{Position}_{\text{AP}}=90\text{-}150\%$) thorax. In the anterior thorax, there is a discrepancy between tissue and ECM motion. In fact, ECM show very low motion, both after ablation or during physiological tissue flows. In this region, tissue migrates fast and in a persistent manner. In the posterior thorax on the contrary, ECM show high mobility, both after ablation and during physiological migration. ECM motion highly resembles tissue motion in this region, and tissue shows poor motion persistence and low global velocity (Figure 10A).

How to interpret the gradient of ECM motion?

The interpretation of these two regimes is not straightforward. First, we do not know whether the mechanical properties of the ECM are patterned across the tissue. It is however likely that the stiffness of the apical ECM is not homogeneous, as its composition varies across the tissue: for example, Dpy levels are high in the anterior thorax and low in the posterior thorax. Second, we do not know whether the mechanical properties of the protrusions vary across the tissue. One could for example envision that protrusions are more deformable in the anterior thorax than in the posterior thorax. As a result, we propose that the gradient of ECM motion after ablation could be interpreted in two non-exclusive ways: (i) the gradient of ECM motion could emerge from a gradient of ECM deformability, with a gradient from stiff anterior ECM to soft posterior ECM, or (ii) the gradient of ECM motion may reflect a gradient of protrusion deformability, with highly deformable protrusions in the anterior thorax and stiff apical protrusions in the posterior thorax.

In order to assess the validity of these two interpretations, direct measurement of the mechanical properties of the inner part of the apical ECM in the anterior and the posterior thorax would be precious. This could be achieved by using traction force microscopy or by using magnetic beads coated with antibodies binding Dpy::YFP network. However, these two techniques require the inner part of the apical ECM to be physically accessible. Yet, thorax cells tightly bind apical ECM. A protocol of decellularization of dorsal thorax that preserves Dpy::YFP layer has thus to be developed beforehand. Our preliminary tests have for the moment not given satisfactory results. As an alternative to decellularization, fresh sagittal sections of tissue could be used. We could also try to use laser ablation to locally free the apical ECM from cells.

Perspectives: Study ECM motion in more contexts

We have here studied ECM and protrusion behaviors after ablation in *sr^l*. Analyzing ECM motion during physiological cell flows in *sr^l* may be an interesting complement to our study. We expect to see higher ECM motions, as well as a reduced tissue motion persistence in this context. Moreover, ECM motion analysis (after ablation or under physiological conditions) could as well be performed in various mutant conditions, like *dsh^l*, *dsh^lsr^l* or *Act>Dpy^{RNAi}*.

We have here restricted our study to a given developmental timing (25hAPF). We could try to extend our study to earlier or later time points. This would enable us to obtain a more complete spatio-temporal description of ECM motion, and confront it with other measurements, like global flow velocity, Dpy deposition rates or protrusion polarity.

Finally, our dataset of *in vivo* analysis of ECM motion during physiological tissue flow is still preliminary (n = 2 timelapse movies). Analyzing a larger sample would be required to test to what extent ECM motion pattern is reproducible from an animal to another.

Perspectives: More deeply characterize ECM motion

We have here used Dpy::YFP as a marker for apical ECM. Unfortunately, Dpy::YFP is not highly expressed everywhere in the tissue, and is lowly expressed in the regions showing high ECM mobility. Piopio (Pio) is a ZP protein that is known to localize in the apical ECM in the wing, and that show a complementary deposition pattern as Dumpy in dorsal thorax (Figure_{part2}30C). We are currently building a fly line expressing a fluorescently labelled version of Pio. Using Pio as a complementary marker of the apical ECM could enable to study ECM motion more precisely in regions in which *Dpy* is lowly expressed.

Besides, our quantitative description of ECM and tissue motion under physiological conditions could be complemented by additional analyses. For example, segmentation of cell contours and cell tracking could be performed in the anterior thorax. This would first enable to analyze whether ECM motion preferentially happen in a particular domain of the cells. In fact, if apical protrusions are used by the cells to exert traction forces of the apical ECM, we expect ECM motion to preferentially happen in the neighborhood of front apical domains of thorax cells. Moreover, cell tracking could enable to check whether ECM motion preferentially happen in specific cells, or whether all cells have the same probability of triggering ECM motion. In the same line of thought, it would be interesting to detect the outlines of apical ECM regions showing significant motions, and analyze their size and their distribution on the tissue.

Towards the idea of a gradient of ECM stiffness and *in vivo* collective durotaxis?

Whether dorsal thorax shows an *in vivo* gradient of ECM stiffness is still unclear and hypothetical. However, this result could lead to two interesting models.

First, gradients of ECM stiffness is known to be at the origin of the phenomenon of collective durotaxis *in vitro*¹⁵⁴. A tempting model would thus be that ECM stiffness gradient could instruct thorax cells migration directionality. Such a model interestingly echoes the fact that *sr* and *Dpy* expression convey a directionality information when core PCP is disrupted. This might thus be explained by the fact the ECM stiffness gradient is sufficient to instruct migration directionality, and could even feedback on planar polarization of microchaetes. To test this hypotheses, modifying *Dpy* expression pattern could be very interesting. We are building a fly line enabling the overexpression of *Dpy::YFP* under UAS control. Combined with patterned GAL4 drivers, like *mirr::GAL4*, this construct could enable to create ectopic gradients of *Dpy::YFP* deposition, and check whether this gives rise to ectopic tissue flows towards zone of high expression of *Dpy*.

Second, a gradient of ECM stiffness could indicate that ECM stiffness is permissive for persistent migration, while too soft ECM dissipates migration force by deforming. This effect could further participate to migration speed gradients, by stabilizing protrusion and favoring persistent migration in the anterior thorax, and by dissipating migration force and favoring passive advection in the posterior thorax.

Material and methods

Material and methods

A/ *Drosophila melanogaster* genetics

1) *Drosophila* stocks list

Fluorescent reporters	
<i>Drosophila</i> stock	Reference
Ecad::GFP	Ref ²¹³
Ecad::3XGFP	Ref ²¹⁴
Ecad::3XmKate2	Ref ²¹⁴
utr::GFP	Ref ¹³⁴
sqh::GFP	Ref ²¹⁵
FRT40A sqh::GFP	Ref ²¹³
FRT40A sqh::RFP	Ref ²¹³
sqh::3XGFP	Ref ²¹⁴
Ubi::PH::GFP	Gift from F. Pichaud
UAS::PH::mCherry	Bloomington Stock Center
Dpy::YFP	DGGR (Kyoto center)
sr::GFP	This study
UAS::LifeAct::Ruby	Bloomington Stock Center
UAS::LifeAct::GFP	Bloomington Stock Center
UAS::ChtVisTomato	Gift from Paul Adler ¹⁹⁸
Mbc::GFP	This study
UAS::Arp3::GFP	Bloomington Stock Center
Mhct::GFP	Ref ²¹⁶
Daam::GFP	This study

Mutants	
Name of the construct	Reference
<i>dsh</i> ¹	Bloomington Stock Center
<i>sr</i> ¹	Bloomington Stock Center

RNAi and overexpression lines	
Name of the construct	Reference
<i>sqh</i> ^{RNAi}	<i>sqh</i> ^{TRIP.HMS00830} (Bloomington Stock Center) ²¹⁷
<i>Rok</i> ^{RNAi}	<i>Rok</i> ^{TRIP.JFO32225} (Bloomington Stock Center) ²¹⁷
<i>Mbs</i> ^{RNAi}	<i>Mbs</i> ^{TRIP.GL01207} (Bloomington Stock Center) ²¹⁷
<i>Dpy</i> ^{RNAi}	VDRC (GD25823)
<i>pot</i> ^{RNAi}	VDRC (GD8316)
<i>Daam</i> ^{RNAi}	<i>Daam</i> ^{TRIP.HMS01978} (Bloomington Stock Center) ²¹⁷
<i>Mbc</i> ^{RNAi}	<i>Mbc</i> ^{TRIP.GLC01361} (Bloomington Stock Center) ²¹⁷
<i>Arp2</i> ^{RNAi}	VDRC (GD29944)
<i>sr</i> ^{RNAi}	VDRC (KK105282)
<i>stan</i> ^{RNAi}	<i>stan</i> ^{TRIP.JFO2047} (Bloomington Stock Center) ²¹⁷
<i>ds</i> ^{RNAi}	<i>ds</i> ^{TRIP.JFO2842} (Bloomington Stock Center) ²¹⁷
<i>fat</i> ^{RNAi}	<i>fat</i> ^{TRIP.JFO3245} (Bloomington Stock Center) ²¹⁷
10XUAS:: <i>Sple</i>	Gift from Masakazu Yamazaki ⁴⁹
10XUAS:: <i>pk</i>	Gift from Masakazu Yamazaki ⁴⁹
UAS:: <i>fj</i>	Ref ⁴²
UAS:: <i>srB</i>	Bloomington Stock Center (#36533)

GAL4 drivers and clonal analysis	
Name of the construct	Reference
<i>Act</i> ::GAL4	Bloomington Stock Center
<i>Ubi</i> ::GAL80ts	Bloomington Stock Center
<i>Dfd</i> ::GAL4	This study
<i>tsh</i> ::GAL4	Bloomington Stock Center
<i>mirr</i> ::GAL4	Bloomington Stock Center
<i>Scut</i> ::GAL4	Bloomington Stock Center (#46255, Janelia Farm GAL4 project ²¹⁸)
<i>hsflp</i>	Bloomington Stock Center
tub-FRT-Gal80-FRT-GAL4	Gift from E. Martin-Blanco
lexAop-UAS-TagBFP:CAAX	Bloomington Stock Center

Dfd::GAL4, *sr*::GFP, *Mbc*::GFP and *Daam*::GFP lines were generated by CRISPR/Cas9-mediated homologous recombination at their respective endogenous loci, using *vas*-Cas9 line²¹⁹.

2) Overexpression and downregulation of protein activity

Down- and up-regulation of protein activity was performed using the UAS/GAL4 system²²⁰, using either *Act::GAL4*, *Dfd::GAL4* or *mirr::GAL4*. In all the experiments involving dsRNA, the expression was controlled in time using the GAL4/GAL80ts system¹⁸⁵. Pupae were raised at 18°C, in order to prevent dsRNA expression, and placed at 29°C 30-34h to induce expression. After 30-34h pre incubation, 12hAPF pupae were collected and imaged at 16hAPF.

3) Genetic mosaicism

Clonal analyses of UAS::LifeAct::Ruby or of UAS::srB was performed using the flip-out system²²¹. To generate small clones of UAS::LifeAct::Ruby expression for protrusion polarity analysis, pupae were collected at 0hAPF, heat-shocked 5 min at 37°C and imaged at appropriate timing. For overexpression of UAS::srB, larvae were heat-shocked for 15min at 37°C, 48h before puparium formation. Mosaics of sqh::GFP and sqh::RFP were generated using the FLP/FRT system²²¹. Thereto, larvae were heat-shocked at 37°C for 1h, and 2 days after heat-shock, 18hAPF pupae were analyzed.

B/ Fixed tissue imaging

Pupae expressing Ecad::3XGFP were dissected and fixed as previously described²²². Primary antibodies used were: mouse anti-Antp (DSHB, #8C11), rabbit anti-Dfd (1:100 dilution, gift from T. Kaufman), rabbit anti-phospho-Sqh (1:50 dilution, Cell Signalling Technology, #3671) and rabbit anti-Pio (1:100 dilution, gift from A. Jazwinska). Secondary antibody used were: Cy-3 conjugated donkey-anti-mouse IgC (Interchim, #715-165-150) and Cy-5 conjugated donkey-anti-rat IgC (Jackson ImmunoResearch).

Samples labelled for p-Sqh were dissected, labeled, imaged and processed under identical conditions to compare signal intensity levels. The Ecad::3XGFP plane was detected in each image (see C/3 section), to project the apical surface. The basal surface was projected by shifting the apical topographic map of 5µm and running a maximum projection on a thickness of 20µm below the shifted topographic map. Background signal was removed using Fiji (Subtract background, with rolling ball radius of 16µm).

To quantify apical p-Sqh intensity, the Ecad::GFP3X signal was segmented to generate a cortical mask of the cells. The head-to-thorax acto-myosin cable was manually segmented, and masks of cortical domains at different distance from the cable were automatically generated (using a homemade Fiji macro) and used to plot along the A-P axis p-Sqh cortical levels.

C/ Live-imaging

1) Pupa collection and mounting

Pupae were collected at white pupa stage (0hAPF), or at head eversion stage (12hAPF), and kept in incubators of appropriate temperature depending on the genetic condition (25°C or 29°C). Pupae were dissected and mounted as previously described²²³. In brief, pupae were ventrally glued to a coverslip using sticky tape, and dorsal pupal case was dissected off using micro-scissors and tweezers. Up to 15 pupae can be mounted on a single coverslip and imaged in the same session. A coverslip was then placed on top of dorsal thorax regions of dissected pupae. Dissection and mounting have been performed at timings varying from 14.5hAPF to 17hAPF. For neck invagination imaging, the anterior side of each pupa was shifted upward by placing additional layers of sticky tape under the head, in order to place neck region in contact with the coverslip.

2) Imaging

4D (x,y,z,t) time-lapse imaging of the samples was performed using an inverted spinning-disk confocal microscopes with wide field (Roper/Nikon/GATACA or Roper/Zeiss), equipped with sCMOS camera (Flash4 Hamamatsu) and temperature control chamber (with $\pm 0.3^\circ\text{C}$ precision and $\pm 0.1^\circ\text{C}$ stability), laser bench with lines 405, 491, 561 and 635nm, with 40X oil immersion objective (numerical aperture: 1.3). Movies of neck invagination dynamics and thorax flows were performed using a time-step of 15min, which is sufficient to efficiently track cells using Particle Image Velocimetry (PIV). Movies were acquired using a z-step of 1 μm , which is sufficient to detect the adherens junction plane and allows deep imaging (covering up to 50 μm for neck invagination imaging) without inducing noticeable damage. Imaging of thorax flow (without imaging neck invagination) was performed with smaller z coverages (around 20 μm). Thorax flows have been imaged during long imaging sessions of minimum 12h and starting before 18hAPF, the longest sessions covering from 13hAPF to 38hAPF. Neck invagination has been typically imaged from 16hAPF to 25hAPF. Autofocus (Metamorph software) enabled keeping the focus on appropriate depth.

High resolution pictures of apical protrusions and of neck cable acto-myosin enrichments were performed using 100X oil immersion objective (numerical aperture: 1.4), and z-steps of 0.1 μm . High resolution time-lapse movies of Ecad::mKate and Dpy::YFP fibers movements were performed using the same 100X oil objective, and using a z-step of 0.3 μm and a time-step of 2min.

3) Detection of the adherens junction plane and projection

For each time-lapse movie of Ecad fluorescent labelling, the adherens junctions plane was detected in each frame using a custom Matlab code. In brief, for each time-point, a 3D variance filter was applied to the hyperstack (x,y,z), the filtered image was then downsampled in (x,y) and maximal variance plane (z) was detected for each pixel (x,y) of the downsampled image. The downsampled image was then progressively up-scaled, and maximal variance plane was detected in progressively up-scaled images, with restraining the search for maximal variance to the neighborhood of the plane of maximal variance identified in downsampled images. This up-scaling and search for topographic map loop was repeated until coming back to the real resolution in (x,y). The output was thus a topographic map for each time-point (t), showing the evolution of the depth (z) of the tissue for each pixel (x,y).

These topographic maps have been used to project signals on specific depth around the adherens junction levels (either around it, or at a given fixed distance of it), and to study neck invagination dynamics. They have also been used to project apical Dpy::YFP signal, apical protrusions labelled with LifeAct::Ruby and nuclear sr::GFP signal. For all other analyses maximal z projections (Fiji) were used. Finally, topographic maps have been used to calculate the distance between the apical surface of the tissue (labelled with LifeAct::GFP) and the inner part of the chitin-rich layer of the cuticle (labelled with ChtVisTomato).

4) Spatio-temporal registration of the time-lapse movies

a) Spatial registration

From 14hAPF to 17hAPF the head-to-thorax boundary, the most anterior pair of thoracic medial macrochaetes and the head-to-thorax boundary are immobile, and represent precise and reproducible spatial marks than can be identified using Ecad::GFP or other cortical markers. We have used the position of these structures before 18hAPF to register all time-lapse movies in space. Along the medio-lateral (ML) axis, the midline position was defined as $\text{Position}_{\text{ML}} = 0\%$, and the most anterior and medial pair of thoracic macrochaetes was defined as $\text{Position}_{\text{ML}} = -100\%$ (left macrochaete) and $\text{Position}_{\text{ML}} = 100\%$ (right macrochaete). In all the quantifications, the two hemi-thoraces were averaged, and values were systematically expressed in the reference of a right hemi-thorax, so that M-L coordinates only vary from 0 to 100%. Along the antero-posterior (A-P) axis, the initial position of the head-to-thorax boundary in a given M-L box ($\text{Position}_{\text{ML}} = 50\%$) was defined as $\text{Position}_{\text{AP}} = 0\%$, and the average A-P position of the most anterior and medial pair of thoracic macrochaetes was defined as $\text{Position}_{\text{AP}} = 100\%$.

b) Temporal registration

Pupa collection was performed with ± 1 h precision. To register more finely all pupae in time, we first identified in each movie the timing at which all microchaete precursors finished their terminal division in a given A-P region ($\text{Position}_{\text{AP}}=20\text{-}50\%$) as an absolute timing marker of 22hAPF ($t_{\text{Microchaete22hAPF}}$). Second, we used the initial A-P acceleration curve averaged of thorax cells for a given region ($\text{Position}_{\text{ML}}=0\text{-}100\%$, $\text{Position}_{\text{AP}}=20\text{-}50\%$ for conditions with normal anterior flow, $\text{Position}_{\text{AP}}=60\text{-}90\%$ for conditions with abnormal anterior flow) to refine time registration between the animals of identical genotypes. The second step of time registration refinement was not performed in conditions showing no clearly defined initial A-P acceleration. For each condition, the time at which $\frac{3}{4}$ of maximal velocity was reached ($t_{3/4v_{\text{max}}}$) was calculated for each animal, and timings were corrected so that $t_{3/4v_{\text{max}}}$ of all animals of the condition coincide, and that the average $t_{\text{Microchaete22hAPF}}$ of the condition coincide with 22hAPF. This correction thus enables to refine time registration based on velocity curves, while keeping the absolute timing of 22hAPF based on microchaetes terminal division, which becomes more precise as averaged for all the animals of the condition. Note that this intra-condition time registration refinement did not triggered deviations of more than ± 1 h from the initial dataset registered based on $t_{\text{Microchaete22hAPF}}$.

5) Quantification of tissue flows**a) PIV analysis and preprocessing**

Thorax flows were calculated based on automatic tracking of cell contours labelled with *Ecad::GFP*, *Ecad::3XGFP* or *Ecad::mKate*⁴⁵. The field of view was subdivided into boxes of approximately $5\mu\text{m}$ length ($16 \times \text{Pixel}_{\text{size}}$, with $\text{Pixel}_{\text{size}} = 0.322\mu\text{m}$), and PIV tracking was applied on each grid for all time intervals. Masks were beforehand generated for filtering out both the zones of the field of view that do not correspond to the tissue (field of view outside tissue region, neck invagination region when it gets too deep to be imaged, and local shallow tissue folds due to mouting pressure). Regions in which masking was required were first manually selected for each time-lapse, and refined by applying a 2D variance filter on the image (with a radius of 2 pixels in x and y, with $\text{Pixel}_{\text{size}} = 0.322\mu\text{m}$) and by manually thresholding the filtered image in order to identify regions of low signal variance, which correspond to non-tissue areas.

Experimental imaging conditions can lead to occasional small global drift of the sample. These translational drifts were corrected for, either by automatic tracking (Fiji plugin MultiStackReg), or by 4D (x,y,z,t) manual tracking of fixed fluorescent particles that are attached to the apical extracellular matrix and remain immobile. Drift correction was applied before PIV analysis.

As dorsal thorax can be considered as flat for A-P position superior to 10%, we did not apply any correction for curvature of the tissue to generate the kymographs of velocity of thorax flow in most of the conditions. However, topography determination and curvature correction of the flows were performed in conditions in which thorax flow next to the folded neck region was analyzed (see C/3 and C/7 sections). All the flow and deformation analyses in part 1 have been corrected for curvature, as well as the analyses of the phenotypes of *Dfd>Rok^{RNAi}*, *Dfd>sqh^{RNAi}*, *Dfd>Mbs^{RNAi}* and the associated controls in part 2.

As the duration of animal development is temperature dependent, a time correction factor of 0.79 was applied to data obtained at 29°C to be able to compare them with data obtained at 25°C²²⁴. Data was linearly interpolated to have a fixed time-step of 15min, a step of 1% along the A-P axis and of 4% along the M-L axis.

b) Lagrangian description

In a Lagrangian description, objects (here tissue sub-regions) are identified by their initial position and are tracked in time. What is studied is the evolution of the velocity of the tracked object in time. Such a description is interesting to study thorax cell movements, as the initial position of the cells on the thorax corresponds to the set of transcription factors they express, hence their genetic identity (their positional information).

We thus pseudo-tracked the cells using the flows calculated by PIV, and transformed Eulerian based mapping of cell flows into Lagrangian maps. In brief, Eulerian maps (x,y,t) have been filtered using masks defining non-tissue positions, interpolated for missing values (Matlab function `inpaintn`²²⁵), smoothed in time and in space (radius of time smoothing of 1.25h, spatial radius of smoothing of 7% along the A-P axis and 28% along the M-L axis, smoothing method: average). Tracking of each region was then performed based on this smoothed matrix, and used to express velocities which were only smoothed in time (1.25h radius) in a Lagrangian manner. Non-tissue regions were then reintroduced in the Lagrangian maps by transforming the Eulerian masks maps into Lagrangian mask maps.

c) Normalization

Variation in animal size was corrected for by normalizing Lagrangian velocity maps by the length of the animal L_{ref} (which corresponds to 100% along the AP axis, defined by the neck-head-boundary and position of anterior macrocheates distance). Velocities were then expressed so that the archetypal length of the animal is set to 375 μm .

d) Mean velocity kymographs and standard deviation kymographs

Kymographs represent the evolution in time of position along a given axis. We here call “velocity kymograph” the graphical representation of the evolution in time of velocity along the A-P axis. Velocity kymographs were generated by averaging the A-P (or the M-L) component of velocity vectors along the M-L axis (for $\text{Position}_{\text{ML}} = 0\text{-}100\%$) for each time point. Mean velocity kymographs were obtained by averaging the kymographs of all the animals obtained for a given condition. Pixels of the mean kymograph covered by less than 3 animals were filtered out. Similarly, the velocity standard deviation among animals was calculated for each pixel of the kymograph, to generate velocity standard deviation kymographs.

e) Comparison of mean velocity kymographs between conditions

In order to compare the mean velocity between two conditions, the mean velocity kymographs of both conditions were calculated, and subtracted from one another to get a kymograph of difference in velocity between the two conditions. In most cases, velocity difference was expressed as a percentage of the velocity of the control.

For each pixel (y,t) of the kymograph, Welch’s tests were performed to test whether the local difference in velocity between the two conditions was significant. The obtained P-value map was used to filter out of the kymograph of difference in velocities the pixels associated with p-values > 0.01.

In order to cope with time imprecision, we performed 50 iterations of random time shifts for each kymograph (ranging from -1h to +1h), and performed Welch’s tests between the two conditions for each pixel (y,t) and for each of the 50 random time shifts iterations. We thus obtained for each pixel 50 p-values corresponding to the 50 random time shifts. We have then picked for each pixel the 95-quantile p-value among the 50 iterations (i.e. the highest p-values) to filter out false positives due to time imprecision.

f) Calculation of global orientation of thorax flow

In order to calculate the global flow and flow orientations, A-P and M-L components of velocity were summed from 18hAPF to 30hAPF for each A-P position, and averaged for a given A-P fork ($\text{Position}_{\text{AP}}=0-75\%$), and the orientation of the obtained average velocity vector was extracted.

6) Quantification of tissue deformations

To quantify tissue deformation, PIV-based velocity fields were first filtered, interpolated and smoothed both in time and in space (radius of time smoothing of 1.25h, spatial radius of smoothing of 7% along the A-P axis and 28% along the M-L axis). Tissue deformation rates can then be inferred from Eulerian velocity maps, using the following formula:

$$\text{Deformation AP}(x, y, t) = \frac{\text{SpeedAP}(x, y-1, t) - \text{SpeedAP}(x, y+1, t)}{2 * \text{Boxsize} * \text{timestep}}$$

$$\text{Deformation ML}(x, y, t) = \frac{\text{SpeedML}(x+1, y, t) - \text{SpeedML}(x-1, y, t)}{2 * \text{Boxsize} * \text{timestep}}$$

with $\text{Boxsize} \approx 5 \mu\text{m}$ (size of the PIV grid)

Note that the deformation score is positive for elongation, and negative for compression.

Eulerian maps of tissue deformation rates can then be expressed with Lagrangian coordinates using PIV-based flows, and averaged along the M-L axis to get a deformation kymograph. Cumulative deformation kymographs can then be calculated by integrating in time deformation rates for each A-P position.

7) Quantification of neck invagination dynamics

a) Quantification of tissue depth

Tissue depth maps and invagination leading edge depth curves were calculated based on topographic maps (see C/3 section). To correct for z-drifts, we registered topographic maps using the depth of a reference region ($\text{Position}_{\text{AP}}=15-35\%$, $\text{Position}_{\text{ML}}=50-150\%$). This region

corresponds to the anterior domain of cells expressing Stripe, which is a region that stays in close proximity to the apical ECM during the time windows we have studied. Topographic maps were divided into boxes of approximately 5µm width ($16 \times \text{Pixel}_{\text{size}}$, $\text{Pixel}_{\text{size}} = 0.322\mu\text{m}$), and the depth of each box was defined as the 95quantile of the distribution of depth within the box (95-quantile was used in order to catch the very localized deep invagination leading edge in the neck). Tissue depth was expressed in Lagrangian coordinates using PIV-based tracking (see C/5/b section), and averaged along the M-L axis ($\text{Position}_{\text{ML}} = 0\text{-}100\%$) to obtain a mean depth kymograph. For each time point, the depth ($\text{Depth}_{\text{leadingedge}}$) and the position of the leading edge of invagination was identified by identifying the point of maximal depth. Speed of deepening of the invagination leading edge was calculated by temporally smoothing $\text{Depth}_{\text{leadingedge}}(t)$ (smoothing radius of 45min), and by deriving it over time.

b) Quantification of local tissue slope and neck indentation

In order to calculate local tissue slopes (along the A-P and M-L axes), topographic maps were divided into boxes of approximately 5µm width ($16 \times \text{Pixel}_{\text{size}}$, $\text{Pixel}_{\text{size}} = 0.322\mu\text{m}$), and tissue curvature along the A-P and M-L axes were obtained for each box by local polynomial fits on the average depth profile along the A-P and M-L axes. Slope maps were expressed in Lagrangian coordinates using PIV-based tracking (see C/5/b section), and averaged along the M-L axis (for $\text{Position}_{\text{ML}} = 0\text{-}100\%$) to obtain a mean slope kymograph.

Indentation was defined as the average of the absolute value of the maximal and minimal slopes along the A-P axis (corresponding to the maximal tissue tilt on the head side, and maximal tilt on the thorax side). Indentation scores thus varies from 0 (no invagination) to $+\infty$ (fold containing vertical sides). To calculate indentation speed curves, indentation was calculated for each time point and temporally smoothed (sliding window of 45min).

$$\text{Indentation speed}(y, t) = \frac{\text{Indentation}(y, t+dt) - \text{Indentation}(y, t)}{dt}$$

$$\text{Indentation speed}(y, t) = \frac{\text{Indentation}(y, t+dt) - \text{Indentation}(y, t)}{dt}$$

c) Correction of velocities and tissue deformation for tissue curvature

Velocity vectors were corrected for local slope using the calculated slope maps (see previous section) using the following formula:

$$\begin{aligned} & \text{if Real speed along AP}(x, y, t) > 0 \\ & \text{Real speed along AP}(x, y, t) = \text{SpeedAP}(x, y, t)^2 \cdot \sqrt{1 + \text{SlopeAP}(x, y, t)^2} \end{aligned}$$

$$\begin{aligned} & \text{if Real speed along AP}(x, y, t) < 0 \\ & \text{Real speed along AP}(x, y, t) = -\text{SpeedAP}(x, y, t)^2 \cdot \sqrt{1 + \text{SlopeAP}(x, y, t)^2} \end{aligned}$$

$$\begin{aligned} & \text{if Real speed along ML}(x, y, t) > 0 \\ & \text{Real speed along AP}(x, y, t) = \text{SpeedML}(x, y, t)^2 \cdot \sqrt{1 + \text{SlopeAP}(x, y, t)^2} \end{aligned}$$

$$\begin{aligned} & \text{if Real speed along ML}(x, y, t) < 0 \\ & \text{Real speed along AP}(x, y, t) = -\text{SpeedML}(x, y, t)^2 \cdot \sqrt{1 + \text{SlopeAP}(x, y, t)^2} \end{aligned}$$

Real velocity maps were then spatially and temporally smoothed (window of time smoothing of 1.25h, radius of spatial smoothing of 7% along the A-P axis and 28% along the M-L axis), and tissue deformation was calculated using the following formula:

$$\text{Deformation AP}(x, y, t) = \frac{\text{RealSpeedAP}(x, y-1, t) - \text{RealSpeedAP}(x, y+1, t)}{2 * \text{RealBoxsize}}$$

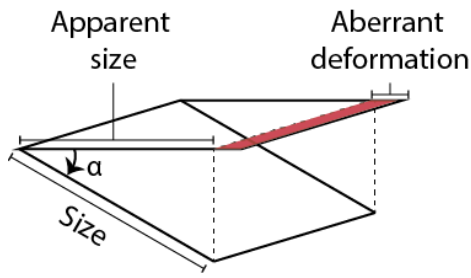
$$\begin{aligned} & \text{with RealBoxsize} = \text{Boxsize} e^2 \cdot \sqrt{1 + \text{SlopeAP}(x, y, t)^2} \\ & (\text{Boxsize} \approx 5 \mu\text{m}) \end{aligned}$$

$$\text{Deformation ML}(x, y, t) = \frac{\text{RealSpeedML}(x+1, y, t) - \text{RealSpeedML}(x-1, y, t)}{2 * \text{RealBoxsize}}$$

$$\text{with RealBoxsize} = \text{Boxsize} e^2 \cdot \sqrt{1 + \text{SlopeML}(x, y, t)^2}$$

Deformation maps were then expressed in Lagrangian coordinates using PIV-based 2D tracking (see C/5/b section).

The obtained deformation maps have been generated under the assumption that the change in local curvature during one time-step is negligible. However, this assumption is not fulfilled in the neck region during folding, where local slopes can vary very fast. Aberrant deformation due to tissue manifold local rotation can however be calculated and corrected for. Indeed, a rotation in z of a given angle gives rise to an apparent deformation that we can calculate as explained below:



$$\cos(\alpha) = \text{Apparent size} / \text{Size}$$

$$\text{Apparent size} = \text{Size} \cdot \cos(\alpha)$$

$$\text{Aberrant deformation} = (\text{Apparent size} - \text{Size}) / \text{Size}$$

$$\text{Aberrant deformation} = (\text{Size} \cdot \cos(\alpha) - \text{Size}) / \text{Size}$$

$$\text{Aberrant deformation} = \cos(\alpha) - 1$$

Thus, knowing the evolution in time of local slopes, we can correct deformations using the following formula:

$$\text{CorrectedDeformationAP}(x, y, t) = \text{DeformationAP}(x, y, t) - \beta$$

$$\text{with } \beta = \cos(\text{Angle}(x, y, t+1) - \text{Angle}(x, y, t)) - 1$$

$$\text{with } \text{Angle}(x, y, t) = \text{atan}(\text{SlopeAP}(x, y, t))$$

$$\text{CorrectedDeformationML}(x, y, t) = \text{DeformationML}(x, y, t) - \beta$$

$$\text{with } \beta = \cos(\text{Angle}(x, y, t+1) - \text{Angle}(x, y, t)) - 1$$

$$\text{with } \text{Angle}(x, y, t) = \text{atan}(\text{SlopeML}(x, y, t))$$

Corrected deformation maps were then averaged along M-L axis (Position_{ML}=0-100%) to get a tissue deformation kymograph of the invaginating region corrected for local tissue curvature.

8) Quantification of cell aspect ratio and anisotropy orientation

2D projected time-lapse movies used for thorax flow and neck invagination analyses were used to measure cell geometry in regions of interest. Cell contours were automatically segmented using a homemade Fiji macro and manually corrected. In order to minimize segmentation aberration due to the poor resolution (cells covering few pixels in the regions of high tissue curvature), images have been beforehand up-scaled by a factor of 4 (Fiji, Scale function). Real apical area outlines were reconstructed by using the topographic maps, and the calculation of local slopes along the A-P and M-L axes (see C/7/b section). Cell aspect ratio and anisotropy orientation were calculated by fitting ellipses onto segmented cell contours (Fiji FitEllipse function).

Using PIV-tracking, Lagrangian coordinates of each cell were calculated allowing the comparison of cells with equivalent coordinates between genotypes (see C/5/b section).

9) 3D visualization of live-imaging data

3D representation of neck invagination regions labelled with Ecad::3XGFP marker was obtained using Imaris software (Figure_{part1} 1B and Figure_{part2} 3A), or by back-projecting 2D projected signal onto the detected surface of the tissue (see C/3 section) using 3D Surface Plot plugin in Fiji (Figures_{part2} 6A-B).

10) Inference of Lagrangian coordinates for pictures taken at late time points

Some of our analyses (protrusion polarity analysis, protrusion stretching after ablation, analysis of Dpy::YFP fibers movements at 25hAPF) require the use of animals older than 18hAPF, in which the initial position of landmarks is unknown. However, in order to compare the measurements made on these older animals with measurements extracted from long time-lapse imaging, it is necessary to infer the initial position of the landmarks and Lagrangian coordinates.

First, overview pictures were taken in order to determine the position of the midline, the two landmarks macrochates (Macrocheates₍₀₎) and of the leading edge of invagination (Boundary₍₀₎) at the timing t ($t > 18\text{hAPF}$). We manually calculated the distance $|\text{Boundary}_{(0)} - \text{Boundary}_{(t)}|$ for many pupae at different time points, and found it is approximately equal to

30µm after 24hAPF (and 15µm at 22hAPF), independently of the size of the animal. This enables to infer $\text{Boundary}_{(0)}$ from $\text{Boundary}_{(t)}$ in every animal. The average velocity kymographs were then used to provide a first equation linking the distance travelled by the landmark macrochaetes (Movement) and $\text{Macrocheates}_{(0)}$:

$$(1) \text{Macrocheates}_{(0)} = \text{Movement} - \text{Macrocheates}_{(t)}$$

However, thorax flow velocity is higher in big animals and smaller in small animals. We thus know that Movement depends on the size of the animal ($L_{\text{ref}} = |\text{Macrochaete}_{(0)} - \text{Boundary}_{(0)}|$). We propose to use the following scaling law:

$$(2) \text{Movement}(\text{Archetype}) / L_{\text{refArchetype}} = \text{Movement} / |\text{Macrocheate}_{(0)} - \text{Boundary}_{(0)}|$$

The system made by the equations (1) and (2) can then be resolved, as only $\text{Macrocheate}_{(0)}$ and Movement are unknown. We can thus infer the size of the animal $L_{\text{ref}} = |\text{Macrocheate}_{(0)} - \text{Boundary}_{(0)}|$.

Knowing L_{ref} , it is then possible to infer the velocity map of the animal using the average archetypal velocity map and the inferred scaling law:

$$\text{VelocityMap}(L_{\text{ref}}) / L_{\text{ref}} = \text{VelocityMap}(L_{\text{refArchetype}}) / L_{\text{refArchetype}}$$

The velocity map $\text{VelocityMap}(L_{\text{ref}})$ can then be used to infer Lagrangian positions, by inferring the distance travelled by each cell, and calculating its coordinates using initial position of landmarks.

11) Quantification of apical protrusion polarity

High resolution pictures of the apical surface of flies expressing *Ecad::3XGFP* and a mosaic labelling of *LifeAct::Ruby* were projected by detecting the plane of adherens junction (see C/3 section), using maximal projection. Only the signal of *LifeAct::Ruby* above the adherens junction plane was projected.

Isolated small clones expressing LifeAct::Ruby (typically 2 cells) were manually picked. For each clone, the Ecad::3XGFP signal was automatically segmented and manually corrected. LifeAct::Ruby signal was segmented by manually adjusting an intensity threshold for each clone.

Using a homemade Fiji macro, each cell of each clone was separated into 24 angular portions. For each angular portion, the area of LifeAct::Ruby signal that spreads beyond the cell contour (defined by Ecad::3XGFP segmented signal) was automatically calculated ($\text{Spreading}_{\text{angular}}$). The length of junction intercepted by each angular portion was as well calculated ($\text{Junction}_{\text{angular}}$). For each angular portion, $\text{Spreading}_{\text{angular}}$ was normalized by $\text{Junction}_{\text{angular}}$, in order to obtain a score that corresponds to the mean length of protrusions in the angular portion ($\text{Length}_{\text{angular}}$). An angular distribution of 24 $\text{Length}_{\text{angular}}$ values was thus obtained for each cell of each clone. For each cell, regions of contact between adjacent cells also labelled with LifeAct::Ruby were filtered out. For each clone, we thus obtained n incomplete angular distributions of $\text{Length}_{\text{angular}}$ values, corresponding to the n cells it contains. These n incomplete angular distributions were then pooled. As only isolated clones were analyzed, a complete angular distribution of $\text{Length}_{\text{angular}}$ values was reconstructed for each clone. Using a Matlab code, we then analyzed the angular distribution of protrusion spreading length of each clone using Fourier analysis. The extraction of the first harmonic of Fourier decomposition enabled us to extract a polarity vector. The orientation of the polarity vector represents the main orientation of protrusion spreading, while the length of the polarity vector represents the intensity of polarization. Polarity vectors were projected onto the A-P axis to obtain a score of polarization along the A-P axis for each clone. Moreover, the amplitude of polarity was defined as the norm of the polarity vector, and the orientation of polarity was defined as the orientation of the polarity vector.

Similar to protrusion spreading, the polarity of cortical apical LifeAct::Ruby levels can be calculated. As each cell expresses a different level of LifeAct::Ruby, we first estimated the levels of LifeAct::Ruby expression ($\text{Expression}_{\text{level}}$) in each cell by measuring the medial intensity of LifeAct::Ruby signal at the level of the adherens junction. Each cell apical area was then separated into angular portions. For each angular portion, cortical LifeAct::Ruby signal was calculated and normalized by $\text{Expression}_{\text{level}}$ and $\text{Junction}_{\text{angular}}$. Similar to the analysis of spreading polarity, angular cortical LifeAct::Ruby intensity values were pooled per

clone, and a polarity vector representing the polarity of apical cortical LifeAct::Ruby levels was calculated for each clone.

Parameters used in Fiji macro for analyzing protrusion polarity

Radius of research of protrusion beyond cell contours for protrusion angular detection	2 μ m
Radius of exclusion of values around cell-cell contacts	0.3 μ m
Thickness of the cortical layer analyzed for LifeAct::Ruby intensity analysis	0.45 μ m
Radius of exclusion of the outermost cortical layer for LifeAct::Ruby intensity analysis	0.2 μ m
Factor of reduction of cell area for analysis of medial LifeAct::Ruby intensity (to get Expression _{level})	1/4

The coordinates of each clone within the thorax was calculated using an overview picture. The orientation of the midline was used for aligning the angular distribution of each clone with body main axes. Lagrangian coordinates for each clone were then inferred from average velocity kymographs of the corresponding genotypes (see C/10 section).

12) Laser ablations

For large-scale ablations and analyses of tissue flow, an inverted spinning-disk confocal microscopes with wide field (Roper/Nikon/GATACA or Roper/Zeiss) coupled with a UV (355nm) ablation set-up was used. All other ablations were performed using a two-photon laser-scanning microscope (LSM 710 NLO, Zeiss). In that cases, imaging was performed using mono-photon excitation, while local laser ablation was performed using a biphoton Ti::Sapphire laser (MaiTai DeepSee, Spectra Physics) at 890nm with <100 fs pulses with a 80MHz repetition rate.

a) Large-scale repeated ablations

Pupae expressing Ecad::GFP3X were imaged using a 40X objective, with 15min time-step and 60 z-step of 1 μ m. Using Metamorph, one (or two) rectangular region was defined before 18hAPF either on the neck region or a specific region of the thorax. For posterior ablations, the most anterior edge of the ablation rectangle lines the landmark macrochaetes (Position_{AP}=100%). For ablation in the middle of the thorax, the most posterior edge of the

ablation rectangle lines $\text{Position}_{\text{AP}}$ of 50%. Laser ablation was performed on 60 planes (z-step = $1\mu\text{m}$) every 3h starting at 18hAPF using a 355nm laser. The size of the ablation region and the frequency of repetition were chosen in order to prevent wound closure.

b) Single-junction ablation and junction tension/friction estimation

For single-junction ablations, pupae expressing *Ecad::GFP* and *sqh::mCherry* were imaged with a 63X oil-immersion objective (numerical aperture: 1.4). Acquisition was restricted to a 200X100 pixels window ($\text{Pixel}_{\text{size}} = 0.13\mu\text{m}$) with a bidirectional scan lasting 500msec. Junctions belonging to the cable (and neighboring junctions) were identified using *sqh::mCherry* as a marker for the cable. As recoil dynamics is linear 7sec after ablation, we have measured the distance travelled by neighboring vertices from 1sec after ablation to 7sec after ablation to estimate initial recoil velocity.

c) Multicellular basal and apical ablations and apical and basal tension/friction estimation

For neck multicellular apical or basal ablations, imaging was performed with a 40X oil-immersion objective (numerical aperture: 1.3). Acquisition was restricted to a 200X200 pixels window ($\text{Pixel}_{\text{size}} = 0.69\mu\text{m}$) with a bidirectional scan lasting 1sec, and ablation was performed in a region of 50X25 pixels (rectangle elongated along the A-P axis). Ablation was performed at one pole of the tissue (apical or basal), recoil dynamic was imaged during 30sec, and ablation on the opposite pole of tissue (basal or apical) was performed 1min following initial ablation. To perform these successive ablations, the laser power was adjusted in order to get a recoil on one side of the tissue without damaging the opposite side of the tissue. As recoil dynamics is globally linear 7sec after ablation, we have measured the distance between the edges of the ablated tissue from 1sec after ablation to 7sec after ablation to estimate initial recoil velocity along the M-L axis.

Differences between apical and basal recoil was calculated for each pair of ablations.

d) Ablation and protrusion stretching

Pupae expressing *Ecad::3XGFP* and a mosaic labelling of *LifeAct::Ruby* were imaged using a 63X oil-immersion objective (numerical aperture: 1.4). Acquisition was restricted to a window of 100X100 pixels window ($\text{Pixel}_{\text{size}} = 0.13\mu\text{m}$) with a bidirectional scan lasting 500msec, and a z-stack of 4 planes (zstep= $0.5\mu\text{m}$) was acquired, starting at the adherens

junction level and covering the apical protrusions domain. Rectangular laser ablation (covering approximately 5 cell diameters in length along the M-L axis) was performed at the front or the back of clones expressing LifeAct::Ruby, at a z-plane located 0.5µm below the adherens junction plane, and taking care that the ablation region was not overlapping with apical protrusions in x and y.

Ecad::3XGFP and LifeAct::Ruby signals were projected in z using a maximal projection (only planes situated above the adherens junction level were projected for LifeAct::Ruby signal, see C/3). The Ecad::3XGFP LifeAct::Ruby signals were segmented as in section explained in section C/11. Junctions of interest were manually chosen and tracked at two timepoint: t_{initial} (right before ablation) and t_{final} (14sec after ablation). The area separating the junctions of interest between t_{initial} and t_{final} was calculated ($\text{Area}_{\text{recoil}}$). The area of spreading of LifeAct::Ruby signal beyond Ecad::3XGFP cell contours were calculated at t_{initial} ($\text{Spreading}_{\text{initial}}$) and t_{final} ($\text{Spreading}_{\text{final}}$) using a homemade Fiji macro. Stretching after ablation was then calculated using the following formula:

$$\text{Stretching}(\%) = \frac{100 \times (\text{Spreading}_{\text{final}} - \text{Spreading}_{\text{initial}})}{\text{Arearecoil}}$$

For each pupa, an overview picture was taken in order to extract the coordinates of each ablation according to spatial landmarks. Lagrangian coordinates of each clone was inferred from average velocity kymographs of the corresponding genotypes (see C/10 section).

e) Ablation and Dpy::YFP recoil analysis

Pupae expressing Ecad::3XmKate and Dpy::YFP were imaged using a 63X oil-immersion objective (numerical aperture: 1.4), acquisition was restricted to a window of 400X400 pixels window ($\text{Pixel}_{\text{size}} = 0.13\mu\text{m}$) with a bidirectional scan lasting 1sec, and a z-stack of 3 planes ($\text{zstep} = 0.5\mu\text{m}$) was acquired, starting at the most apical z-plane of adherens junction network, and covering proximal Dpy layer domain. Circular laser ablation of 26µm diameter was performed in the middle of the acquisition field, at a z-plane located 0.5µm below the adherens junction plane, in order to induce tissue recoil while minimizing the effect of the

ablation on Dpy layer. Control ablations were performed in the z-plane of Dpy layer, 1µm above the adherens junction plane.

Ecad::3XmKate and Dpy::YFP signals were projected using maximal projections. Only Dpy::YFP situated from 0.5 to 1µm above the adherens junction plane was projected (see C/3 section). This corresponds to the proximal layer of Dpy::YFP network. The field of view was subdivided into boxes of approximately 1µm length ($8 \times \text{Pixel}_{\text{size}}$, with $\text{Pixel}_{\text{size}} = 0.1318\mu\text{m}$), and PIV tracking was applied on each grid for all time intervals.

Masks were beforehand generated for filtering out both the zones of the field of view that do not overlap with cell contours labelled with Ecad::3XmKate. These masks were generated by applying a 2D variance filter on the Ecad::3XmKate signal (with a radius of 2 pixels in x and y, with $\text{Pixel}_{\text{size}} = 0.1318\mu\text{m}$) and by manually thresholding the filtered image in order to identify regions of low signal variance. Boxes with less than 25% of Ecad::3XmKate signal were not analyzed.

Recoil 5sec after ablation was analyzed for both cell contours labelled with Ecad::3XmKate and Dpy::YFP fibers. For all PIV boxes, recoil vectors were radially projected to obtain a velocity of displacement away from the center of the circular ablation. Dpy mean recoil was obtained by averaging these Dpy radial recoil velocities for the whole field of view. In order to compare tissue and Dpy recoils, the difference between radial recoil velocity of the tissue and of Dpy was calculated for each PIV box, and averaged for the whole field of view.

f) Muscle ablation in control and *Act>Dpy*^{RNAi}

MhctGFP was used as marker to visualize longitudinal indirect flight muscles precursors before 18hAPF²²⁶. Ablation of these muscles was performed prior to time-lapse imaging. The precision in z of the biphoton laser used (MaiTai DeepSee, Spectra Physics) enabled to perform ablation of the underlying muscles without damaging the tissue. The ablation laser was used at 810nm with high laser power, in order to efficiently ablate muscles. For each muscle precursor, outlines of the muscle were manually drawn to perform laser ablation specifically in the muscle without affecting its surrounding. Ablation was repeated in many successive z (typically 10) in order to ablate the entire volume of muscles.

13) Dpy::YFP levels quantification

a) Repetitive bleaching

Homozygote Dpy::YFP flies were imaged using inverted spinning-disk confocal microscopes with wide field (Roper/Nikon/GATACA or Roper/Zeiss) coupled with a FRAP module. Dpy::YFP signal was automatically bleached across the whole field of view every 2h using a 491nm laser an Metamorph software. Dpy::YFP recovery after photobleaching was imaged with a 15min time resolution. Images prior to the time step of bleaching was used to extract a local pattern of Dpy::YFP deposition within 1h45min. Correlation between two successive Dpy::YFP deposition patterns was calculated for regions of interest in the anterior thorax using Fiji PairwiseStitching plugin, allowing the calculation of correlation between two images without being affected by global sample drift.

b) Estimation of deposition rates

Pupae expressing Ecad::3XmKate and Dpy::YFP were imaged as described in C/2 section, with 1 μ m z-step and 30min time resolution. Note that all the individuals used for quantifying and comparing Dpy::YFP levels in control and *sr^l* mutants were acquired with the same microscope, with the exact same imaging conditions and parameter, in three successive days. Thus, Dpy::YFP intensity can be compared between each animal and between each condition. Signals were projected using maximal projections. Only the Dpy::YFP signal found above the adherens junction plane was used to project Dpy::YFP signal (see C/3 section).

Thorax flow was analyzed by PIV, and Dpy::YFP apical levels were calculated using the same boxes as used for PIV analysis (see C/5 section). For each animal, a kymograph of Dpy::YFP apical levels was generated by averaging values along the M-L axis (Position_{ML}=0-100%). Kymographs were smoothed in time (smoothing radius of 1h30min), and Dpy deposition rate kymographs were calculated by deriving Dpy::YFP total levels from the kymographs. Finally, average kymographs of both total Dpy::YFP levels and Dpy:YFP deposition rate were calculated by averaging the maps of all the individuals.

c) Calculation of Dpy::YFP enrichment in clones overexpressing *sr*

Outlines of clones overexpressing *sr* were manually segmented using the positive clone labelling TagBFP:CAAX. Dpy::YFP signal was projected using maximal projection. Average

intensity of Dpy::YFP signal within clone overexpressing *sr* was quantified, and compared to average intensity of Dpy::YFP signal surrounding the clone outlines.

14) Quantification of sr::GFP levels

Pupae expressing Ecad::3XmKate and sr::GFP were imaged as described in C/2 section, with 1µm z-step and 15min time resolution and projected (maximal projection). Sr::GFP is located in nuclei (5 to 15µm below the adherens junction), and this plane was specifically projected as described in C/3 section.

As sr::GFP localizes in nuclei, projection of sr::GFP signal is composed of nuclear signals surrounded by non-fluorescent regions. In order to quantify nuclear intensity only (and avoid bias due to the heterogeneous nuclear density across the tissue), we have applied a series of filters. First, a Gaussian filter was applied (radius of 2 pixels, $\text{Pixel}_{\text{size}}=0.322\mu\text{m}$) in order to attenuate aberrantly fluorescent pixels. A maximum filter of high radius (25 pixels) was then applied in order to propagate maximal fluorescence of nuclei to their neighborhood, and to eliminate non-fluorescent regions between nuclei. Finally, a Gaussian filter of high radius (15 pixels) was applied to smooth the sharp transitions between adjacent nuclei.

Thorax flow was analyzed by PIV, and sr::GFP levels were calculated using the same boxes as used for PIV analysis (see C/5/a section). For each animal, a kymograph of sr::GFP levels was generated by averaging values along the M-L axis ($\text{Position}_{\text{ML}}=0-100\%$). The average kymograph of sr::GFP levels was calculated by averaging the maps of all the individuals.

15) Cell body tilt analysis

Overview images of thorax of pupae expressing Ecad::3XGFP and a mosaic labelling of LifeAct::Ruby were projected using a maximal projection. In small isolated clones, cell apical domains and cell basolateral domains can be distinguished in these projections. The orientation of cell body tilt was manually measured on these projections. The coordinates within the thorax of each measurement was registered using spatial landmarks, allowing the spatial mapping of cell body tilt across the thorax (see C/10 section).

16) Quantification of the distance between tissue and cuticle chitin-rich layer

To calculate the tissue-to-cuticle distance, pupae expressing UAS::LifeAct::GFP and UAS:ChtVisTomato were imaged. The apical surface of the tissue was extracted by applying a variance filter on UAS::LifeAct::GFP signal in z (radius of 2 pixel, $\text{Pixel}_{\text{size}} = 0.5\mu\text{m}$), and by detecting for each pixel the most apical plane of sufficiently high variance (see C/3 section). Similarly, a variance filter in z on ChtVisTomato was applied, and the basal surface of the cuticle was extracted by detecting for each pixel the most basal plane of sufficiently high variance (see C/3 section). Topographic maps of apical tissue surface and basal cuticle surface were then used to calculate a map of distance between the tissue and the cuticle.

LifeAct::GFP signal was projected around the detected plane of apical surface. Using Fiji function `SubtrackBackground` with a small rolling ball radius (4pixels, with $\text{Pixel}_{\text{size}}=0.322\mu\text{m}$), medial LifeAct::GFP signal was filtered out, and only the dynamic cortical LifeAct::GFP signal was extracted, thus allowing thorax flow tracking using PIV in a similar manner as Ecad::GFP signal (see C/5 section). The calculated displacement A-P velocities were used to temporally register the time-lapse movies.

Based on spatio-temporally registered maps of distance tissue-to-cuticle distance, the average kymographs of distance between tissue and cuticle was calculated by averaging M-L position corresponding to the midline ($\text{Position}_{\text{ML}}=0\text{-}30\%$) or to the rest of the tissue ($\text{Position}_{\text{ML}}=30\text{-}100\%$).

17) Quantification of basal fibers alignment

Pupae expressing utr::GFP were imaged from 15hAPF to 25hAPF with $1\mu\text{m}$ z -step, with a 15min time-step, and with 60 z -step of $1\mu\text{m}$, in order to image the apical and the basal side of the invaginating neck tissue. The apical surface plane was detected as previously described (see C/3 section). Apical projections were used to register movies in space and in time. The basal surface was projected by shifting the apical topographic map of $5\mu\text{m}$ and running a maximum projection on a thickness of $20\mu\text{m}$ below the shifted topographic map. The basal projection was then analyzed using a pipeline based on Fourier transform²²⁷. In brief, Fourier transform of a pattern reveals the spatial periods and orientations present in it. In the case of fluorescently labelled fibers, the repeating pattern is linked to the orientation and distance

between the fibers, that means the anisotropy of the fiber network. This method was used to extract the basal fibers network anisotropy for each time point and for boxes of approximately 25µm wide. The obtained tensors have been projected on the M-L axis, to obtain a score of fibers anisotropy along the M-L axis.

18) Quantification of MyosinII enrichment on the head and the thorax side

Pupae expressing mosaic labelling of sqh::GFP and sqh::RFP were imaged. Clones lining the acto-myosin boundary cable on the head side or on the thorax side facing unlabeled tissues were manually selected. Maximal projection around the adherens junction plane was performed. The intensity of sqh::GFP or sqh::RFP was measured by manually segmenting the junctions contributing to the cable and intensities were compared with the intensity of neighboring junctions facing unlabeled tissue.

19) Quantification of microchaetes orientation

Projected time-lapse movies used for thorax flow analysis were used to quantify microchaetes orientation at 24hAPF, 28hAPF, 32hAPF and 36hAPF. Only a region of interest was analyzed (Position_{AP}=0-100%, Position_{ML}=0-100%). For each presumptive microchaete, the orientation was manually measured by tracing a line starting at the center of the hair, and separating the socket in two symmetric halves (Figure 1). The Lagrangian coordinates within the thorax of each microchaete was extracted from PIV-based tracking and spatial registration, allowing the spatial mapping of microchaetes orientation across the thorax (see C/5 section).

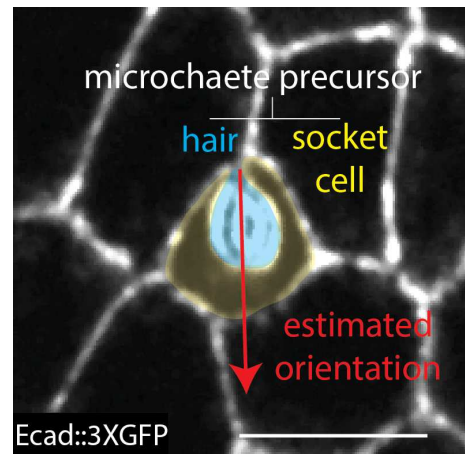


Fig.1: Manual estimation of microchaete orientation (scale bar: 5µm)

In order to avoid circular representations, orientations from $-\pi$ to 0 have been symmetrized to only obtain angles from 0 to π . 0 corresponds to microchaetes pointing towards the posterior (wild type phenotype), while π corresponds to microchaetes pointing towards the anterior (reversal phenotype).

20) Adult scutellum aspect ratio calculation

Adults were pinned on a petri Dish, and their dorsal thorax was imaged using a stereoscopic microscope (SteREO Discovery.V20, Zeiss), equipped with an AxioCam ICc 1 camera (Zeiss) and a 20X objective. Maximal height and width of the scutellum, the most posterior part of the thorax, were manually measured, in order to calculate scutellum aspect ratio.

21) *Ex vivo* experiments

Pupae were collected at 24hAPF and were dorsally glued at the bottom of a Petri dish containing a central coverslip. Pupae were subsequently dissected in Schneider's medium (supplemented or not with 25nM ecdysone) using micro-scissors. In these conditions, dorsal thorax explants could be imaged for 10h.

Chitinase mix¹⁹⁹, composed of a 6:1 ratio of chitinase and N-acetylglucosamidase, was added just before starting live-imaging. Concentrations reported correspond to the concentration of the chitinase component of the mix.

Thorax flow were analyzed using PIV, and averaged for the first 8h of incubation for a region of interest ($\text{Position}_{\text{AP}}=0-100\%$, $\text{Position}_{\text{ML}}=0-100\%$), in order to extract a mean thorax flow velocity for each explant.

List of reagents used *ex vivo*:

Name of the reagent	Source
Schneider's <i>Drosophila</i> medium	ThermoFisher (#21720024)
20-Hydroxyecdysone (ecdysone)	Sigma Aldrich (H5142)
Chitinase	Sigma Aldrich (from <i>Streptomyces griseus</i> , C6137)
β -N-Acetylglucosamidase	Sigma Aldrich (from <i>Canavalia ensiformis</i> , A2264)

22) Analysis of tissue and ECM motion

a) Imaging and PIV analysis of Dpy::YFP fibers and cell contours motion within 2min intervals

Pupae expressing Ecad::3XmKate and Dpy::YFP were imaged using an inverted spinning-disk confocal microscopes with wide field (Roper/Zeiss), equipped with sCMOS camera (Flash4 Hamamatsu) and a 100X oil immersion objective (numerical aperture: 1.4), with 0.3µm z-step and 2min time resolution for 30min. The adherens junction plane was detected using Ecad::3XmKate signal (see C/3 section). Using the detected plane, successive layers of Dpy::YFP signal were projected (3 successive layers from 0.9µm to 1.5µm above the adherens junction plane). Ecad::3XmKate signal was used to detect the plane of adherens junction, and projected around the detected plane. The field of view was subdivided into boxes of approximately 2µm length (16 X Pixel_{size}, with Pixel_{size} = 0.13µm), and PIV tracking was applied on each grid for all time intervals, for all successive Dpy::YFP layers and Ecad::3XmKate signal. Masks were generated in order to filter out boxes covering less than 25% of cell contour or Dpy::YFP fibers signal. For each box, the maximal movement detected across the 3 projected layers of Dpy::YFP was selected. This pipeline thus enabled to obtain for each time interval 2D fields of velocity vectors of tissue and Dpy::YFP fibers movement with a 2min time resolution.

b) Calculation of mobility, global movement, fluctuation around global movement and persistence

Mobility of Dpy signal within 2min intervals (Mobility_{Dpy}) was calculated for each PIV box by using the sum of the amplitude of velocity vectors of all time intervals of the 30min-long movie (ΣvDpy).

$$\text{Mobility}_{\text{Dpy}}(\mu\text{m}/h) = \frac{\sum v_{\text{Dumpy}}(\mu\text{m}/h) * \text{Timestep}(h)}{0.5(h)}$$

Similarly, mobility of the cell contours (Mobility_{Tissue}) was calculated:

$$\text{Mobility}_{\text{Tissue}}(\mu\text{m}/h) = \frac{\sum v_{\text{Tissue}}(\mu\text{m}/h) * \text{Timestep}(h)}{0.5(h)}$$

Global movement within 30min of Dpy (GlobalMovement_{Dpy}) and of the tissue (GlobalMovement_{Tissue}) were calculated for each PIV box by averaging displacements calculated within 2min intervals for the whole duration of the timelapse movie (30min).

Fluctuation around global movement was calculated for each PIV box by subtracting global movement scores to mobility scores.

$$\text{Fluctuation}_{\text{Tissue}}(\mu\text{m/h}) = \text{Mobility}_{\text{Tissue}} - \text{GlobalMovement}_{\text{Tissue}}$$

Persistence of movement was calculated for each PIV box by dividing global movement scores by mobility scores.

$$\text{Persistence}_{\text{Tissue}}(\mu\text{m/h}) = \text{GlobalMovement}_{\text{Tissue}} / \text{Mobility}_{\text{Tissue}}$$

Fluctuation around global movement and persistence of tissue movement can be subdivided into two components, one along the A-P axis and one along the M-L axis ($\text{Fluctuation}_{\text{AP}}$, $\text{Fluctuation}_{\text{ML}}$, $\text{Persistence}_{\text{AP}}$ and $\text{Persistence}_{\text{ML}}$). To calculate $\text{Fluctuation}_{\text{AP}}$ and $\text{Persistence}_{\text{AP}}$, only the absolute value of A-P component of velocity vectors was used to calculate $\Sigma v_{\text{Tissue}_{\text{AP}}}$ and $\text{GlobalMovement}_{\text{Tissue}_{\text{AP}}}$ for each PIV box. Similarly, for the calculation of $\text{Fluctuation}_{\text{ML}}$ and $\text{Persistence}_{\text{ML}}$, only the absolute value of M-L component of velocity vectors was used to calculate $\Sigma v_{\text{Tissue}_{\text{ML}}}$ and $\text{GlobalMovement}_{\text{Tissue}_{\text{ML}}}$ for each PIV box.

c) Comparison between tissue and Dpy displacements fields

For each 2min interval, for each PIV box, the amplitude of the difference between tissue and Dpy velocity vectors was calculated. This score was expressed as a percentage of amplitude of tissue motion, to obtain a score of difference between tissue and Dpy movements in percentage. Similarity between tissue and Dpy movements was then calculated based on this score (a score of 100% correspond to a perfect similarity). Similarity scores were averaged in time for each PIV box, to obtain a 2D map of similarity between tissue and Dpy movements across the dorsal thorax. Similar analyses were performed to compare Dpy and tissue displacement fields with a lag of $\pm 2\text{min}$.

For each 2min interval and for each PIV box, tissue deformation was inferred from displacement fields (see C/6 section). Tissue displacement fields have been beforehand spatially smoothed (smoothing radius of 3 PIV boxes, corresponding to approximately $6\mu\text{m}$). Tissue deformation was used to compare Dpy displacement velocity and orientation with local tissue deformation for each 2min interval and for each PIV box.

D/ Statistics

In all the plots shown, we used the following convention: ***: p-value<0.001, **: p-value<0.01, *: p-value<0.05 and n.s.: p-value>0.05.

Pairwise Welch tests and t-tests were performed using Matlab.

In all kymographs showing differences in velocity or differences of deformation between two conditions, only statically significant differences are shown (see C/5/e section). Non-significant differences and missing data are both represented in dark blue.

Statistical analysis of protrusion orientation and global thorax flow orientation were performed in Matlab using the Toolbox CircStat²²⁸, enabling to calculate standard deviation of a circular distribution, to perform ANOVA tests adapted for circular data, and to test for non-randomness of a circular distribution using a Rao's spacing test. To study the orientation of microchaetes, we have only considered the orientation along the A-P axis, thus obtaining distributions varying from 0 (pointing towards the posterior) to π (pointing towards the anterior). The use of statistical tools adapted to circular data was not required in that case. To test for differences between two distributions of orientation of microchaete along the A-P axis, we have used Kolmogorov-Smirnov tests.

Conclusion

Conclusion

In conclusion, my PhD work highlights the relevance of head-thorax interface invagination and thorax flow during *Drosophila* metamorphosis as a novel model system for studying epithelial folding, epithelial migration and their interplay.

We have first provided a detailed description of head-thorax interface invagination, a previously uncharacterized event of epithelial folding that leads to the formation of *Drosophila* adult neck. We have discovered that neck fold formation is associated with two prominent supra-cellular contractile acto-myosin structures: a boundary apical cortical acto-myosin cable, and a basal furrow composed of parallel actin bundles. Our functional study indicates that these structures actively participate to neck folding. Based on their geometry, marked by a circumferential curvature, we propose that these two structures may act as a “tissue-scale cytokinetic furrow”, promoting tissue bending in a comparable way to the mechanism of membrane bending by the contractile ring during cell cytokinesis, but at the tissue-scale. Future research on the role of supra-cellular structures in neck folding will further test the relevance of this novel folding mechanism.

As neck invagination is an active morphogenetic event, we have studied its impact on the neighboring thorax tissues. We have first shown that neck invagination is synchronized with a directional flow of thorax cells towards the invagination site. We have found that thorax flow is (i) locally dependent on a pulling force exerted by neck invagination and (ii) is driven by collective migration on the apical ECM. Thorax collective active migration can thus provide a pushing force towards the site of invagination, leading to the compaction of the tissue adjacent to the neck when neck invagination is abrogated. While our first analyses have shown that initial neck invagination is independent from thorax pushing force, we foresee that thorax migration might actively participate to later phases of neck folding to prevent excessive elongation of cell neighboring the neck fold.

We have provided novel mechanistic insights into tissue collective migration. Our data show that polarized apical protrusions, regulated by core PCP pathway and the transcription factor *stripe*, are mechanically coupled to the apical ECM and can trigger ECM constituents motion during thorax migration. We provide evidence that the apically located protein Dpy is a critical regulator of thorax migration. We further show that the patterned deposition of Dpy

is associated with a pattern in migration speed, migration persistence and ECM motion during migration. These results open exciting new research horizons. In particular, they might suggest the existence of *in vivo* durotaxis, or lead to the establishment of *in vivo* traction force microscopy methods. Moreover, we propose that patterned migration could represent a mechanism of epithelial morphogenesis. As a result of the conversion of a transcription factor gradient into a gradient of regulators of migration, a gradient of migration velocity can emerge and lead to tissue deformation. Taken together, our findings on thorax migration highlight the importance of considering the interaction with the ECM and ECM mechanical properties to understand the mechanical and cellular driving forces behind epithelial morphogenesis.

How cell coordinate their behaviors to allow tissue-scale deformations is a central multi-scale question in development. We here describe new mechanisms linking cell contractility and motility to tissue folding and migration, and highlight the complementarity between these two processes in shaping the neck and the thorax of *Drosophila*. More generally, we propose that epithelial collective cell migration may be a widespread morphogenetic force, that could not only drive tissue translocation towards folding regions, but could actively participate to tissue folding and tissue planar deformation.

Table of figures

Introduction

Fig.1: Apico-basal and planar polarities allow the emergence of specialized domains in epithelial cells.....	30-31
Fig.2: Linear bending (groove geometry) and circular bending (pit geometry).....	33
Fig.3: Apico-basal forces can drive epithelial bending.....	33
Fig.4: Phase diagram representing the effect of apico-basal shrinkage on apical curvature.....	36
Fig.5: Additivity in time of apico-basal forces bending mechanisms.....	37
Fig.6: Lewis physical model.....	38
Fig.7: A differential modulation of apical and basal surfaces can lead to tissue bending.....	39
Fig.8: Cell wedging through two distinct mechanisms.....	43
Fig.9: Circumferential tension gives rise to radial pushing.....	45
Fig.10: Contraction of a curved cable could lead to apico-basal resultant forces and bending.....	47
Fig.11: Typology of epithelial dynamics.....	48
Fig.12: Typology of in-plane morphogenetic processes.....	50
Fig.13: Deformability of lateral and basal domains, as well as connection with the ECM may regulate which output apical constriction leads to (in-plane or out-of-plane output).....	52
Fig.14: Mechanisms of epithelial surface expansion.....	54
Fig.15: Mechanisms of convergent extension.....	56
Fig.16: Cryptic lamellipodia can extend below front neighbors and enable crawling within the epithelium.....	57
Fig.17: The gradient a single cell is exposed to is smaller than the gradient a group of cells is exposed to.....	59
Fig.18: Principle of cell-based crawling.....	61
Fig.19: Principle and limits of a model of conversion of circumferential contractility into antero-posterior movement.....	66
Fig.20: Typology of tissue surface changes as a result of coupling with adjacent tissues.....	68-69
Fig.21: From local and anisotropic forces to global hydrodynamic swirling.....	71
Fig.22: Typology of mechanisms leading to in-plane epithelial morphogenesis.....	73

Part1: Analysis of neck invagination dynamics

Contraction of a curved acto-myosin cable is associated with epithelial folding

Fig.1: Presumptive neck region gradually bends during metamorphosis.....	79
Fig.2: Bending region constricts along the direction parallel to the fold axis.....	81
Fig.3: Neck invagination is associated with a contractile acto-myosin cable.....	83
Fig.4: Neck acto-myosin cable is curved and could act as a «tissue-scale cytokinetic ring».....	85
Fig.5: A basal contractile supra-cellular network is present in neck folding region.....	87
Fig.6: Phospho-MyosinII levels and contractility are affected in <i>Dfd>Rok^{RNAi}</i> , <i>Dfd>sqh^{RNAi}</i> and <i>Dfd>Mbs^{RNAi}</i>	90
Fig.7: Neck invagination dynamics is affected in <i>Dfd>Rok^{RNAi}</i> , <i>Dfd>sqh^{RNAi}</i> and <i>Dfd>Mbs^{RNAi}</i>	91
Fig.8: Tissue deformations and flows patterns are affected in <i>Dfd>Rok^{RNAi}</i> , <i>Dfd>sqh^{RNAi}</i> and <i>Dfd>Mbs^{RNAi}</i>	92
Fig.9: Supplementary figures of the Discussion.....	100

Part2: Analysis of anterior thorax flows

Collective cell migration on the apical extracellular matrix participate to thorax morphogenesis

Fig.1: Thorax flow shows a reproducible pattern.....	106
Fig.2: Thorax tissue deforms while flowing.....	107
Fig.3: Thorax flow is coordinated with neck invagination.....	108
Fig.4: Repeated neck ablation does not abrogate thorax flow.....	110
Fig.5: Defects in neck invagination speed trigger local displacements and tissue deformations changes in the anterior thorax.....	112
Fig.6: Defects in neck invagination speed trigger local cell shape changes in the thorax.....	113
Fig.7: Repeated posterior thorax ablation only locally affects thorax flow.....	115
Fig.8: Lateral domains contractility regulates thorax flow along the M-L axis.....	117
Fig.9: Lateral domains contractility does not affect thorax flow along the A-P axis.....	118
Fig.10: Thorax cells are more likely to use apical than basal ECM for migration.....	120
Fig.11: The apical ECM is required for thorax flows <i>ex vivo</i>	121
Fig.12: Polarized apical protrusive activity is patterned across dorsal thorax.....	123
Fig.13: Cells are anchored to the apical ECM in a polarized manner.....	125
Fig.14: Ft/ds pathway is not required for A-P thorax flow, but locally buffers M-L flows.....	127
Fig.15: <i>Dishevelled</i> is required for proper planar polarization of apical protrusions.....	129
Fig.16: <i>Dishevelled</i> regulates A-P velocity and A-P deformation patterns.....	131
Fig.17: <i>Act>stan^{RNAi}</i> phenocopies <i>dsh^l</i> planar polarity, flow and deformation phenotypes.....	132
Fig.18: Overexpression of <i>Sple</i> triggers planar polarity reversal in the posterior thorax, and accordingly affect thorax flow and deformation.....	133
Fig.19: Overexpression of <i>pk</i> triggers planar polarity defects in the anterior thorax, and accordingly affect thorax flow and deformation.....	134

Fig.20: <i>Stripe</i> regulates A-P flows and A-P deformations in the anterior thorax.....	136
Fig.21: <i>Stripe</i> regulates polarized apical protrusions emission.....	137
Fig.22: <i>Stripe</i> and core PCP pathway synergize to regulate polarized protrusion emission.....	139
Fig.23: Thorax flow is almost completely inhibited in <i>dsh¹sr¹</i> double mutant.....	140
Fig.24: The combination of RNAi against <i>sr</i> and <i>pk</i> overexpression highlights the cross-talk between <i>sr</i> and core PCP pathway.....	142
Fig.25: Dpy::YFP deposition rate pattern correlates with thorax A-P velocity pattern.....	144
Fig.26: <i>Stripe</i> controls Dpy deposition pattern.....	145
Fig.27: Muscle laser ablation prevents vortex formation in <i>Act>Dpy^{RNAi}</i>	147
Fig.28: <i>Dpy</i> expression is necessary for most of thorax flow to occur.....	148
Fig.29: <i>Dpy</i> expression in the scutellum is required for preventing scutellum collapse.....	149
Fig.30: A combination of patterns of apically located ZP domain proteins may contribute to thorax migration.....	151
Fig.31: Thorax migration is not required for early neck invagination.....	152
Fig.32: Posterior thorax displacement is robust to core PCP and <i>pot</i> genetic disruptions from 24hAPF to 35hAPF.....	154
Fig.33: Posterior thorax displacement from 24hAPF to 35hAPF is affected by anterior thorax migration defects.....	155
Fig.34: Posterior thorax is advected by anterior thorax from 24hAPF to 35hAPF.....	157
Fig.35: Supplementary figures of the Discussion (1/3).....	160
Fig.36: Supplementary figures of the Discussion (2/3).....	162
Fig.37: Supplementary figures of the Discussion (3/3).....	165

Part3: Analysis of matrix motion *in vivo*

Low deformation of the apical extracellular matrix is associated with persistent migration *in vivo*

Fig.1: Stretching after ablation is patterned across the tissue.....	171
Fig.2: Tissue recoil is almost completely transmitted to proximal Dpy::YFP fibers in the posterior thorax.....	173
Fig.3: Cells of the posterior thorax are mechanically coupled to the apical ECM.....	175
Fig.4: Around 40% of the anterior protrusions are not attached to the ECM in the wild type.....	177
Fig.5: The pattern of ECM motion after ablation is shifted toward the anterior in <i>sr¹</i>	178
Fig.6: Study of the relationships between migration velocity, Dpy deposition rates, protrusion polarity, difference of recoil between Dpy::YFP and tissue, and protrusion stretching after ablation.....	180
Fig.7: Dpy::YFP fibers show local movements of various amplitudes across the thorax.....	181
Fig.8: Thorax cells show a pattern of migration persistence, especially along the A-P axis.....	183
Fig.9: Comparison between cell contours and Dpy::YFP movements reveals similarities between tissue and ECM movements.....	185
Fig.10: Anterior and posterior thorax show different mechanical regimes of interaction with the ECM.....	186

Bibliography

1. Fristrom, D. & Fristrom, J. in *The development of Drosophila melanogaster* (ed. Press, C. S. H. L.) 843–897 (1993).
2. Tonning, A. *et al.* A transient luminal chitinous matrix is required to model epithelial tube diameter in the *Drosophila* trachea. *Dev. Cell* **9**, 423–430 (2005).
3. Shao, L., Devenport, M. & Jacobs-Lorena, M. The peritrophic matrix of hematophagous insects. *Arch. Insect Biochem. Physiol.* **47**, 119–125 (2001).
4. Goodyear, R. J. & Richardson, G. P. *Structure, Function, and Development of the Tectorial Membrane: An Extracellular Matrix Essential for Hearing. Current Topics in Developmental Biology* **130**, (Elsevier Inc., 2018).
5. Ray, R. P. *et al.* Patterned Anchorage to the Apical Extracellular Matrix Defines Tissue Shape in the Developing Appendages of *Drosophila*. *Dev. Cell* **34**, 310–322 (2015).
6. Bökel, C., Prokop, A. & Brown, N. H. Papillote and Piopio: *Drosophila* ZP-domain proteins required for cell adhesion to the apical extracellular matrix and microtubule organization. *J. Cell Sci.* **118**, 633–642 (2005).
7. Munster, S. *et al.* Integrin-mediated attachment of the blastoderm to the vitelline envelope impacts gastrulation of insects. *Nature* **568**, 395–399 (2019).
8. Walton, K. D., Freddo, A. M., Wang, S. & Gumucio, D. L. Generation of intestinal surface: an absorbing tale. *Development* **143**, 2261–2272 (2016).
9. Bennett, K. M., Walker, S. L. & Lo, D. D. Epithelial microvilli establish an electrostatic barrier to microbial adhesion. *Infect. Immun.* **82**, 2860–2871 (2014).
10. Lange, K. Regulation of cell volume via microvillar ion channels. *J. Cell. Physiol.* **185**, 21–35 (2000).
11. Hudspeth, A. J. Integrating the active process of hair cells with cochlear function. *Nat. Rev. Neurosci.* **15**, 600–614 (2014).
12. Fernandes, I. *et al.* Zona Pellucida Domain Proteins Remodel the Apical Compartment for Localized Cell Shape Changes. *Dev. Cell* **18**, 64–76 (2010).
13. Mahuzier, A. *et al.* Ependymal cilia beating induces an actin network to protect centrioles against shear stress. *Nat. Commun.* **9**, 1–14 (2018).
14. Bustamante-Marin, X. M. & Ostrowski, L. E. Cilia and mucociliary clearance. *Cold Spring Harb. Perspect. Biol.* **9**, 1–17 (2017).
15. Niessen, C. M. Tight Junctions / Adherens Junctions

18. Harrison, O. J. *et al.* The Extracellular Architecture of Adherens Junctions Revealed by Crystal Structures of Type I Cadherins. *Structure* **19**, 244–256 (2011).
19. Wu, Y., Vendome, J., Shapiro, L., Ben-shaul, A. & Honig, B. Transforming binding affinities from three dimensions to two with application to cadherin clustering. *Nature* **475**, 510–513 (2011).
20. Bajpai, S. *et al.* Alpha-Catenin mediates initial E-cadherin-dependent cell – cell recognition and subsequent bond strengthening. **105**, 18331–18336 (2008).
21. Peng, X., Cuff, L. E., Lawton, C. D. & DeMali, K. A. Vinculin regulates cell-surface E-cadherin expression by binding to β -catenin. *J. Cell Sci.* **123**, 567–577 (2010).
22. Leckband, D. E. & de Rooij, J. Cadherin Adhesion and Mechanotransduction. *Annu. Rev. Cell Dev. Biol.* **30**, 291–315 (2014).
23. St Johnston, D. & Sanson, B. Epithelial polarity and morphogenesis. *Curr. Opin. Cell Biol.* **23**, 540–546 (2011).
24. Diaz-de-la-Loza, M. del C. *et al.* Apical and Basal Matrix Remodeling Control Epithelial Morphogenesis. *Dev. Cell* **46**, 23–39 (2018).
25. Sherrard, K., Robin, F., Lemaire, P. & Munro, E. Sequential activation of apical and basolateral contractility drives ascidian endoderm invagination. *Curr. Biol.* **20**, 1499–1510 (2010).
26. Halfter, W. *et al.* New concepts in basement membrane biology. *FEBS J.* **282**, 4466–4479 (2015).
27. Brown, N. H. Cell-cell adhesion via the ECM: Integrin genetics in fly and worm. *Matrix Biol.* **19**, 191–201 (2000).
28. Cetera, M. *et al.* Epithelial rotation promotes the global alignment of contractile actin bundles during *Drosophila* egg chamber elongation. *Nat. Commun.* **5**, 1–12 (2014).
29. Horikoshi, Y. *et al.* Interaction between PAR-3 and the aPKC-PAR-6 complex is indispensable for apical domain development of epithelial cells. *J. Cell Sci.* **122**, 1595–1606 (2009).
30. Krahn, M. P., Bückers, J., Kastrup, L. & Wodarz, A. Formation of a Bazooka-Stardust complex is essential for plasma membrane polarity in epithelia. *J. Cell Biol.* **190**, 751–760 (2010).
31. Tanentzapf, G. & Tepass, U. Interactions between the crumbs, lethal giant larvae and bazooka pathways in epithelial polarization. *Nat. Cell Biol.* **5**, 46–52 (2003).
32. Takahashi, M., Nokihara, K. & Mihara, H. Mammalian Lgl Forms a Protein Complex with PAR-6 and aPKC Independently of PAR-3 to Regulate Epithelial Cell Polarity. *Curr. Biol.* **10**, 53–60 (2003).
33. Malt, A. L. *et al.* Par3 is essential for the establishment of planar cell polarity of inner ear hair cells. *Proc. Natl. Acad. Sci. U. S. A.* **116**, 4999–5008 (2019).
34. Maung, S. M. T. W. & Jenny, A. Planar cell polarity in *Drosophila*. *Organogenesis* **7**, 165–179 (2011).

35. Ghosh, M. & Schweisguth, F. Frizzled signalling controls orientation of asymmetric sense organ precursor cell divisions in *Drosophila*. *Nature* **435**, 19–22 (2005).
36. Adler, P. N. Planar signaling and morphogenesis in *Drosophila*. *Dev. Cell* **2**, 525–535 (2002).
37. Vladar, E. K., Antic, D. & Axelrod, J. D. Planar Cell Polarity Signaling : The Developing Cell's Compass. *Cold Spring Harb. Perspect. Biol.* 1–19 (2009). doi:10.1101/cshperspect.a002964
38. Narimatsu, M. *et al.* Regulation of Planar Cell Polarity by Smurf Ubiquitin Ligases. *Cell* **137**, 295–307 (2009).
39. Cho, B., Pierre-Louis, G., Sagner, A., Eaton, S. & Axelrod, J. D. Clustering and Negative Feedback by Endocytosis in Planar Cell Polarity Signaling Is Modulated by Ubiquitylation of Prickle. *PLoS Genet.* **11**, 1–29 (2015).
40. Wu, J., Roman, A. C., Carvajal-Gonzalez, J. M. & Mlodzik, M. Wg and Wnt4 provide long-range directional input to planar cell polarity orientation in *Drosophila*. *Nat. Cell Biol.* **15**, 1045–1055 (2013).
41. Rawls, A. S., Guinto, J. B. & Wolff, T. The cadherins fat and dachsous regulate dorsal/ventral signaling in the *Drosophila* eye. *Curr. Biol.* **12**, 1021–1026 (2002).
42. Zeidler, M. P., Perrimon, N. & Strutt, D. I. The four-jointed gene is required in the *Drosophila* eye for ommatidial polarity specification. *Curr. Biol.* **9**, 1363–1372 (1999).
43. Thomas, C. & Strutt, D. The roles of the cadherins Fat and Dachshous in planar polarity specification in *Drosophila*. *Dev. Dyn.* **241**, 27–39 (2012).
44. Adler, P. N., Charlton, J. & Liu, J. Mutations in the cadherin superfamily member gene dachsous cause a tissue polarity phenotype by altering frizzled signaling. *Development* **125**, 959–968 (1998).
45. Bosveld, F. *et al.* Mechanical Control of Morphogenesis by Fat/Dachshous/Four-Jointed Planar Cell Polarity Pathway. *Science* **336**, 724–727 (2012).
46. Ma, D., Yang, C. hui, McNeill, H., Simon, M. A. & Axelrod, J. D. Fidelity in planar cell polarity signalling. *Nature* **421**, 543–547 (2003).
47. Matakatsu, H. Interactions between Fat and Dachshous and the regulation of planar cell polarity in the *Drosophila* wing. *Development* **131**, 3785–3794 (2004).
48. Merkel, M. *et al.* The balance of prickle/spiny-legs isoforms controls the amount of coupling between core and fat PCP systems. *Curr. Biol.* **24**, 2111–2123 (2014).
49. Ayukawa, T. *et al.* Dachshous-Dependent Asymmetric Localization of Spiny-Legs Determines Planar Cell Polarity Orientation in *Drosophila*. *Cell Rep.* **8**, 610–621 (2014).
50. Mangione, F. & Martín-Blanco, E. The Dachshous/Fat/Four-Jointed Pathway Directs the Uniform Axial Orientation of Epithelial Cells in the *Drosophila* Abdomen. *Cell Rep.* **25**, 2836–2850 (2018).

51. Mao, Y., Francis-West, P. & Irvine, K. D. Fat4/Dchs1 signaling between stromal and cap mesenchyme cells influences nephrogenesis and ureteric bud branching. *Dev.* **142**, 2574–2585 (2015).
52. Saburi, S. *et al.* Loss of Fat4 disrupts PCP signaling and oriented cell division and leads to cystic kidney disease. *Nat. Genet.* **40**, 1010–1015 (2008).
53. Zakaria, S. *et al.* Regulation of neuronal migration by Dchs1-Fat4 planar cell polarity. *Curr. Biol.* **24**, 1620–1627 (2014).
54. Aigouy, B. *et al.* Cell Flow Reorients the Axis of Planar Polarity in the Wing Epithelium of *Drosophila*. *Cell* **142**, 773–786 (2010).
55. Olguín, P., Glavic, A. & Mlodzik, M. Intertissue mechanical stress affects frizzled-mediated planar cell polarity in the *drosophila notum* epidermis. *Curr. Biol.* **21**, 236–242 (2011).
56. Lawrence, P. A. Cell interactions and planar polarity in the abdominal epidermis of *Drosophila*. *Development* **131**, 4651–4664 (2004).
57. Zallen, J. A. & Wieschaus, E. Patterned Gene Expression Directs Bipolar Planar Polarity in *Drosophila*. *Dev. Cell* **6**, 343–355 (2004).
58. Paré, A. C. *et al.* A positional Toll receptor code directs convergent extension in *Drosophila*. *Nature* **515**, 523–527 (2014).
59. Barlan, K., Cetera, M. & Horne-Badovinac, S. Fat2 and Lar Define a Basally Localized Planar Signaling System Controlling Collective Cell Migration. *Dev. Cell* **40**, 467–477 (2017).
60. Squarr, A. J. *et al.* Fat2 acts through the WAVE regulatory complex to drive collective cell migration during tissue rotation. *J. Cell Biol.* **212**, 591–603 (2016).
61. Drees, F., Pokutta, S., Yamada, S., Nelson, W. J. & Weis, W. I. α -catenin is a molecular switch that binds E-cadherin- β -catenin and regulates actin-filament assembly. *Cell* **123**, 903–915 (2005).
62. Schulte, J., Tepass, U. & Auld, V. J. Gliotactin, a novel marker of tricellular junctions, is necessary for septate junction development in *Drosophila*. *J. Cell Biol.* **161**, 991–1000 (2003).
63. Byri, S. *et al.* The Triple-Repeat Protein Anakonda Controls Epithelial Tricellular Junction Formation in *Drosophila*. *Dev. Cell* **33**, 535–548 (2015).
64. Letizia, A. *et al.* Sidekick Is a Key Component of Tricellular Adherens Junctions that Acts to Resolve Cell Rearrangements. *Dev. Cell* **50**, 313–326 (2019).
65. Spencer, M. A., Jabeen, Z. & Lubensky, D. K. Vertex stability and topological transitions in vertex models of foams and epithelia. *Eur. Phys. J. E* **40**, 1–17 (2017).
66. Alt, S., Ganguly, P. & Salbreux, G. Vertex models: From cell mechanics to tissue morphogenesis. *Philos. Trans. R. Soc. B Biol. Sci.* **372**, 1–10 (2017).
67. Bertet, C., Sulak, L. & Lecuit, T. Myosin-dependent junction remodelling controls planar cell intercalation and axis elongation. *Nature* **429**, 667–671 (2004).

68. Röper, K. Supracellular actomyosin assemblies during development. *Bioarchitecture* **3**, 45–9 (2013).
69. Umetsu, D. *et al.* Local increases in mechanical tension shape compartment boundaries by biasing cell intercalations. *Curr. Biol.* **24**, 1798–1805 (2014).
70. Monier, B., Péliissier-Monier, A. & Sanson, B. Establishment and maintenance of compartmental boundaries: Role of contractile actomyosin barriers. *Cell. Mol. Life Sci.* **68**, 1897–1910 (2011).
71. Scarpa, E., Finet, C., Blanchard, G. B. & Sanson, B. Actomyosin-Driven Tension at Compartmental Boundaries Orients Cell Division Independently of Cell Geometry In Vivo. *Dev. Cell* **47**, 727–740 (2018).
72. Mason, F. M., Tworoger, M. & Martin, A. C. Apical domain polarization localizes actin-myosin activity to drive ratchet-like apical constriction. *Nat. Cell Biol.* **15**, 926–36 (2013).
73. Solon, J., Kaya-Çopur, A., Colombelli, J. & Brunner, D. Pulsed Forces Timed by a Ratchet-like Mechanism Drive Directed Tissue Movement during Dorsal Closure. *Cell* **137**, 1331–1342 (2009).
74. Bischoff, M. Lamellipodia-based migrations of larval epithelial cells are required for normal closure of the adult epidermis of *Drosophila*. *Dev. Biol.* **363**, 179–190 (2012).
75. Sui, L. *et al.* Differential lateral and basal tension drive folding of *Drosophila* wing discs through two distinct mechanisms. *Nat. Commun.* **9**, 1–13 (2018).
76. Monier, B. *et al.* Apico-basal forces exerted by apoptotic cells drive epithelium folding. *Nature* **518**, 245–248 (2015).
77. Gracia, M. *et al.* Mechanical impact of epithelial–mesenchymal transition on epithelial morphogenesis in *Drosophila*. *Nat. Commun.* **10**, 1–17 (2019).
78. Wang, Y. C., Khan, Z., Kaschube, M. & Wieschaus, E. F. Differential positioning of adherens junctions is associated with initiation of epithelial folding. *Nature* **484**, 390–393 (2012).
79. Martin, A. C. & Goldstein, B. Apical constriction: themes and variations on a cellular mechanism driving morphogenesis. *Development* **141**, 1987–1998 (2014).
80. Ogura, Y., Wen, F. L., Sami, M. M., Shibata, T. & Hayashi, S. A Switch-like Activation Relay of EGFR-ERK Signaling Regulates a Wave of Cellular Contractility for Epithelial Invagination. *Dev. Cell* **46**, 1–11 (2018).
81. Manjón, C., Sánchez-Herrero, E. & Suzanne, M. Sharp boundaries of Dpp signalling trigger local cell death required for *Drosophila* leg morphogenesis. *Nat. Cell Biol.* **9**, 57–63 (2007).
82. Ambrosini, A., Rayer, M., Monier, B. & Suzanne, M. Mechanical Function of the Nucleus in Force Generation during Epithelial Morphogenesis. *Dev. Cell* **50**, 197–211 (2019).

83. Lohmann, I., McGinnis, N., Bodmer, M. & McGinnis, W. The *Drosophila* Hox gene *Deformed* sculpts head morphology via direct regulation of the apoptosis activator reaper. *Cell* **110**, 457–466 (2002).
84. Yamaguchi, Y. *et al.* Live imaging of apoptosis in a novel transgenic mouse highlights its role in neural tube closure. *J. Cell Biol.* **195**, 1047–1060 (2011).
85. Weil, M., Jacobson, M. D. & Raff, M. C. Is programmed cell death required for neural tube closure? *Curr. Biol.* **7**, 281–284 (1997).
86. Kalluri, R. & Weinberg, R. A. The basic of epithelial-mesenchymal transition. *J. Clin. Invest.* **119**, 1420–1428 (2009).
87. Urbansky, S., Avalos, P. G., Wosch, M. & Lemke, S. Folded gastrulation and T48 drive the evolution of coordinated mesoderm internalization in flies. *Elife* **5**, 1–20 (2016).
88. Takeda, M., Sami, M. M. & Wang, Y. C. A homeostatic apical microtubule network shortens cells for epithelial folding via a basal polarity shift. *Nat. Cell Biol.* **20**, 36–45 (2018).
89. Ninov, N., Chiarelli, D. & Martín-Blanco, E. Extrinsic and intrinsic mechanisms directing epithelial cell sheet replacement during *Drosophila* metamorphosis. *Development* **134**, 367–379 (2007).
90. Ambrosini, A. *et al.* Apoptotic forces in tissue morphogenesis. *Mech. Dev.* **144**, 33–42 (2017).
91. Geudens, I. & Gerhardt, H. Coordinating cell behaviour during blood vessel formation. *Development* **138**, 4569–4583 (2011).
92. Lewis, W. H. Mechanics of invagination. *Anat. Rec.* **97**, 139–156 (1947).
93. Rhumbler, L. Zur Mechanik des Gastrulationsvorganges insbesondere der Invagination. *Arch. für Entwicklungsmechanik der Org.* **14**, 401–476 (1902).
94. Hardin, J. & Keller, R. The behaviour and function of bottle cells during gastrulation of *Xenopus laevis*. *Development* **103**, 211–30 (1988).
95. McShane, S. G. *et al.* Cellular basis of neuroepithelial bending during mouse spinal neural tube closure. *Dev. Biol.* **404**, 113–124 (2015).
96. Lee, J.-Y. Mechanisms of cell positioning during *C. elegans* gastrulation. *Development* **130**, 307–320 (2003).
97. Kimberly, E. L. & Hardin, J. Bottle cells are required for the initiation of primary invagination in the sea urchin embryo. *Dev. Biol.* **204**, 235–250 (1998).
98. Eiraku, M. *et al.* Self-organizing optic-cup morphogenesis in three-dimensional culture. *Nature* **472**, 51–58 (2011).
99. Matt, G. & Umen, J. *Volvox*: A simple algal model for embryogenesis, morphogenesis and cellular differentiation. *Dev. Biol.* **419**, 99–113 (2016).
100. Fernandes, V. M., McCormack, K., Lewellyn, L. & Verheyen, E. M. Integrins Regulate Apical Constriction via Microtubule Stabilization in the *Drosophila* Eye Disc Epithelium. *Cell Rep.* **9**, 2043–2055 (2014).

101. Leptin, M. & Grunewald, B. Cell shape changes during gastrulation in *Drosophila*. *Development* **110**, 73–84 (1990).
102. Costa, M., Wilson, E. T. & Wieschaus, E. A putative cell signal encoded by the folded gastrulation gene coordinates cell shape changes during *Drosophila* gastrulation. *Cell* **76**, 1075–1089 (1994).
103. Kölsch, V., Seher, T., Fernandez-Ballester, G. J., Serrano, L. & Leptin, M. Control of *drosophila* gastrulation by apical localization of adherens junctions and RhoGEF2. *Science* **315**, 384–386 (2007).
104. Fox, D. T. & Peifer, M. Abelson kinase (Abl) and RhoGEF2 regulate actin organization during cell constriction in *Drosophila*. *Development* **134**, 567–578 (2007).
105. Barrett, K., Leptin, M. & Settleman, J. The Rho GTPase and a putative RhoGEF mediate a signaling pathway for the cell shape changes in *Drosophila* gastrulation. *Cell* **91**, 905–915 (1997).
106. Munjal, A., Philippe, J. M., Munro, E. & Lecuit, T. A self-organized biomechanical network drives shape changes during tissue morphogenesis. *Nature* **524**, 351–355 (2015).
107. Yevick, H. G., Miller, P. W., Dunkel, J. & Martin, A. C. Structural Redundancy in Supracellular Actomyosin Networks Enables Robust Tissue Folding. *Dev. Cell* **50**, 1–13 (2019).
108. He, B., Dubrovinski, K., Polyakov, O. & Wieschaus, E. Apical constriction drives tissue-scale hydrodynamic flow to mediate cell elongation. *Nature* **508**, 392–396 (2014).
109. Lee, J. & Harland, R. M. Actomyosin contractility and microtubules drive apical constriction in *Xenopus* bottle cells. **311**, 40–52 (2007).
110. Popov, I. K., Ray, H. J., Skoglund, P., Keller, R. & Chang, C. The RhoGEF protein Plekhg5 regulates apical constriction of bottle cells during gastrulation. *Development* **145**, 1–10 (2018).
111. Lee, J. Y. & Harland, R. M. Endocytosis Is Required for Efficient Apical Constriction during *Xenopus* Gastrulation. *Curr. Biol.* **20**, 253–258 (2010).
112. Chanet, S. *et al.* Actomyosin meshwork mechanosensing enables tissue shape to orient cell force. *Nat. Commun.* **8**, 1–13 (2017).
113. Sweeton, D., Parks, S., Costa, M. & Wieschaus, E. Gastrulation in *Drosophila* : the formation of the ventral furrow and posterior midgut invaginations. **789**, 775–789 (1991).
114. Hannezo, E., Prost, J. & Joanny, J.-F. Theory of epithelial sheet morphology in three dimensions. *Proc. Natl. Acad. Sci.* **111**, 27–32 (2014).
115. Nishimura, M., Inoue, Y. & Hayashi, S. A wave of EGFR signaling determines cell alignment and intercalation in the *Drosophila* tracheal placode. *Development* **134**, 4273–4282 (2007).

116. Röper, K. Anisotropy of Crumbs and aPKC Drives Myosin Cable Assembly during Tube Formation. *Dev. Cell* **23**, 939–953 (2012).
117. Biellemeier, C. *et al.* Interface Contractility between Differently Fated Cells Drives Cell Elimination and Cyst Formation. *Curr. Biol.* **26**, 563–574 (2016).
118. Czerniak, N. D., Dierkes, K., D’Angelo, A., Colombelli, J. & Solon, J. Patterned Contractile Forces Promote Epidermal Spreading and Regulate Segment Positioning during *Drosophila* Head Involution. *Curr. Biol.* **26**, 1895–1901 (2016).
119. Zhao, J. & Wang, Q. Modeling cytokinesis of eukaryotic cells driven by the actomyosin contractile ring. *Int. j. numer. method. biomed. eng.* **26**, 807–827 (2016).
120. Urbano, J. M., Naylor, H. W., Scarpa, E., Muresan, L. & Sanson, B. Suppression of epithelial folding at actomyosin-enriched compartment boundaries downstream of Wingless signalling in *Drosophila*. *Development* **145**, 1–13 (2018).
121. Liu, S., Sun, J., Wang, D., Pflugfelder, G. O. & Shen, J. Fold formation at the compartment boundary of *Drosophila* wing requires Yki signaling to suppress JNK dependent apoptosis. *Sci. Rep.* **6**, 1–7 (2016).
122. Saia, L. *et al.* Decrease in Cell Volume Generates Contractile Forces Driving Dorsal Closure. *Dev. Cell* **33**, 611–621 (2015).
123. Gelbart, M. A. *et al.* Volume conservation principle involved in cell lengthening and nucleus movement during tissue morphogenesis. *Proc. Natl. Acad. Sci. U. S. A.* **109**, 19298–19303 (2012).
124. Widmann, T. J. & Dahmann, C. Dpp signaling promotes the cuboidal-to-columnar shape transition of *Drosophila* wing disc epithelia by regulating Rho1. *J. Cell Sci.* **122**, 1362–1373 (2009).
125. Grego-Bessa, J. *et al.* The tumor suppressor PTEN and the PDK1 kinase regulate formation of the columnar neural epithelium. *Elife* **5**, 1–22 (2016).
126. Muliyl, S., Krishnakumar, P. & Narasimha, M. Spatial, temporal and molecular hierarchies in the link between death, delamination and dorsal closure. *Development* **138**, 3043–3054 (2011).
127. Delpire, E. & Gagnon, K. B. *Water Homeostasis and Cell Volume Maintenance and Regulation. Current Topics in Membranes* **81**, (Elsevier Ltd, 2018).
128. Sawyer, J. M. *et al.* Apical constriction : A cell shape change that can drive morphogenesis. *Dev. Biol.* **341**, 5–19 (2010).
129. Bischoff, M. & Cseresnyés, Z. Cell rearrangements, cell divisions and cell death in a migrating epithelial sheet in the abdomen of *Drosophila*. *Development* **136**, 2403–2411 (2009).
130. Gorfinkiel, N., Schamberg, S. & Blanchard, G. B. Integrative Approaches to Morphogenesis : Lessons From Dorsal Closure. **533**, 522–533 (2011).
131. Gomez, J. M., Wang, Y. & Riechmann, V. Tao controls epithelial morphogenesis by promoting fasciclin 2 endocytosis. *J. Cell Biol.* **199**, 1131–1143 (2012).

132. Nakajima, Y.-I., Kuranaga, E., Sugimura, K., Miyawaki, A. & Miura, M. Nonautonomous apoptosis is triggered by local cell cycle progression during epithelial replacement in *Drosophila*. *Mol. Cell. Biol.* **31**, 2499–512 (2011).
133. Werner, M. E. *et al.* Radial intercalation is regulated by the par complex and the microtubule-stabilizing protein CLAMP/Spf1. *J. Cell Biol.* **206**, 367–376 (2014).
134. Rauzi, M., Lenne, P. F. & Lecuit, T. Planar polarized actomyosin contractile flows control epithelial junction remodelling. *Nature* **468**, 1110–1115 (2010).
135. Sun, Z. *et al.* Basolateral protrusion and apical contraction cooperatively drive *Drosophila* germ-band extension. *Nat. Cell Biol.* (2017). doi:10.1038/ncb3497
136. Chisholm, A. D. & Hardin, J. Epidermal morphogenesis. *WormBook*

148. Shellard, A., Szabó, A., Trepát, X. & Mayor, R. Supracellular contraction at the rear of neural crest cell groups drives collective chemotaxis. *Science* **362**, 339–343 (2018).
149. Shellard, A. & Mayor, R. Supracellular migration - Beyond collective cell migration. *J. Cell Sci.* **132**, 1–11 (2019).
150. Polarity, C. C. *et al.* Collective Chemotaxis Requires Contact-Dependent Cell Polarity. *Dev. Cell* **19**, 39–53 (2010).
151. Donà, E. *et al.* Directional tissue migration through a self-generated chemokine gradient. *Nature* **503**, 285–289 (2013).
152. Theveneau, E. *et al.* Chase-and-run between adjacent cell populations promotes directional collective migration. *Nat. Cell Biol.* **15**, 763–772 (2013).
153. Majumdar, R., Sixt, M. & Parent, C. A. New paradigms in the establishment and maintenance of gradients during directed cell migration. *Current Opinion in Cell Biology* **30**, 33–40 (2014).
154. Sunyer, R. *et al.* Collective cell durotaxis emerges from long-range intercellular force transmission. **353**, 1157–1162 (2016).
155. Stedden, C. G. *et al.* Planar-Polarized Semaphorin-5c and Plexin A Promote the Collective Migration of Epithelial Cells in *Drosophila*. *Curr. Biol.* **29**, 1–13 (2019).
156. Haigo, S. L. & Bilder, D. Global Tissue Revolutions in a Morphogenetic Movement Controlling Elongation. *Science* **331**, 1071–1074 (2017).
157. Arata, M., Sugimura, K. & Uemura, T. Difference in Dachsous Levels between Migrating Cells Coordinates the Direction of Collective Cell Migration. *Dev. Cell* **42**, 479–497 (2017).
158. Lash, J. W., Gosfield, E., Ostrovsky, D. & Bellairs, R. Migration of chick blastoderm under the vitelline membrane: The role of fibronectin. *Dev. Biol.* **139**, 407–416 (1990).
159. Ducuing, A. & Vincent, S. The actin cable is dispensable in directing dorsal closure dynamics but neutralizes mechanical stress to prevent scarring in the *Drosophila* embryo. *Nat. Cell Biol.* **18**, 1149–1160 (2016).
160. Levayer, R., Dupont, C., Levayer, R., Dupont, C. & Moreno, E. Tissue Crowding Induces Caspase-Dependent Competition for Space Tissue Crowding Induces Caspase-Dependent Competition for Space. *Curr. Biol.* **26**, 670–677 (2016).
161. Szabó, A. *et al.* The Molecular Basis of Radial Intercalation during Tissue Spreading in Early Development. *Dev. Cell* **37**, 213–225 (2016).
162. Morita, H. *et al.* The Physical Basis of Coordinated Tissue Spreading in Zebrafish Gastrulation. *Dev. Cell* **40**, 354–366 (2017).
163. Kolahi, K. S. *et al.* Quantitative analysis of epithelial morphogenesis in *Drosophila* oogenesis : New insights based on morphometric analysis and mechanical modeling. *Dev. Biol.* **331**, 129–139 (2009).
164. Etournay, R. *et al.* Interplay of cell dynamics and epithelial tension during morphogenesis of the *Drosophila* pupal wing. *Elife* **4**, 1–51 (2015).

165. Ray, R. P. *et al.* Patterned Anchorage to the Apical Extracellular Matrix Defines Tissue Shape in the Developing Appendages of *Drosophila*. *Dev. Cell* **34**, 310–322 (2015).
166. Layton, A. T. *et al.* *Drosophila* morphogenesis : tissue force laws and the modeling of dorsal closure. **3**, 441–460 (2009).
167. Behrndt, M., Roensch, J., Grill, S. W. & Heisenberg, C. Forces Driving Epithelial Spreading in Zebrafish Gastrulation. **257**, 10–14 (2013).
168. Hardin, J. The role of secondary mesenchyme cells during sea urchin gastrulation studied by laser ablation. **324**, 317–324 (1988).
169. Hardin, J. & Weliky, M. Cell rearrangement induced by filopodial tension accounts for the late phase of convergent extension in the sea urchin archenteron. *Mol. Biol. Cell* **30**, 1911–1919 (2019).
170. Affolter, M. & Caussinus, E. Tracheal branching morphogenesis in *Drosophila*: new insights into cell behaviour and organ architecture. *Development* **135**, 2055–2064 (2008).
171. Lye, C. M. *et al.* Mechanical Coupling between Endoderm Invagination and Axis Extension in *Drosophila*. *PLoS Biol.* **13**, 1–28 (2015).
172. Collinet, C., Rauzi, M., Lenne, P. F. & Lecuit, T. Local and tissue-scale forces drive oriented junction growth during tissue extension. *Nat. Cell Biol.* **17**, 1247–1258 (2015).
173. Zhang, H. *et al.* A tension-induced mechanotransduction pathway promotes epithelial morphogenesis. *Nature* **471**, 99–103 (2011).
174. Vuong-Brender, T. T. K., Ben Amar, M., Pontabry, J. & Labouesse, M. The interplay of stiffness and force anisotropies drives embryo elongation. *Elife* **6**, 1–49 (2017).
175. Quintin, S. *et al.* Non-centrosomal epidermal microtubules act in parallel to LET-502/ROCK to promote *C. elegans*. *Development* **145**, 160–173 (2018).
176. Saadaoui, M., Corson, F., Rocancourt, D., Roussel, J. & Gros, J. A tensile ring drives tissue flows to shape the gastrulating amniote embryo. *bioRxiv* (2018). doi:10.1101/412767
177. Smutny, M. *et al.* Friction forces position the neural anlage. *Nat. Cell Biol.* **19**, 306–317 (2017).
178. Firmino, J. *et al.* Cell Division Drives Epithelial Cell Rearrangements during Gastrulation in Chick Cell Division Drives Epithelial Cell Rearrangements during Gastrulation in Chick. *Dev. Cell* **36**, 249–261 (2016).
179. Petridou, N. I., Grigolon, S., Salbreux, G., Hannezo, E. & Heisenberg, C. P. Fluidization-mediated tissue spreading by mitotic cell rounding and non-canonical Wnt signalling. *Nat. Cell Biol.* **21**, 169–178 (2019).
180. Odell, G. M., Oster, G., Alberch, P. & Burnside, B. The mechanical basis of morphogenesis. I. Epithelial folding and invagination. *Dev. Biol.* **85**, 446–462 (1981).

181. Hocevar Brezavšek, A., Rauzi, M., Leptin, M. & Ziherl, P. A model of epithelial invagination driven by collective mechanics of identical cells. *Biophys. J.* **103**, 1069–1077 (2012).
182. Monier, B., Péliissier-Monier, A., Brand, A. H. & Sanson, B. An actomyosin-based barrier inhibits cell mixing at compartmental boundaries in *Drosophila* embryos. *Nat. Cell Biol.* **12**, 60–65 (2010).
183. Hughes, C. L. & Kaufman, T. C. Hox genes and the evolution of the arthropod body plan. *Evol. Dev.* **499**, 459–499 (2002).
184. Krueger, D., Tardivo, P., Nguyen, C. & De Renzis, S. Downregulation of basal myosin II is required for cell shape changes and tissue invagination. *EMBO J.* **37**, 1–16 (2018).
185. McGuire, S. E., Le, P. T., Osborn, A. J., Matsumoto, K. & Davis, R. L. Spatiotemporal Rescue of Memory Dysfunction in *Drosophila*. *Science* **302**, 1765–1768 (2003).
186. Ogura, Y., Wen, F. L., Sami, M. M., Shibata, T. & Hayashi, S. A Switch-like Activation Relay of EGFR-ERK Signaling Regulates a Wave of Cellular Contractility for Epithelial Invagination. *Dev. Cell* **46**, 162–172 (2018).
187. Spencer, A. K., Siddiqui, B. A. & Thomas, J. H. Cell shape change and invagination of the cephalic furrow involves reorganization of F-actin. *Dev. Biol.* **402**, 192–207 (2015).
188. Calzolari, S., Terriente, J. & Pujades, C. Cell segregation in the vertebrate hindbrain relies on actomyosin cables located at the interhombomeric boundaries. *EMBO J.* **33**, 686–701 (2014).
189. Guirao, B. *et al.* Unified quantitative characterization of epithelial tissue development. *Elife* **4**, e08519 (2015).
190. Munjal, A. & Lecuit, T. Actomyosin networks and tissue morphogenesis. *Development* **141**, 1789–1793 (2014).
191. Rosenblatt, J., Raff, M. C. & Cramer, L. P. An epithelial cell destined for apoptosis signals its neighbors to extrude it by an actin- and myosin-dependent mechanism. *Curr. Biol.* 1847–1857 (2001).
192. Heisenberg, C. P. & Bellaïche, Y. Forces in tissue morphogenesis and patterning. *Cell* **153**, 948–962 (2013).
193. Schwyer, C., Sikora, M., Slovák, J., Kardos, R. & Heisenberg, C. P. Actin Rings of Power. *Dev. Cell* **37**, 493–506 (2016).
194. Friedl, P. & Gilmour, D. Collective cell migration in morphogenesis, regeneration and cancer. *Nat. Rev. Mol. Cell Biol.* **10**, 445–457 (2009).
195. Scarpa, E. & Mayor, R. Collective cell migration in development. *J. Cell Biol.* **212**, 143–155 (2016).
196. Barriga, E. H., Franze, K., Charras, G. & Mayor, R. Tissue stiffening coordinates morphogenesis by triggering collective cell migration in vivo. *Nature* **554**, 523–527 (2018).

197. Reig, G., Pulgar, E. & Concha, M. L. Cell migration: From tissue culture to embryos. *Dev.* **141**, 1999–2013 (2014).
198. Sobala, L. F., Wang, Y. & Adler, P. N. ChtVis-Tomato, a genetic reporter for in vivo visualization of chitin deposition in *Drosophila*. *Development* **142**, 3974–3981 (2015).
199. Turner, C. M. & Adler, P. N. Morphogenesis of *Drosophila* pupal wings in vitro. *Mech. Dev.* **52**, 247–255 (1995).
200. Wilkin, M. B. *et al.* *Drosophila* dumpy is a gigantic extracellular protein required to maintain tension at epidermal-cuticle attachment sites. *Curr. Biol.* **10**, 559–567 (2000).
201. Metcalfe, J. a. Of dumpy. *Genet* **65**, 627–654 (1970).
202. Weitkunat, M., Kaya-Çopur, A., Grill, S. W. & Schnorrer, F. Tension and force-resistant attachment are essential for myofibrillogenesis in *drosophila* flight muscle. *Curr. Biol.* **24**, 705–716 (2014).
203. Proag, A., Monier, B. & Suzanne, M. Physical and functional cell-matrix uncoupling in a developing tissue under tension. *Development* **146**, 1–9 (2019).
204. Wilkin, M. B. *et al.* *Drosophila* Dumpy is a gigantic extracellular protein required to maintain tension at epidermal – cuticle attachment sites. *Curr. Biol.* **10**, 559–567 (2000).
205. Lye, C. M. *et al.* Mechanical Coupling between Endoderm Invagination and Axis Extension in *Drosophila*. *PLoS Biol.* **13**, 1–27 (2015).
206. Huang, X. *et al.* Matrix stiffness-induced myofibroblast differentiation is mediated by intrinsic mechanotransduction. *Am. J. Respir. Cell Mol. Biol.* **47**, 340–348 (2012).
207. Frye, M. *et al.* Matrix stiffness controls lymphatic vessel formation through regulation of a GATA2-dependent transcriptional program. *Nat. Commun.* **9**, 1–16 (2018).
208. Wang, H. B., Dembo, M. & Wang, Y. L. Substrate flexibility regulates growth and apoptosis of normal but not transformed cells. *Am. J. Physiol. - Cell Physiol.* **279**, 1345–1350 (2000).
209. Raab, M. *et al.* Crawling from soft to stiff matrix polarizes the cytoskeleton and phosphoregulates myosin-II heavy chain. *J. Cell Biol.* **199**, 669–683 (2012).
210. Wehner, R. *et al.* Collective cell durotaxis emerges from long-range intercellular force transmission. *Science* **353**, 1157–1161 (2019).
211. Butcher, D. T., Alliston, T. & Weaver, V. M. A tense situation: Forcing tumour progression. *Nat. Rev. Cancer* **9**, 108–122 (2009).
212. Lu, P., Weaver, V. M. & Werb, Z. The extracellular matrix: A dynamic niche in cancer progression. *J. Cell Biol.* **196**, 395–406 (2012).
213. Huang, J., Zhou, W., Dong, W., Watson, A. M. & Hong, Y. Directed, efficient, and versatile modifications of the *Drosophila* genome by genomic engineering. *Proc. Natl. Acad. Sci. U. S. A.* **106**, 8284–8289 (2009).
214. Pinheiro, D. *et al.* Transmission of cytokinesis forces via E-cadherin dilution and actomyosin flows. *Nat. Publ. Gr.* **545**, 103–107 (2017).

215. Royou, A., Field, C., Sullivan, J., William, C. S. & Karess, R. Reassessing the Role and Dynamics of Nonmuscle Myosin II during Furrow Formation in Early *Drosophila* Embryos. *Mol. Biol. Cell* **15**, 1623–1634 (2004).
216. Schnorrer, F. *et al.* Systematic genetic analysis of muscle morphogenesis and function in *Drosophila*. *Nature* **464**, 287–291 (2010).
217. Ni, J. Q. *et al.* A genome-scale shRNA resource for transgenic RNAi in *Drosophila*. *Nat. Methods* **8**, 405–407 (2011).
218. Jenett, A. *et al.* A GAL4-Driver Line Resource for *Drosophila* Neurobiology. *Cell Rep.* **2**, 991–1001 (2012).
219. Gratz, S. J. *et al.* Highly specific and efficient CRISPR/Cas9-catalyzed homology-directed repair in *Drosophila*. *Genetics* **196**, 961–971 (2014).
220. Brand, A. H. & Perrimon, N. Targeted gene expression as a means of altering cell fates and generating dominant phenotypes. *Development* **118**, 401–415 (1993).
221. Xu, T. & Rubin, G. M. Analysis of genetic mosaics in developing and adult *Drosophila* tissues. *Development* **117**, 1223–1237 (1993).
222. Ségalen, M. *et al.* The Fz-Dsh Planar Cell Polarity Pathway Induces Oriented Cell Division via Mud/NuMA in *Drosophila* and Zebrafish. *Dev. Cell* **19**, 740–752 (2010).
223. David, N. B. *et al.* *Drosophila* Ric-8 regulates Gai cortical localization to promote Gai-dependent planar orientation of the mitotic spindle during asymmetric cell division. *Nat. Cell Biol.* **7**, 1083–1090 (2005).
224. Bainbridge, S. P. & Bownes, M. Staging the metamorphosis of *Drosophila melanogaster*. *J. Embryol. Exp. Morphol.* **66**, 57–80 (1981).
225. Garcia, D. Robust smoothing of gridded data in one and higher dimensions with missing values. *Comput. Stat. Data Anal.* **54**, 1167–1178 (2010).
226. Kuleesha, Y., Puah, W. C. & Wasser, M. Live imaging of muscle histolysis in *Drosophila* metamorphosis. *BMC Dev. Biol.* **16**, 1–18 (2016).
227. Durande, M. *et al.* Fast determination of coarse-grained cell anisotropy and size in epithelial tissue images using Fourier transform. *Phys. Rev. E* **99**, 1–13 (2019).
228. Philipp Berens. CircStat: A MATLAB Toolbox for Circular Statistics. *Wiley Interdiscip. Rev. Comput. Stat.* **1**, 128–129 (2009).

